SC

MAGNETIC PHENOMENA AND HYSTERESIS LOSSES IN RIBBONS OF TYPE II SUPERCONDUCTORS IN ORTHOGONAL OSCILLATING AND BIAS MAGNETIC FIELDS

André Lachaine

Dissertation submitted to the School of Graduate Studies of the University of Ottawa in partial fulfillment of the requirements for the degree Doctor of Philosophy

1976

DEDICACE

A Carole, Martin et Alexis

ACKNOWLEDGEMENTS

I wish to thank my thesis director, Dr. Marcel LeBlanc, for his excellent guidance, his keen interest and his friendly encouragement in the accomplishment of this project.

I am indebted to Raymond Gauthier, Raymond Boyer and Jean Bussière for the friendship and advice with which they provided me throughout the experiments.

I gratefully acknowledge the aid of Raymond Boyer in the computer calculations.

I wish to express my immense gratitude to my parents and my uncle, Emile Latendresse, who have made it possible for me to pursue my education.

I cannot begin to thank my wife, Carole, for the self-sacrifice and encouragement she has provided me throughout this project.

Finally, I am indebted to Miss Lise Menard for typing this thesis.

This research was supported by the Defense Research Board and by the National Research Council of Canada.

TABLES OF CONTENTS

LIST OF FIGURES

List of Tables

Abstract

We investigate the magnetic response of ribbons of type II superconductors (NbTi and VTi) subjected to a slowly varying transverse magnetic field $H_{\perp}$ directed along the wide face immersed in a static longitudinal bias magnetic field $H_{//}$. This is equivalent to measuring the complex susceptibility of these materials at low frequency when a driving or oscillating field of large amplitude is applied orthogonally to a bias field. The situation we explore is also analogous to that where an alternating conduction current fed from a current supply is made to flow along a ribbon placed in a steady longitudinal magnetic field. In our experiments, the persistent transport currents are generated by induction as the externally applied driving transverse field is varied and cycled. In all these situations, the magnetic field at the surface of the ribbon rotates as its magnitude varies. Consequently flux of varying density and direction enters (or leaves) the body of the specimen as the surface field is swept and oscillates.

We monitor the evolution of the magnetization hence the variation of the permeability along both the length and width of the ribbon simultaneously as the driving transverse field is impressed, removed and varied through complete cycles during which its polarity either reverses or does not reverse (corresponding to full wave and half wave A.C.). These measurements show that the transverse component of the magnetization hence the average longitudi-

dinal critical current density are considerably enhanced and that the energy dissipation per cycle can be dramatically reduced as the bias static longitudinal field is made larger over a broad range $0 < H_{//}/H_{c2} \lesssim 1/2$.

The critical state concept $F_L = F_p$, where F_L is the driving Lorentz force density and F_p is the opposing pinning force density, successfully accounts for the magnetic behaviour and critical current curves of irreversible type II superconductors when the external magnetic field varies in intensity only. In our work however the configuration of magnetic induction $\vec{B}$ and the pattern of persistent current densities $\vec{J}$ undergo changes both in magnitude and direction concurrently with position and time. The literature contains the basis of two radically different schemes to treat this situation: (i) no constraints impede the rotation and displacement of the vortices as they adopt force free configurations with $\vec{J} \times \vec{B} = 0$ and (ii) the vortices maintain their orientation of creation at the surface as they are subsequently compressed and advance in the sample. In our analysis we view the ribbons as infinite slabs. We pursue the consequences of these contrasting concepts in much detail. Among the many solutions of the force free problem we focus on a few physically interesting and analytically simple cases. We examine the predictions of the non-rotation model in the two possible contexts where pinning a) does not exist and b) does exist and impedes the advance of the flux lines. We explore the behaviour expected in the latter case for pinning functions with significantly different characteristics. We conclude that both of these schemes are unsuitable to account for our observations. Indeed we show that the concept that rotation is not allowed, although a pleasure to unfold and develop, leads to physically unacceptable phenomena. Further we bring out that the basic idea is a one way street and intrinsically incapable of describing the events encountered in this work.

Finally, we develop on a phenomenological basis, a critical state equation to govern the rotation of the vortices. We show that the simple prescription $d\theta/dx = \pm \gamma F_p/B^2 \tan\theta$ (where γ is the only adjustable parameter for a given material) in tandem with the corresponding critical state equation can establish sequences of θ and B profiles which account quite satisfactorily for the extensive assortment of observations we have accumulated on two materials. These include families of curves of the evolution of both the longitudinal and transverse components of the magnetization as $H_\perp$ is applied or removed as well as the locus of these quantities as $H_\perp$ is cycled over several amplitudes through different mid or central values for various static $H_{//}$. From the last measurements we extract data on the variation of hysteresis losses.

CHAPTER 1

INTRODUCTION

The critical state model (Bean 64) adequately describes the penetration (or exit) of magnetic flux in hard type II superconductors, as an external magnetic field is varied slowly. According to this model, a critical current density, J_c (B, T), exists which depends on the local magnetic induction, B, and the temperature, T, and any emf, however small, will induce the full critical current density to flow locally inside the superconductor. Therefore, in the regions which experienced a change in magnetic induction (hence an emf), a persistent current is flowing whose magnitude is determined by the limiting value of J_c and whose sense of circulation is determined by the Faraday-Lenz law of induction.

The relation between current density and magnetic field is given by Maxwell's equation

$$\mathrm{curl}\ \vec{H} = \frac{4\pi}{c}\vec{J}_c$$

which, in the case of a slab, infinite in the y and z directions, takes the form

$$\frac{\partial H}{\partial x} = \pm \frac{4\pi}{c} J_c$$

This model adequately reproduces the hysteretic magnetization curves in hard type II superconductors. The model leads to magnetic field profiles inside a superconductor which depend on the way in which the field is applied, i.e., on "magnetic history". Flux in type II superconductors has been shown to exist in the form of quantized vortices as predicted by Abrikosov (Abrikosov 57) and observed "directly" by Trauble and Essman (Trauble 68). In "hard" type II superconductors these vortices are strongly pinned by lattice defects, impurities, imperfections, grain boundaries, etc. A strong pinning of these vortices leads to high critical current densities and also to very irreversible magnetic behaviour.

According to prevailing views, the critical current density, J_c, is reached when the Lorentz force density on the fluxons, $\vec{J} \times \vec{B}$, exceeds the opposing pinning force density, F_p (T, B). This concept suggests that for a given magnetic induction $\vec{B}$, the critical current density can be made larger if $\vec{J}$ is caused to flow along the lines of magnetic induction. Indeed, in the limit where $\vec{J}$ is perfectly parallel to $\vec{B}$, the current flow is said to be force-free ($\vec{J} \times \vec{B} = 0$) and the critical state concept imposes no limit on J_c.

Experimentally, Sekula et al (Sekula 63) discovered that the critical currents in NbZr, MoRe, and TaTi wires were enhanced in the presence of a magnetic field directed along the length of the sample. Bergeron (Bergeron 63) explained this by assuming that the current density flowed everywhere parallel to the total local magnetic induction, thus reducing the Lorentz force to zero. As a consequence, the azimuthal component of the force-free current generates a longitudinal paramagnetic magnetization (i.e. the field inside the sample will be greater than the applied field). This was experimentally verified by LeBlanc et al (LeBlanc 65) who observed both the paramagnetic effect and the enhancement of critical currents in NbZr and NbTa wires. Calculations based on the Bergeron model, however, did not fit the data adequately.

Campbell and Evetts (Campbell 72), focussing on infinite slab geometry, have recently proposed a model where flux is conserved as it it penetrates into the sample. In their model, fluxons are created at the surface of the sample and maintain their angle of creation as they penetrate into the specimen, i.e., the fluxons can be compressed, but do not change their orientation or cross each other. Calculations based on their model lead to magnetic moments which are much larger than observed experimentally.

We propose an empirical equation to describe the sequences of orientation of the vortices as they penetrate (or exit from) the sample. This equation implicitly permits fluxons to cross or cut each other. As a consequence, the comparison between theory and experiment is greatly improved.

CHAPTER 2

EXPERIMENTAL PROCEDURE

A- Description of Samples.

The measurements were made on samples of two different materials. These samples are described below.

1- $Nb_{0.52}\ Ti_{0.48}$

These samples were cut from a length of NbTi ribbon fabricated by cold-rolling commercial (Supercon T48B) bare wire. Each sample is a rectangular piece of ribbon 4.8 cm long, 0.135 cm wide and 0.020 cm thick. Photographs of a longitudinal and transverse cross-section of the sample are presented on the next page.

2- $V_{0.24}\ Ti_{0.76}$

This sample was cut with a wire saw from an arc-melted ingot of high-purity VTi (obtained from Materials Research Corp.). It was mounted without any chemical treatment after cutting. The ribbon was 3.6 cm long, 0.51 cm wide and 0.15 cm thick.

B- Experimental Arrangement and Measurements.

A non-inductively (bifilar) wound manganin wire heater embraces the sample and enables us to raise its temperature above T_c. The heater-sample assembly fits tightly inside a bakelite holder which holds it firmly in place and is designed so that the

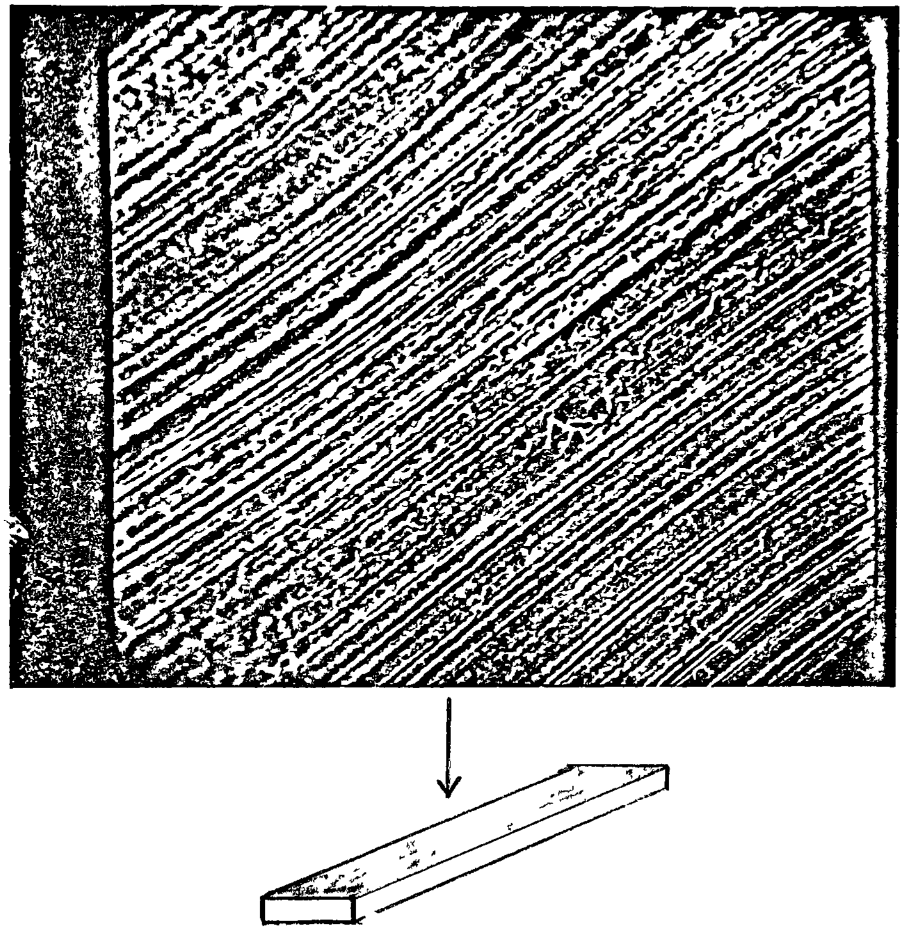

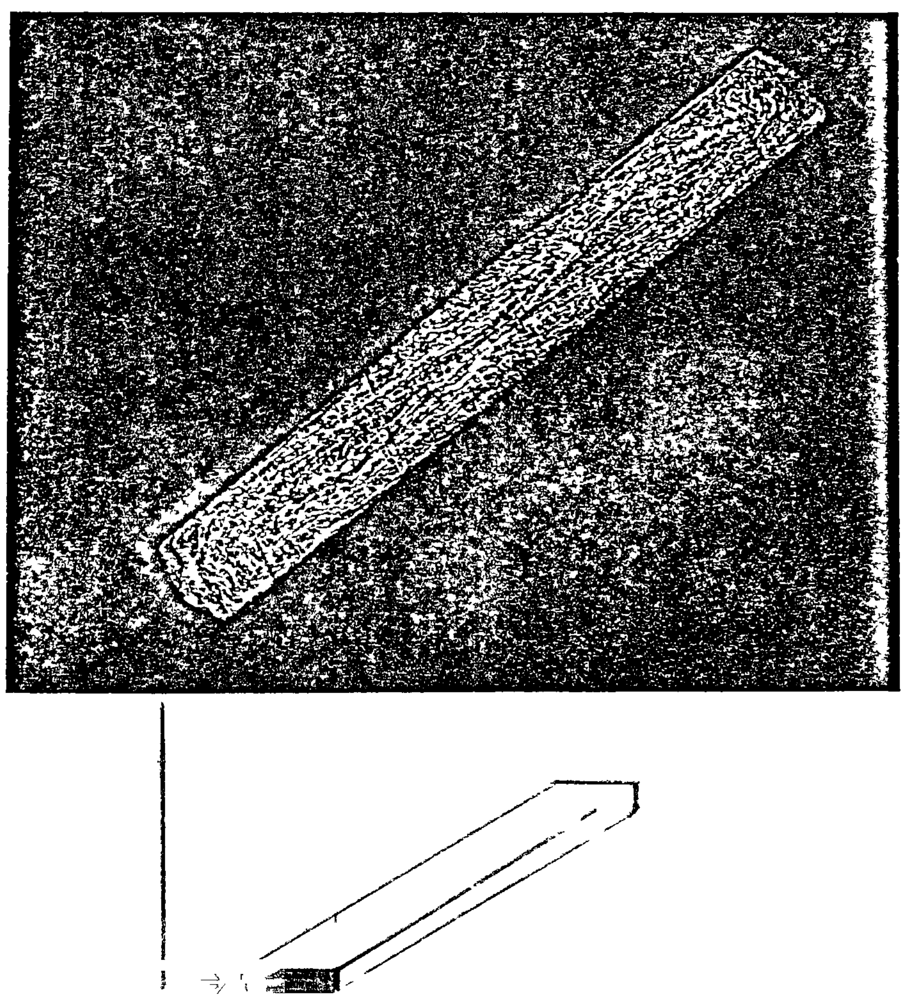

length and width of the ribbon can be accurately aligned with respect to the components of the applied magnetic field.

The longitudinal and transverse magnetic fields are produced separately and independently by using two orthogonal superconducting coils. The coil providing the longitudinal ($H_{\parallel}$) field is a long solenoid which is positioned inside and rigidly clamped to a rectangular coil which produces the transverse magnetic field, $H_{\perp}$.

We continuously monitor the magnetization of the sample, hence the average magnetic induction which permeates it, using two orthogonal pick-up coils, one measuring the magnetization $\langle 4\pi M\rangle_{\parallel}$ along the length, and the other, $\langle 4\pi M\rangle_{\perp}$ along the width of the ribbon. As is standard practice, each pick-up coil is series opposition connected to a bucking coil which senses the corresponding applied field but does not "see" the sample.

Each balanced pick-up coil feeds an electronic integrator-amplifier which drives the Y axis of an X-Y recorder. A signal proportional to the transverse field, $H_{\perp}$, drives the X axis of the recorders. In our arrangement, using two X-Y recorders (or an $X - Y_1 - Y_2$ recorder) we can monitor the longitudinal and transverse components of the magnetization of the sample continuously and separately as the transverse field is varied slowly over desired ranges.

The pick-up coil which monitored $\langle 4\pi M\rangle_{\perp}$ was calibrated by measuring the signal obtained while varying $H_{\perp}$ from zero to a value $H_\perp < H_{c1}$. Since, for $H_\perp < H_{c1}$, the superconductor excludes all flux (B = 0 inside the sample), the signal observed then yields

$$<4\pi M>_\perp \text{ (in volts)} = -K_\perp H_\perp \text{(oersteds)}.$$

where $K_\perp$ is a coefficient of the experimental setup and the given sample. If $H_\perp$ is known, then the conversion from volts to Oersteds is achieved. The same procedure was done to calibrate the parallel pick-up coil, except in this case, $H_{/\!/}$ was varied from zero to $H_{/\!/} < H_{c1}$, and a different coefficient, $K_{/\!/}$, was obtained.

There are basically two types of measurements which were performed.

1- Magnetization Measurements

The sample was cooled to below T_c in the presence of two fields, $H_{/\!/}$ and $H_\perp$. Subsequently, $H_\perp$ was varied (either increased or decreased) while $H_{/\!/}$ remained fixed. The signal in each of the pickup coils was monitored continuously as $H_\perp$ was varied. Then, the sample was heated to above T_c, and with the sample in the normal state, the measurement was repeated. This is necessary to determine the background signal.

2- Hysteresis Measurements

The selected longitudinal field ($H_{/\!/}$) is applied and maintained constant. Then, the transverse field, $H_\perp$, is cycled several times over the chosen range of the measurement. This is necessary because of hysteresis in the superconducting coils. Next, the background signal is determined with the sample in the normal state. Finally, the sample is allowed to cool through T_c to $4.2^{o}K$ in the selected initial $H_{\perp}$ (the chosen $H_{//}$ is kept fixed throughout) and with the sample in the superconducting state, the evolution of its magnetization along its length and width is monitored continuously as $H_{\perp}$ is varied slowly and repeatedly over the chosen cycle. The area enclosed by the hysteresis curve is therefore equal to the loss per cycle.

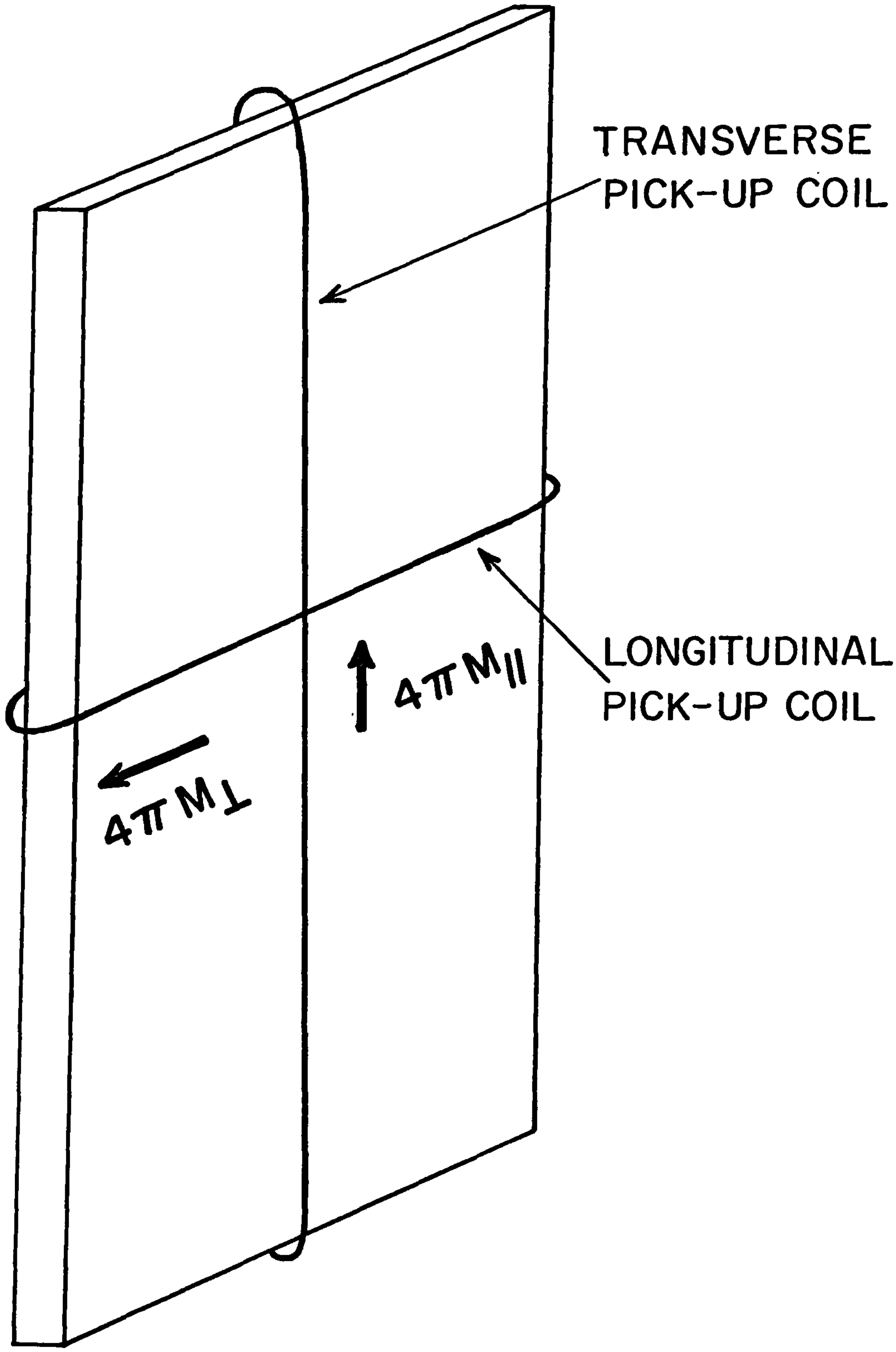

FIG. 1: Schematic of sample and pickup coils

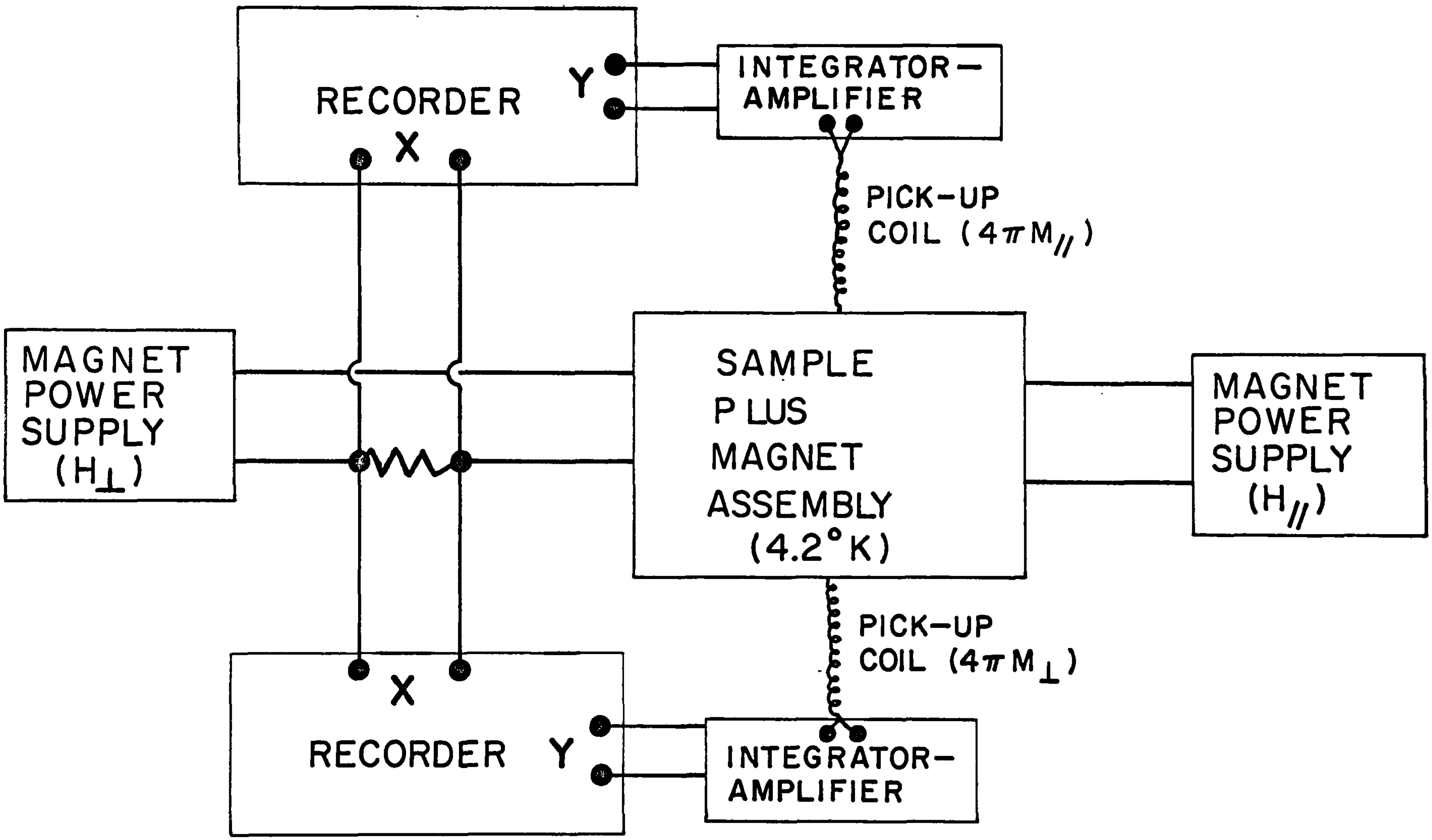

FIGURE 2: Schematic of experimental set-up.

CHAPTER 3

THE CRITICAL STATE CONCEPT IN IRREVERSIBLE TYPE II SUPERCONDUCTORS

Magnetic flux in type II superconductors has been shown to exist in the form of quantized vortices (fluxons) as predicted by Abrikosov (Abrikosov 57) and exhibited visually by Trauble and Essman (Trauble 68).

Abrikosov defines a local average (over several fluxons) of magnetic induction as

$$B\ (x) = n\ \phi_o \qquad 3\text{-}1$$

where n = number of fluxons per unit area

ϕ_o = flux quantum = $\frac{hc}{2e}$ = 2×10^{-7} Gauss - cm^2

We consider a local magnetic field $H(x)$ defined by

$$H\ (x) = H_a + \int \frac{4\pi}{c}\ J\ (x')\ dx' \qquad 3\text{-}2$$

where $\vec{J} = \frac{c}{4\pi}\ \vec{\nabla} \times \vec{H}$, and H_a is the externally applied field and the surface of the sample is at $x = 0$. $H(x)$ is a macroscopic average taken over a width of a few rows of vortices. There will be a density of fluxons in equilibrium with this H. The B(H) versus H curve calculated by Abrikosov is shown schematically below.

Below a lower critical field, H_{c1}, $B = 0$. Above H_{c1}, B tends rapidly to H, and at an upper critical field, H_{c2}, the sample

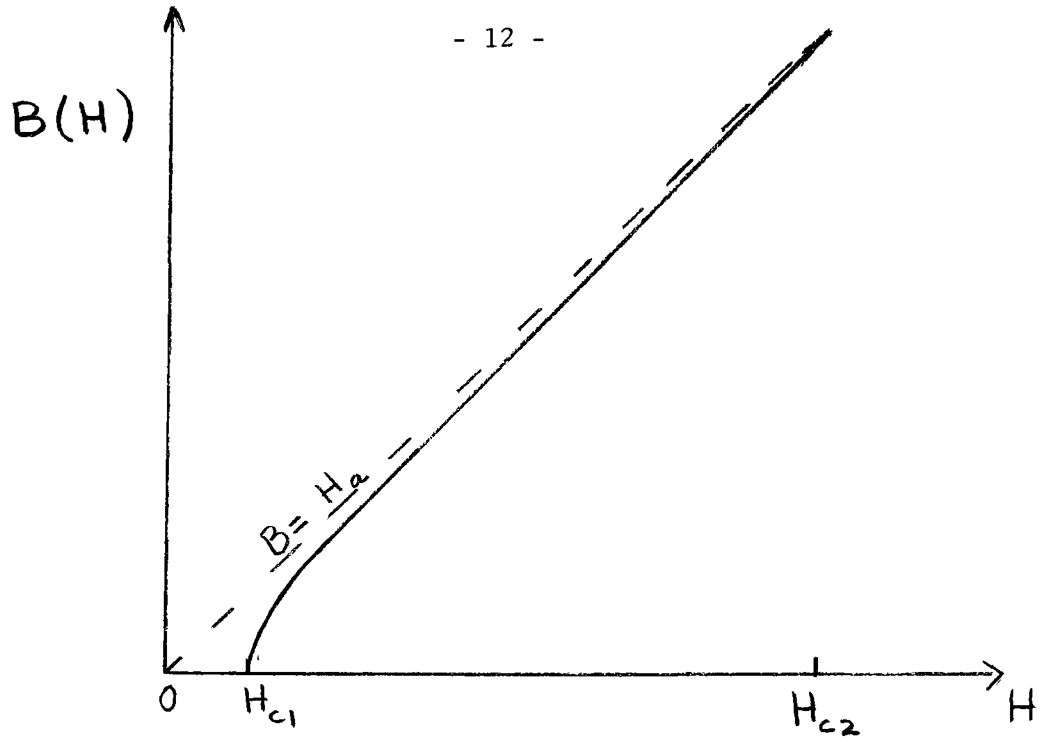

ceases to be superconducting.

According to equation 3-2, a transport current introduced into a type II superconductor produces a magnetic field which is superimposed on the externally applied field and that due to any macroscopic persistent currents which may be present. A magnetic induction, B(x), exists in equilibrium with the resultant H(x).

Similarly, if an externally applied field is impressed, macroscopic currents are induced in the bulk of the superconductor, the direction of which is governed by the Faraday-Lenz law. The magnetic field generated by these induced macroscopic currents must be taken into account in determining H(x) according to equation 3-2. If $H \gg H_{c1}$, (as in most of our measurements) then Abrikosov's derivation leads to $B \approx H$, that is the superconductor is only weakly diamagnetic. The materials we have studied are non-magnetic in the normal state so Abrikosov's results apply without any modification.

The critical state concept (Bean 64) permits the calculation of magnetic induction profiles inside the superconductor, for various magnetic histories. Before reviewing this concept, it would be useful to define the symbols used in the discussion.

Since we are dealing with a ribbon of superconducting material, with length and width much greater than its thickness, it is reasonable to assume infinite slab geometry.

Consider a slab which is infinite in the y and z directions, with its origin at $x = 0$, and thickness $2a$.

The superconductor is cooled to below the transition temperature, T_c, in the presence of a magnetic field $H_{\parallel}$, directed along the length of the ribbon (z direction), and in a magnetic field $H_{\perp}$, directed along the wide face of the ribbon (y direction). Since our samples are heavily cold-worked, hence highly irreversible, there is no detectable Meissner effect (flux expulsion), thus after cooling, B_y and B_z are constant within the sample and equal to $H_{\perp}$ and $H_{\parallel}$ respectively. Subsequently, the field $H_{\perp}$ is varied (either increased or decreased), while $H_{\parallel}$ remains static. This will induce currents to flow in the y-z plane, whose sense of circulation is given by the Faraday-Lenz law. Thus at a point x we may define a current density $\vec{J}(x)$, which will depend spatially only on x ($\vec{J}$ is constant in any y-z plane because of the symmetry of "infinite" geometry in this plane).

The following are definitions

$\vec{J}(x) = \vec{J}_y(x) + \vec{J}_z(x)$ = total current density at x

$\vec{J}_y(x) \equiv j_y\vec{k}$ = component of $\vec{J}$ in the y-direction, at x

$\vec{J}_z(x) = j_z\vec{k}$ = component of $\vec{J}$ in the z-direction at x.

$\vec{H}(x) = \vec{H}_y(x) + \vec{H}_z(x)$ = total magnetic field at point x

$\vec{H}_y(x) = h_y\vec{j}$ = component of $\vec{H}$ in the y-direction, at x

$\vec{H}_z(x) = h_z\vec{k}$ = component of $\vec{H}$ in the z-direction, at x

$\vec{H}_s = \vec{H}(o)$ = total applied magnetic field, at the surface

$\vec{H}_\perp = \vec{H}_y(o)$ = component of applied magnetic field in the y-direction, at the surface. (this is the field component that is made to vary).

$\vec{H}_{//} \equiv \vec{H}_z(o)$ = component of applied magnetic field in the z-direction, at the surface (this field component remains static).

$H_s = |\vec{H}_s|$, $H_\perp = |\vec{H}_\perp|$ and $H_{//} = |\vec{H}_{//}|$

$\vec{B}(x) = \vec{B}_y(x) + \vec{B}_z(x)$ = total magnetic induction at x.

where $\vec{B}_y(x) = b_y(x)\vec{j}$ and $\vec{B}_z(x) = b_z(x)\vec{k}$.

Also, $B(x) \equiv |\vec{B}(x)|$.

Since, as noted above, we take $\vec{B}(x) = \vec{H}(x)$ (i.e. we consider the intrinsic Abrikosov diamagnetism as negligible), we will use the following notation: inside the sample, $o < x \leq a$, the symbol $\vec{B}(x)$ will be used, while at the surface, $x = o$, the symbol $\vec{H}$ will be used.

A modified Gaussian system of units is used throughout the calculations, where

$$\vec{\nabla} \times \vec{H}(x) = \vec{\nabla} \times \vec{B}(x) = \frac{4\pi}{10} \vec{J} \qquad 3\text{-}3$$

where $\vec{J}$ is in amperes/cm^2, and $B(x)$ and $H(x)$ are in Gauss. $\vec{B}(x)$ is the total magnetic induction at point x in the sample. It is the sum of the total externally applied field and the field arising from the persistent macroscopic currents induced in the sample.

According to the critical state concept, if an external magnetic field is varied, a critical current density $J_c(B, T)$ is induced. $J_c(B, T)$ depends on the local magnetic induction, the temperature and parameters of the particular material, and any emf, however small, will induce the full critical current density to flow locally inside the superconductor. Therefore, in the regions which experienced a change in magnetic induction (hence an emf), a persistent current is flowing whose magnitude is determined by the limiting value of J_c and whose sense of circulation is determined by the Faraday-Lenz law of induction.

The macroscopic conduction or transport current flowing in the sample interacts with the fluxons. We may then define a Lorentz force density,

$$\vec{F}_L = \vec{J} \times \vec{B} \tag{3-4}$$

which acts on the vortices or flux filaments and where $\vec{J}$ and $\vec{B}$ are averaged over the dimensions of several such entities.

At equilibrium, i.e., when the applied field is no longer varying, the resultant force on the fluxons is zero. The Lorentz force is then exactly balanced at every point by a pinning force, $\vec{F}_p$ (which is due to impurities, imperfections, dislocations, etc.).

Thus the critical state concept can be succintly expressed by the the equation:

$$\vec{F}_L = \vec{F}_p$$

for all regions where B(x) has varied, hence where currents flow.

Many workers have postulated and many experimental results have confirmed that the pinning forces can be expressed as a product of two independent functions, namely

$$F_p = \alpha(T) \; F\,(B/H_{c2}) \tag{3-5}$$

where $\alpha(T)$ and $F(B)$ are characteristic of the sample. F_p depends on T explicitly through $\alpha(T)$ and implicitly through $F\,(B/H_{c2})$ since H_{c2} varies with T, but is a function of B only through the latter.

Collecting these results we may write

$$\vec{J}_c \times \vec{B} = \alpha \, \vec{F}\,(B)$$

for all x where a current flows. Since, in our approximation, $\vec{B} = \vec{H}$, then

$$\vec{\nabla} \times \vec{B} = \frac{4\pi}{10} \vec{J}_c \qquad 3\text{-}6$$

and

$$\vec{F}_L = \frac{10}{4\pi} \vec{\nabla} \times \vec{B} \times \vec{B} = \alpha \vec{F} (B) \qquad 3\text{-}7$$

Accordingly, the explicit relation

$$\vec{\nabla} \times \vec{B} = \begin{vmatrix} \vec{i} & \vec{j} & \vec{k} \\ \frac{d}{dx} & \frac{d}{dy} & \frac{d}{dz} \\ 0 & b_y(x) & b_z(x) \end{vmatrix}$$

leads to

$$\vec{\nabla} \times \vec{B} = -\vec{j} \frac{db_z}{dx} + \vec{k} \frac{db_y}{dx} \quad \text{for an infinite slab.}$$

Also, in this geometry

$$\vec{\nabla} \times \vec{B} \times \vec{B} = \begin{vmatrix} \vec{i} & \vec{j} & \vec{k} \\ 0 & -\frac{db_z}{dx} & \frac{db_y}{dx} \\ 0 & b_y & b_z \end{vmatrix}$$

$$= -\vec{i} \left(b_z \frac{db_z}{dx} + b_y \frac{db_y}{dx}\right)$$

$$\therefore |\vec{F}_L| = \frac{10}{4\pi} \left(b_z \frac{db_z}{dx} + b_y \frac{db_y}{dx}\right)$$

$$= \frac{10}{4\pi} \left[\frac{1}{2} \frac{d}{dx} (b_z{}^2) + \frac{1}{2} \frac{d}{dx} (b_y{}^2) \right]$$

$$= \frac{10}{4\pi} \left[\frac{1}{2} \frac{d}{dx} (B^2) \right]$$

so

$$|\vec{F}_L| = \frac{10}{4\pi} B \frac{dB}{dx} \qquad 3\text{-}8$$

where $B = |\vec{B}(x)|$ = magnitude of the total magnetic induction at x.

The critical state equation then takes the simple form

$$B \frac{dB}{dx} = \frac{4\pi\alpha}{10} F(B) \qquad 3\text{-}9$$

Thus, if F(B) is specified, equation 3-9 may be integrated to give B(x) analytically or numerically, and the magnetic induction profile is then known. With the magnitude of B(x) known everywhere in the sample, the problem is reduced to a determination of the direction of $\vec{B}(x)$ at every plane, i.e., we need to establish the components, $b_y(x)$ and $b_z(x)$.

Once these are known, we may calculate,

$$\langle B\rangle_{\perp} = \frac{1}{a}\int_0^a b_y(x)\, dx$$

and

$$\langle B\rangle_{//} = \frac{1}{a}\int_0^a b_z(x)\, dx$$

where

$\langle B\rangle_{\perp}$ = average magnetic induction in y-direction in the sample (parallel to the wide face of the sample).

$\langle B\rangle_{//}$ = average magnetic induction in the z-direction (parallel to the length of the sample).

It is useful and common practice to introduce the following relations:

$$\langle B\rangle_{\perp} = H_{\perp} + \langle 4\pi M\rangle_{\perp}$$

$$\langle B\rangle_{//} = H_{//} + \langle 4\pi M\rangle_{//}$$

Since the applied fields are known, we may calculate $\langle 4\pi M\rangle_{\perp}$ and $\langle 4\pi M\rangle_{\parallel}$. It is important to note that $\langle 4\pi M\rangle$ is due to macroscopic persistent currents flowing in the sample and is not a "magnetization" arising from the alignment of microscopic, discrete magnetic dipoles. This quantity, however, indicates that the field inside the sample is either less than the applied field (diamagnetic) or greater than the applied field (paramagnetic). In our experimental arrangement it is generally this "excess" (or "deficit") of flux along the corresponding orthogonal directions which we measure directly, rather than $\langle B\rangle_{\perp}$ and $\langle B\rangle_{\parallel}$, the components of the average magnetic induction. Following the terminology current in the literature, we refer to $\langle 4\pi M\rangle$ as the magnetization of the sample.

CHAPTER 4

THE BERGERON MODEL

In order to account for the increase in current carrying capacity observed by Sekula et al (63) in wires of type II superconductors immersed in a longitudinal magnetic field, Bergeron (63) proposed that the current and the magnetic induction adopted a force-free configuration throughout the cylinder. In his paper, he exploited known mathematical solutions of this problem for cylindrical geometry together with a formulation of prevailing ideas regarding the energy of the system to derive expressions relating the critical current I_c and the axial magnetic moment $\langle 4\pi M \rangle_{/\!/}$ at I_c to the applied axial field $H_{/\!/}$. These final expressions have been criticized as internally inconsistent. Further, their agreement with experiment, although encouraging, left considerable room for improvement.

In this chapter, we adapt the concept of force-free flow to an infinite slab geometry. We pursue in detail the physical results which arise in the situation where the induced currents flow perfectly parallel (or antiparallel) to the total magnetic induction, $\vec{B}$, throughout the sample. The category of mathematical solutions we utilize in this chapter constitute one set of possible solutions of the force-free flow problem in this geometry. Since these solutions are the mathematical analogue for an infinite slab of the solutions considered by Bergeron for a cylinder, we give this application of the force-free concept the name "Bergeron Model".

In the next chapter, we will develop in detail another type of solutions of the force-free flow problem originally proposed by Campbell and Evetts (Campbell 72).

We consider a ribbon which is infinite in the y-z plane, and of thickness, 2a, in the x-direction.

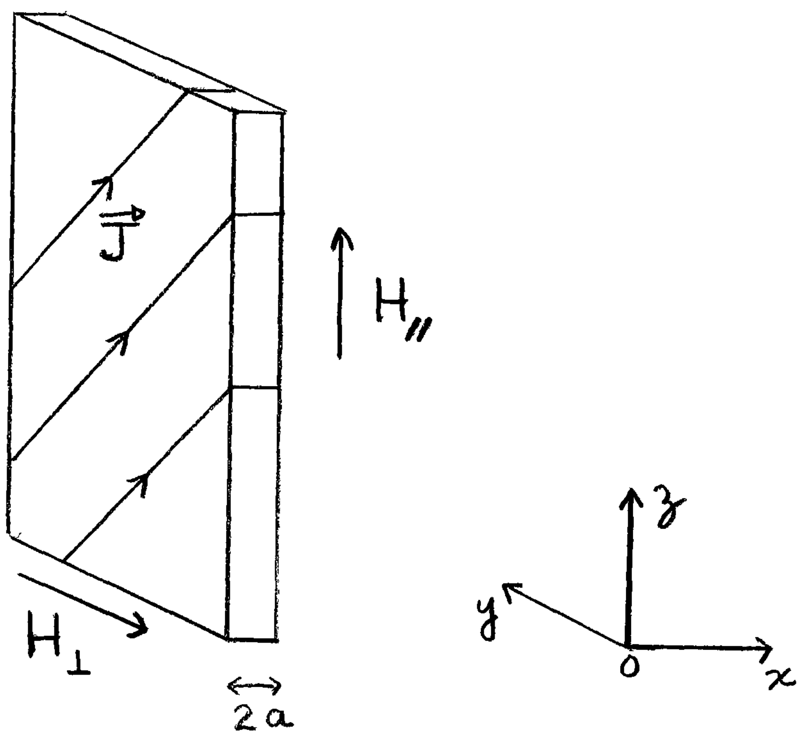

The sample is cooled to below the transition temperature, T_c, in the presence of a static magnetic field, $H_{\parallel}$, directed along the length of the ribbon (+z direction). Subsequently, a magnetic field, $H_{\perp}$, is applied along the wide face of ribbon (-y direction), thereby inducing shielding currents to flow in the y-z plane. As a consequence, in one half of the slab, 0 < x < a, a current flows parallel to $\vec{B}$ at every point, while in the other half, $a < x < 2a$, the return current flows antiparallel to $\vec{B}$. The magnetic field profile is symmetric about the center, a, therefore we may consider only one half of the sample thickness, $0 < x < a$.

Since the total Lorentz force on the fluxons is assumed to be zero,

$$\vec{F}_L = \vec{J} \times \vec{B} = 0 \qquad \text{for all } x \qquad 4\text{-}1$$

therefore, (see equation 3-8, chapter 3)

$$B \frac{dB}{dx} = \frac{1}{2} \frac{d}{dx} (B^2) = 0 \qquad 4\text{-}2$$

thus B^2 and $|\vec{B}|$ are constant throughout the sample and $|\vec{B}|$ is equal to the total field at the surface, H_s.

$$B(x) = \sqrt{b_y^2(x) + b_z^2(x)} = H_s \qquad 4\text{-}3$$

Although the total field, B, is constant, its components, $b_y(x)$ and $b_z(x)$ are not. The angle, $\theta(x)$, that the fluxons make with the z- axis varies with the depth x. We next determine the variation of $b_y(x)$ and $b_z(x)$.

Since $\vec{J}$ is everywhere parallel to $\vec{B}$ we may write

$$\vec{J}(x) = k(x)\, \vec{B}(x) \qquad 4\text{-}4$$

Since $\vec{\nabla} \times \vec{H}(x) = \vec{\nabla} \times \vec{B}(x) = \frac{4\pi}{10} \vec{J}(x)$, introducing equation 4-4 into Maxwell's equation above, we obtain

$$\frac{10}{4\pi} \vec{\nabla} \times \vec{B} = k\vec{B}$$

or $$\vec{\nabla} \times \vec{B} = \gamma\vec{B} \qquad 4\text{-}5$$

where $\gamma = \frac{4\pi k}{10}$.

For simplicity, we assume that k is spatially constant.

Since $\vec{\nabla} \times \vec{B} = -\vec{j}\,\frac{db_z}{dx} - \vec{k}\,\frac{db_y}{dx}$ and $\vec{B} = -b_y\vec{j} + b_z\vec{k}$,

equation 4-5 becomes

$$-\vec{j}\,\frac{db_z}{dx} - \vec{k}\,\frac{db_y}{dx} = -\gamma b_y\vec{j} + \gamma b_z\vec{k}$$

or

$$\frac{db_z}{dx} = \gamma b_y \qquad 4\text{-}6$$

and

$$\frac{db_y}{dx} = -\gamma b_z \qquad 4\text{-}7$$

From equation 4-6, $b_y = \frac{1}{\gamma}\frac{db_z}{dx}$ therefore $\frac{db_y}{dx} = \frac{1}{\gamma}\frac{d^2b_z}{dx^2}$,

and substituting this into equation 4-7 gives

$$\frac{d^2b_z}{dx^2} = -\gamma^2 b_z \qquad 4\text{-}8$$

Similarly,

$$\frac{d^2b_y}{dx^2} = -\gamma^2 b_y \qquad 4\text{-}9$$

Solutions to equations 4-9 and 4-8 are

$$b_y(x) = A_1 \cos(\gamma x + \phi_1) \qquad 4\text{-}10$$

and

$$b_z(x) = A_2 \sin(\gamma x + \phi_2) \qquad 4\text{-}11$$

If β is defined as the angle between the y-direction and total $\vec{B}$,

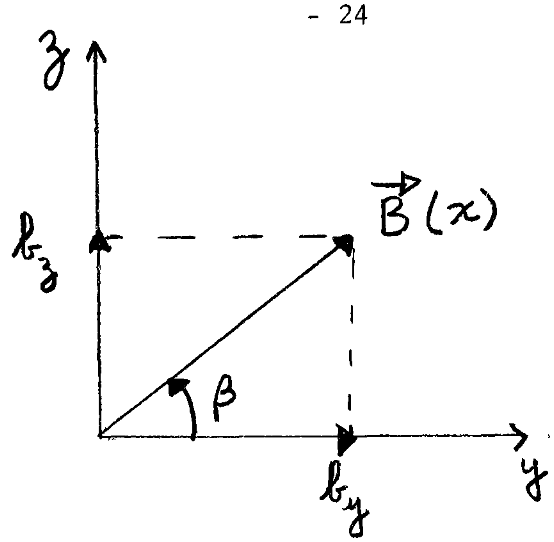

we then see that

$$b_y(x) = B \cos \beta \text{ and } b_z(x) = B \sin \beta$$

therefore we must have

$$A_1 = A_2 = B = H_s$$

and $\gamma x + \phi_1 = \gamma x + \phi_2 = \beta$

$$\text{i.e.} \quad \phi_1 = \phi_2 = \phi$$

and $\gamma = \dfrac{d\beta}{dx}$ 4-12

Therefore equations 4-10 and 4-11 become

$$b_y(x) = H_s \cos (\gamma x + \phi) \qquad 4\text{-}13$$

and $b_z(x) = H_s \sin (\gamma x + \phi)$ 4-14

where we require that $0 < \beta < \frac{\pi}{2}$, since solutions of shorter "wavelength" (hence several oscillations) appear to be unphysical. From equation 4-12, we see that β varies linearly inside the sample, since γ is assumed constant. Bergeron (63) also made this assumption in his analysis.

Since, at the surface,

$$b_y(0) \;=\; H_{\perp} \text{ and } b_z(0) \;=\; H_{/\!/}$$

then, from equations 4-13 and 4-14,

$$\sin\phi \;=\; \frac{H_{/\!/}}{H_s} \text{ and } \cos\phi = \frac{H_{\perp}}{H_s} \text{ or } \tan\phi = \frac{H_{/\!/}}{H_{\perp}} \qquad \text{4-15}$$

We note that the phase constant ϕ is not an arbitrary parameter, but is completely determined by the relative magnitude of the components of the magnetic field at the surface of the slab.

The component of magnetic induction in the y-direction, $b_y(x)$, has a value $H_{\perp}$ at the surface, and decreases with depth x, until it becomes zero at a distance, x_o. At that point $b_z(x_o) = H_s$. We now turn our attention to the different possible profiles of $b_y(x)$ and $b_z(x)$ and the role of the parameter γ.

We now consider two possible sequences of "sinusoidal" types of force-free field distributions.

1- <u>$b_y(a) \;=\; 0$</u>

We may envisage that as the transverse field, $H_{\perp}$, is increased, since there is no pinning, hence no opposition to the migration and reorientation of the flux lines, the flux already permeating the slab and the additional flux which is entering, will adjust in density and direction so that induced persistent currents, flowing in a force-free manner, will fill the entire slab. Thus, regardless of the magnitude of the change in $H_{\perp}$, the assumption is made that the induced currents appear everywhere in the sample.

This implies that the concept of a critical current density which is a unique function of B (at constant T) does not apply. Further, we postulate that the transverse magnetic induction $b_y(x)$ remains fixed at the value of zero at the centre of the slab [$b_y(a) = 0$].

We then visualize that as $H_\perp$ (and hence H_s) is increased, sequences of magnetic induction profiles are encountered where $b_y(x)$ decreases monotonically from $H_\perp$ at the surface ($x = 0$) to zero at the centre ($x = a$). Since $|\vec{B}(x)| = H_s$, it follows that $b_z(a) = H_s$. The situation we have just described corresponds to the case explored by Bergeron (Bergeron 63) and Walmsley (Walmsley 72) for cylindrical geometry. In the latter geometry, $B_\theta(r)$, the azimuthal or circular component of the magnetic induction, plays the role equivalent to the "transverse" field, $b_y(x)$, in the slab.

In the present situation, since the boundary conditions

$$b_y(o) = H_\perp \quad \text{and} \quad b_y(a) = 0$$

and the complementary boundary conditions

$$b_z(o) = H_{/\!/} \quad \text{and} \quad b_z(a) = H_s = \sqrt{H_\perp^2 + H_{/\!/}^2}$$

are specified, the parameter γ, as a consequence, is completely determined by the ratio $\dfrac{H_{/\!/}}{H_\perp}$ and the half-width, a, of the slab.

We now develop the pertinent expressions for $\langle B\rangle_y$, $\langle B\rangle_z$, and γ as a function of the applied field and its components.

The sequence of magnetic induction profiles, as H_s is increased, are shown schematically on the next page (Figure 3).

The average magnetic induction in the y-direction is

$$\langle B\rangle_y = \frac{1}{a}\int_0^a b_y(x)\,dx$$

$$= \frac{H_s}{a}\int_0^a \cos(\gamma x + \phi)\,dx$$

$$= \frac{H_s}{\gamma a}\left[\sin(\gamma a + \phi) - \sin\phi\right]$$

Since $b_y(a) = 0$ then $H_s \cos(\gamma a + \phi) = 0$ and

$$\gamma a + \phi = \frac{\pi}{2} \qquad 4\text{-}16$$

Since from equation 4-15, $\sin\phi = \dfrac{H_{/\!/}}{H_s}$, then

$$\langle B\rangle_y \equiv \langle B\rangle_{\perp} = \frac{H_s - H_{\perp}}{\gamma a}$$

Introducing this into the definition $\langle B\rangle_{\perp} = H_{\perp} + \langle 4\pi M\rangle_{\perp}$ we obtain

$$\langle 4\pi M\rangle_{\perp} = \frac{H_s - H_{\perp}}{\gamma a} - H_{\perp} \qquad 4\text{-}17$$

Also,

$$\langle B\rangle_z = \frac{1}{a}\int_0^a b_z(x)\,dx$$

$$= \frac{H_s}{a}\int_0^a \sin(\gamma x + \phi)\,dx$$

$$= -\frac{H_s}{\gamma a}\left[\cos(\gamma a + \phi) - \cos\phi\right]$$

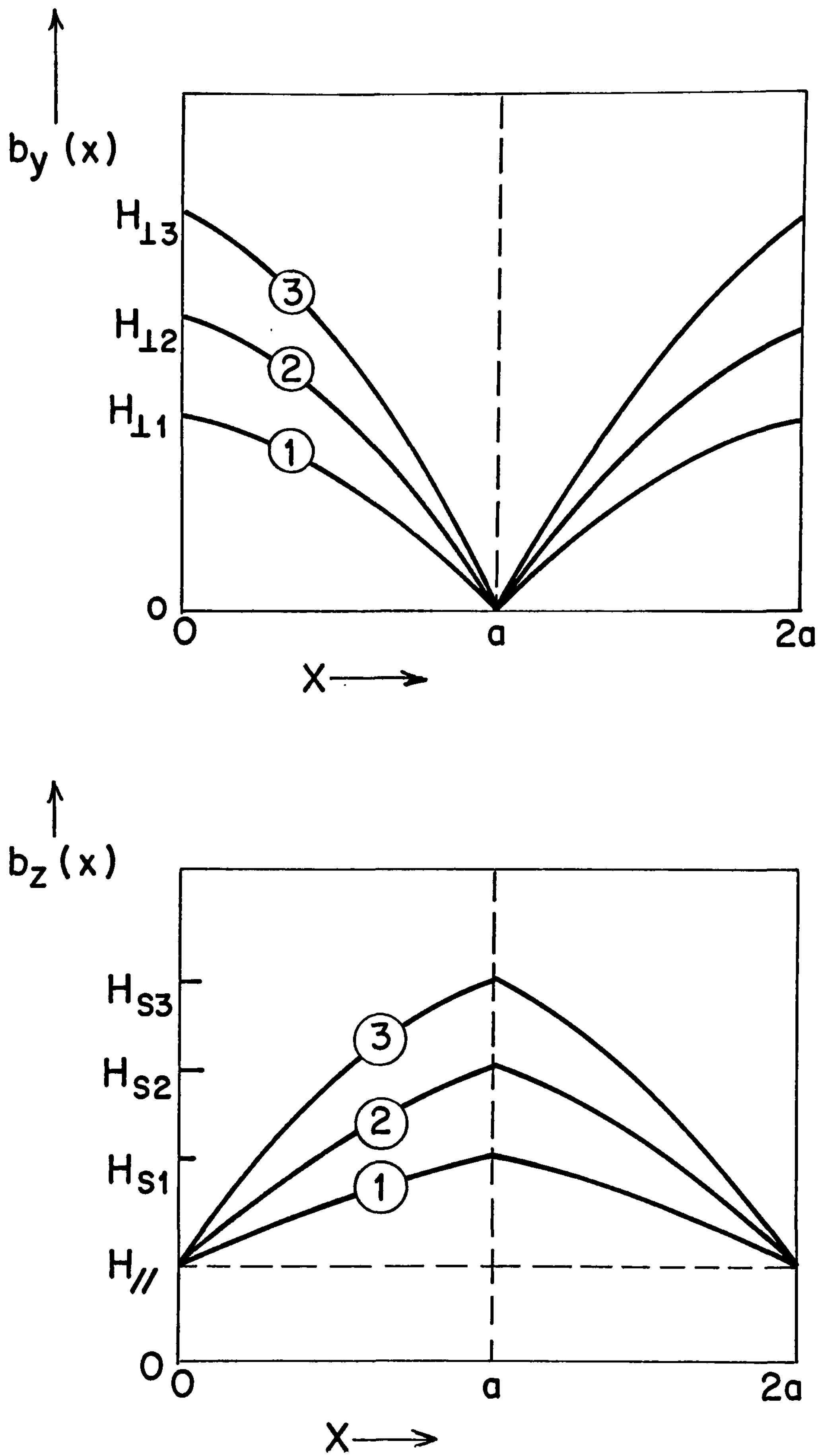

FIGURE 3: Sequence of magnetic induction profiles for tne Bergeron

$$= \frac{H_s \cos\phi}{\gamma a} = \frac{H_\perp}{\gamma a}$$

Since $\langle B \rangle_z \equiv \langle B \rangle_{/\!/} = H_{/\!/} + \langle 4\pi M \rangle_{/\!/}$, then

$$\langle 4\pi M \rangle_{/\!/} = \frac{H_\perp}{\gamma a} - H_{/\!/} \qquad 4\text{-}18$$

An interesting feature of equation 4-18 is its "prediction" that, even at $H_{/\!/} = 0$, the current can flow in a force-free manner and generate a magnetic moment in the z-direction, which increases with $H_\perp$. We have not encountered such a phenomenon in our experimental work. This is not suprising since in our samples, pinning is far from negligible and pure force-free configurations are not expected to occur. However, Walmsley et al (Walmsley 72) have seen an effect very similar to this "prediction" in very weak fields ($H_{/\!/} \approx 0.1$ Gauss) in well annealed PbTℓ cylinders, where the pinning is weak.

Combining equations 4-15 and 4-16, we obtain

$$\gamma = \frac{\frac{\pi}{2} - \tan^{-1}\left(\frac{H_{/\!/}}{H_\perp}\right)}{a} \qquad 4\text{-}19$$

In Figure 4, γa is plotted as a function of $H_\perp$, for four different values of $H_{/\!/}$. We see that, for a given $H_{/\!/}$, γa increases with $H_\perp$, and tends towards the limit $\frac{\pi}{2}$ at very large $H_\perp$. Also, for a given $H_\perp$, γa decreases with $H_{/\!/}$.

Thus, for a chosen $H_{/\!/}$, we can calculate γ, $\langle 4\pi M \rangle_\perp$ and

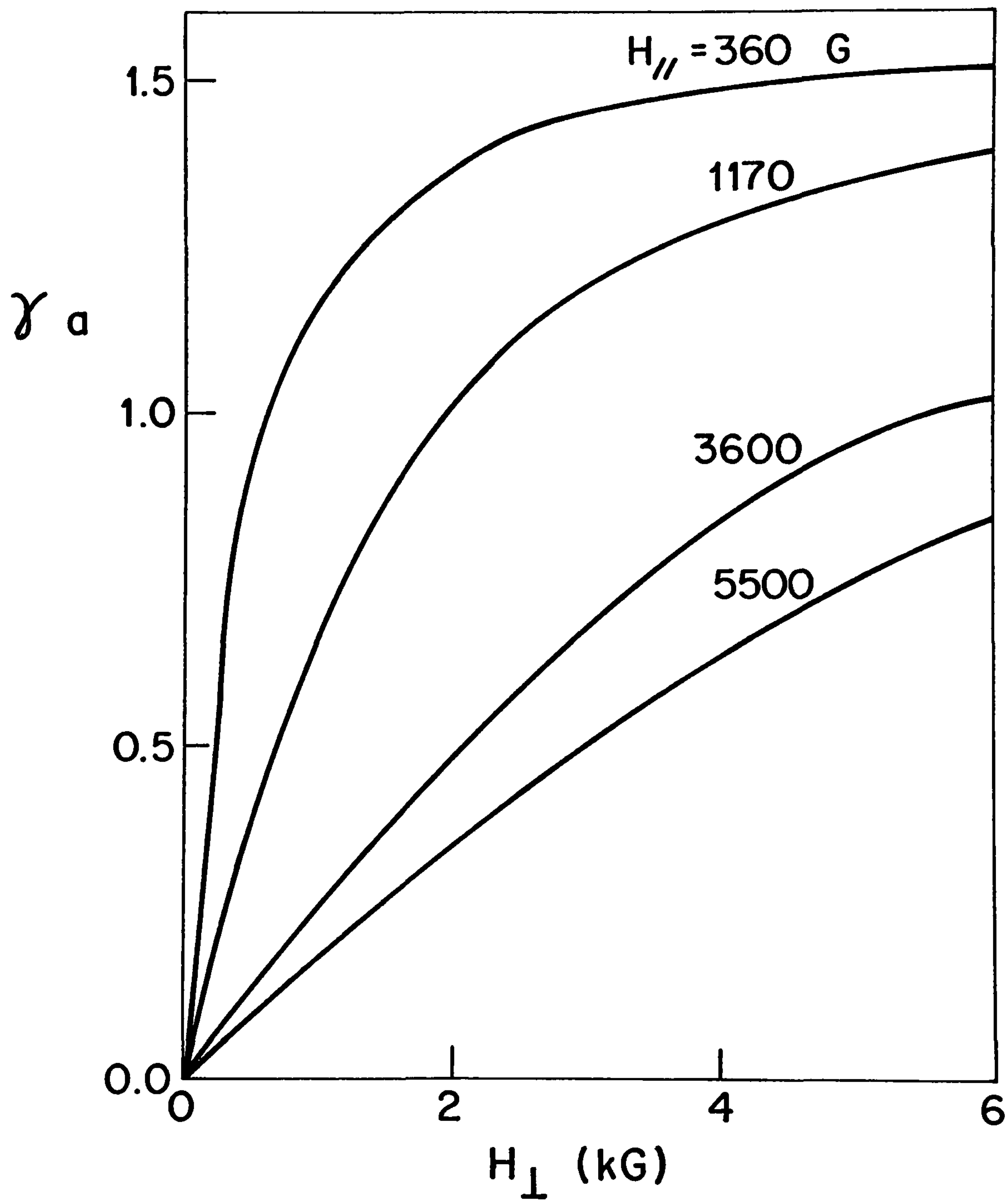

FIGURE 4: Variation of γa versus $H_\perp$ for the Bergeron Model (where $b_y(a) = 0$).

$\langle 4\pi M \rangle_{\parallel}$, as a function of $H_{\perp}$, using equations 4-17, 4-18 and 4-19.

Figures 5 and 6 present the results of such calculations where we have selected values of $H_{\parallel}$ and a range of $H_{\perp}$ which permit a comparison of the theoretical curves with experimental data.

We note that the comparison with experimental values for VTi (Figures 37, 39, 41 and 43) is very poor. The calculated magnetizations are not only an order of magnitude too large, but, as expected, these increase monotonically with $H_{\perp}$, while the experimental values pass through a maximum and then decrease. This monotonic increase is a consequence of the fact that the force-free model explored in this section implies an upper critical field H_{c2} which is infinite. The large difference with observations encountered at low fields $H_s << H_{c2}$ suggests that the field configurations introduced in the model are unrealistic even in cases where the pinning is small.

2- $\underline{b_y(x_o) = 0}$ where $x_o < a$ and $b_y(a) \geq 0$

In the previous section the "wave length" parameter γ was fixed by imposing the physical requirement that the transverse induction $b_y(x)$ fall to zero exactly at the centre of the slab regardless of the strength of the transverse field $H_{\perp}$ at the surface. Such configurations have constituted a basic ingredient in the analysis of critical currents and magnetic behaviour in slabs pursued by previous workers (Sugahara 71). This situation also corresponds to that exploited in investigations of force-free flow in cylinders (Bergeron

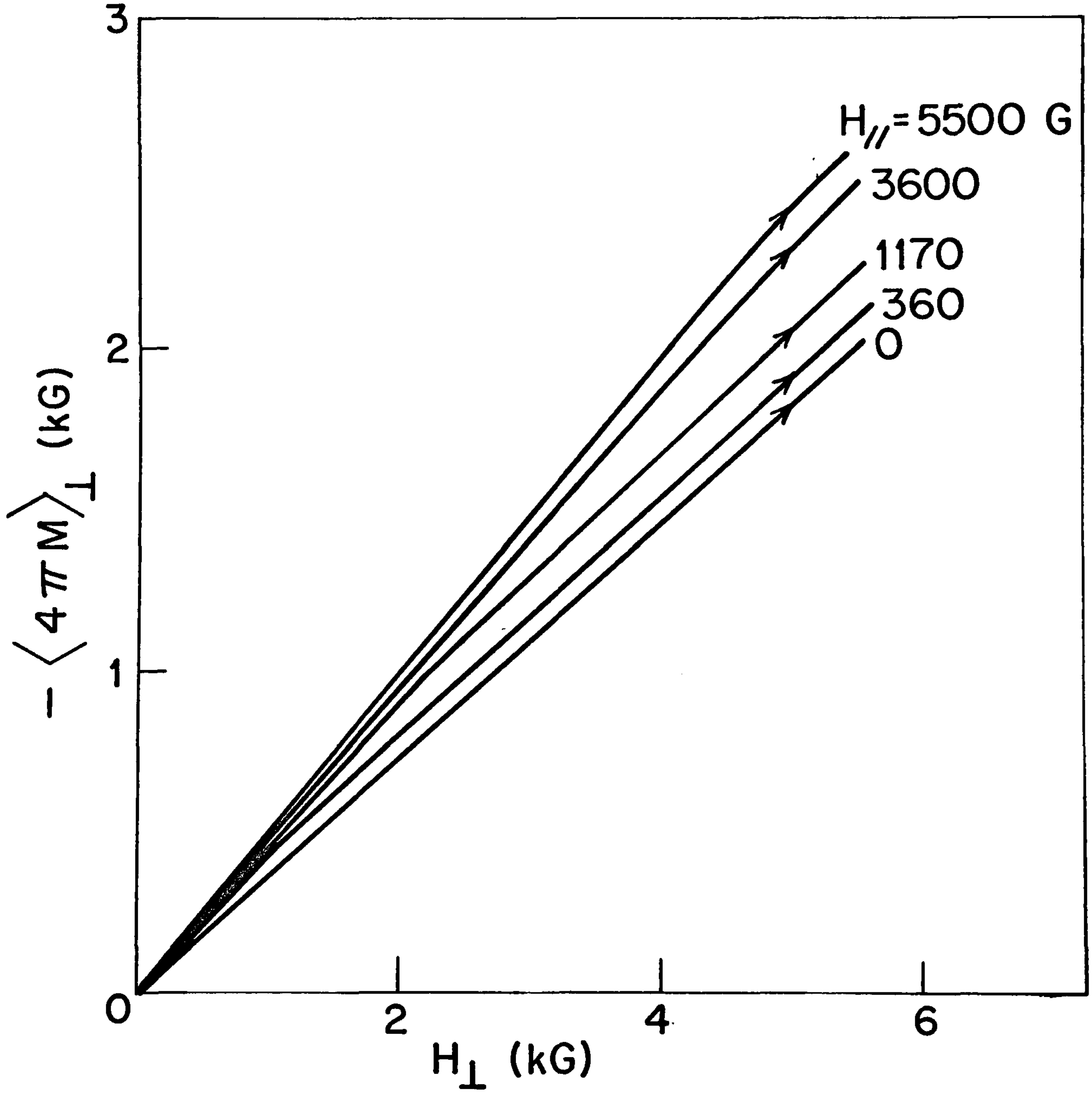

FIGURE 5: Variation of $\langle 4\pi M \rangle_\perp$ versus $H_\perp$, calculated from Bergeron Model (where $b_y(a) = 0$).

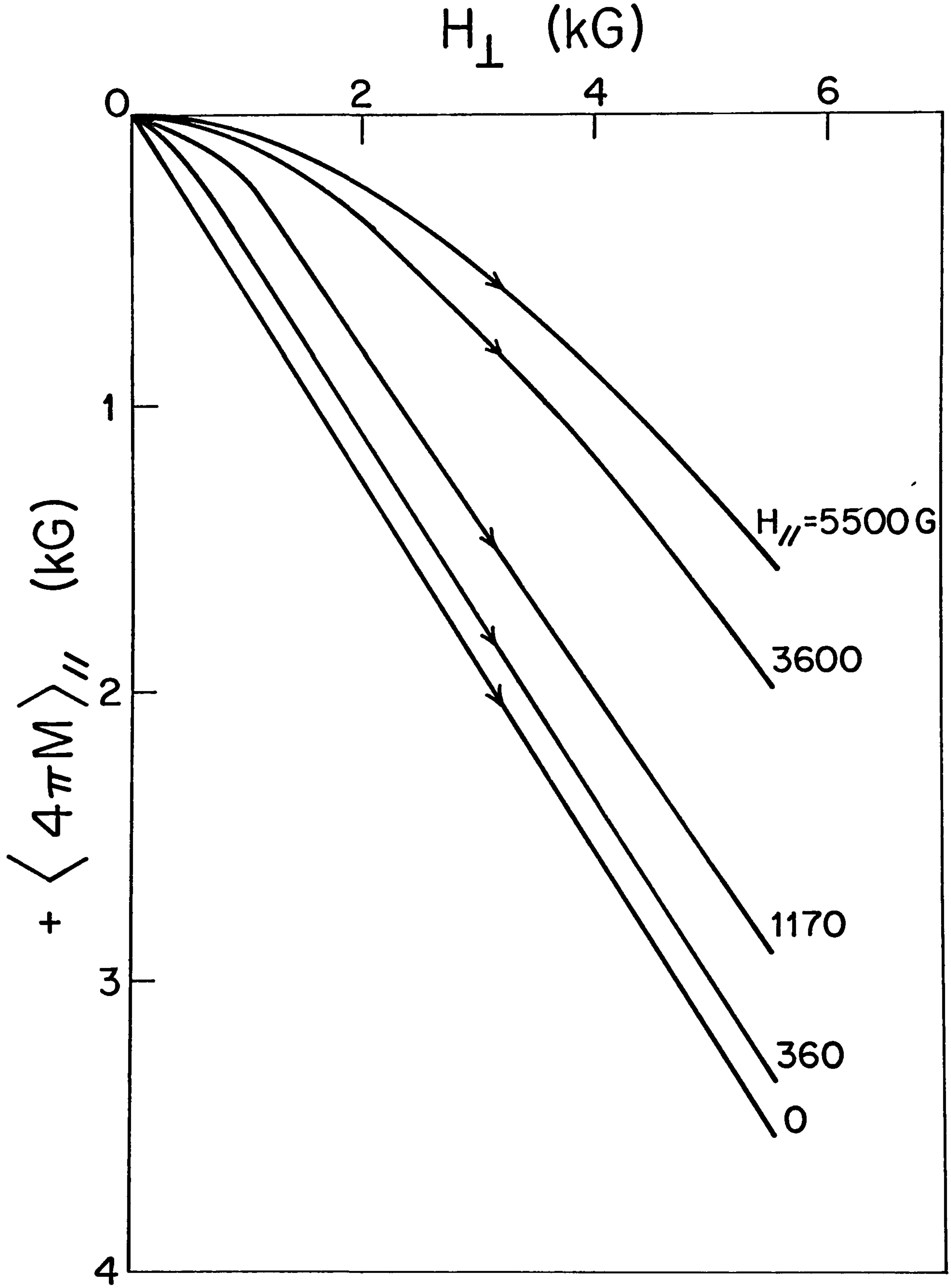

FIGURE 6: Variation of $<4\pi M>_{//}$ versus $H_{\perp}$, calculated from Bergeron Model (where $b_y(a) = 0$).

63, Walmsley 72). The postulate that $b_y(x) = 0$ only at $x = a$ implies that the "wavelength" decreases monotonically as $H_\perp$ increases. This choice of boundary condition, however, leads to magnetic moments which are much too large even at weak fields, and which increase without limit.

While remaining within the context of "sinusoidal" field profiles we can construct force-free configurations which lead to more realistic magnetic moments by choosing a more suitable functional form for the the parameter γ. The results of the previous section can guide us in this effort. These results indicate that the parameter γ versus $H_\perp$ should exhibit a resonance form, passing through a maximum and decreasing to zero as H_s approaches H_{c2}. Clearly an attempt to derive expressions for γ from first principles is desirable. This is an arduous task. As background for such an enterprise and in order to obtain further insight into the behaviour of the parameter γ we have pursued the following empirical approach. We determine the parameter γ using the measured transverse magnetic moments $\langle 4\pi M \rangle_\perp$. We then use this empirically derived γ to evaluate the corresponding parallel magnetic moment $\langle 4\pi M \rangle_{/\!/}$ which can then be compared with our observations. This exercise not only outlines the qualitative and quantitative variation of γ versus different combinations of $H_\perp$ and $H_{/\!/}$ but also provides some estimate of the degree of force-free flow encountered in our samples.

We visualize that as $H_\perp$ is increased after cooling below T_c in a static $H_{//}$ which is maintained constant, the field profiles gradually advance into the slab, adopting "sinusoidal" force-free configurations in the region where currents are induced by the change in the applied field H_s. Further, as this occurs the flux lines ahead of the advancing flux front are compressed in the progressively shrinking region where currents have not yet appeared. No restriction is imposed on the conservation of the number of flux lines in this region other than that the gradient of flux density remain zero in order that the force-free requirement be satisfied. The latter condition also means that $b_z = B = H_s$ in this diminishing volume.

Typical field profiles encountered during this initial sequence of events are shown schematically in Figure 7. We denote the depth of the region where currents exist by x_o. We will show in (i) below how x_o and hence γ can be extracted from the boundary conditions $b_y(0) = H_\perp$ and $b_z(0) = H_{//}$, and the measured transverse magnetic moment $\langle 4\pi M \rangle_\perp$. Eventually, the induced currents fill the entire width of the slab. Subsequently, the transverse magnetic induction at the centre of the slab, $b_y(a)$, rises monotonically as $H_\perp$ is increased further and "catches up" with $H_\perp$ as H_s approaches H_{c2}. As this takes place, $b_z(a)$ after attaining a maximum value then decreases to $H_{//}$ as H_s goes to H_{c2}. We continue to evaluate γ from the boundary conditions at the surface and the experimentally obtained transverse magnetic moments. The pertinent expressions for γ and $\langle 4\pi M \rangle_{//}$ are developed in section (ii) below.

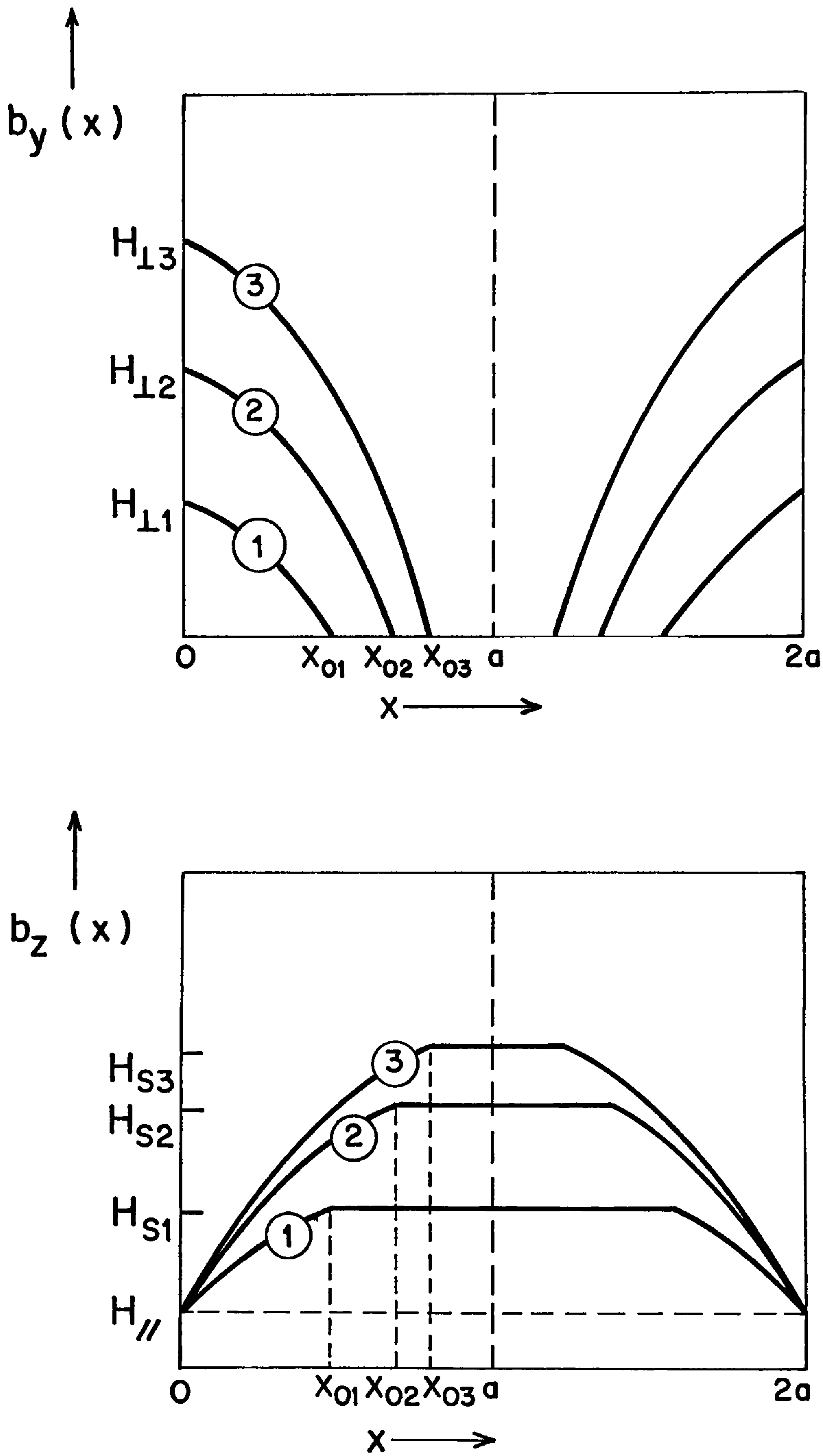

FIGURE 7: Sequence of magnetic induction profiles for the Bergeron Model (where $b_y(x_o) = 0$, $x_o < a$).

i) $\underline{b_y(x_o) = 0}$ where $x_o < a$

In this situation, b_y falls to zero at some point $x_o < a$, while b_z increases from $b_z(0) = H_{/\!/}$ at $x = 0$ to $b_z(x_o) = H_s$ at $x = x_o$. Since the total field is constant with position, then $b_z(x) = H_s$ for $x_o < x < a$. At $x = x_o$ we have

$$b_y(x_o) = H_s \cos(\gamma x_o + \phi) = 0$$

and $b_z(x_o) = H_s \sin(\gamma x_o + \phi) = H_s$

then

$$\gamma x_o + \phi = \frac{\pi}{2} \tag{4-20}$$

and

$$\langle B\rangle_{\perp} = \frac{H_s}{a}\int_0^{x_o} \cos(\gamma x + \phi)\,dx$$

$$= \frac{H_s}{\gamma a}\left[\sin(\gamma x_o + \phi) - \sin\phi\right]$$

and finally

$$\langle B\rangle_{\perp} = \frac{H_s - H_{/\!/}}{\gamma a} \tag{4-21}$$

and

$$\langle 4\pi M\rangle_{\perp} = \frac{H_s - H_{/\!/}}{\gamma a} - H_{\perp} \tag{4-22}$$

Also,

$$\langle B\rangle_{/\!/} = \frac{1}{a}\int_0^a b_z(x)\,dx$$

$$= \frac{H_s}{a}\int_0^{x_o} \sin(\gamma x + \phi)\,dx + \frac{H_s}{a}(a - x_o)$$

$$= -\frac{H_s}{\gamma a}\left[\cos(\gamma x_o + \phi) - \cos\phi\right] + \frac{H_s(a - x_o)}{a}$$

$$= \frac{H_s \cos \phi}{\gamma a} + \frac{H_s (a - x_o)}{a}$$

$$= \frac{H_\perp}{\gamma a} + \frac{H_s (a - x_o)}{a}$$

Therefore,

$$\langle 4\pi M\rangle_{/\!/} = \frac{H_\perp + H_s (\gamma a - \gamma x_o)}{\gamma a} - H_{/\!/} \qquad 4\text{-}23$$

where $\gamma x_o = \frac{\pi}{2} - \phi$

In order to predict both $\langle 4\pi M\rangle_\perp$ and $\langle 4\pi M\rangle_{/\!/}$ we need to specify γ. We can, however, determine γ using experimental values for $\langle 4\pi M\rangle_\perp$ and equation 4-22 in the form

$$\gamma = \frac{H_s - H_{/\!/}}{a (H_\perp + \langle 4\pi M\rangle_\perp)} \qquad 4\text{-}24$$

We then use γ obtained this way to evaluate $\langle 4\pi M\rangle_{/\!/}$ for the corresponding values of $H_\perp$ and $H_{/\!/}$.

ii) $\underline{b_y(a) > 0}$

As $H_\perp$ is increased, b_y penetrates further into the sample, and eventually reaches the center. As $H_\perp$ is further increased, $b_y(a)$ also increases. A typical field profile is shown schematically in Figure 8. In this situation,

$$\langle B\rangle_\perp = \frac{H_s}{a} \int_0^a \cos (\gamma x + \phi)\, dx$$

$$= \frac{H_s}{\gamma a} [\sin (\gamma a + \phi) - \sin \phi]$$

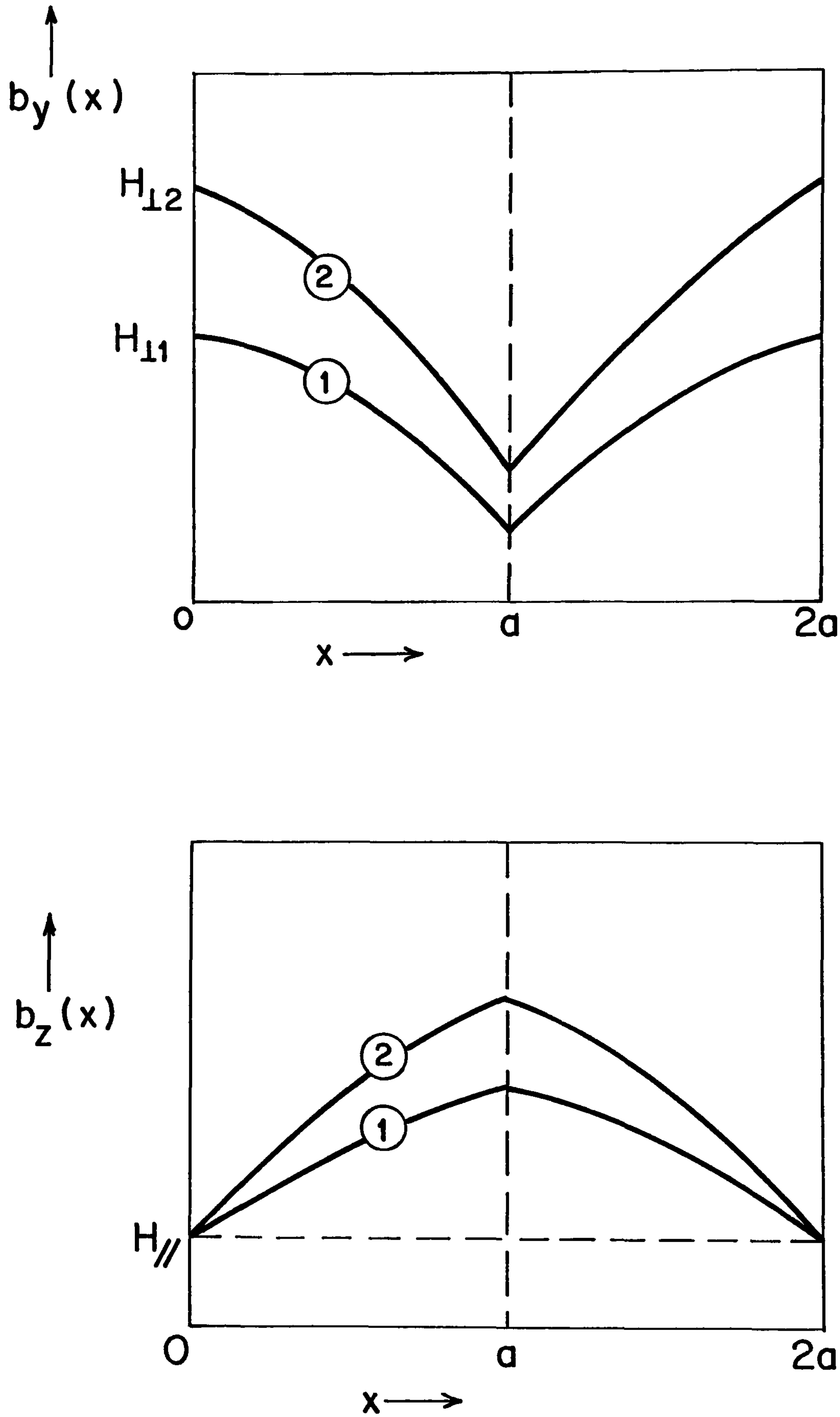

FIGURE 8: Sequence of magnetic induction profiles for the Bergeron Model (where $b_y(a) > 0$).

$$= \frac{H_s \sin(\gamma a + \phi) - H_{/\!/}}{\gamma a}$$

$$= H_{\perp} + \langle 4\pi M\rangle_{\perp}$$

Thus we obtain a transcendental relation

$$H_s \sin(\gamma a + \phi) - H_{/\!/} = \gamma a \, (H_{\perp} + \langle 4\pi M\rangle_{\perp}) \qquad 4\text{-}25$$

between γ and $\langle 4\pi M\rangle_{\perp}$. Again, we introduce observed values of $\langle 4\pi M\rangle_{\perp}$ for a given $H_{\perp}$ and $H_{/\!/}$, and solve for the corresponding γ. Since

$$\langle B\rangle_{/\!/} = \frac{H_s}{a} \int_0^a \sin(\gamma x + \phi) \, dx$$

$$= -\frac{H_s}{\gamma a} [\cos(\gamma a + \phi) - \cos\phi]$$

$$= \frac{H_{\perp} - H_s \cos(\gamma a + \phi)}{\gamma a}$$

$$= H_{/\!/} + \langle 4\pi M\rangle_{/\!/}$$

then

$$\langle 4\pi M\rangle_{/\!/} = \frac{H_{\perp} - H_s \cos(\gamma a + \phi)}{\gamma a} - H_{/\!/} \qquad 4\text{-}26$$

Thus we can evaluate the z- component of the magnetization having determined γ as indicated above.

In summary, when the y-component of the magnetic induction has not penetrated to the centre, equation 4-24 is used to determine γ, and equation 4-23 is used to calculate $\langle 4\pi M\rangle_{/\!/}$. If b_y has reached the centre, equation 4-25 is used to determine γ and equation 4-26 is used to calculate $\langle 4\pi M\rangle_{/\!/}$.

In Figure 9, γ is plotted against $H_{\perp}$, for fixed values of $H_{\parallel}$. Contrary to Figure 4, γ does not increase monotonically with $H_{\perp}$, but the curves exhibit a resonance shape. In Figure 10, γ is plotted against $H_{\parallel}$, for fixed values of $H_{\perp}$. For low values of $H_{\perp}$, γ again attains a maximum value before decreasing with $H_{\parallel}$, whereas in Figure 4, γ decreased monotonically with $H_{\parallel}$.

In Table I, we compare calculated values of $\langle 4\pi M\rangle_{\parallel}$ with experimental results. Four values of $H_{\perp}$ were chosen, and for each of these, calculations were made for various longitudinal fields, $H_{\parallel}$.

Here again, the model predicts a large value of $\langle 4\pi M\rangle_{\parallel}$, even when $H_{\parallel} = 0$. We have not encountered such behaviour in our samples.

Conclusion

In this chapter, we have exploited the consequences of a force-free model, which we call the Bergeron model, where the field profiles have simple sinusoidal forms:

$b_y(x) = H_s \cos(\gamma x + \phi)$

and $b_z(x) = H_s \sin(\gamma x + \phi)$

and where the total magnetic induction $B(x) = \sqrt{b_y^2 + b_z^2}$ is equal to the total externally applied field. $H_s = \sqrt{H_{\perp}^2 + H_{\parallel}^2}$, and $\phi = \tan^{-1}\left(\frac{H_{\parallel}}{H_{\perp}}\right)$ and the parameter γ is taken to be position independent.

The simplifying assumption that γ is independent of x implies

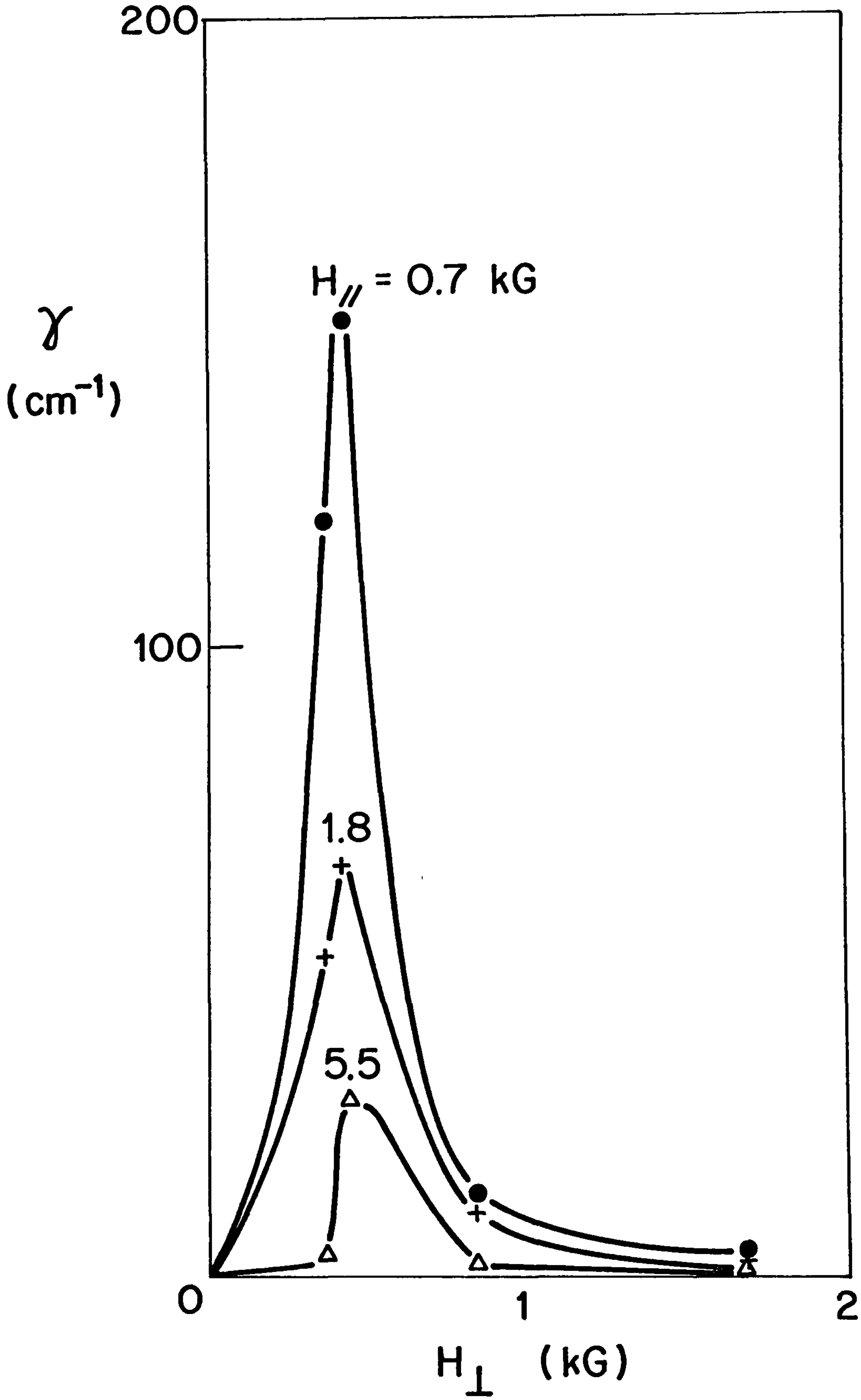

FIGURE 9: Variation of γ versus $H_\perp$ for the Bergeron Model (where $b_y(x_o) = 0$).

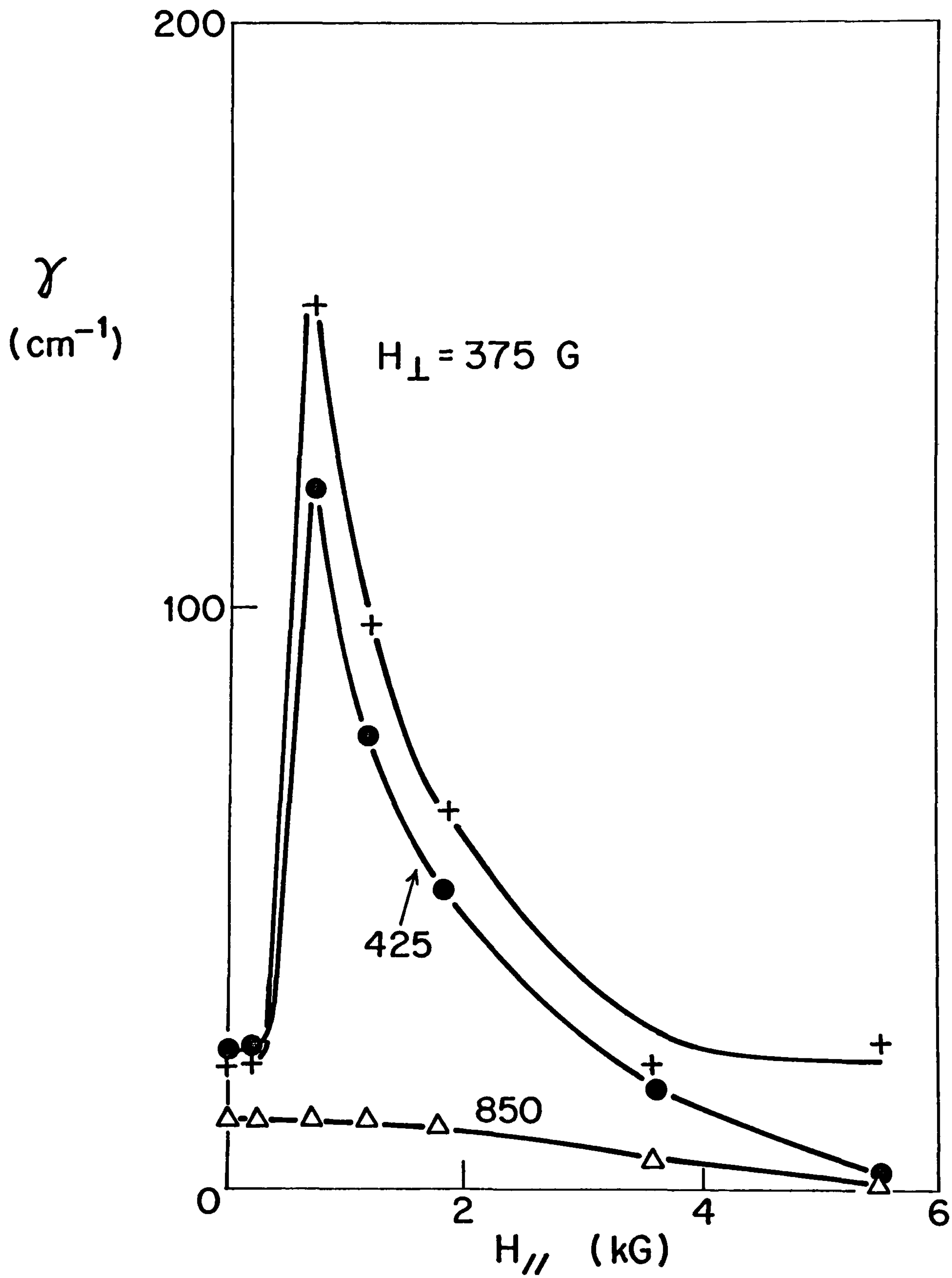

FIGURE 10: Variation of γ versus $H_{//}$ for the Bergeron Model (where $b_y(x_o) = 0$).

TABLE I

$H_{\perp}$ (Gauss)	$H_{//}$ (Gauss)	$<4\pi M>_{\perp}$ (EXP.) (Gauss)	γ (cm^{-1})	$<4\pi M>_{//}$ (Gauss) CALC.	EXP.
375	0	160	22.1	264	0
	360	275	22.2	128	120
	720	365	120.8	91	25
	1170	365	77.6	56	50
	1800	365	50.9	38	25
	3600	360	17.1	19	15
	5500	320	3.1	12	12
425	0	175	20.4	282	0
	360	275	20.6	152	135
	720	415	153.0	114	25
	1170	415	97.0	71	62
	1800	415	65.0	49	35
	3600	410	21.9	24	20
	5500	345	27.0	14	20
850	0	120	12.4	371	0
	360	234	10.9	292	180
	720	427	12.3	268	207
	1170	540	11.7	210	220
	1800	619	10.8	156	163
	3600	596	5.1	79	75
	5500	396	1.9	42	40
1700	0	70	6.6	416	0
	360	94	5.5	290	105
	720	136	4.0	247	130
	1170	193	3.8	229	155
	1800	253	3.4	200	125
	3600	283	2.0	116	82
	5400	208	1.0	59	47

TABLE I: Comparison of experimental values of $<4\pi M>_{//}$ for VTi with those calculated from the Bergeron Model.

that the direction of the flux lines varies linearly with depth since $\beta = \gamma x + \phi = \tan^{-1}\left(\frac{b_z}{b_y}\right)$. In a more general sinusoidal type of force-free model, this crucial restriction could be removed.

We have pursued two possible sinusoidal force-free configurations which are physically realistic and simple. In both cases, an increase in the externally applied field, H_s, however minute, is "felt" or "transmitted" equally throughout the volume of the slab. This is an immediate consequence that in an infinite slab the force-free condition becomes $\frac{d(B^2)}{dx} = 0$, hence requires that the total flux density be uniform (zero gradient). As H_s increases, the flux density increases uniformly everywhere in the sample in step with the change in applied field since there is no pinning to oppose such a uniform distribution of flux lines. In force-free situations, however, gradients can occur in the profiles of the components of the magnetic induction. We have visualised and investigated two special cases.

In the first case, we stipulate that an increase in the transverse component of the applied field, however small, causes a field gradient in both the y and z components of the magnetic induction to appear and change simultaneously throughout the entire volume of the slab. As a consequence, both components of the magnetic induction are made to vary throughout the sample (consistent with the boundary condition that at the surface, $b_y(0) = H_\perp$ and $b_z(0) = H_{/\!/}$). Further, we may impose the important restriction that along the mid-plane of the slab, the transverse component of the magnetic induction remain fixed at zero, regardless of the magnitude of the change in the applied transverse field. There is no particular physical justification for this last requirement in the experimental situation where an externally applied transverse field is swept up from zero. It is however a meaningful boundary condition when the external field is made to vary by introducing a conduction current along the z-direction in the slab. Here, $b_y(a)$ must remain zero unless we are prepared to envisage a sheet at the mid-plane supporting an infinite current density such that a finite current flows there. The condition we invoke leads immediately to a determination of the parameter γ and to predictions for the behaviour of both the y and z components of the magnetization ($\langle 4\pi M \rangle_{\perp}$ and $\langle 4\pi M \rangle_{/\!/}$).

We also considered a second case where the region in which gradients appear in the y and z field profiles advances gradually into the slab as the externally applied field is increased. Later, once field gradients (hence persistent induced currents) have been generated in the entire volume of the sample, the transverse magnetic induction is allowed to increase everywhere as the applied transverse field is made to grow further. In order to explore the consequences of this postulated behaviour we use one set of measurements (the transverse magnetic moments $\langle 4\pi M \rangle_{\perp}$) to determine the parameter γ and hence to calculate the expected complementary set of behaviour, the the parallel magnetic moments $\langle 4\pi M \rangle_{/\!/}$.

It is of some interest to compare the predictions of these two models with our observations. Since the samples we have investigated exhibit strong pinning and hence are very irreversible (hysteretic), it is not suprising that these models yield results which correspond very poorly with our data. Nevertheless, the comparison, particularly in the second case we have developed, provides some indications on the occurence and degree of force-free flow in our samples. We note in closing that measurements on materials with weaker pinning, hence more reversible behaviour than ours, have been carried out by Zahradnitsky (Zahradnitsky 73). A comparison with his data however also shows very poor agreement. Indeed an inspection of these experimental curves and the predictions of the models developed above suggest that major modifications are required and additional concepts need to be introduced in these models.

CHAPTER 5

THE CAMPBELL & EVETTS MODEL

Introduction

In the previous chapter we examined configurations of magnetic fields and persistent currents which are force-free. Among the possible mathematical descriptions of the force-free situation we selected harmonic solutions because these are analytically straight-forward. Further, from energy considerations, the oscillations were cut-off at a quarter-wave or less. To simplify the analysis we also assumed a wave-length parameter γ which is spatially constant. In this context we explored the magnetization curves expected for two physically meaningful sets of boundary conditions. In our analysis we did not focus attention on the fact that magnetic flux in type II superconductors is known to exist in the form of a lattice of discrete and quantized flux lines. Implicitly, we visualized that the planes of flux lines freely adjusted their orientation and density to achieve the desired sinusoidal force-free profiles and to match the specified boundary conditions as the externally applied field increased in strength and changed its direction. This picture, however, overlooks certain features which need to be taken into account and which we now outline.

The sequences of field profiles which we have considered require that there be no impediments to the migration and also to the rotation of flux lines. We postulated an idealized situation where there was no pinning to obstruct the motion of the flux lines. The planes of flux lines were thus considered free not only to migrate into and out of the sample but also to swing from one orientation to another within the specimen. At first glance then, the picture we developed appears consistent although very idealistic. There is however, besides pinning, an additional mechanism known as viscous drag or friction which opposes the motion of flux lines. It is not our purpose to delve into this concept but only to outline a consequence of bearing in our work. To a first approximation viscous drag is thought to increase linearly with the velocity of the flux lines. In order that viscous drag effects can be neglected, the rate of displacement of vortices must be kept sufficiently small.

To ensure that the flux lines already present in the specimen and the new vortices created at the surface migrate sufficiently slowly so that viscous effects can be ignored, the rate of increase of the externally applied field must not be excessive. In the "standard" situation where the direction of the magnetic field is kept fixed, this requirement is well satisfied when $dH/dt \lesssim 100$ G/sec as it is in our work. The maximum distance a flux line is expected to travel under these circumstances is half the thickness of the slab i.e. $\lesssim 0.1$ cm for our samples. We will derive expressions for the velocity of flux lines later in this chapter. The situation however is significantly and basically different when flux lines are made to rotate. The displacements envisaged when a flux line is rotated are a few orders of magnitude greater than that involved in the transporting of a vortex from the surface to the mid-plane . This is readily appreciated by considering a flux line initially threading the length of a long and wide ribbon (infinite slab) and focussing on any segment of this flux line located at a distance r from the "axis" of rotation. Such a segment must traverse an arc $S = r\theta$ when the flux line, considered as a continuous, straight entity, is made to change its orientation by an angle θ. A typical variation in the direction of the externally applied field in our work is of the order of a radian. Further, our samples are a few centimeters long, hence we need to envisage displacements in the range of centimeters. As a consequence, in order that viscous drag can be neglected, the rate of change of the transverse field $dH_{\perp} / dt$ must be chosen considerably slower when this field component is superimposed on a static (or varying) longitudinal field since flux lines are now required to rotate as they advance into the specimen.

If we take into account that in practice pinning can be diminished but very rarely made to vanish completely, the considerations we have just outlined lead to the conclusion that rotation of a long unbroken flux line is exceedingly more difficult to achieve than a lateral displacement of the entire line from the surface of the slab to the mid-plane (the maximum distance of travel). For bodily rotation to be accomplished most of the flux line must be dragged through a broad sweeping arc filled with obstacles in the form of pinning sites.

To circumvent the problem of bodily rotation workers have explored various schemes to change the orientation of an array of planes of flux lines while minimizing the total displacement required. It is beyond the scope of this thesis to enter into the details of such processes. We refer the reader to the discussion presented by Campbell and Evetts (1972). The essential feature of any such scheme is that two adjacent planes of flux lines oriented differently (θ_1 and θ_2), are allowed to intersect. During this occurence, the "individual" segments between the points of intersection, reorient and change their direction to θ_1' and θ_2' where $\theta_1 < \theta_1' < \theta_2' < \theta_2$. Subsequently the two planes separate. This entire operation is sometimes referred to as the cutting or crossing of flux lines. It requires that two discrete and separate flux quanta coalesce temporarily and form a doubly quantized region at the point of intersection (at the center of an x). The destruction of the two single flux quanta to create a doubly quantized region requires a local and transient increase in energy density comparable to the condensation energy. This scheme is consequently viewed as difficult to implement. Nevertheless the mechanism offers a possible method of achieving a reorientation of flux lines involving small displacements of a large number of short sections which add up to a total displacement considerably less than that necessary for the bodily rotation of an array of unbreakable continuous flux lines.

In view of the many physical obstacles encountered in changing the direction of flux filaments, Campbell and Evetts have opted to explore the extreme viewpoint that flux lines can move into or out of a sample but cannot change their orientation in the slightest degree. In this chapter we adopt their approach and pursue the consequences of the concept that flux lines can advance (or retreat) within an infinite slab but cannot rotate. We apply this constraint of no rotation to the basic situation of zero and finite pinning. In other words, pinning is effectively infinitely strong when opposing rotation of flux lines (azimuthal pinning) but either zero (force-free) or finite in hindering displacements perpendicular to the surface of the slab (transverse pinning). For the case where transverse pinning exists, we examine in some detail the differences in behaviour which are expected for various pinning functions spanning a broad spectrum of dependence on magnetic induction. In the latter circumstances we encounter configurations of magnetic field profiles and patterns of persistent circulating currents which are partially force-free since the macroscopic induced currents flow with a component along as well as perpendicular to the lines of magnetic induction. Finally we compare the predictions of this model with and without pinning with the pertinent curves from our experimental results.

Development of the Campbell and Evetts Model

Campbell and Evetts derive the following equation to describe the motion of vortices in an infinite superconducting slab as an external field is varied (Campbell 72, appendix IIe).

$$\left.\frac{\partial U}{\partial t}\right|_x = - v \left.\frac{\partial U}{\partial x}\right|_t - 2U \left.\frac{\partial v}{\partial x}\right|_t \qquad 5\text{-}1$$

where $U\ (x,t) = b_x^2 + b_y^2 = B^2(x,t)$

and $v(x,t)$ = velocity of a vortex, at a depth x from the surface as the external field is increased (these velocities are assumed slow enough for viscosity effects to be neglected).

Since $U = B^2$, equation 5-1 becomes

$$\left.\frac{\partial B}{\partial t}\right|_x = - v \left.\frac{\partial B}{\partial x}\right|_t - B \left.\frac{\partial v}{\partial x}\right|_t \qquad 5\text{-}2$$

We note that this result may be rewritten as follows

$$\vec{\nabla} \cdot (B\vec{v}) = - \frac{\partial B}{\partial t} \qquad 5\text{-}3$$

and constitutes an equation of continuity for the magnetic flux density, or equivalently, for the density of vortices.

It may be useful in appreciating the physical meaning of this expression for magnetic flux density to recall the more familiar equation of continuity for electric currents.

$$\vec{\nabla} \cdot \vec{J} = - \frac{\partial \rho}{\partial t}$$

where the current density $\vec{J} = \rho\vec{v}$ and ρ is the electric charge density. The physical quantity that is conserved is the electric charge. In our situation, the quantity that is "counted" inside the superconductor is the number of vortices, hence the magnetic flux, since each vortex carries a quantum of flux $\phi_0 = hc/2e$. Thus in our case, the density of vortices $n = |B|/\phi_0$ plays the role analogous to the charge density and we may write by analogy or derive in the same way as is done for electric charge density or in hydrodynamics for fluid density, the equation:

$$\vec{\nabla} \cdot \left(\frac{|B|\ \vec{v}}{\phi_0}\right) = \frac{1}{\phi_0}\ \frac{\partial |B|}{\partial t}$$

We will next apply the equation of continuity for flux lines to the special case of a superconducting infinite slab which has been cooled to below T_c in the presence of a magnetic field, $H_{//}$. Subsequently, a field, $H_{\perp}$, is increased from zero to a final value. Following Campbell and Evetts, we postulate that flux lines, once created, cannot change their orientation.

As a result of applying $H_{\perp}$, the total external field is increased in strength and changed in direction. Consequently, additional vortices nucleate at the surface of the slab parallel to the new applied field. These however will not be parallel to the vortices already threading the slab and are unable to cross them according to the hypothesis we are pursuing. They will therefore compress the original vortices toward the center until the resultant force on all the fluxons is zero. As $H_{\perp}$ is increased further, more and more vortices enter at greater and greater angles to $H_{//}$, and the "earlier" vortices gradually move nearer to the center of the slab.

A fluxon is nucleated at the surface at an angle θ_c (angle of creation) with the z-axis. Subsequently, as it penetrates the sample, it retains this angle θ_c, while the angle θ_s of new fluxons being generated at the surface is changing. Initially, $b_y(x) = 0$ and $b_z(x) = H_{//}$ for all x. Consider that the perpendicular field has been raised from zero to a "final" value, $H_\perp$, so that now the total field at the surface, $H_s = \sqrt{H_\perp^2 + H_{//}^2}$. The first group of fluxons created at the surface when $H_\perp$ began to increase have now penetrated to some distance x_o. In so doing, this plane of fluxons and planes subsequently created have compressed all the original fluxons initially occupying the volume between the surface ($x = 0$) and x_o into the region between x_o and the center ($x = a$). We will therefore need to examine two distinct regions in the sample.

(i) $x_o \leq x \leq a$

This region contains the original fluxons, all of angle $\theta = 0$, which initially (before the application of $H_\perp$) occupied the space $0 \leq x \leq a$, (half of the width of the slab) but have since been compressed at constant angle, into the smaller volume $x_o \leq x \leq a$. This compression of the original array of flux lines, although interesting, produces no change in the total magnetic moment of the specimen and is therefore not detected by the pick up coils embracing the sample.

(ii) $0 \leq x \leq x_o$

This region contains all of the new fluxons, created at the surface as $H_{\perp}$ was applied and which have penetrated to different depths into the sample. The angle of these fluxons, θ (with respect to the z axis) varies from $\theta = \theta_s$ at $x = 0$ to $\theta = 0$ at x_o. Since in the present scheme vortices are not allowed to rotate and are conserved, the total number of additional vortices together with their orientation determine the growth of the magnetic moment of the sample and its y and z components.

A fluxon created at the surface with an angle θ_c penetrates the sample with a velocity $v_s(t)$ and constant angle θ_c as the total field at the surface is varying. As a vortex enters the sample, the total flux inside the sample changes by an amount ϕ_o. The changes in the total flux occur only when the vortex enters the sample since, once the flux line is inside the specimen, the amount of flux it carries and its orientation do not change (ϕ_o is constant and θ_c is assumed constant). Therefore, all flux changes for the sample as a whole occur at the surface only. Further, since fluxons are not allowed to rotate once inside the slab, the rates of change of flux of the sample in the y and z direction ($d\phi_{//}/dt$ and $d\phi_{\perp}/dt$) are fixed by the rate of entry of vortices at the surface and their orientation at the time of entry.

Within the context of infinite slab geometry we visualize that a long thin ribbon sample consists of a section of width ℓ_y and height ℓ_z of an infinite slab of thickness 2a. We wish to calculate $\Delta\phi_{//}$, the change of magnetic flux threading a pick up coil which embraces an area $\vec{A}$ of dimension ℓ_y along the y direction and depth a extending from the surface of the slab chosen at x = 0 to its mid-plane (hence a is the half-thickness of the slab).

The magnetic field at the surface of the slab has an instantaneous intensity $H_s(t)$ and is directed at an angle $\theta_S(t) = \cos^{-1}(H_{//}/H_s(t))$ with respect to the z-axis. The flux lines already threading the area $\vec{A}$ are oriented at various angles $\theta(x)$ different from that existing at the surface. Since we postulate that all flux lines already existing in the slab cannot rotate nor vanish, any change in the magnetic flux threading the area $\vec{A}$ must arise from the entry of additional flux lines. As new planes of vortices enter (appear) at the surface, the planes of vortices previously occupying the space adjacent to the surface are displaced into the slab to accomodate the newcomers thereby themselves forcing their neighbouring planes of vortices to migrate further into the slab and so on. This "domino" process of adjustment takes place until the new gradient of flux density $d|B|/dx$ assumes a critical state in the region where changes are made to occur. Focussing on a particular group of planes or sheets of flux lines, we observe, according to our assumptions, that the "packing" or density of these flux lines increases as they migrate inwards but their total number and their orientation through the new area $\ell_y \Delta\, x(x,t)$ remains constant.

As a consequence, the infinitesimal increment in the number of vortices threading the area $\vec{A}$ can be written

$$\delta N_{//} = v_s(t) \left(\frac{H_S}{\phi_o}\right) \ell \delta t$$

where $\left(\frac{H_S}{\phi_o}\right)$ is the density of flux lines at the surface, $v_s(t)$ is their velocity of entry and $\ell(t) = \ell_y \cos \theta_s(t)$ is a length in the y-z plane directed perpendicularly to $H_s(t)$. We refer the reader to the sketch for aid in visualizing the situation we envisage. Introducing $\ell = \ell_y H_{//}/H_s(t)$ into this expression we write the infinitesimal increment in the flux through $\vec{A}$ as

$$\delta\phi_{//} = \phi_o \delta N_{//} = v_s H_{//} \ell_y \delta t$$

This can be integrated over the time t' elapsed as $H_{\perp}$ varies from 0 to some final value, hence as H_s varies from $H_{//}$ to $\sqrt{H^2_{\perp} + H^2_{//}}$ to give the total increase in flux seen by a pick up coil embracing the area $\vec{A}$

$$\Delta\phi_{//} = \ell_y \int_{t=0}^{t=t} v_s H_{//} dt$$

The change of flux permeating the area $\vec{A}$ can also be written

$$\Delta\phi_{//} = \Delta\left(\int_{\vec{A}} \vec{B} \cdot d\vec{A}\right) = \Delta\left(\ell_y \int_0^{a} B_z\, dx\right)$$

$$= \Delta\,(\langle B\rangle_{//}\ell_y a) = \Delta(H_{//} + \langle 4\pi M\rangle_{//})\,\ell_y a$$

$$= \Delta\,\langle 4\pi M\rangle_{//}\ell_y a$$

where we make use of our experimental condition that $H_{//}$ is stationary. Finally we obtain for the evolution of the magnetization in the z direction the expression

$$\langle 4\pi M\rangle_{//} = \frac{1}{a}\int_0^{t'} v_s H_{//}\,dt \qquad 5\text{-}4$$

since in our work $\langle 4\pi M\rangle_{//} = 0$ at $t = 0$, i.e., after cooling the sample through T_c in a constant $H_{//}$.

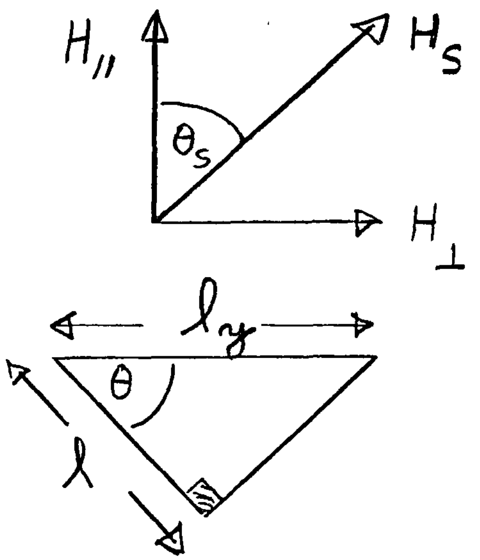

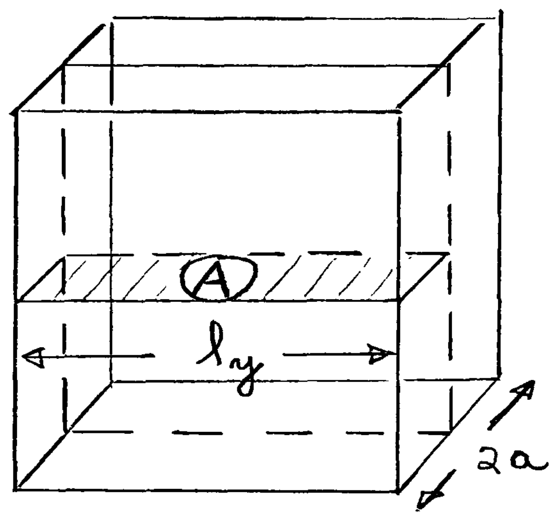

Pursuing the same line of reasoning for the change of flux threading an area A' of height ℓ_z and thickness a extending from the surface to the mid-plane of an infinite slab we can write

$$\delta\phi_\perp = \phi_o \delta N_\perp = \phi_o\left(v_s \frac{H_s}{\phi_o}\,\ell\,\delta t\right) = v_s\,H_\perp\,\ell_z \delta t$$

where $\ell = \ell_z \sin\theta_s$ and $\theta_s = \sin^{-1}(H_\perp / H_s)$

and $\Delta\phi_\perp = \ell_z \int_{t=0}^{t=t'} v_s H_\perp dt$

again $\Delta\phi_\perp = \Delta\left(\int_{A'} \vec{B} \cdot d\vec{A}\right) = \Delta\ (\ell_z \int_0^a B_y dx\ )$

$$= \Delta\ (\ \langle B\rangle_\perp\ \ell_z\ a) = \Delta\ (H_\perp + \langle 4\pi M\rangle\quad)\ \ell_z a$$

Finally we obtain for the evolution of the magnetization in the y-direction

$$\langle 4\pi M\rangle_\perp = \frac{1}{a} \int_0^{t'} v_s\ H_\perp\ dt - H_\perp \qquad \text{5-5}$$

where we make use of the fact that $H_\perp = 0$ and $\langle 4\pi M\rangle_\perp = 0$ at $t = 0$.

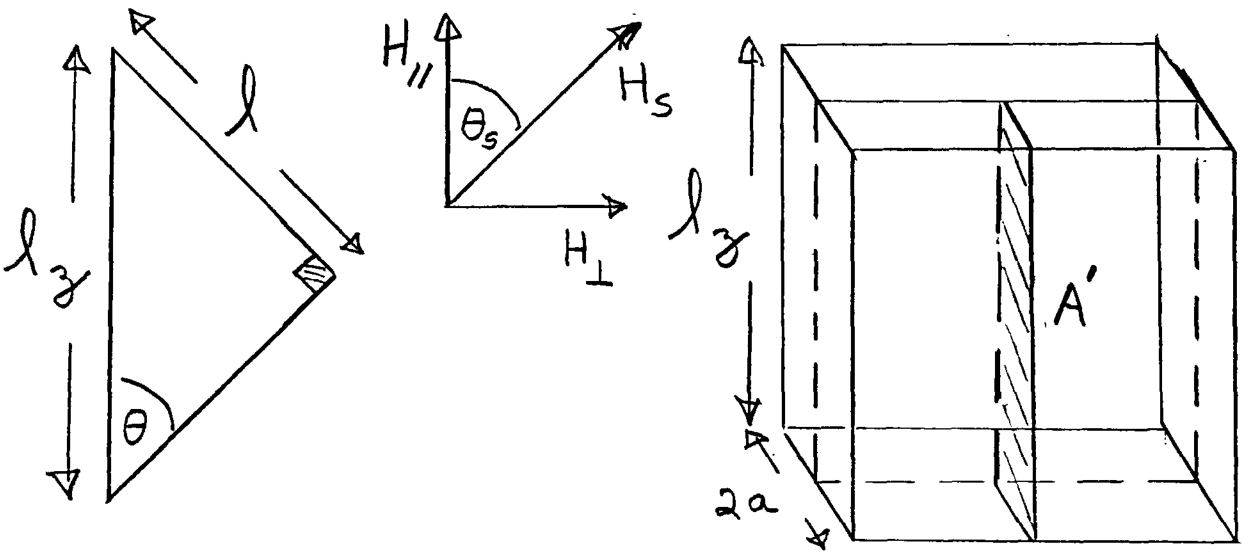

To calculate the evolution of the total magnetic moment and its components as $H_{\perp}$ increases we need to know the rate of entry, hence the velocity $v_s(t)$ of the vortices at the surface. The velocity of propagation of the fluxons $v(x,t)$ and in particular, their velocity as they enter the sample can be obtained by solving the equation of continuity (equation 5-2) once the total magnetic induction $B(x,t)$ is known as a function of time and space. The critical state equation $B \frac{dB}{dx} = F_p(B)$ enables us to determine the critical profile of the total magnetic induction either analytically or numerically for various H_s in sequence, hence versus time and position. Consequently we can obtain analytical or numerical solutions for $v(x, t \text{ or } H_s)$ and $\frac{dv}{dx}(x, t \text{ or } H_s)$ by introducing these results for the field profiles (in absolute values) in the differential equation of continuity.

Alternatively we can integrate the equation of continuity directly

$$\int_x^a \frac{d}{dx}(Bv)\, dx' = -\int_x^a \frac{d}{dt} B\, dx'$$

This yields $B(x)\, v(x) = \int_x^a \frac{dB}{dt}\, dx'$

Since the velocity of the vortices must be zero at the mid-plane of the slab (by symmetry) and in the adjoining volume where the density of vortices remains constant.

We obtain the velocity of the vortices at the surface by taking $x = 0$,

$$v_s\ (t) = \frac{1}{H_S(t)} \int_0^a \frac{dB}{dt}\, dx' \qquad 5\text{-}6$$

The right hand side of this equation can be evaluated analytically or numerically from the critical state equation. As noted previously, use of the critical state equation implies that all changes occur sufficiently slowly, hence velocities are small enough that viscous effects can be ignored.

In these calculations we take the absolute value of the magnetic induction because it is used as a measure of the density of vortices and consequently in counting the number of vortices occupying, entering and leaving elements of area. This number is independent of the orientation of the vortices in the y-z plane. As a consequence, the elements of area $\delta\vec{A}$ used in counting the vortices are not arbitrary but must be chosen parallel to the local magnetic induction. Accordingly an increment in the number of vortices can be written

$$\delta N = \frac{\delta\phi}{\phi_o} = \frac{\vec{B} \cdot \delta\vec{A}}{\phi_o} = \frac{B\ell\delta x}{\phi_o}$$

where ℓ is the magnitude of a vector lying in the y-z plane of the infinite slab whose length is arbitrary but fixed and which is directed perpendicularly to the local magnetic induction being "measured". B/ϕ_o is the local density of vortices.

Finally, introducing $v_s(t)$ from equation 5-6 into the expressions for the evolution of the components of the magnetization gives

$$\langle 4\pi M\rangle_{//} = \frac{1}{a}\int_0^{t'} \frac{H_{//}}{H_s}\, dt \int_0^a \frac{dB}{dt}\, dx' \qquad 5\text{-}7$$

and

$$\langle 4\pi M\rangle_{\perp} = \frac{1}{a}\int_0^{t'} \frac{H_{\perp}}{H_s}\, dt \int_0^a \frac{dB}{dt}\, dx' - H_{\perp} \qquad 5\text{-}8$$

Equations 5-4 and 5-5 can be derived more formally as follows.

We take the Maxwell-Faraday equation

$$\nabla \times \vec{E} = -\frac{\partial \vec{B}}{\partial t}$$

Since for our infinite slab situation the electric field

$$\vec{E} = \hat{j}\, E_y(x) + \hat{k}\, E_z\,(x)$$

and the magnetic induction

$$\vec{B} = \hat{j}\, B_y\,(x) + \hat{k}\, B_z\,(x), \text{ this yields}$$

$$\hat{j}\left(-\frac{\partial E_z}{\partial x}\right) + \hat{k}\left(\frac{\partial E_y}{\partial x}\right) = -\hat{j}\left(\frac{\partial B_y}{\partial t}\right) - \hat{k}\left(\frac{\partial B_z}{\partial t}\right)$$

Taking the vector components separately and integrating with respect to x gives

$$E_y = -\int_0^a \frac{\partial B_z}{\partial t}\, dx' \quad \text{and} \quad E_z = \int_0^a \frac{\partial B_y}{\partial t}\, dx'$$

since $E_y(a) = 0$ and $E_z\,(a) = 0$ by symmetry.

Next we use the Lorentz equation

$$\vec{E} = \vec{v} \times \vec{B}$$

where the vortices are visualized as moving with velocity $\vec{v}$ instead of the electric charges. Since for our situation $\vec{v} = \hat{i}v(x)$ this yields

$$\hat{j}\ E_y(x) + \hat{k}\ E_z(x) = -\ \hat{j}\ (vB_z) + \hat{k}\ (vB_y)$$

and at the surface

$$\hat{j}\ E_y + \hat{k}\ E_z = -\ j\ (v_s H_{//}) + \hat{k}\ (vH_{\perp}\ )$$

Equating components from this result with the corresponding components from the Maxwell-Faraday equation leads to the expressions we derived earlier in this chapter

$$E_y = v_s H_{//} = \int_o^a \frac{\partial B_z}{\partial t}\, dx' = a \frac{d}{dt} <B>_{//} =$$

$$a \frac{d}{dt} (H_{//} + <4\pi M>_{//})$$

$$E_z = v_s H_{\perp} = \int_o^a \frac{\partial B_y}{\partial t}\, dx' = a \frac{d}{dt} <B>_{\perp} =$$

$$a \frac{d}{dt} (H_{\perp} + <4\pi M>_{\perp})$$

These lead to equations 5-4 and 5-5 upon integration over time.

We note that in this "formal" derivation from basic equations, the statement that the velocity of the vortices $\vec{v} = \hat{i}v(x)$ is equivalent to the requirement that the vortices are not allowed to rotate inside the infinite slab.

Application of the Model

We now exploit the general results we have developed to calculate the evolution of the components of the magnetic moment in two basic situations. Firstly we consider the unique and ideal case where there is absolutely no pinning, hence pure force-free configurations prevail. Then we explore the application of the model to various cases where pinning exists. These cases are selected so that our survey of the predictions of the model spans a broad range of pinning behaviour.

1. Zero Pinning (Pure Force-Free)

$$\vec{F}_L = \vec{F}_P = 0$$

We have shown earlier that if the current density is everywhere circulating parallel to the total magnetic induction $\vec{B}$, hence $\vec{F}_L = \vec{J} \times \vec{B} = 0$, then the magnitude of the total induction, B(x) is constant throughout the sample, and $B(x) = H_s$ the total field at the surface.

Since $\frac{\partial B}{\partial x} = 0$ then $\frac{\partial B}{\partial t} = \frac{\partial H_s}{\partial t} \equiv \dot{H}_s$ and the equation of continuity (5-2) has the simple form

$$\dot{H}_s = - H_s \frac{\partial v}{\partial x}$$

This may readily be integrated over the half width of the slab

$$\int_v^o \left(\frac{\partial v}{\partial x} \right) dx' = - \frac{\dot{H}_s}{H_s} \int_x^a dx'$$

and yields

$$v\ (x,t) = \frac{\dot{H}_s\ (t)}{H_s\ (t)}\ (a - x) \qquad 5\text{-}9$$

since the velocity of the fluxons is zero at the centre of the slab.

This relates the velocity of propagation of the fluxons, at a depth x, in the sample, to the "instantaneous" field at the surface and the rate of change of this field. We note that the velocity of the fluxons decreases linearly to zero with distance from the surface. The velocity at the surface is

$$v_s = \frac{\dot{H}_s\ a}{H_s} \qquad 5\text{-}10$$

Introducing this result into equations 5-4 and 5-5 we obtain

$$\langle 4\pi M\rangle_{//} = \int_{H_{//}}^{H_s} \frac{H_{//}}{H_s}\ dH_s = H_{//} \log \frac{H_s}{H_{//}} =$$

$$\frac{H_{//}}{2} \log \left(1 + \left(\frac{H_\perp}{H_{//}}\right)^2\right) \qquad 5\text{-}11$$

and

$$\langle 4\pi M\rangle_\perp = \int_{H_{//}}^{H_s} \frac{H_\perp}{H_s}\ dH_s - H_\perp \qquad 5\text{-}12$$

Since $H_\perp = \sqrt{H_s^{\,2} - H_{//}^{\,2}}$ we can readily integrate equation 5-12 and obtain

$$\langle 4\pi M\rangle_\perp = H_s^{\,2} - H_{//}^{\,2} \Big|_{H_{//}}^{H_s} - H_{//} \sec^{-1} \frac{H_s}{H_{//}} \Big|_{H_{//}}^{H_s} - H_\perp$$

$$\langle 4\pi M\rangle_{\perp} = - H_{//} \sec^{-1} \frac{H_s}{H_{//}} =$$

$$= - H_{//} \sec^{-1} \sqrt{1 + \left(\frac{H_{\perp}}{H_{//}}\right)^2} \qquad 5\text{-}13$$

We note that $\langle 4\pi M\rangle_{//}$ is paramagnetic, i.e. $\langle B\rangle_{//} > H_{//}$ and $\langle 4\pi M\rangle_{\perp}$ is diamagnetic, i.e. $\langle B\rangle_{\perp} < H_{\perp}$.

As expected, the Campbell and Evetts model, where vortices are not permitted to rotate, leads, for the idealized situation where there is zero (transverse) pinning, to universal curves for the evolution of the components of the magnetization, independent of the "material" used in fabricating the infinite slab. In Figures 11 and 12 we present the predictions of this model as $H_{\perp}$ increases for several $H_{//}$ selected to correspond to the values for which we have made measurements in a ribbon of VTi. Although this model in its present form incorporates no ceiling, presumably its range of "validity" ceases when H_s attains H_{c2}.

It is remarkable that with this model we do not need to know the profiles of the magnetic induction either in the y or in the z direction in order to calculate the growth and variation of the components of the magnetic moment. It is sufficient to know the sequence of profiles of the absolute value of the total magnetic induction. This was noted earlier and emerges from inspection of equations 5-7 and 5-8. These profiles are nevertheless of interest and we now proceed to their determination.

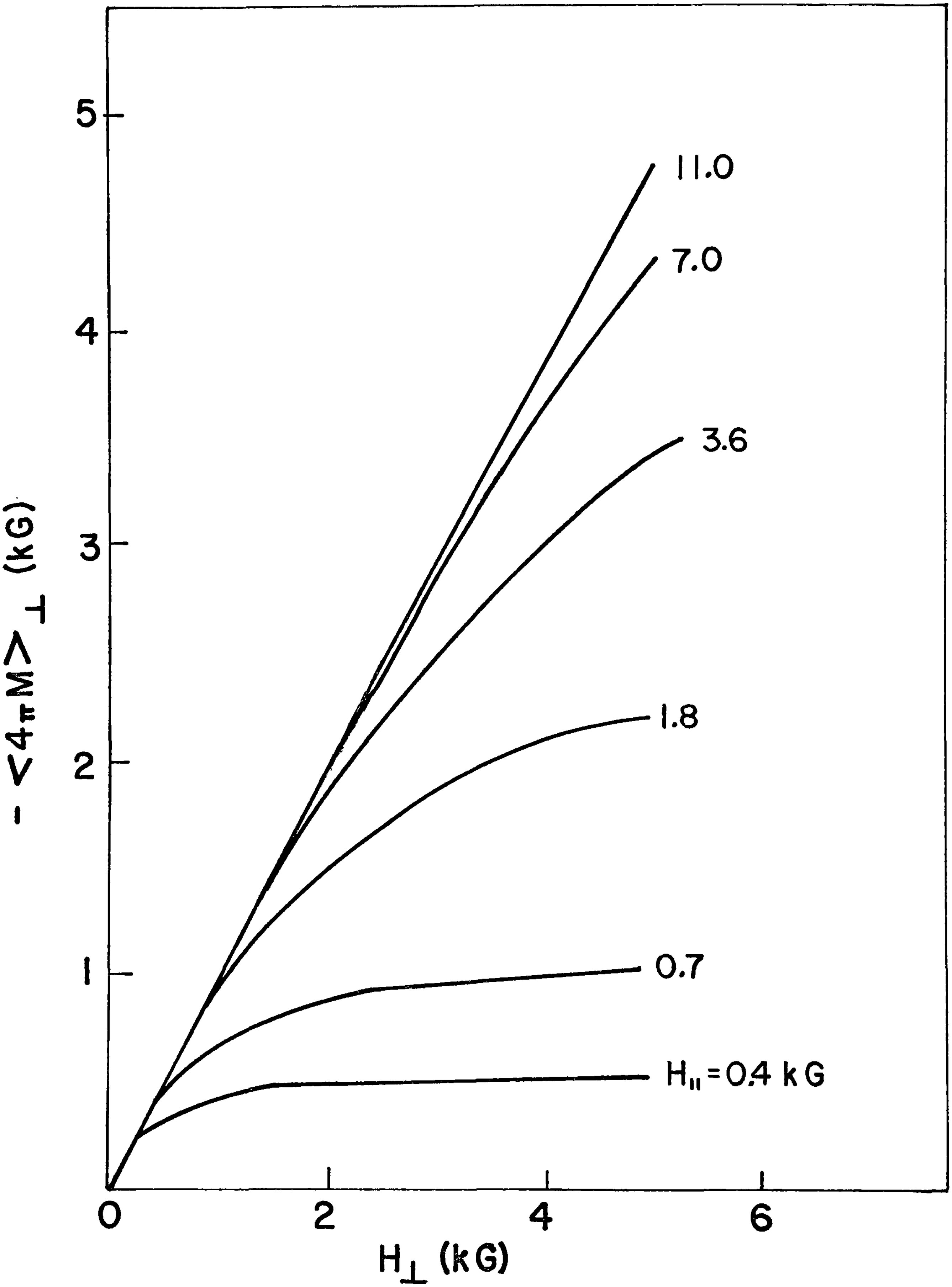

FIGURE 11: Variation of $\langle 4\pi M \rangle_{\perp}$ versus $H_{\perp}$ calculated from the Campbell-Evetts model (Zero Pinning).

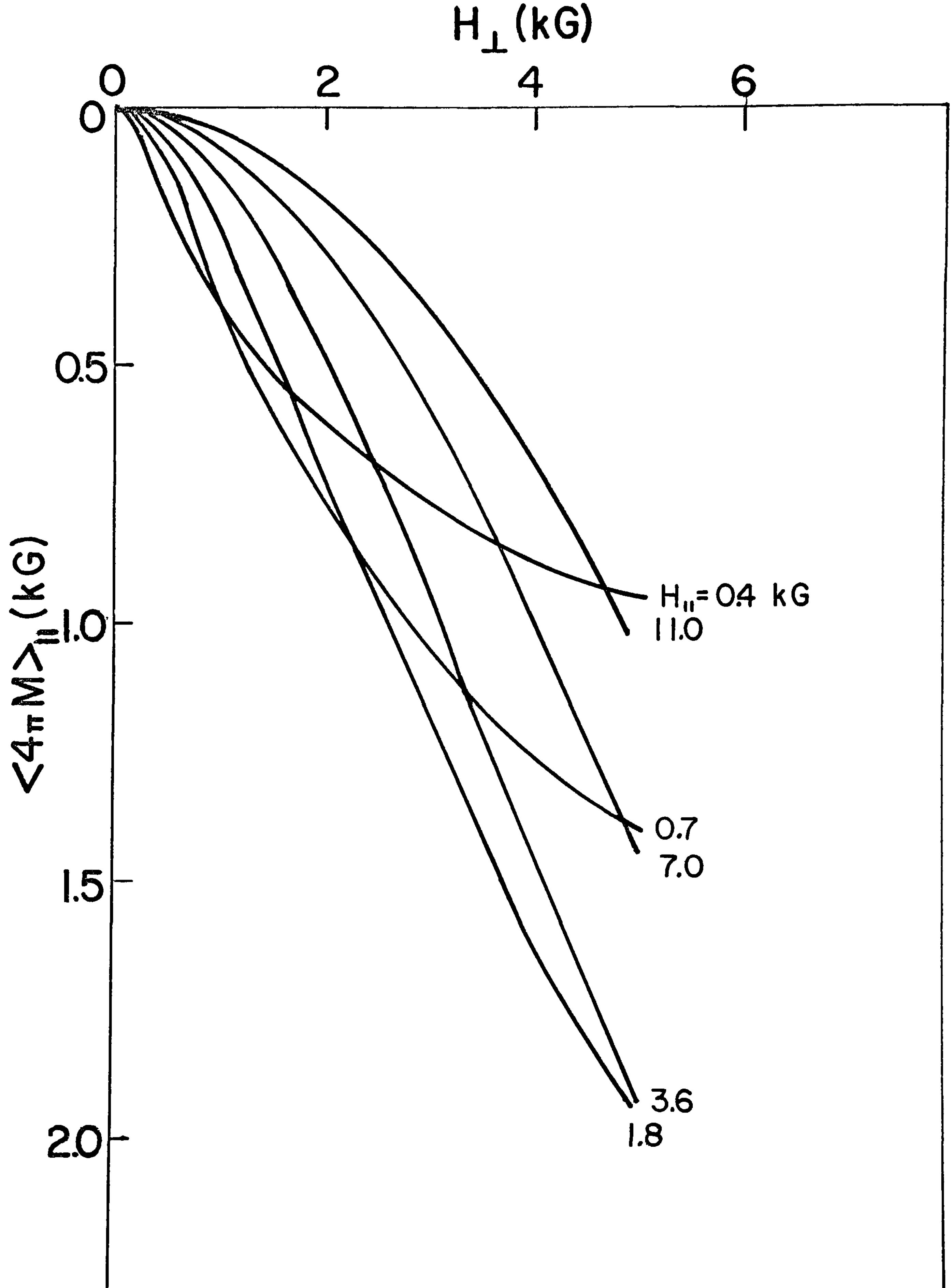

FIGURE 12: Variation of $<4\pi M>_{//}$ versus $H_\perp$ calculated from the Campbell-Evetts model (Zero Pinning).

This is possible because we know the instantaneous velocity with which any group of vortices advances into the sample. We focus on a group of vortices produced at the surface at some earlier time t_1 at an angle θ_1 when the total field there was $H_s(t_1)$.

We denote this field at creation $H_c = \sqrt{H_{\perp c}^2 + H_{//}^2}$, and the corresponding angle of creation θ_c ($\cos\theta_c = \frac{H_{//}}{H_c}$). Subsequently at a later time t_2, when the total field at the surface has changed to $H_s = \sqrt{H_{\perp}^2 + H_{//}^2}$, this vortex has moved, at constant angle, to a depth x inside the sample, where the total field is now $B(x) = H_s$, since the magnetic induction has the same intensity throughout the slab in the force-free situation. Thus

$$\cos\theta_c = \frac{H_{//}}{H_c} = \frac{b_z(x)}{B(x)} = \frac{b_z(x)}{H_s} \qquad 5\text{-}14$$

Hence $$b_z(x) = \frac{H_{//}H_s}{H_c} \qquad 5\text{-}15$$

In order to evaluate $b_z(x)$ at an arbitrary time t_2 when the field at the surface is H_s we need to establish the field of creation H_c for every plane of fluxons in the sample.

In a time interval dt, the plane of the fluxons moves a distance $dx = v(x,t)\,dt$ where $v(x,t)$ is given by equation 5-9.

$$dx = \frac{\dot{H}_s}{H_s}(a - x)\,dt = (a - x)\frac{dH_s}{H_s}$$

We can now determine the position in the sample of fluxons originally at the surface (x = 0) when the field there was H_c now that the field at the surface has increased to H_s.

$$\int_{H_c}^{H_s} \frac{dH_s}{H_s} = \int_{o}^{x} \frac{dx}{a - x}$$

Thus
$$H_c = \frac{(a - x)}{a} H_s \tag{5-16}$$

Introducing this result into equation 5-15, the statement of conservation of angle of creation we obtain

$$b_z(x) = \frac{H_{//} a}{a - x} \tag{5-17}$$

which describes the variation of $b_z(x)$ over a distance $0 \leq x \leq x_o$.

and
$$b_y(x) = \{ H_s^2 - \frac{H_{//}^2 a^2}{(a - x)^2} \}^{\frac{1}{2}} \tag{5-18}$$

For $x \geq x_o$, the value of $b_y = 0$.

These profiles, as required, also satisfy the boundary conditions that $b_z(o) = H_{//}$ and $b_y(o) = H_{\perp}$. We rewrite equation 5-17 in terms of the angle θ (x)

$$\cos \theta \ (x) = \frac{b_z(x)}{B(x)} = \frac{b_z(x)}{H_s} = \frac{H_{//} a}{H_s(a - x)} \tag{5-19}$$

Thus, as required, $\theta = \theta_s = \cos^{-1} \frac{H_{//}}{H_s}$ at x = 0 and decreases to $\theta = 0$ at a distance x_o where

$$x_o = \frac{a(H_s - H_{//})}{H_s} \tag{5-20}$$

is determined by letting $\cos \theta = 1$ in equation 5-19 or $b_y(x) = 0$

in equation 5-18 or $b_z(x) = H_s$ in equation 5-17

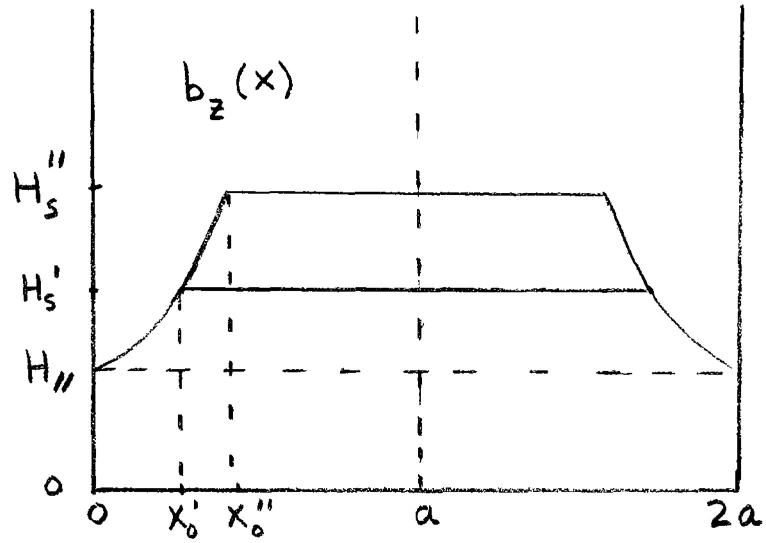

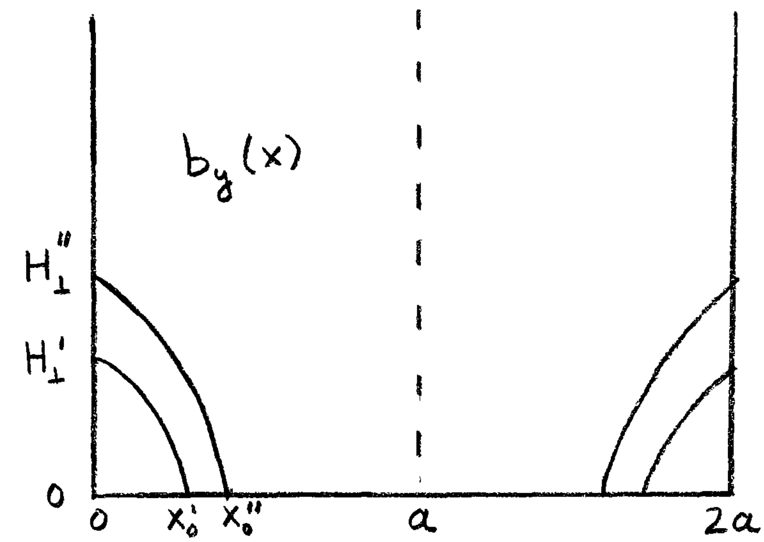

Finally we verify that all of the vortices originally threading the half slab at t = 0 when $H_s = H_{//}$ are now contained (compressed) in the region between x_o and the mid-plane x = a.

Initially the number of vortices in the z-direction is given by $H_{//}\, a\ell_y/\phi_o$ which is seen to be equal to $H_s(a - x_o)\ell_y/\phi_o$, the number contained in the reduced area $(a - x_o)\ell_y$ when we introduce x_o from equation 5-20 into the latter expression.

The expressions for the profiles of the components of the magnetic induction (equations 5-17 and 5-18) may be integrated to give $\langle B\rangle_{//}$ and $\langle B\rangle_{\perp}$, hence $\langle 4\pi M\rangle_{//}$ and $\langle 4\pi M\rangle_{\perp}$, as the transverse field $H_{\perp}$ is applied. The results are of course identical to equations 5-11 and 5-13 obtained without knowing the separate profiles explicitly.

General Observations

We have developped the predictions of a force-free model originally proposed by Campbell and Evetts where vortices are not permitted to rotate. The behaviour emerging from this model is most appropriately to be compared with that flowing from the Bergeron model with sinusoidal profiles (less than quarter-wave) which fill the width of an infinite slab. The latter force-free model allows complete freedom to the flux-lines to rotate. In both models no upper field boundary is imposed on the superconducting response, hence both implicitly take H_{c2} as infinite. As a consequence, if any behaviour ensuing from these models occurs in real samples it should be sought and may be encountered in the low field range above H_{c1} and far below H_{c2}.

An inspection and comparison of the families of curves for the evolution of the // and $\perp$ magnetizations vs $H_{\perp}$ displayed by these two models and a perusal of the corresponding experimental families of curves presented in this thesis and in the literature reveals that certain qualitative trends exhibited by the Campbell and Evetts model correspond much better with the observations. We may conclude that vortices, even in weak pinning samples are severely impeded from rotating. We may surmise that force-free and partly force-free configurations which require substantial adjustments in the orientation of existing vortices are not in tune with reality.

We note that the Campbell and Evetts model leads to appreciable enhancements of the transverse moments with increasing $H_{//}$. Such increases, although less dramatic, have been observed and are reported in the next chapter. The Bergeron version however fails to provide any significant increases of this component vs $H_{//}$. Further, the Campbell and Evetts model exhibits a rapid growth through a maximum and subsequent decline in the $\langle 4\pi M\rangle_{//}$ vs $H_{\perp}$ curves with increasing $H_{//}$. This is a striking feature encountered in the experimental data. The Bergeron model, by contrast, leads to large // moments even when $H_{//} = 0$ which then decrease monotonically with increasing $H_{//}$. Finally we note that both models predict moments which are much too large. Since they have the virtue of incorporating no adjustable parameters we must seek agreement with observations by adding new features to these models or modifying their basic assumptions. In the following section we explore the consequences of introducing pinning forces in the Campbell and Evetts model.

2. Finite Transverse Pinning (Partially Force-Free)

$$\vec{F}_L = \vec{F}_p \neq 0$$

When the current density flows at an angle $0 < \phi < \pi/2$ with the total magnetic induction $\vec{B}$, the Lorentz force on the fluxons is not zero and in the critical state this force is exactly balanced by the maximum pinning force $\vec{F}_p$ everywhere in the sample where currents circulate. Campbell and Evetts briefly discuss the application of their model to this situation in general terms and explore only the special case where F_p is a constant. There is considerable information accumulated in the literature indicating that pinning behaviour can be adequately described by expressions of the general form

$$F_p = \alpha (T) B^n \{ 1- (\frac{B}{H_{c2}})^{\ell} \}^m \qquad 5\text{-}21$$

where $0 \leq n \leq 1$ and ℓ, $m > 0$. These equations exhibit a resonance shape, i.e. the pinning force is zero for $B = 0$ and $B = H_{c2}$ and traverse a maximum at an intermediate field as shown schematically in the sketch below.

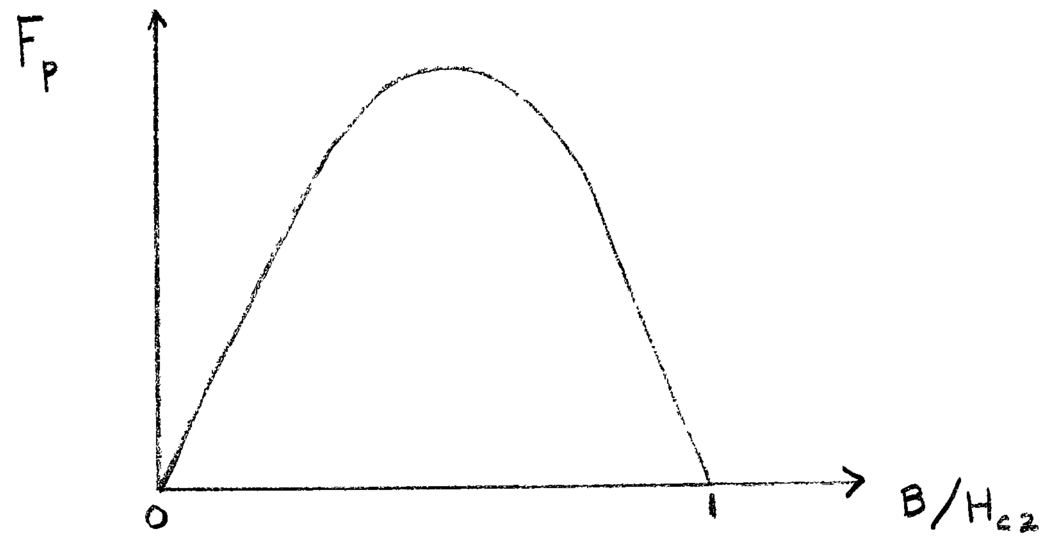

In order to investigate the role of pinning in describing magnetic behaviour in the Campbell and Evetts model where rotation of vortices is forbidden we wish to examine pinning functions which span the extremes permitted by realistic expressions of the form presented in equation 5-21. In the range of low fields, the factor $(1 - (\frac{B}{H_{c2}})^{\ell})^{m}$ is not significant and can be ignored. Further, most of the pertinent data available is in this range. Accordingly we focus our attention on the factor B^n in equation 5-21. As noted above, Campbell and Evetts have already considered the case where $F_p = \alpha$ hence where $n = 0$. We also study the cases where $n = \frac{1}{2}$ and $n = 1$.

These three choices are of special interest because they have already been extensively exploited in diverse contexts and become enshrined in the literature on pinning in type II superconductors. They also have received some theoretical justification in various analyses of pinning. Each of these powers of B in the pinning function are historically associated with a particular worker or group of workers in the field; with Kim et al ($n = 0$), Yasukochi et al ($n = \frac{1}{2}$) and Bean ($n = 1$).

To describe the phenomena over a broad range of magnetic fields we need to take the factor $(1 - (B/H_{c2})^{\ell})^{m}$ into account. To guide us in selecting a specific form for the pinning function we focus on the magnetization curve obtained when $H_{//} = 0$, hence where vortices enter and leave the surface and migrate in the sample at constant angle ($\theta = \pi/2$) and no rotation of vortices is encountered. We find that the magnetic behaviour of the samples we have studied and others investigated by other workers in our laboratory can be adequately described under these circumstances by using a factor with the simple form $(1 - B/H_{c2})^2$.

Consequently we proceed to develop the Campbell and Evetts model for the case where the pinning force has the form

$$F_p = \alpha B \left(1 - \frac{B}{H_{c2}} \right)^2$$

Subsequently we will ignore the factor $(1-B/H_{c2})^2$ and examine the consequences of neglecting this term at low fields. Finally we will develop the model for the case where $n = 0$ and $n = \frac{1}{2}$ and compare the results of all these cases with each other and with our data.

I $\quad \underline{F_p = \alpha B \left(1 - \frac{B}{H_{c2}}\right)^2}$

For infinite slab geometry where the applied magnetic field is increasing, the appropriate critical state equation can be written

$$B \frac{dB}{dx} = - \alpha B \{1 - \frac{B}{H_{c2}}\}^2 \qquad 5\text{-}22$$

or

$$\frac{dB}{(H_{c2} - B)^2} = - \frac{\alpha \, dx}{H_{c2}^{\;2}}$$

Inserting the boundary condition that at $x = 0$, $B = H_s = \sqrt{H_\perp^{\;2} + H_{//}^{\;2}}$ and integrating

$$\int_{H_s}^{B} \frac{dB}{(H_{c2} - B)^2} = - \frac{\alpha}{H_{c2}^{\;2}} \int_0^x dx$$

gives

$$B\,(x) = H_{c2} - \frac{H_{c2}^{\;2}\,(H_{c2} - H_s)}{H_{c2}^{\;2} - (H_{c2} - H_s)\,\alpha x} \qquad 5\text{-}23$$

At low fields ($H_s < H_s^*$) the total field decreases from $B(o) = H_s$ at the surface to $B(x_1) = H_{//}$, at a point $x_1 < a$. Between x_1 and the center, the total field is constant and is equal to $H_{//}$. This is the situation that prevails when the critical state has not yet penetrated to the center of the slab.

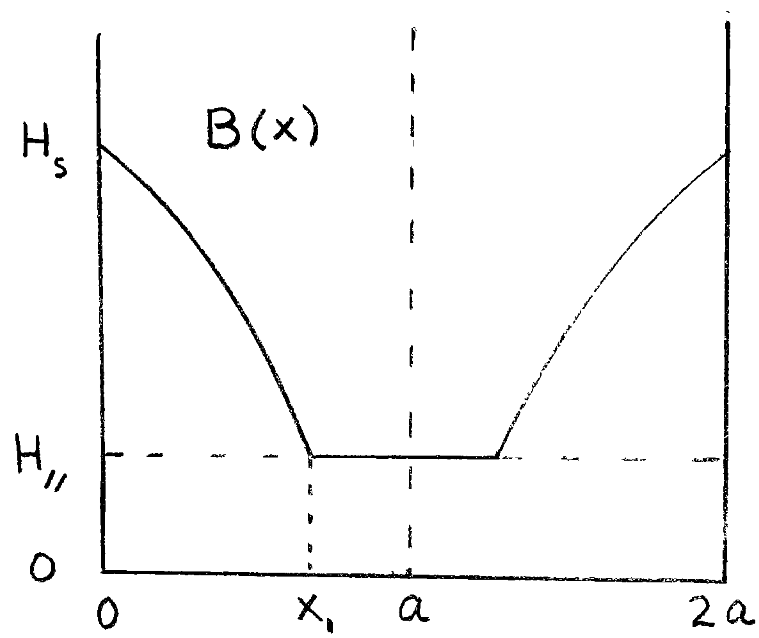

The penetration depth, x_1, is determined by setting $B(x_1) = H_{//}$ in equation 5-23. This gives

$$x_1 = \frac{H_{c2}^2}{\alpha} \left\{ \frac{H_s - H_{//}}{(H_{c2} - H_s)(H_{c2} - H_{//})} \right\} \qquad 5\text{-}24$$

As the external field is increased, the critical state penetrates further into the sample, until, at some field, H_s^*, it reaches the center. This full penetration field, H_s^* is determined by setting $x_1 = a$ for $H_s = H_s^*$ in equation 5-24. Thus,

$$H_s^* = \frac{H_{c2}\,[H_{c2}H_{//} + \alpha\, a\,(H_{c2} - H_{//})]}{H_{c2}^2 + \alpha\, a\,(H_{c2} - H_{//})} \qquad 5\text{-}25$$

and, since $\quad H_s^* = \sqrt{H_\perp^{*2} + H_{//}^2}$, then

$$H_\perp^* = \left\{ \frac{H_{c2}^2\,[H_{c2}H_{//} + \alpha a\,(H_{c2} - H_{//})]^2}{[H_{c2}^2 + \alpha a\,(H_{c2} - H_{//})]^2} - H_{//}^2 \right\}^{1/2}$$

5-26

Consequently, if the perpendicular field is greater than $H_\perp^*$, the critical state reaches the center of the sample and $B(x)$ is greater than $H_{//}$ throughout the sample.

In these circumstances the total field at the center is

$$B(a) = H_{c2} - \frac{H_{c2}^2\,(H_{c2} - H_s)}{H_{c2}^2 - (H_{c2} - H_s)\alpha a} \qquad 5\text{-}27$$

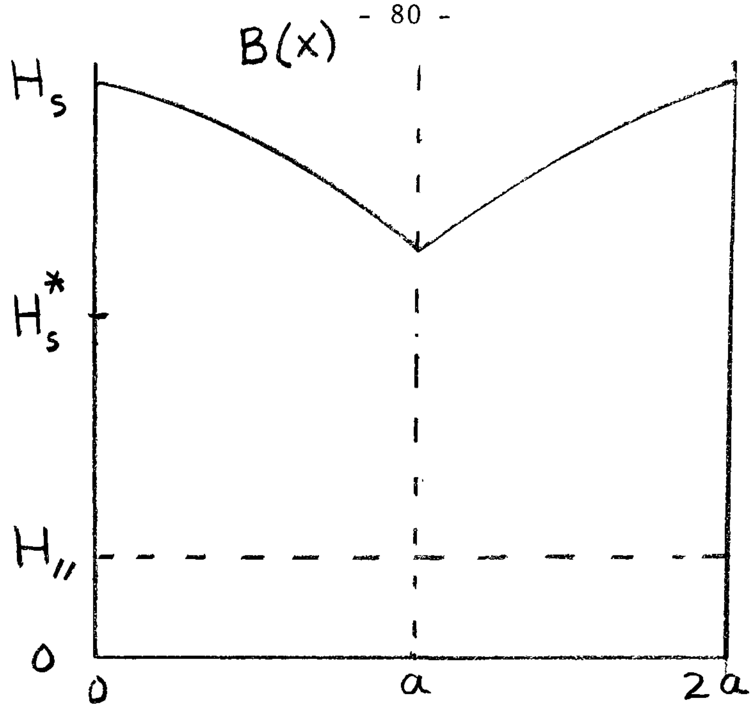

Differentiating equation 5-23 for the profile of the total field with respect to time we obtain

$$\frac{\partial B}{\partial t} = \frac{H_{c2}^{\,2}\,(H_{c2} - H_s)\alpha x\,\dot{H}_s}{\{H_{c2}^{\,2} - (H_{c2} - H_s)\,\alpha x\}^2} + \frac{H_{c2}^{\,2}\,\dot{H}_s}{H_{c2}^{\,2} - (H_{c2} - H_s)\alpha x}$$

$$= \frac{H_{c2}^{\,4}\,\dot{H}_s}{\{H_{c2}^{\,2} - (H_{c2} - H_s)\,\alpha x\,\}^2}$$

This result can be simplified by noting that the denominator according to equation 5-23 can be written

$$\{\,H_{c2}^{\,2} - (H_{c2} - H_s)\,\alpha x\} = H_{c2}\,\frac{(H_{c2} - H_s)}{(H_{c2} - B)}$$

Finally we obtain

$$\frac{\partial B}{\partial t} = \dot{H}_s\,\frac{(H_{c2} - B)^2}{(H_{c2} - H_s)^2}$$

Introducing the critical state equation in the form $(H_{c2} - B)^2 = - \frac{H_{c2}{}^2}{\alpha} \frac{dB}{dx}$ into this expression enables us to write the equation of continuity as follows

$$\frac{\dot{H}_s H_{c2}{}^2 \, dB}{\alpha (H_{c2} - H_s)^2} = d(vB) \qquad \text{5-28}$$

This may readily be integrated since the velocity falls to zero at known depths in the sample. There are two possible cases to consider.

a) $\underline{H_s < H_s^*, \text{ i.e., } 0 < x_1 < a}$

The critical state has not yet penetrated to the center. The velocity of the fluxons is zero at $x = x_1$, where $B(x_1) = H_{//}$. All the fluxons between $0 < x < x_1$ are moving, but those within the region $x_1 < x < a$ are stationary; v is zero when $B = H_{//}$. Integrating equation 5-28

$$\int_B^{H_{//}} \frac{\dot{H}_s H_{c2}{}^2 \, dB}{\alpha (H_{c2} - H_s)^2} = \int_{vB}^{o} d\,(vB) \qquad \text{5-29}$$

we obtain

$$v(x) = \frac{\dot{H}_s H_{c2}{}^2 (B - H_{//})}{\alpha\, B\, (H_{c2} - H_s)^2} \qquad \text{5-30}$$

In particular, at the surface,

$$v_s = \frac{\dot{H}_s H_{c2}{}^2 (H_s - H_{//})}{\alpha H_s (H_{c2} - H_s)^2} = \frac{\dot{H}_s (H_s - H_{//})}{F_p(H_s)} \qquad \text{5-31}$$

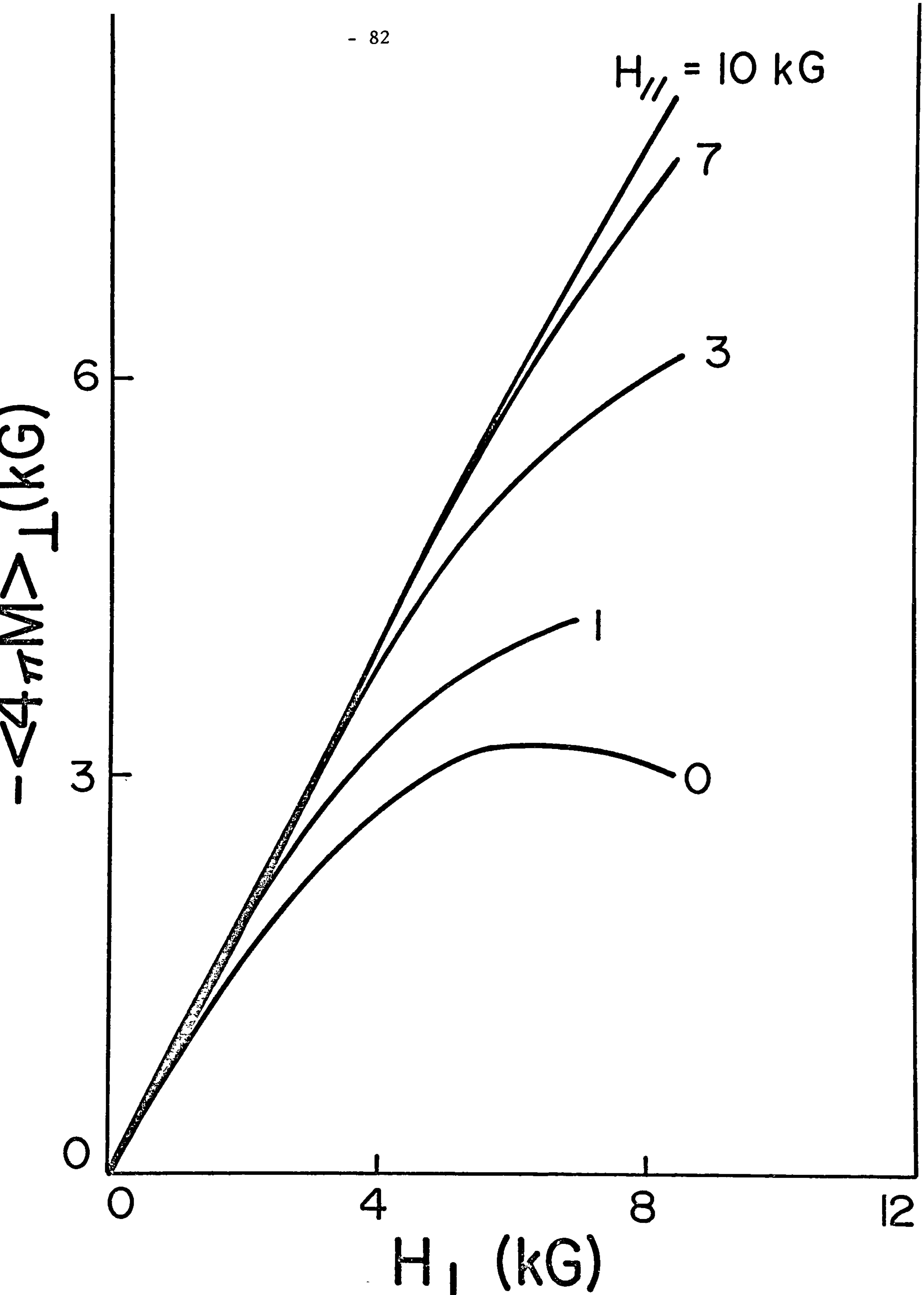

FIGURE 13: Variation of $\langle 4\pi M\rangle_{\perp}$ versus $H_{\perp}$ calculated from the Campbell-Evetts model ($F_p = \alpha B\{1 - \frac{B}{H_{c2}}\}^2$; $\alpha = 6.5 \times 10^5$ A/cm^2 ; $.1 \times 10^5$ Gauss)

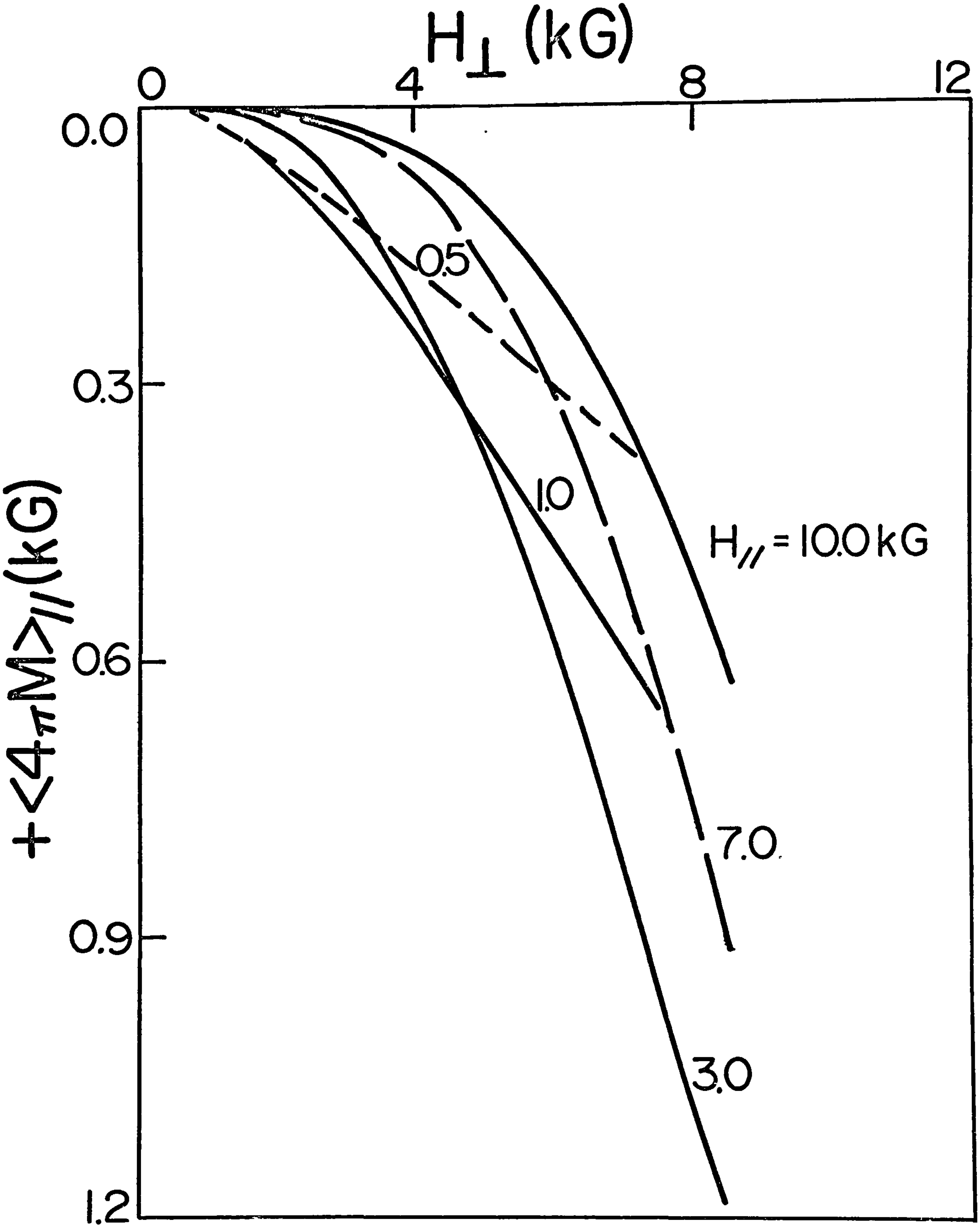

FIGURE 14: Variation of $\langle 4\pi M\rangle_{//}$ versus $H_\perp$ calculated from the Campbell-Evetts model ($F_p = \alpha B\{1 - \frac{B}{H_{c2}}\}^2$; $\alpha = 6.5 \times 10^5$ A/cm^2 ; $H_{c2} = 1.1 \times 10^5$ A/cm^2).

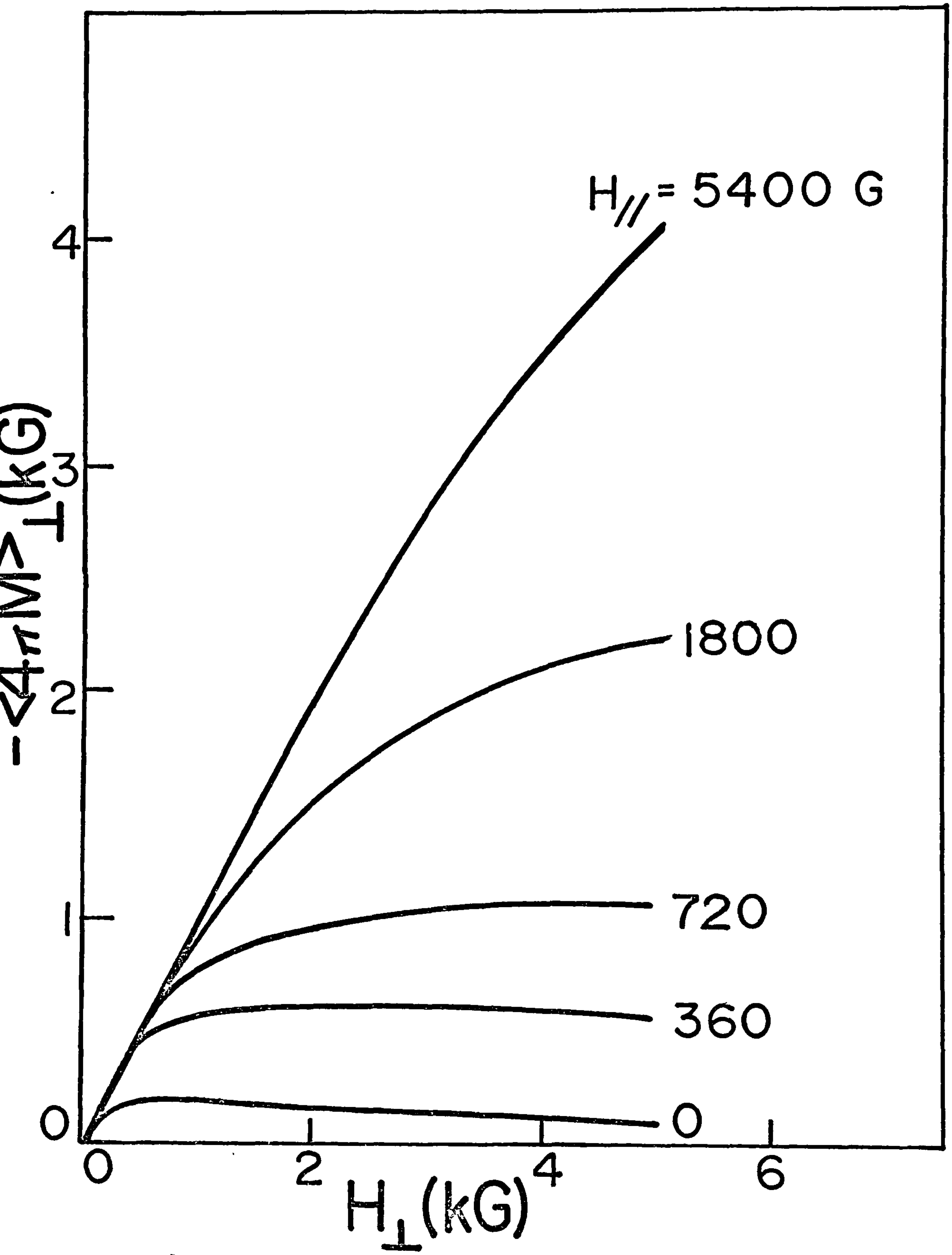

FIGURE 15: Variation of $\langle 4\pi M\rangle_{\perp}$ versus $H_{\perp}$ calculated from the Campbell-Evetts model ($F_p = \alpha B\{1 - \frac{B}{H_{c2}}\}^2$; $\alpha = 5.4 \times 10^3$ A/cm^2 ; $H_{c2} = 2 \times 10^4$ Gauss).

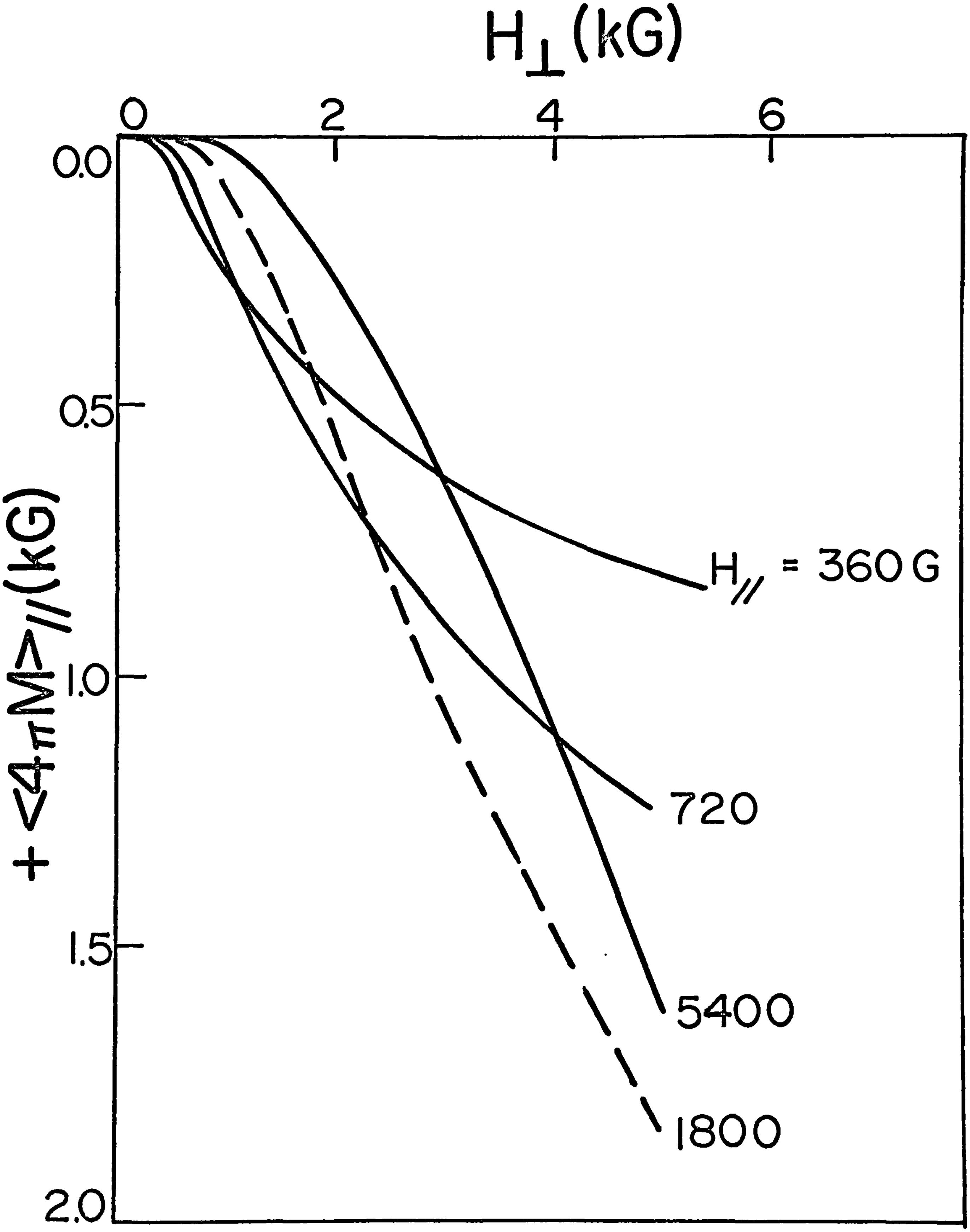

FIGURE 16: Variation of $\langle 4\pi M \rangle_{//}$ versus $H_{\perp}$ calculated from the Campbell-Evetts model ($F_p = \alpha B\{1 - \frac{B}{H_{c2}}\}^2$; $\alpha = 5.4 \times 10^3$ A/cm^2 ; $H_{c2} = 2 \times 10^4$ Gauss).

where $F_p(H_s)$ is the pinning function evaluated at the surface, where $B = H_s$

b) <u>$H_s \geq H_s^*$ (Full field penetration)</u>

The critical state has reached the center and the only point where the fluxons are stationary is at the center where the field $B(a)$ is given by equation 5-26. Replacing $H_{//}$ by $B(a)$ and integrating the equation of continuity as in equation 5-29 yields

$$v^* = \frac{\dot{H}_s\, H_{c2}^2\, [B - B(a)]}{\alpha B\, (H_{c2} - H_s)^2}$$

and the velocity at the surface is

$$v_s^* = \frac{\dot{H}_s\, H_{c2}^2\, [H_s - B(a)]}{\alpha H_s\, (H_{c2} - H_s)^2} = \frac{\dot{H}_s [H_s - B(a)]}{F_p(H_s)} \qquad 5\text{-}32$$

We now turn to the expressions for the evolution of the components of the magnetic moment (equations 5-4 and 5-5)

i) For $H_s < H_s^*$

$$\langle 4\pi M\rangle_{\perp} = \frac{1}{a} \int_{H_{//}}^{H_s} \frac{\sqrt{H_s^2 - H_{//}^2}\,(H_s - H_{//})\, dH_s}{F_p(H_s)} - H_{\perp} \qquad 5\text{-}33$$

and

$$\langle 4\pi M\rangle_{//} = \frac{H_{//}}{a} \int_{H_{//}}^{H_s} \frac{(H_s - H_{//})\, dH_s}{F_p(H_s)} \qquad 5\text{-}34$$

ii) For $H_s \geq H_s^*$

$$<4\pi M>_{\perp} = \frac{1}{a}\int_{H_{//}}^{H_s^*} \frac{\sqrt{H_s^2 - H_{//}^2}\,(H_s - H_{//})\,dH_s}{F_p(H_s)}$$

$$+ \frac{1}{a}\int_{H_s^*}^{H_s} \frac{\sqrt{H_s^2 - H_{//}^2}\,[H_s - B(a)]\,dH_s}{F_p(H_s)} - H_{\perp} \qquad 5\text{-}35$$

and

$$<4\pi M>_{//} = \frac{H_{//}}{a}\int_{H_{//}}^{H_s^*} \frac{(H_s - H_{//})\,dH_s}{F_p(H_s)}$$

$$= \frac{H_{//}}{a}\int_{H_s^*}^{H_s} \frac{[H_s - B(a)]\,dH_s}{F_p(H_s)} \qquad 5\text{-}36$$

We have integrated these equations numerically for different values of $H_{//}$ selected to correspond to that used in our measurements on samples of NbTi and VTi ribbon. Further for purpose of comparison of the predictions of this model with our data on these specimens we have chosen the parameters α and H_{c2} in each case to yield good agreement with the corresponding magnetization curves observed when $H_{//} = 0$.

Figures 13 and 14 present the results of the calculations where $\alpha = 6.5 \times 10^5$ A/cm ^{2} and $H_{c2} = 1.1 \times 10^5$ Gauss are selected to provide a comparison with our NbTi data.

Figures 15 and 16 present the results of the calculations where $\alpha = 5.4 \times 10^3$ A/cm^2 and $H_{c2} = 2 \times 10^4$ Gauss are chosen to give a good comparison with our data on a VTi ribbon.

II $\underline{F_p = \alpha B^{\frac{1}{2}}}$

For our geometry the critical state equation in increasing field becomes

$$B\frac{dB}{dx} = -\alpha B^{\frac{1}{2}}$$

which we integrate

$$\int_{H_s}^{B} B^{\frac{1}{2}}\, dB = -\alpha \int_{0}^{x} dx$$

to obtain

$$B(x) = \{ H_s^{3/2} - \frac{3}{2}\alpha x \}^{2/3} \qquad 5\text{-}37$$

for the variation of the profile of the total magnetic induction.

The critical state penetrates to a distance

$$x_1 = \frac{2}{3\alpha}\{ H_s^{3/2} - H_{//}^{3/2}\} \qquad 5\text{-}38$$

and the field for full penetration is

$$H_s^* = \{ H_{//}^{3/2} + \frac{3\alpha a}{2} \}^{2/3}$$

For $H_s \geq H_s^*$, the field at the center is

$$B(a) = \{H_s^{3/2} - \frac{3\alpha a}{2}\}^{2/3} \qquad 5\text{-}39$$

Differentiating the equation for the field profile (equation 5-37) with respect to time and simplifying the denominator using equation 5-37 we obtain

$$\frac{\partial B}{\partial t} = \frac{H_s^{\frac{1}{2}} \dot{H}_s}{\{H_s^{3/2} - \frac{3\alpha x}{2}\}^{1/3}} = \frac{H_s^{\frac{1}{2}} \dot{H}_s}{B^{\frac{1}{2}}}$$

Introducing the critical state equation in the form $B^{\frac{1}{2}} = -\frac{BdB}{\alpha dx}$ into this result and turning to the equation of continuity we obtain

$$\frac{H_s^{\frac{1}{2}} \dot{H}_s \, dB}{\alpha} = d(vB) \qquad 5\text{-}40$$

i) $H_s < H_s^*$

Integrating equation 5-40

$$\int_B^{H_{//}} \frac{H_s^{\frac{1}{2}} \dot{H}_s \, dB}{\alpha} = \int_{vB}^{o} d(vB)$$

leads to

$$v(B) = \frac{H_s^{\frac{1}{2}} \dot{H}_s \, (B - H_{//})}{\alpha B}$$

since $v = 0$ at $x = x_1$ where $B = H_{//}$. In particular the velocity at $x = 0$ is

$$v_s = \frac{\dot{H}_s \, (H_s - H_{//})}{\alpha \, H^{\frac{1}{2}}} = \frac{\dot{H}_s \, (H_s - H_{//})}{F_p(H_s)} \qquad 5\text{-}41$$

ii) $H_s \geq H_s^*$

Integration of the equation of continuity leads to

$$v_s^* = \frac{\dot{H}_s \, [H_s - B(a)]}{\alpha \, H_s^{\frac{1}{2}}} = \frac{\dot{H}_s \, [H_s - B(a)]}{F_p(H_s)} \qquad 5\text{-}42$$

where $v = 0$ at the center only and $B(a)$ is given by equation 5-39.

III $\underline{F_p = \alpha}$

The critical state equation in increasing field becomes

$\frac{BdB}{dx} = -\alpha$ which we integrate

$$\int_{H_s}^{B} BdB = -\alpha \int_{o}^{x} dx$$

to obtain $$B(x) = \{H_s^2 - 2\alpha x\}^{\frac{1}{2}} \qquad 5\text{-}43$$

for the variation of the profile of the total magnetic induction.

The critical state penetrates to a depth

$$x_1 = \frac{H_s^2 - H_{//}^2}{2\alpha}$$

and the field for full penetration is

$$H_s^* = \{H_{//}^2 + 2\alpha a\}^{\frac{1}{2}}$$

When $H_s \geq H_s^*$, the field at the center of the slab is

$$B(a) = \{H_s^2 - 2\alpha a\}^{\frac{1}{2}} \qquad 5\text{-}44$$

Differentiating the expression for the field profile (equation 5-43) with respect to time and simplifying the denominator yields

$$\frac{\partial B}{\partial t} = \frac{H_s\dot{H}_s}{\{H_s^2 - 2\alpha x\}^{\frac{1}{2}}} = \frac{H_s\dot{H}_s}{B}$$

Introducing the critical state equation in the form $B = -\alpha \frac{dx}{dB}$ into this result and turning to the equation of continuity we obtain

$$\frac{H_s\dot{H}_s dB}{\alpha} = d\,(vB)$$

i) $H_s < H_s^*$

Integration of the equation of continuity for this case yields

$$v(x) = \frac{H_s \dot{H}_s \, (B(x) - H_{//})}{\alpha B}$$

The velocity at the surface then becomes

$$v_s = \dot{H}_s \, \frac{(H_s - H_{//})}{\alpha} = \frac{\dot{H}_s (H_s - H_{//})}{F_p(H_s)} \qquad 5\text{-}45$$

This result introduced into the equations for the evolution of the components of the magnetization (equations 5-4 and 5-5) can, in this case, be readily integrated analytically:

$$<4\pi M>_{//} = \frac{H_{//}}{\alpha a} \int_{H_{//}}^{H_s} (H_s - H_{//}) \, dH_s =$$

$$\frac{H_{//}}{\alpha a} \left\{ \frac{H_s^2 - H_{//}}{2} - H_{//} H_s + H_{//}^2 \right\} =$$

$$\frac{H_{//}}{\alpha a} \left\{ \frac{H_\perp^2}{2} + H_{//}^2 - H_{//} \sqrt{H_\perp^2 + H_{//}^2} \right\} \qquad 5\text{-}46$$

and

$$<4\pi M>_\perp = \frac{1}{\alpha a} \int_{H_{//}}^{H_s} (H_s - H_{//}) \sqrt{H_s^2 - H_{//}^2} \, dH_s - H_\perp$$

$$= \frac{1}{\alpha a} \left\{ \frac{(H_s^2 - H_{//}^2)^{3/2}}{3} - \frac{H_{//} H_s}{2} \sqrt{H_s^2 - H_{//}^2} \right.$$

$$\left. + \frac{H_{//}^3}{2} \log \left(\frac{H_s + \sqrt{H_s^2 \quad H_{//}^2}}{H_{//}} \right) \right\} - H_\perp$$

$$= \frac{1}{\alpha a} \left\{ \frac{H_{\perp}^{3}}{3} - \frac{H_{//}H_{\perp}}{2} \sqrt{H_{\perp}^{2} + H_{//}^{2}} + \right.$$

$$\left. \frac{H_{//}^{3}}{2} \log \left(\frac{H_{\perp} + \sqrt{H_{\perp}^{2} + H_{//}^{2}}}{H_{//}} \right) \right\} - H_{\perp} \qquad \text{5-47}$$

ii) $H_s \geq H_s{}^*$

Integration of the equation of continuity yields

$$v(x)^* = \frac{\dot{H}_s \{B(x) - B(a)\}}{\alpha}$$

hence, the velocity at the surface becomes

$$v_s^* = \frac{\dot{H}_s \{H_s - B(a)\}}{\alpha} = \frac{\dot{H}_s \{H_s - B(a)\}}{F_p(H_s)} \qquad \text{5-48}$$

where $B(a) = \{H_s{}^2 - 2\alpha a\}^{\frac{1}{2}}$ (equation 5-44). This result is introduced into equations 5-4 and 5-5 which can also be readily integrated analytically

$$\langle 4\pi M\rangle_{//} = \frac{H_{//}}{\alpha a} \left\{ \int_{H_{//}}^{H_s{}^*} (H_s - H_{//})\, dH_s + \right.$$

$$\left. \int_{H_s{}^*}^{H_s} (H_s - B(a))dH_s \right\}$$

$$= \frac{H_{//}}{2\alpha a} \{H_{\perp}^{2} + 2H_{//} - H_{//}H_s{}^*$$

$$- \sqrt{(H_{\perp}^{2} + H_{//}^{2})(H_{\perp}^{2} + H_{//}^{2} - 2\alpha a)}$$

$$+ 2\alpha a \log \left(\frac{\sqrt{H^{2} + H_{//}^{2}} + \sqrt{H^{2} + H_{//}^{2} - 2\alpha a}}{H_s^{*} + H_{//}} \right)\}$$

5-49

and
$$\langle 4\pi M\rangle_{\perp} = \frac{1}{\alpha a}\left\{\int_{H_{//}}^{H_s^*}(H_s - H_{//})\sqrt{H_s^2 - H_{//}^2}\, dH_s\right.$$
$$\left. + \int_{H_s^*}^{H_s}\{H_s - \sqrt{H_s^2 - 2\alpha a}\}\sqrt{H_s^2 - H_{//}^2}\, dH_s\right\} - H_{\perp}$$
$$= \frac{1}{\alpha a}\left\{\frac{H_{\perp}^3}{3} - \frac{H_{//}H_s^*}{2}\sqrt{2\alpha a} + \frac{H_{//}^3}{2}\log\left(\frac{H_s^*\sqrt{2\alpha a}}{H_{//}}\right)\right\}$$
$$- H_{\perp} - \frac{1}{\alpha a}\int_{H_s^*}^{H_s}\sqrt{(H_s^2 - 2\alpha a)(H_s^2 - H_{//}^2)}\, dH_s \qquad 5\text{-}50$$

IV. $F_p = \alpha B$

The critical state equation in increasing field becomes $\frac{dB}{dx} = -\alpha$ which we integrate to obtain

$$B(x) = H_s - \alpha x \qquad 5\text{-}51$$

for the profile of the total magnetic induction. The critical state penetrates to a depth $x_1 = (H_s - H_{//})/\alpha$ and the field for full penetration is $H_s^* = H_{//} + \alpha a$. When $H_s \geq H_s^*$ the field at the mid-plane is

$$B(a) = H_s - \alpha a \qquad 5\text{-}52$$

Proceeding as before we obtain $v(x) = \frac{H_s(B - H_{//})}{\alpha B}$

then
$$v_s = \frac{\dot{H}_s(H_s - H_{//})}{\alpha H_s} = \frac{\dot{H}_s(H_s - H_{//})}{F_p(H_s)} \qquad 5\text{-}53$$

when $H_s < H_s^*$ and

$$v_s^* = \frac{\dot{H}_s(H_s - B(a))}{\alpha H_s} = \frac{\dot{H}_s(H_s - B(a))}{F_p(H_s)} \qquad \text{5-54}$$

when $H_s \geq H_s^*$.

Introducing these results in equations 5-4 and 5-5 leads to expressions which can be readily integrated analytically when $H_s \leq H_s^*$

$$<4\pi M>_{//} = \frac{H_{//}}{\alpha a} \int_{H_{//}}^{H_s} \frac{(H_s - H_{//})}{H_s} \, dH_s$$

$$= \frac{H_{//}}{\alpha a} \left\{ \sqrt{H_\perp^2 + H_{//}^2} - H_{//} - H_{//} \log\left(\frac{\sqrt{H_\perp^2 + H_{//}}}{H_{//}}\right) \right. \qquad \text{5-55(a)}$$

and

$$<4\pi M>_\perp = \frac{1}{\alpha a} \int_{H_{//}}^{H_s} \frac{(H_s - H_{//})}{H_s} \sqrt{H_s^2 - H_{//}^2} \, dH_s - H_\perp$$

$$= \frac{1}{\alpha a} \left\{ \frac{H_\perp \sqrt{H_\perp^2 + H_{//}^2}}{2} - \frac{H_{//}^2}{2} \log\left\{\frac{H_\perp + \sqrt{H_\perp^2 + H_{//}^2}}{H_{//}}\right\} \right.$$

$$\left. - H_{//}H_\perp + H_{//}^2 \cos^{-1}\left(\frac{H_{//}}{\sqrt{H_\perp^2 + H_{//}^2}}\right)\right\} - H_\perp \qquad \text{5-55(b)}$$

In Figures 17 through 20 we present the growth of the transverse and longitudinal components of the magnetization we calculate from these applications of the Campbell and Evetts model. In each case we have selected the pinning strength parameter α to yield a curve which gives a good fit to our data on a VTi ribbon sample at low transverse fields and when $H_{//} = 0$. Hence α is chosen in the range of field where pinning functions are applica-

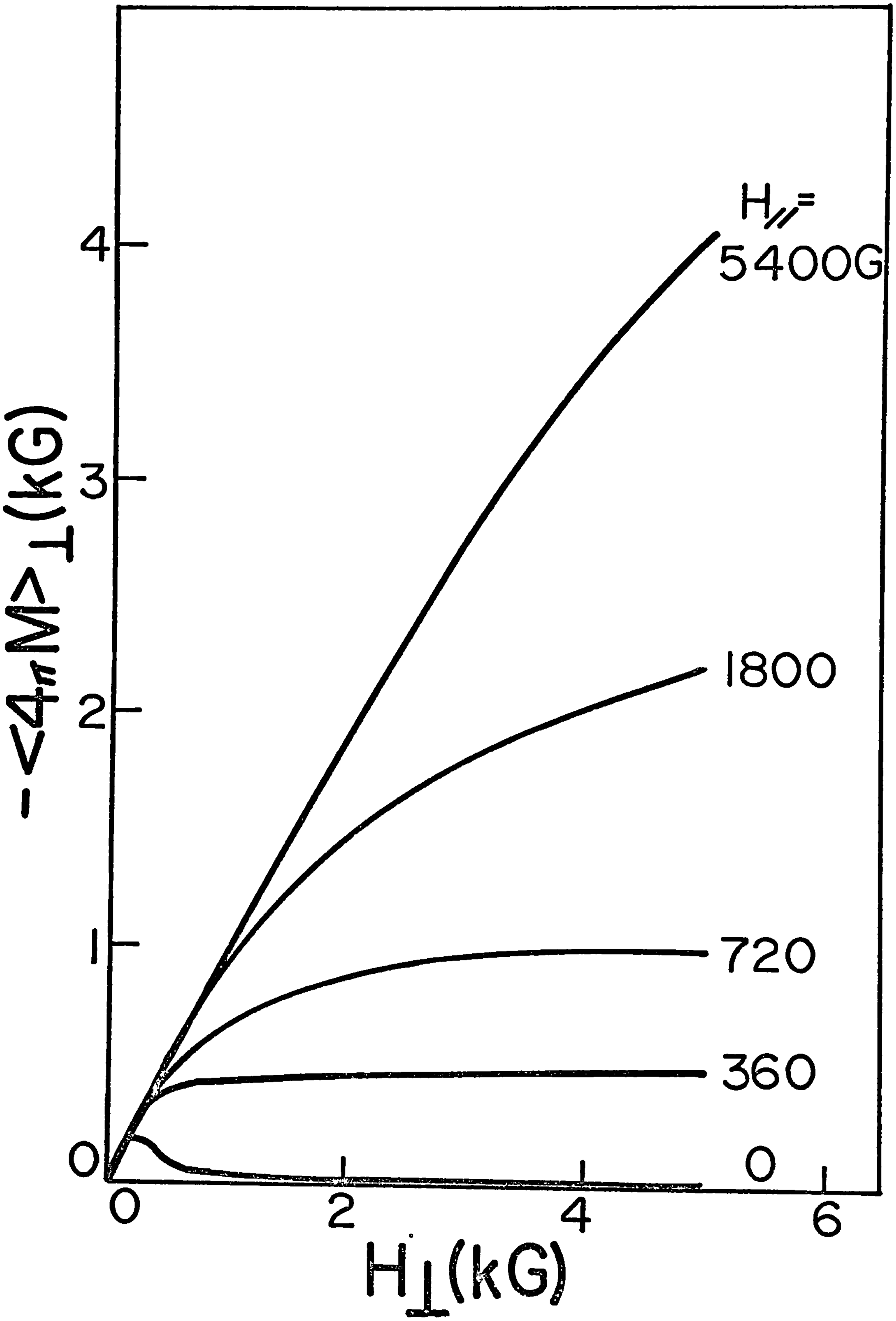

FIGURE 17: Variation of $\langle 4\pi M \rangle_\perp$ versus $H_\perp$ calculated from the Campbell-Evetts model ($F_p = \alpha = 1.2 \times 10^6$ A - G/cm^2).

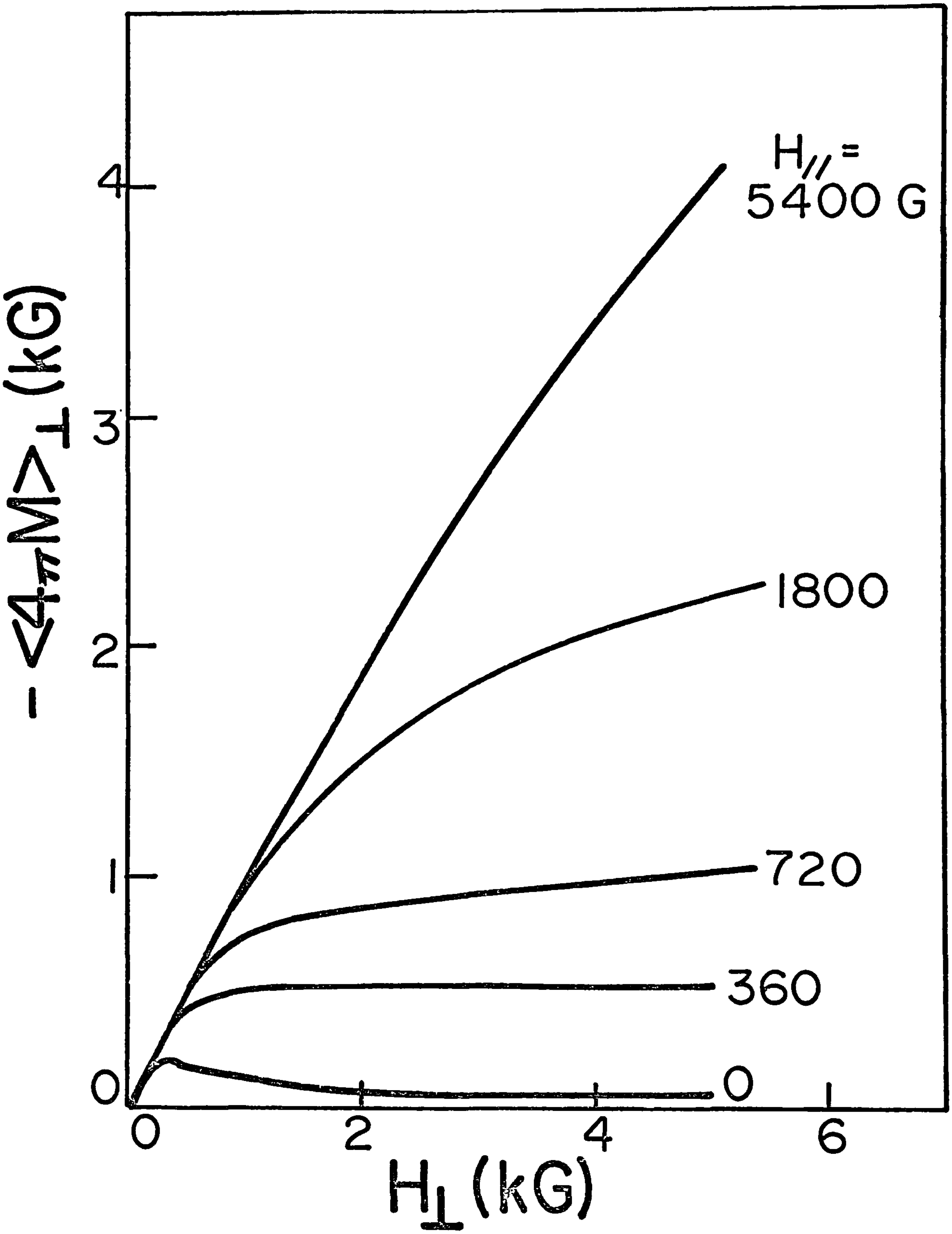

FIGURE 18: Variation of $<4\pi M>_\perp$ versus $H_\perp$ calculated from the Campbell-Evetts model ($F_p = \alpha B^{1/2}$; $\alpha = 1.0 \times 10^5$ A - $G^{1/2}/cm^2$).

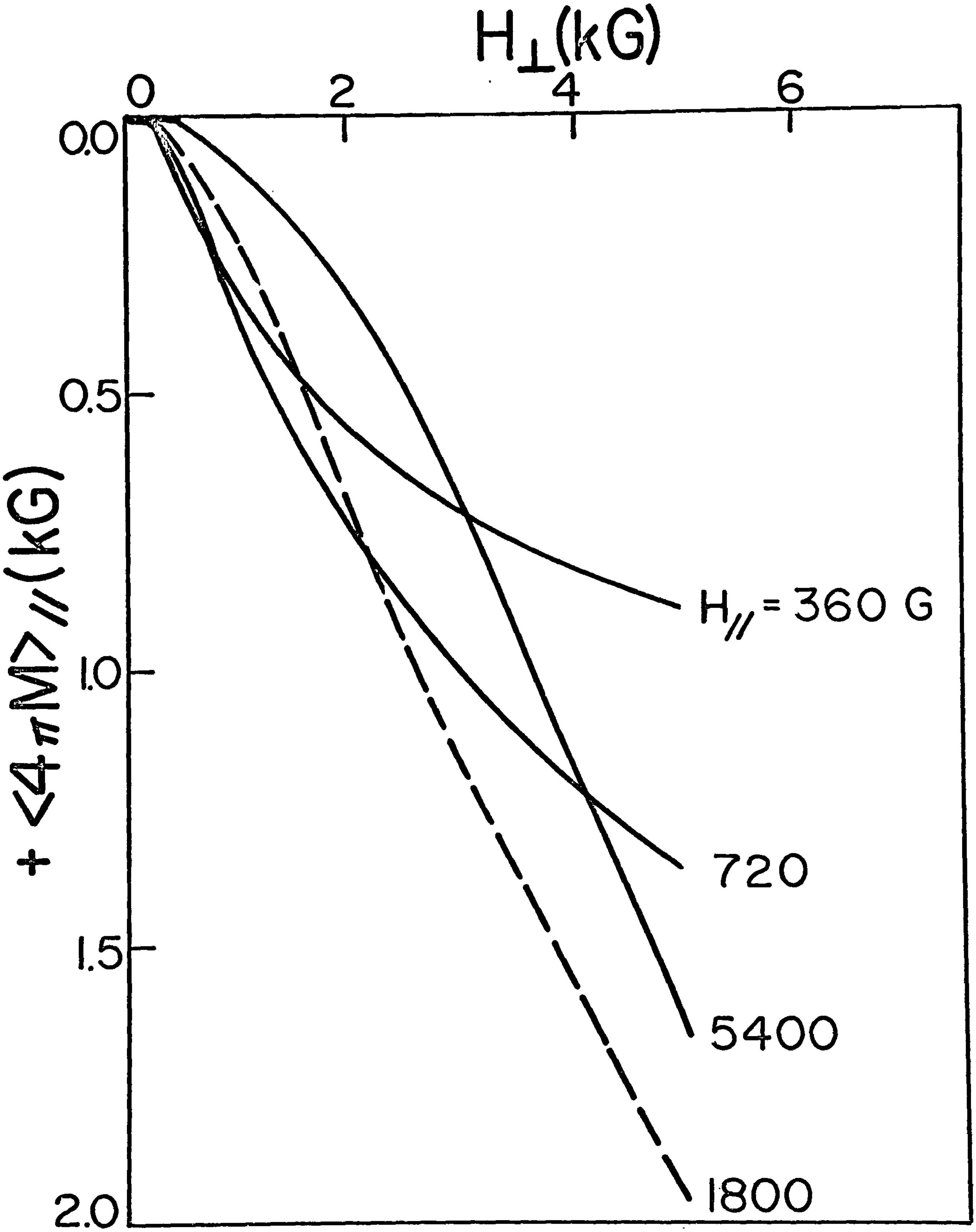

FIGURE 19: Variation of $\langle 4\pi M\rangle_{//}$ versus $H_\perp$ calculated from the Campbell-Evetts model ($F_p = \alpha = 1.2 \times 10^6$ A - G/cm^2).

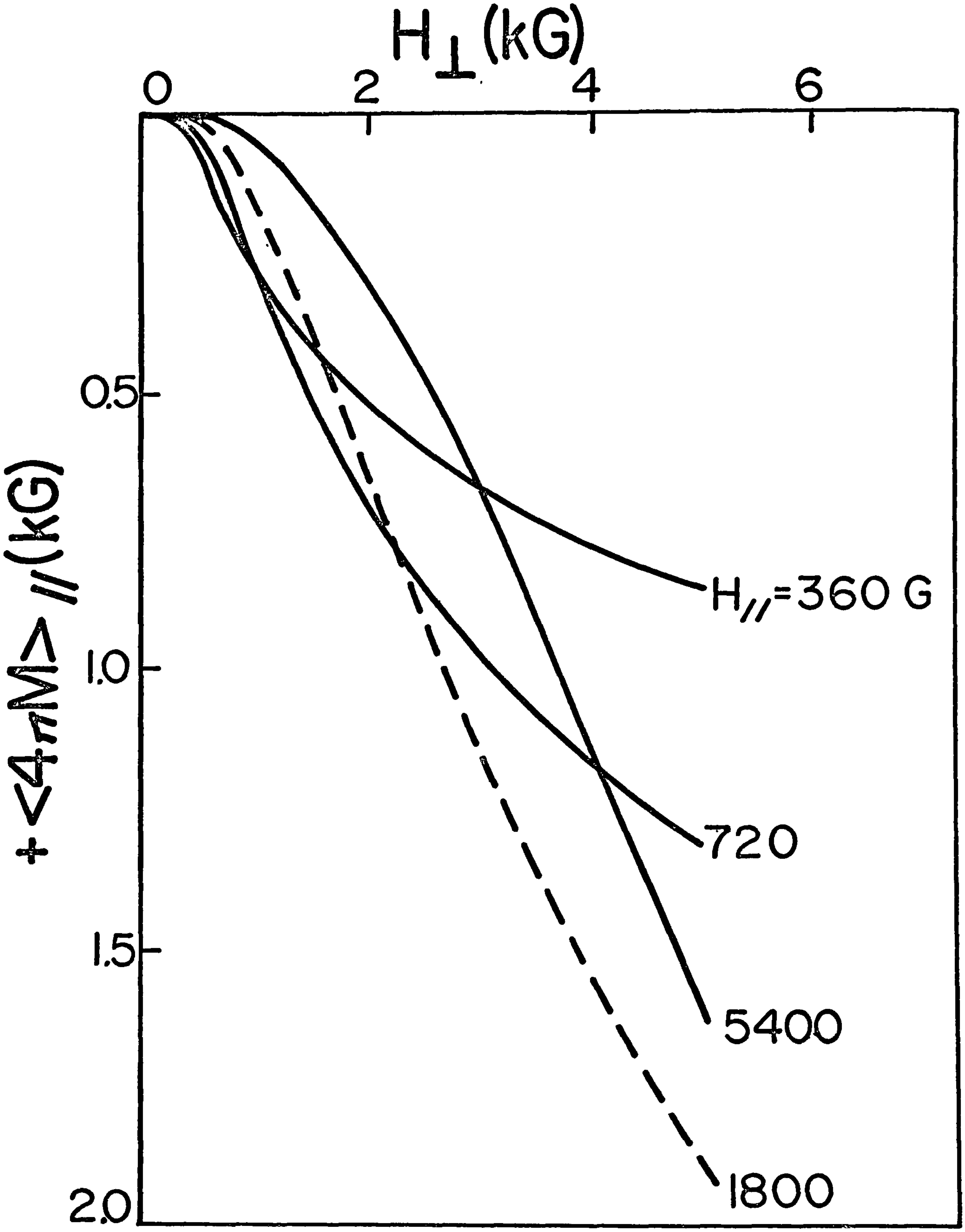

FIGURE 20: Variation of $<4\pi M>_{//}$ versus $H_{\perp}$ calculated from the Campbell-Evetts model ($F_p = \alpha B^{1/2}$; $\alpha = 1.0 \times 10^5$ A - $G^{1/2}/cm^2$).

ble and in a situation where the direction of the vortices is constant so the choice of this parameter is independent of the model. The table below lists the values we have used for the various pinning functions presented in this chapter.

TABLE II

Parameter α	Pinning Function F_p	H_{c2} (kG)
1.2×10^6 A-G/cm^2	α	∞
1.0×10^5 A-G$^{1/2}$/cm^2	$\alpha B^{1/2}$	∞
5.4×10^3 A/cm^2	αB	∞
5.4×10^3 A/cm^2	$\alpha B(1 - \frac{B}{H_{c2}})^2$	20
6.5×10^5 A/cm^2	$\alpha B(1 - \frac{B}{H_{c2}})^2$	110

We have computed curves of the evolution of $\langle 4\pi M\rangle_{\perp}$ and $\langle 4\pi M\rangle_{//}$ as $H_{\perp}$ increases with different static $H_{//}$ chosen to correspond to some of the fields used in our measurements on the VTi sample. For the case where $F_p = \alpha B^{1/2}$ we present in more detail the behaviour predicted by this model in the range of low fields where $0 \leq H_s \leq H_s^*$, in Figures 21 and 23 . These two curves are of particular interest since the model we develop in the next chapter yields good agreement with the observed families of curves for the VTi sample when a $B^{1/2}$ factor is exploited.

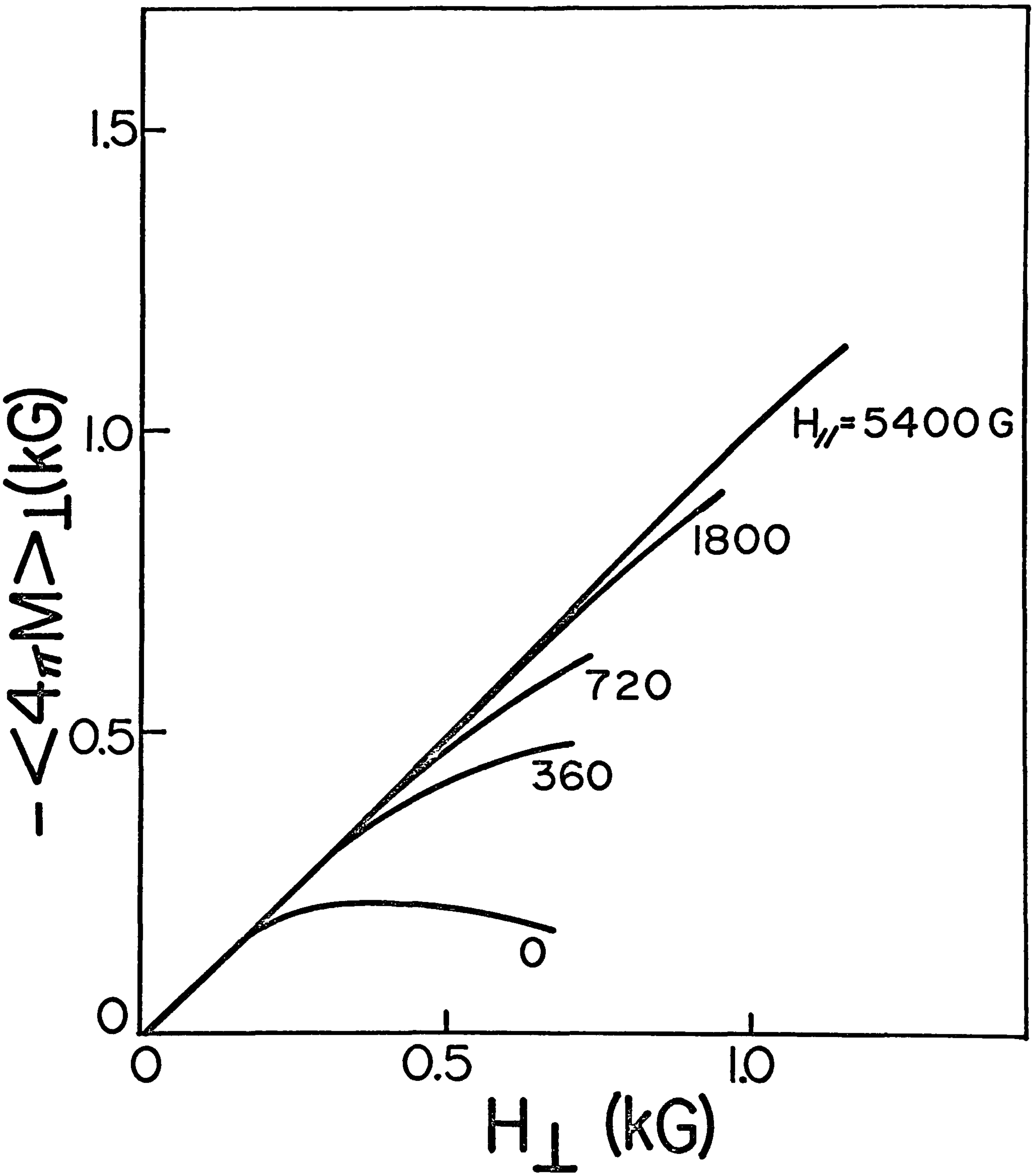

FIGURE 21: Variation of $\langle 4\pi M \rangle_\perp$ versus $H_\perp$ ($<H_\perp{}^*$) calculated from the Campbell-Evetts model ($F_p = \alpha B^{1/2}$; $\alpha = 1.0 \times 10^5$ A - $G^{1/2}/cm^2$).

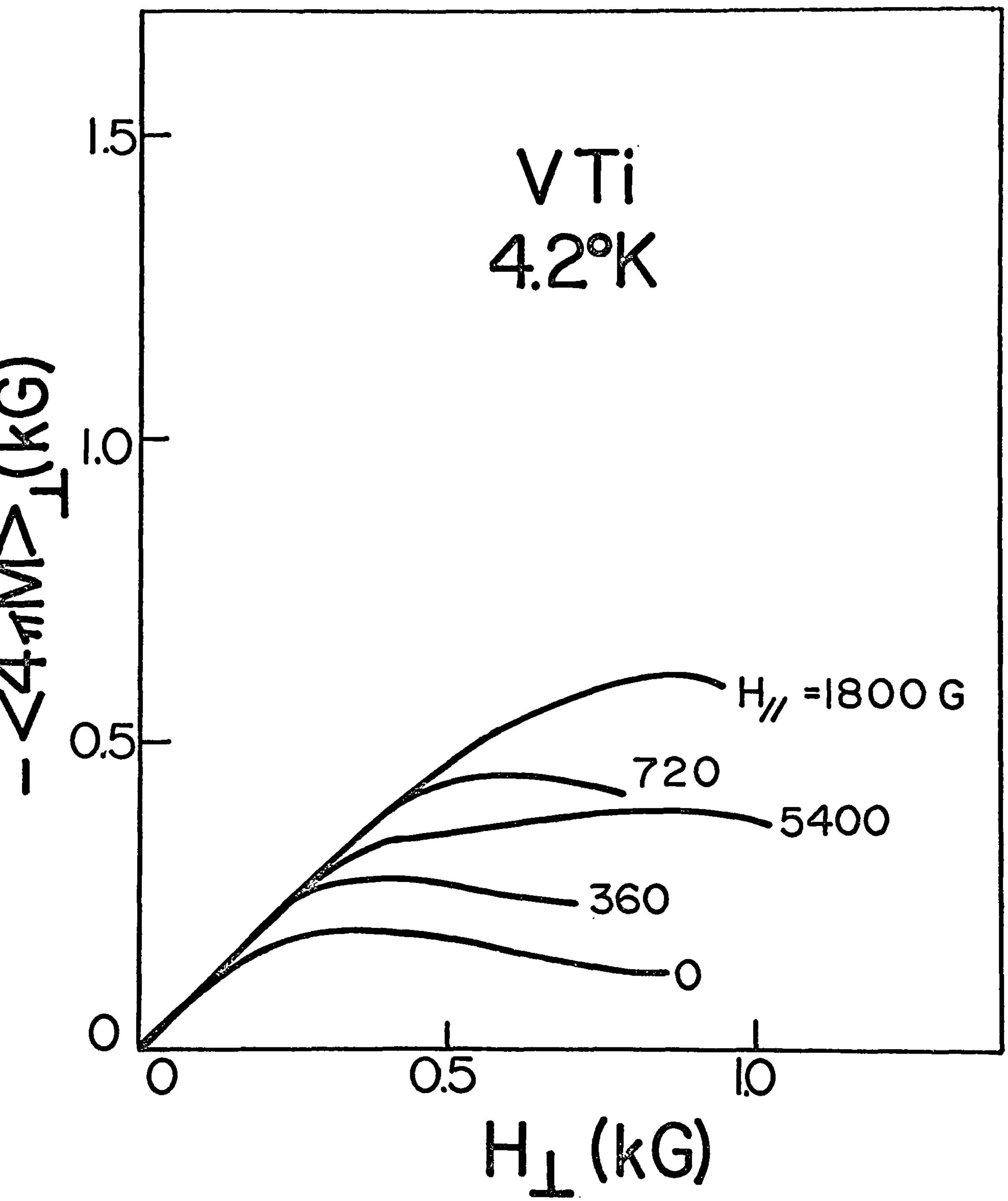

FIGURE 22: Variation of $\langle 4\pi M\rangle_\perp$ versus $H_\perp$ as measured experimentally for VTi.

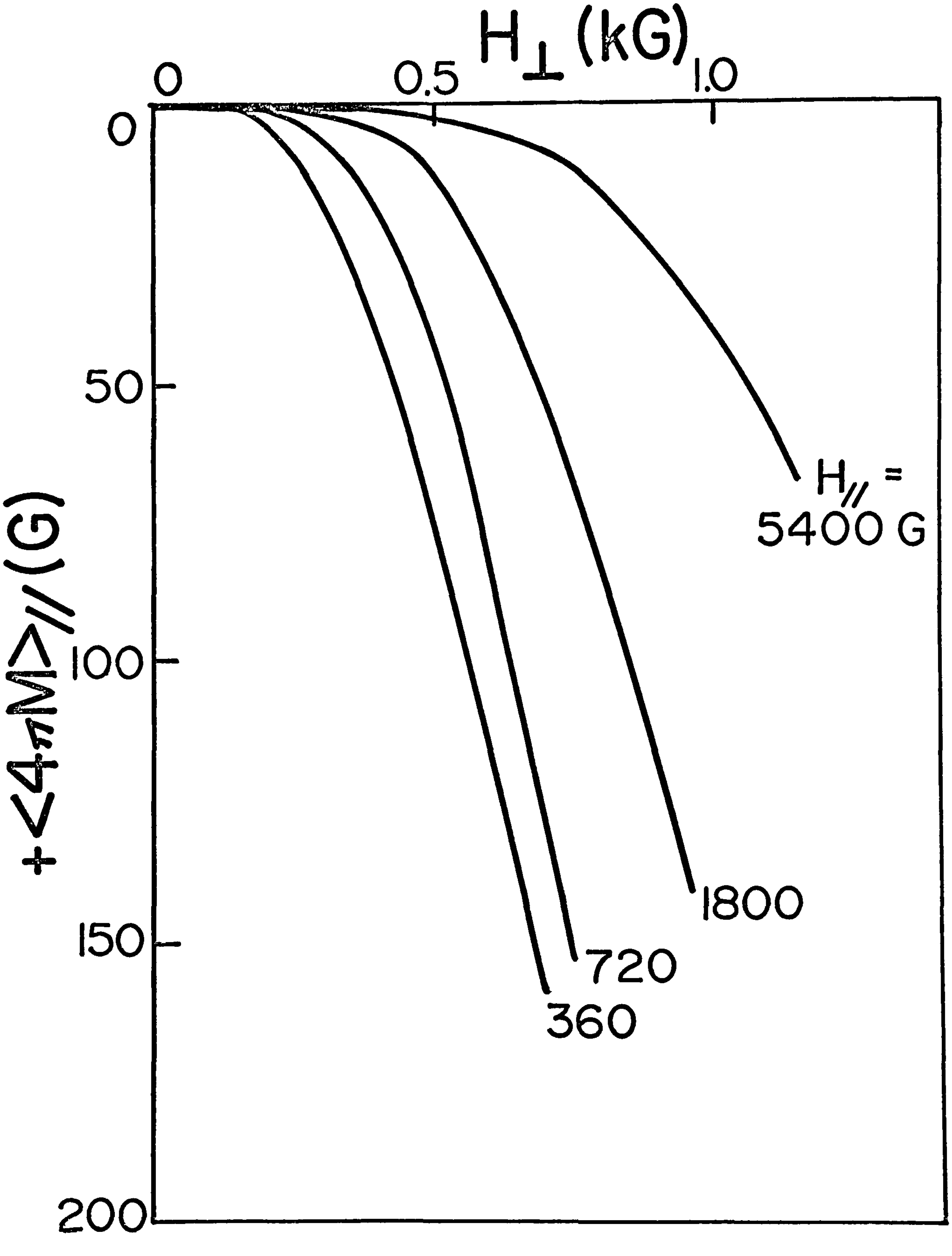

FIGURE 23: Variation of $\langle 4\pi M\rangle_{//}$ versus $H_{\perp}$ ($<H_{\perp}^*$) calculated from the Campbell-Evetts model ($F_p = \alpha B^{1/2}$; $\alpha = 1.0 \times 10^5$ A - $G^{1/2}/cm^2$).

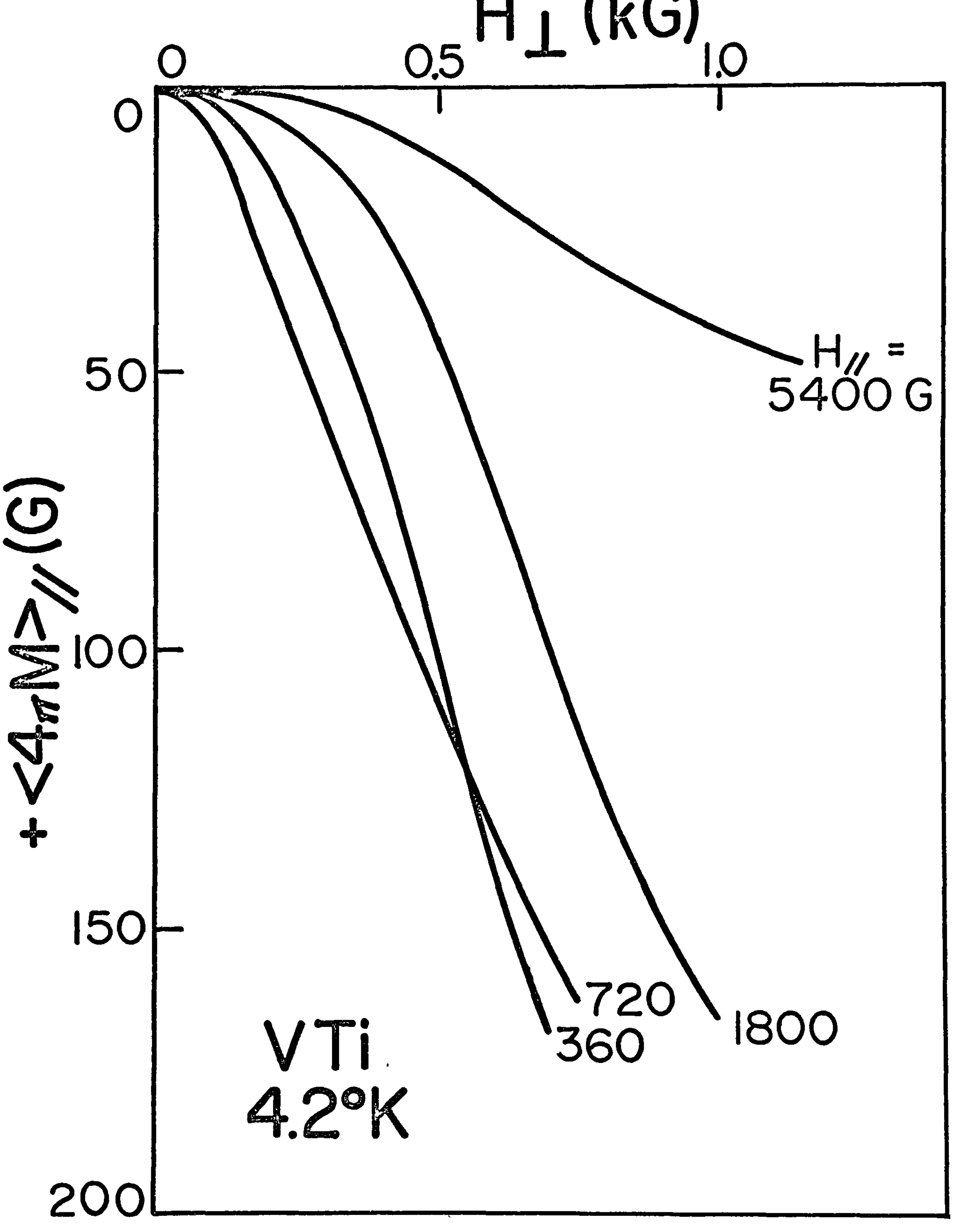

FIGURE 24: Variation of $<4\pi M>_{//}$ versus $H_{\perp}$ ($<H_{\perp}^{*}$) as measured experimentally for VTi.

Earlier in this chapter we presented two sets of curves using $F_p = \alpha B\ (1 - B/H_{c2})^2$. One set explored the range $0 < B/H_{c2} < 0.13$ with $H_{c2} = 110$ kG and $\alpha = 6.5 \times 10^5$ A/cm^2. The second set examined a broader range of field $0 < B/H_{c2} < 0.36$ with $H_{c2} = 20$ kG and $\alpha = 5.4 \times 10^3$ A/cm^2. As expected, the first set of curves are nearly identical with curves obtained with $F_p = \alpha B$ and the same pinning parameter. The second set also closely matches the results calculated using $F_p = \alpha B$. This is perhaps surprising since at the upper end of the field range under scrutiny, the factor $(1 - B/H_{c2})^2$ deviates significantly from unity. We return to this feature later in this chapter when we discuss the results.

To obtain all of the curves presented in this chapter we developed a general computer program to perform the required integrations (equations 5-33 through 5-36) numerically using a pinning function of the form $F_p = \alpha B^n\ (1 - (B/H_{c2})^{\ell})^m$. The results of all our calculations with this program are well-behaved, physically reasonable within the assumptions of the model and internally consistent. To further check that the computer program is free of errors we have also computed all of the curves starting from the analytical results of integration for the case where such expresoins could be readily derived i.e. where $F_p = \alpha$ and αB.

The reader may have noticed that for each pinning function we have used, the expressions for the velocity of the vortices at the surface of the infinite slab all have the same form

$$v_s = \frac{\dot{H}_s (H_s - H_{//})}{F_p (H_s)} \quad \text{when} \quad H_s \leq H_s^*$$

and

$$v_s^* = \frac{\dot{H}_s (H_s - B(a))}{F_p (H_s)} \quad \text{when} \quad H_s \geq H_s^*$$

These results are quite general and are developed in Appendix I. This derivation was provided by Dr. R.C. Smith of our department.

Orientation of the Flux Lines

We have remarked earlier in the application of the Campbell and Evetts model that it is not necessary to determine the sequence of profiles of the magnetic induction in the y and z directions separately in order to compute the growth of the parallel and perpendicular components of the magnetization. Nevertheless the individual profiles and the variation of the direction of the vortices with distance into the slab are of some interest. In this section we develop the pertinent expressions for the case where the pinning force has the simple form $F_p = \alpha B$ since here complete analytical results can be readily obtained which are not excessively complicated. The approach we use can be applied to the other pinning functions we have exploited in this chapter. In these cases however the derivation of analytic expressions becomes algebraically tedious and cumbersome and is not pursued in this thesis.

In a time interval Δt, a plane of vortices advances a distance

$$\Delta x = v(B(x))\,\Delta t \qquad 5\text{-}56$$

We may also express the distance travelled by a plane of vortices in terms of increments of magnetic fields using the total differential

$$\Delta B = \left(\frac{\partial B}{\partial x}\right)_{H_s} \Delta x + \left(\frac{\partial B}{\partial H_s}\right)_x \Delta H_s \qquad 5\text{-}57$$

where B is the profile of the total magnetic induction

Recalling that

$$B(x) = H_s - \alpha x \qquad \text{when } F_p = \alpha B$$

$$B(x) = \{H_s^{3/2} - \tfrac{3}{2}\alpha x\}^{2/3} \qquad \text{when } F_p = \alpha B^{\frac{1}{2}}$$

$$B(x) = (H_s^2 - 2\alpha x)^{\frac{1}{2}} \qquad \text{when } F_p = \alpha$$

this yields

$$\alpha\Delta x = \Delta H_s - \Delta B \qquad 5\text{-}58a$$

$$\alpha\Delta x = H_s^{\frac{1}{2}}\,\Delta H_s - B^{\frac{1}{2}}\Delta B \qquad 5\text{-}58b$$

$$\alpha\Delta x = H_s\,\Delta H_s - B\Delta B \qquad 5\text{-}58c$$

for these three cases respectively.

Next we introduce the appropriate expression for the velocity $v\,(B\,(x))$ in equation 5-56 and equate to the corresponding equation from 5-58. We recall that the pertinent expressions for the velocity are the following

$$\frac{\dot{H}_s(B - H_{//})}{\alpha B} \qquad \text{or} \qquad \frac{\dot{H}_s\,(B - B(a))}{\alpha B}$$

$$\frac{\dot{H}_s H_s^{1/2}\ (B - H_{//})}{\alpha B} \quad \text{or} \quad \frac{\dot{H}_s H_s^{1/2}\ (B - B(a)\ )}{\alpha B}$$

$$\frac{\dot{H}_s H_s\ (B - H_{//})}{\alpha B} \quad \text{or} \quad \frac{\dot{H}_s H_s\ (B - B\ (a)\ )}{\alpha B}$$

where the left and right columns are denoted v(B) and v*(B) and apply when $H_s \leq H_s^*$ and $H_s \geq H_s^*$ respectively for the three corresponding cases under consideration.

We let H_c denote the applied magnetic field H_s' and the magnetic field intensity B'(x) at the surface when a plane of flux lines is created, hence we write $H_s' = B'(o) = H_c$. Later, when the field at the surface has increased to H_s, this group of planes of flux lines has migrated a distance x into the slab and have been compressed. The magnetic induction B(x, t) associated with this group of planes of vortices can be obtained from the following integrals for the three cases respectively, where the primes on B and H_s in the integrands are omitted.

$$\int_{H_c}^{B} BdB = H_{//} \int_{H_c}^{H_s^*} dH_s + \int_{H_s^*}^{H_s} (H_s - \alpha a)dH_s \qquad \text{5-59a}$$

$$\int_{H_c}^{B} B^{3/2}dB = H_{//} \int_{H_c}^{H_s^*} H_s^{1/2} dH_s +$$

$$\int_{H_s^*}^{H_s} H_s^{1/2}\ \{H_s^{3/2} - \frac{3}{2}\,\alpha a\ \}^{3/2}\ dH_s \qquad \text{5-59b}$$

$$\int_{H_c}^{B} B^2 dB = H_{//} \int_{H_c}^{H_s^*} H_s dH_s + \int_{H_s^*}^{H_s} H_s \{H_s^2 - 2\alpha a\}^{\frac{1}{2}} dH_s \qquad \text{5-59c}$$

Clearly when $H_s < H_s^*$ the second term on the right hand side of these expressions vanishes and the limit on the integral of the remaining term becomes H_s.

We now pursue only the case where $F_p = \alpha B$ since here analytic results can be obtained with a moderate amount of algebra.

i) $H_s \leq H_s^*$

Integrating equation 5-59 (a) we obtain a quadratic equation for H_c which leads to

$$H_c = H_{//} + \sqrt{B^2(x) - 2H_{//} H_s + H_{//}^2} \qquad \text{5-60}$$

For the very first group of vortices created at the surface at time t = 0 when H_s began to increase, the field of creation is given by $H_c = H_{//}$ since then $H_{\perp} = 0$ hence $H_s' = B'(o) = H_{//}$. These vortices are now found at a distance x_o from the surface. Letting $H_c = H_{//}$ and $B = H_s - \alpha x_o$ in equation 5-60 we obtain

$$\alpha x_o = H_s - \sqrt{H_{//} (2H_s - H_{//})} \qquad \text{5-61}$$

We can then identify three regions in the slab. We refer the reader to the accompanying sketch for aid in visualizing the field profiles in these three regions.

I. $0 \leq x \leq x_o$

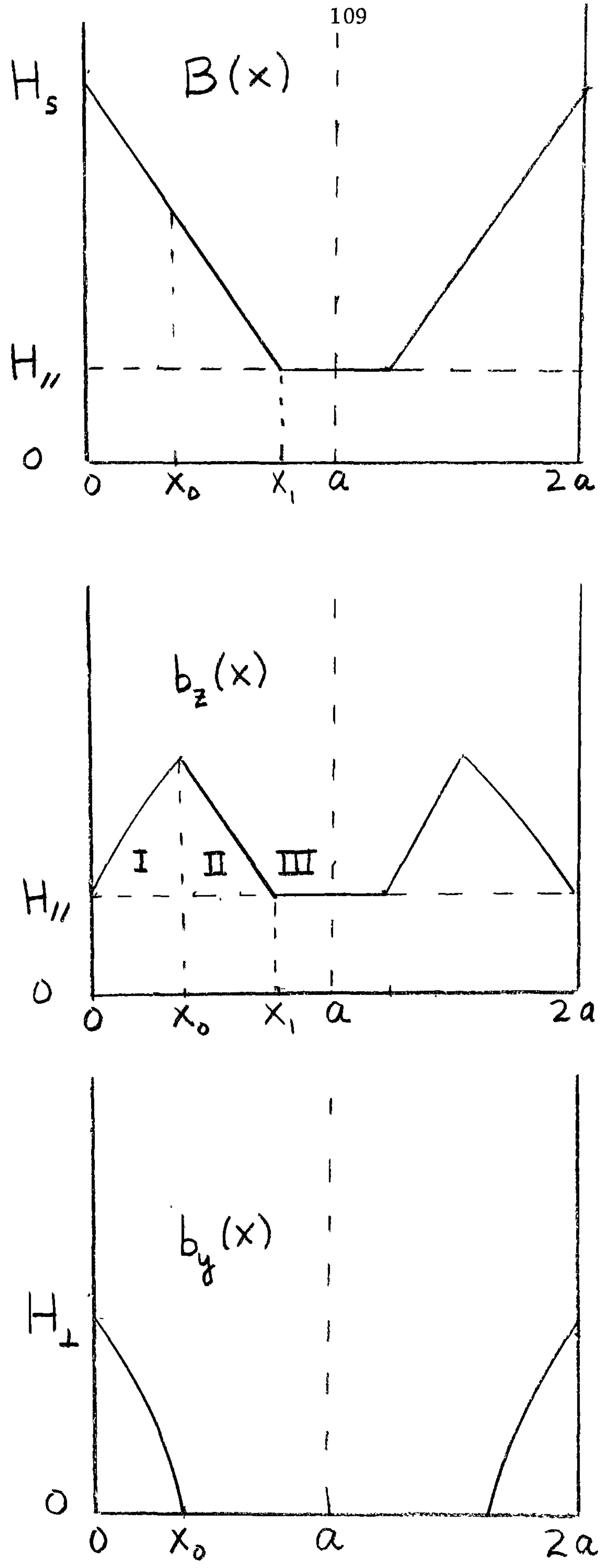

B(x)
H_s
H_∥
0
0
x_0
x_1
a
2a
b_z(x)
I
II
III
H_∥
0
0
x_0
x_1
a
2a
b_y(x)
H_⊥
0
0
x_0
a
2a

This region contains all the fluxons created by the application of $H_\perp$ hence the increase in H_s. In this region the total magnetic induction decreases from H_s to $B(x_o) = H_s - \alpha x_o = \sqrt{H_{//}(2H_s - H_{//})}$ and the orientation $\theta(x)$ of the vortices changes from $\theta_s = \cos^{-1}(H_{//}/H_s)$ to $\theta = 0$ at x_o in a manner which we now determine.

Since the fluxons are assumed to migrate without rotating we can write

$$\frac{b_z(x)}{B(x)} = \frac{b_z'(x')}{B'(x')} = \frac{b_z'(o)}{B'(o)} = \frac{H_{//}}{H_s'} = \frac{H_{//}}{H_c}$$

Thus $$b_z(x) = \frac{H_{//}\,B(x)}{H_c} \tag{5-62}$$

Also then

$$\theta = \cos^{-1}\left\{\frac{b_z(x)}{B(x)}\right\} = \cos^{-1}\left(\frac{H_{//}}{H_c}\right) \tag{5-63}$$

Introducing H_c from equation 5-60 into these expressions we can determine $b_z(x)$, $\theta(x)$ and also

$$b_y(x) = B\sin\theta = \sqrt{B^2 - b_z^2} = \frac{B}{H_c}\sqrt{H_c^{\,2} - H_{//}^{\,2}} \tag{5-64}$$

We verify that indeed $b_z(x) = \sqrt{H_{//}(2H_s - H_{//})}$, $b_y(x) = 0$ and $\theta(x) = 0$ when $x = x_o$.

II $\quad x_o \leq x \leq x_1$

The vortices originally contained in region I have migrated to this region where they are compressed while maintaining their initial orientation of $\theta = 0$ according to the basic assumption of the model. The total magnetic induction $B(x) = b_z(x)$ in this region varies from $\sqrt{H_{//}(2H_s - H_{//})}$ at $x = x_o$ to $H_{//}$ at $x = x_1$. We note that the vortices originally occupying this region at $t = 0$ still remain there but are compressed in the vicinity of $x = x_1$. We have verified that, as postulated, the number of vortices (the magnetic flux) added to this region corresponds to that originally threading region I by checking that

$$\int_{x_o}^{x_1} (B(x) - H_{//})\, dx = H_{//} x_o$$

III. $\quad x_1 \leq x \leq a$

No vortices from region II have yet entered this region and it is occupied solely by the undisturbed vortices originally permeating it when the sample became superconducting in the chosen static $H_{//}$. Here by the assumptions of the model and the specified experimental conditions

$$B(x) = b_z(x) = H_{//}, \quad b_y(x) = 0, \quad \theta(x) = 0.$$

ii) $\quad H_s \geq H_s^*$

As H_s increases beyond H_s^* , the vortices created earlier while H_s varied from $H_{//}$ to H_s^* migrate further into the sample. Their progression is obtained by integrating equation 5-59(a). We again obtain a quadratic equation for H_c which leads to

$$H_c = H_{//} + \{B^2 - 2H_{//}H_s^* + H_{//}^2 - H_s^2 + H_s^{*2}$$
$$+ 2\alpha a\ (H_s - H_s^*)\}^{\frac{1}{2}}$$

$$= H_{//} + \{B^2 - 2H_{//}\alpha a - (H_s - \alpha a)^2\}^{\frac{1}{2}} \qquad (5\text{-}65)$$

where we have introduced $H_s^* = H_{//} + \alpha a$.

The very first group of vortices created at the surface when $H_c = H_{//}$ at time $t = 0$ are now found at a distance x_o from the surface. Letting $H_c = H_{//}$ and $B = H_s - \alpha x_o$ in equation 5-65 we obtain

$$\alpha x_o = H_s - \{H_{//}(2H_s^* - H_{//}) + H_s^2 - H_s^{*2}$$
$$- 2\alpha a\ (H_s - H_s^*)\}^{\frac{1}{2}}$$

$$= H_s - \{H_s^2 + 2\alpha a\ (H_{//} - H_s) + (\alpha a)^2\}^{\frac{1}{2}} \qquad (5\text{-}66)$$

The vortices created at the surface when $H_s = H_s^*$ are now found at a depth x_o^*. Letting $H_c = H_s^* = H_{//} + \alpha a$ and $B = H_s - \alpha x_o^*$ in equation 5-65 we obtain

$$\alpha x_o^* = H_s - \{H_s^2 + 2\alpha a(H_{//} - H_s) + 2(\alpha a)^2\}^{\frac{1}{2}} \qquad (5.67)$$

The progression of the newer vortices created as H_s increases beyond H_s^* can be obtained by integrating equation 5-59(a) but with the first term on the right hand side not present and the remaining term is integrated from H_c instead of H_s^*. This yields

$$H_c = \frac{B^2 - H_s^2}{2\alpha a} + H_s \qquad (5\text{-}68)$$

We verify that letting $H_c = H_s^* = H_{//} + \alpha a$ and $B = H_s - \alpha x_o^*$ in this equation we obtain 5-67 as expected.

We can still identify three regions in the slab. We refer the reader to the accompanying sketch for aid in visualizing the field profiles in these three regions.

I*. $0 \leq x \leq x_o^*$

This region contains all the fluxons created since the applied field attained the full penetration value $H_s^* = H_{//} + \alpha a$, i.e. since the flux front reached the center of the slab. Here $b_z(x)$, $\theta(x)$ and $b_y(x)$ are determined by introducing H_c from equation 5-68 in 5-62, 5-63 and 5-64 respectively. In this region $B(x)$ decreases from H_s to $H_s - \alpha x_o^*$ where x_o^* is given by equation 5-67.

I. $x_o^* \leq x \leq x_o$

The discussion presented above for region I still applies except that H_c as given by equation 5-65 is to be used in calculating $b_x(x)$, $\theta(x)$ and $b_y(x)$. In this region $B(x)$ varies from $H_s - \alpha x_o^*$ to $H_s - \alpha x_o$ where x_o^* and x_o are given by equation 5-67 and 5-66 respectively. This region contains all the vortices created as H_s varied from $H_{//}$ to H_s^*.

II. $x_o \leq x \leq a$

The discussion presented above for region II still applies except that the region now extends to the center plane of the slab. The total magnetic induction in this region varies from $H_s - \alpha x_o$ with x_o given by equation 5-66 to $(H_s - \alpha a) \geq H_{//}$ at $x = a$. The vortices in this region all have the same angle $\theta = 0$ hence,

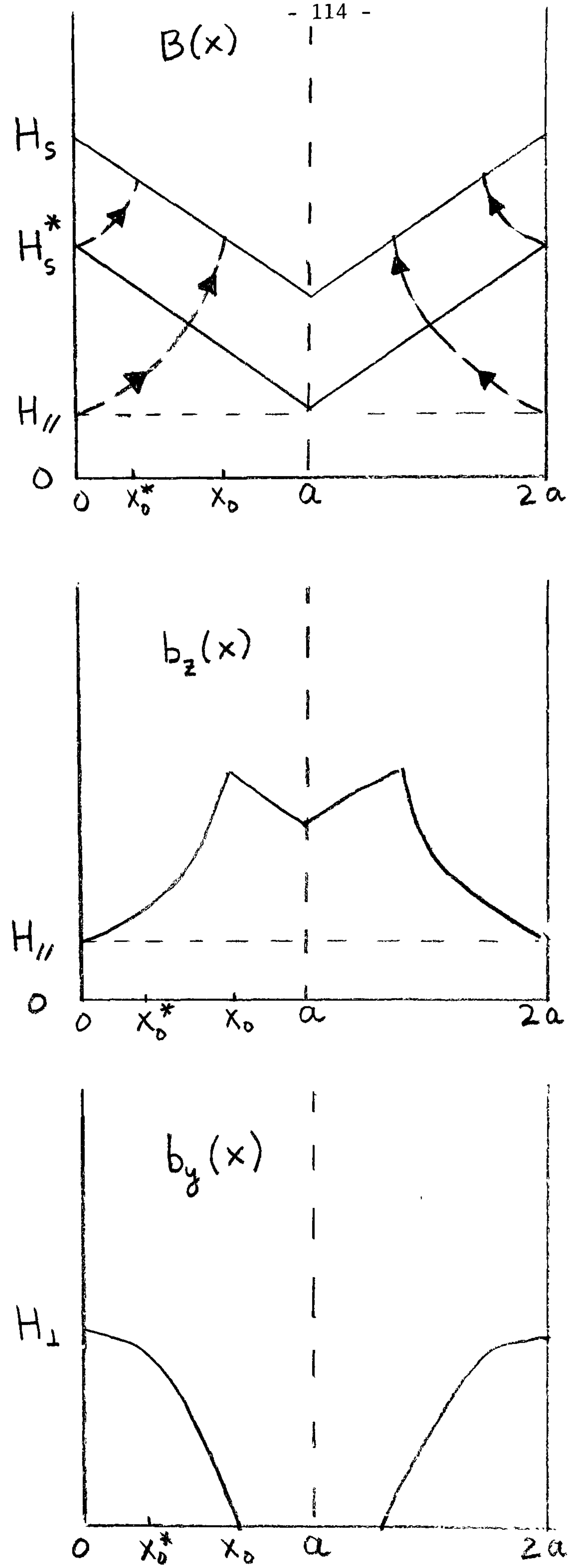
B(x)
H_s
H_s^*
$H_{//}$
0
0
x_0^*
x_0
a
2a
$b_z(x)$
$H_{//}$
0
0
x_0^*
x_0
a
2a
$b_y(x)$
$H_\perp$
0
x_0^*
x_0
a
2a

$b_z(x) = B(x)$ and $b_y(x) = 0$. We now verify that the increase in the number of vortices in this region corresponds to the number removed from region I* and I (where they have been replaced by vortices whose direction varies from $\theta = 0$ at x_o to $\theta = \theta_s$ at the surface).

$$\ell_y\{\int_{x_o}^{a} (H_s - \alpha x)dx - H_{//}(a - x_o)\} = H_{//}x_o\ell_y \qquad (5\text{-}69)$$

where the left-hand side is the increase in the flux threading region II and the right-hand side is the flux originally permeating regions I* and I.

Integrating and rearranging yields

$$\alpha(a - x_o)\ \{2H_s - \alpha(a + x_o)\} = 2H_{//}a\alpha$$

Introducing x_o from equation 5-66 into this and rearranging we find that the left-hand side reduces to $2H_{//}a\alpha$ as required by the basic assumption of the model that flux is conserved and does not rotate.

We note that there is no longer a central region (III) where the density of vortices is unchanged.

Conclusion

An examination of the predictions of the Campbell and Evetts model with our observations shows that the model combined with a suitable pinning function is adequate in describing the behaviour encountered in the range of low fields $H_s \leq H_s^*$. This approximate qualitative and quantitative agreement at low fields between the families of curves calculated using this model and our measurements can be appreciated by comparing Figures 21 and 23 with Figures 22 and 24 which present the corresponding low field portion of our data for VTi. This agreement emerges further from a scrutiny of Figures 13 and 14 and the pertinent results for NbTi presented in the next chapter on Figures 30 and 32. For the latter sample our apparatus restricts the measurements to the "low" field range since here $H_{c2} \approx 110$ kG at 4.2°K and the highest transverse and longitudinal fields our magnets can generate simultaneously are ≈ 10 kG.

The predictions of the Campbell and Evetts model however diverge further and further from the observations as H_s and $H_{\perp}$ grow beyond H_s^* and $H_{\perp}^*$ and $H_{//}/H_{c2}$ becomes a significant fraction. Indeed the model intrinsically leads to unphysical consequences at progressively higher fields and in particular as H_s approaches H_{c2}.

We expect and observe that the locus of the magnetic moment and its components after traversing a maximum will diminish monotonically to zero as H_s approaches H_{c2} since bulk superconductivity and the pinning strength are being gradually suppressed by the magnetic induction. Further as the transverse field $H_{\perp}$ is applied with progressively stronger $H_{//}$ we anticipate and observe that the maximum magnetizations which occur to be relatively weaker and weaker. The Campbell and Evetts model however leads to magnetic moments which increase continuously when $H_{//}/H_{c2}$ exceeds the peak in the pinning function and drop precipitously to zero from extremely large values as H_s attains H_{c2}. This is shown in Figures 25 and 26 where we present the behaviour calculated for the entire range $0 \leq H_s \leq H_{c2}$ using the pinning function $F_p = \alpha B(1 - B/H_{c2})^2$. This particular pinning function is exploited in the next chapter and reaches a peak at $B/H_{c2} = 1/3$.

Because of the postulate that vortices cannot rotate, the flux originally threading the sample is compressed into an ever decreasing area as H_s increases. Meanwhile magnetic induction with a component in the z-direction is continously being introduced into the slab (although at a decreasing) rate as H_s increases all the way to H_{c2}. The model requires that these additional vortices maintain their initial orientation hence, intuitively, we can see that the magnetic induction in the z-direction must grow monotonically up to $H_s = H_{c2}$. Next we consider the configuration of the field profile in the y (transverse) direction. In this model, the front of the transverse field profile penetrates deeper and deeper into the sample and advances closer and closer to the centre of the slab as H_s attains H_s^* and the profile of the total magnetic induction fills the entire slab. Even when H_s increases beyond H_s^* and grows to H_{c2}, the front of the transverse field profile never reaches the mid-plane of the slab but drops to zero at a depth $x_o < a$. The central region must remain occupied only by the vortices originally filling the sample. These are directed along the z-axis, are assumed not to rotate and are compressed more and more densely. As a consequence the transverse field profile becomes steeper and steeper as $H_\perp$ grows since its height at the surface increases but it still must descent to zero in the vicinity of the center of the slab. This means that the transverse magnetization $(H_\perp - \langle B \rangle_\perp)$ remains appreciable right up to $H_s = H_{c2}$.

Further, the evolution of the components of the magnetization flowing from this model becomes independent at intermediate and high fields , whether transverse pinning is present or not and hence is not sensitive to the particular pinning behaviour. This can be seen in the following way. We refer the reader to equations 5-7 and 5-8. At intermediate and more correctly at high fields, the difference between the field at the surface and the total magnetic induction at the center is not appreciable compared with H_s or $B(a)$, i.e. $(H_s - B(a)) \ll H_s$. Under these circumstances the rate of increase in the number of vortices threading the slab is nearly linear with ΔH_s, the augmentation in H_s, regardless of the particular curve describing the magnetic induction inside the slab hence independently of the detailed pinning involved. At corresponding $H_{//}$ and H_s, the growth in the components of the magnetic induction is determined by the rate of entry of fluxons. Hence in this situation the increase in the components of the magnetization becomes insensitive to the pinning in the Campbell and Evetts model.

From inspection of our data and the predictions of the Campbell and Evetts model we conclude that the assumption that vortices do not rotate is approximately valid at low fields but corresponds less and less with reality in the range of intermediate fields and must be abandoned completely at high fields.

Finally we note that the Campbell and Evetts model seems, by its very nature, incapable of describing the behaviour of type II superconductors encountered when H_s while changing in direction is made to decrease instead of increasing. In these circumstances vortices must migrate to the surface without rotating and exit from the sample at the surface. The model requires that the magnetic field changes its direction abruptly across the surface. This means that $B_y(x)$ and $B_z(x)$ are discontinuous at the surface hence unphysically large current densities arise there.

In the next chapter we abandon the stringent postulate that vortices cannot change their orientation. We propose a simple empirical expression to describe the variation of direction of flux which enables us to adequately account for all of our observations. This empirical expression incorporates the crucial feature that the opposition to rotation decreases as B increases and vanishes gradually as B approaches H_{c2}.

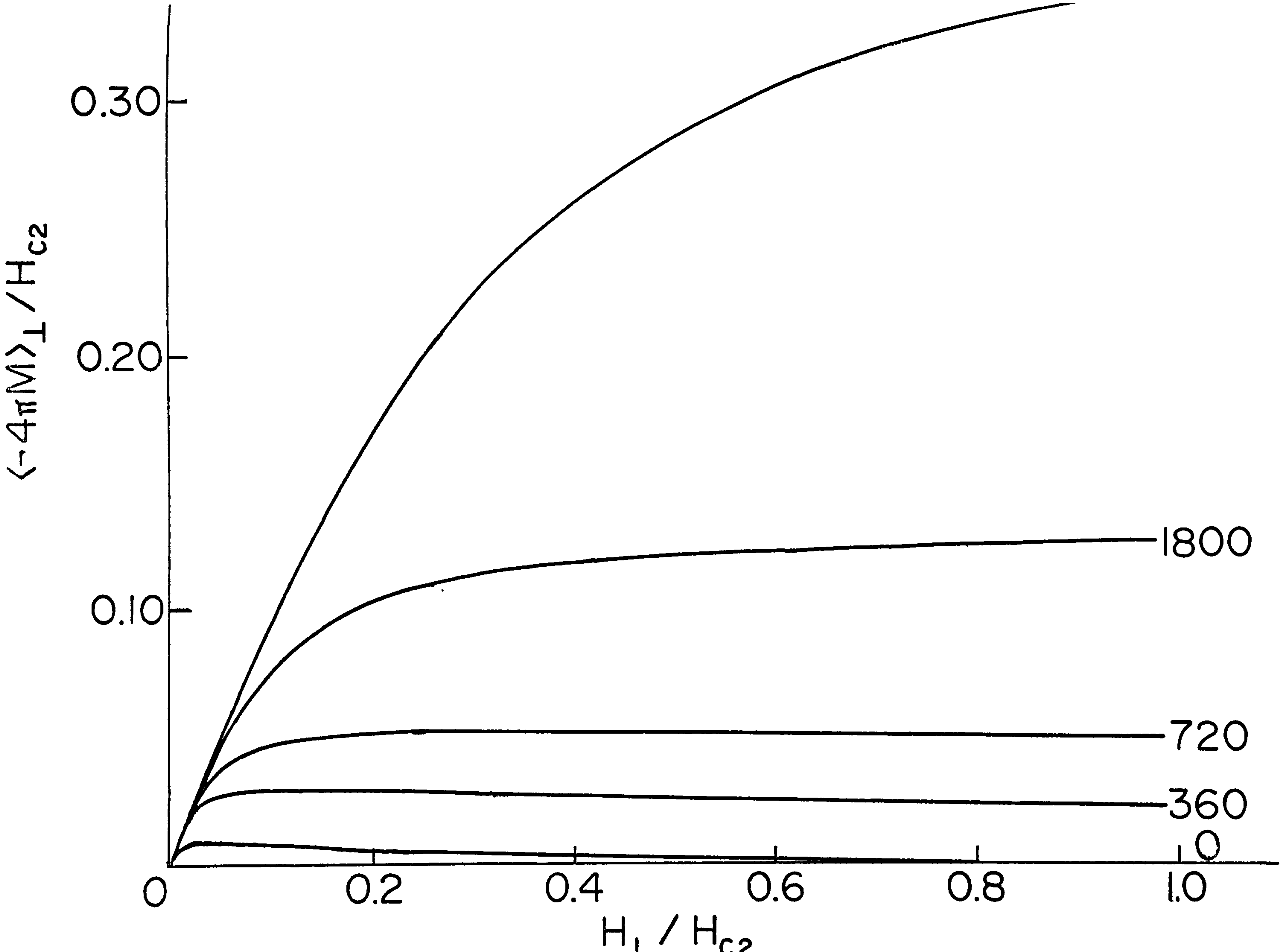

FIGURE 25: Variation of $\langle 4\pi M\rangle_\perp$ versus $H_\perp$ for the Campbell-Evetts model;

$0 \le H_s \le H_{c2}$ ($F_p = \alpha B\{1 - \frac{B}{H_{c2}}\}^2$; $\alpha = 5.4 \times 10^3$ G/cm ; $H_{c2} = 2 \times 10^4$ Gauss).

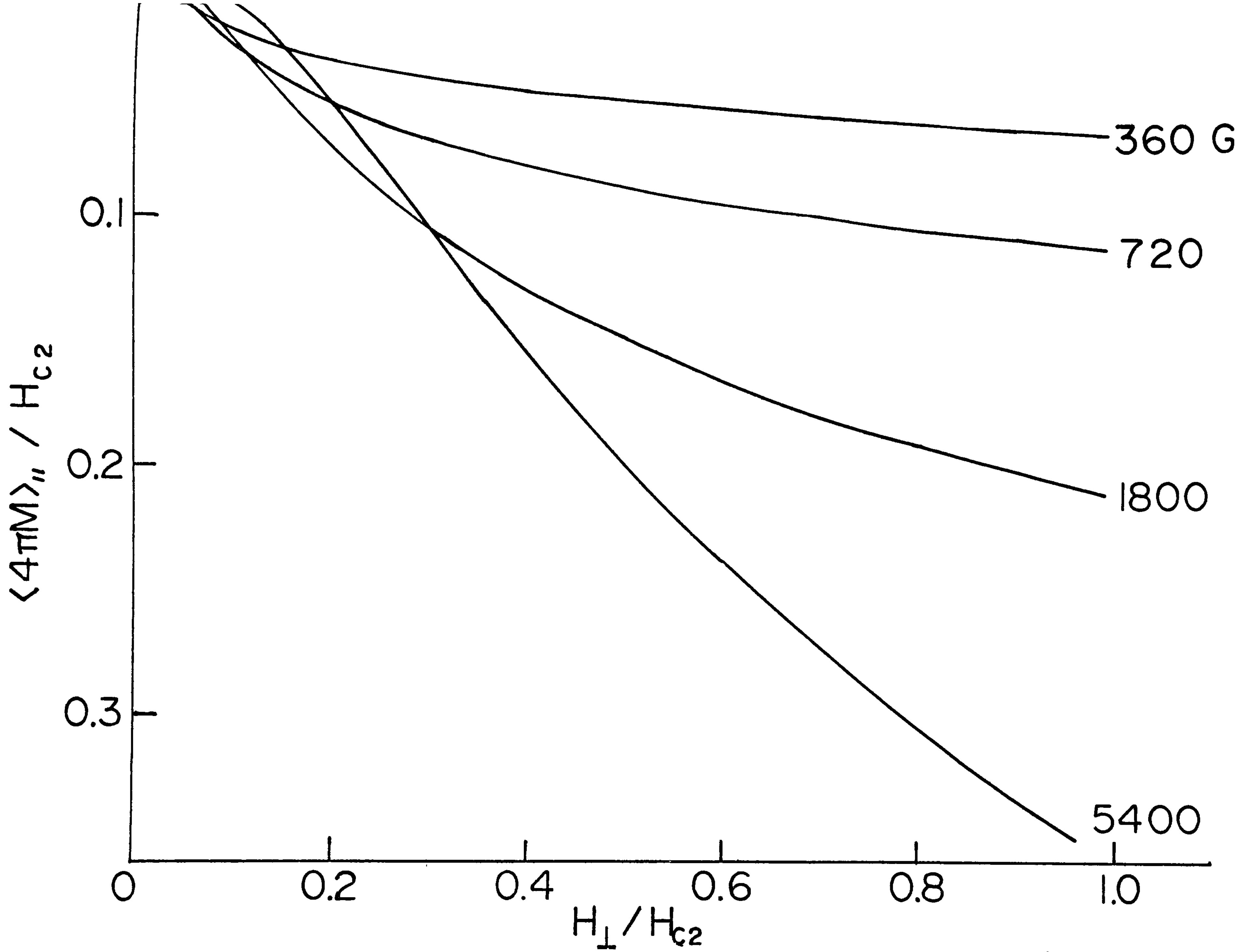

FIGURE 26: Variation of $\langle 4\pi M\rangle_{//}$ versus $H_{\perp}$ for the Campbell-Evetts model; $0 \le H \le H_{c2}$ ($F_p = \alpha B\{1 - \frac{B}{H_{c2}}\}^2$; $\alpha = 5.4 \times 10^3$ G/cm ; $H_{c2} = 2 \times 10^4$ Gauss).

CHAPTER 6

EMPIRICAL VORTEX ROTATION MODEL

Introduction

In the preceding two chapters we have investigated in some detail the predictions and limitations of two models concerning the freedom of vortices to change their orientation after they are created and as they penetrate into the body of a type II superconductor. The two models we have explored represent the two extreme positions regarding the possibility of rotation: viz, complete freedom of flux lines to change direction and changes in direction completely forbidden.

In the first case we have pursued the consequences of a force-free model frequently considered in the literature because of its mathematical simplicity. No impediment exists to the migration of vortices into or out of the specimen. Also vortices are visualized as adjusting their orientation without any restrictions to allow the persistent current densities to flow along the lines of magnetic induction and to achieve configurations where the components of the magnetic induction vary as sine (or cosine) functions. The myriad of possible sinusoidal configurations however are restricted to quarter wave lengths or less for physical reasons and to the special case where the angular variation with depth is linear. We gave this category of force-free configurations the name Bergeron model after the first worker to envisage this type of solutions.

Next we considered the contrasting view that vortices cannot alter their orientation whatsoever as they advance into the volume of the specimen. This is equivalent to stipulating that the pinning forces opposing rotation are extremely strong and/or that the forces tending to cause rotation are negligible. On a microscopic scale this postulate means that processes whereby flux lines cut, cross or intersect each other are forbidden. In this context we have examined both the situation where the advance of the vortices is not hindered in the least by any pinning (force-free or zero transverse pinning) and where pinning resists the progress of flux into the sample. In the latter situation we considered the behaviour expected for a range of "modes" of pinning.

Both these extreme viewpoints lead to results which are unsatisfactory under several respects. We find that the magnetic moment and its components generally increase monotonically until H_{c2} is attained whereas we observe and expect that these quantities after traversing some maxima will be decreasing as H_{c2} is approached. To avoid this continual growth catastrophe in the Bergeron model we resorted to an empirical constraint on the choice for the linear variation of the direction of flux lines. Further we noted that a description of the migration of vortices out of the specimen which is qualitatively in harmony with observations could not be achieved if the requirement that flux lines cannot rotate is maintained.

In this chapter we exploit a description of the migration of vortices into and out of an infinite slab where the requirement that flux lines cannot rotate is relaxed. On the other hand we visualize that flux lines are not entirely free to swing from one orientation to another but that their rotation is impeded by pinning forces. Thus in contrast to the Bergeron model pinning forces prevent the fluxons from establishing completely force-free configurations. As a consequence as the externally applied magnetic field varies in magnitude and direction the planes of flux lines adopt sequences of critical state profiles with respect to orientation as well as density. As in the development of the Campbell and Evetts model we again postulate that the profiles of flux density are determined by the critical state concept. The crucial new feature is the introduction of a simple empirical rule to prescribe the sequences of angular variation of the flux lines with depth. The configurations of magnetic induction and persistent currents which ensue when $F_p \neq 0$ are partially force-free (i.e. a component of the current density vector lies along the magnetic induction vector) as in the Campbell and Evetts model.

This empirical expression together with the critical state concept are applied to the analysis of the variety of situations examined in this thesis where the transverse field $H_{\perp}$ is varied slowly while the longitudinal component $H_{//}$ is maintained constant. In particular we calculate the evolution of the magnetic moment and its components as the transverse field $H_\perp$ hence the total external field H_S (i) is increased (hence flux enters the slab), (ii) is decreased (hence flux leaves the slab) and (iii) undergoes complete cycles (hence flux alternately enters and leaves). In the latter instances the transverse field may be chosen to oscillate with or without changing its polarity. In both cases we also compute the hysteretic losses versus the amplitude of the variation of $H_\perp$ for different $H_{//}$. Finally for every situation examined we also present the corresponding results of measurements performed on samples of VTi and NbTi. A comparison shows that the families of curves computed using this model are all in good or adequate agreement with the observations.

Development of the Vortex Rotation Model

We assume as in the previous chapter that the sequence of profiles of magnetic induction in the infinite slab during and after slow changes of the externally applied field can be described by invoking the critical state concept of equilibrium between the driving Lorentz force density $\vec{F}_L = \vec{j} \times \vec{B}$ and the restraining force density $F_p(B)$ without any modifications. Again we will rely on simple analytic functions of the resonant form

$$F_p \;=\; \alpha\,(T)\; B^n\; (1 - B/H_{c2}(T)^{\ell})^m \qquad (6\text{-}1)$$

to express the dependence of the pinning force on magnetic flux density, temperature and pinning strength. Also we select the pinning parameter α and the values of n and m to yield a good fit to the magnetization curve observed in a given material when the longitudinal field $H_{//} = 0$. Theoretical investigations have provided some framework and justification for pinning functions of this form and predicted specific values for the exponents involved. Generally however, in analyzing their results workers have relied on an empirical approach similar to that which we adopt in selecting a particular form for the pinning function. In our case the "test" which our choice must pass is considerably more demanding than in the standard situation. Usually the experimentalist is concerned solely with accounting for the locus of the magnetization as H is increased from zero and swept from $+H_{c2}$ through 0 to $-H_{c2}$. In our work the choice we make must also generate an acceptable family of curves since the magnetic behaviour depends on $H_{//}$ and changes dramatically with different values of $H_{//}/H_{c2}$ hence as rotational effects come into play.

To progress any further in the analysis of our results we need, besides a suitable pinning function, an additional formula, principle or concept in order to determine the evolution of both components of the magnetic flux density. We propose that the variation of the direction of the magnetic induction with depth in different static longitudinal fields $H_{//}$ can be accurately described by the simple expression

$$b_z(x) = \frac{H_{//}H_s}{B(x)} \tag{6-2}$$

where $H_s = \sqrt{H_\perp^2 + H_{//}^2}$ is the magnetic field at the surface and $B(x) = \sqrt{b_y^2(x) + b_z^2(x)}$ is the magnetic induction in the volume of the slab. As we have done throughout this thesis we assume, for simplicity, that any abrupt variation of the magnetic induction in the surface layer due to a B(H) dependence, surface barrier and/or surface pinning can be ignored.

It is useful to examine the consequences of this empirical prescription qualitatively. We know from experiments that as $H_\perp$, hence H_s is increased with $H_{//}$ maintained fixed, the average magnetic induction in the longitudinal direction, $\langle b_z \rangle$ increases gradually, passes through a maximum and subsequently declines smoothly to vanish as H_s approaches H_{c2}. In other words, we witness the evolution of a paramagnetic magnetization ($\langle b_z \rangle > H_{//}$) under these circumstances. Further when $H_\perp$ is lowered to zero hence H_s decreases to $H_{//}$ after cooling through T_c to a final T_f in a stationary H_s, a diamagnetic magnetization develops in the longitudinal direction ($\langle b_z \rangle < H_{//}$) which increases monotonically until $H_\perp = 0$. The magnitudes of the longitudinal component of the magnetization $\langle 4\pi M \rangle_{//} = \langle b_z \rangle - H_{//}$ are observed to depend on $H_{//}$. The maximum of $\langle 4\pi M \rangle_{//}$ with $H_\perp$ increasing and its largest value when $H_\perp$ is decreased both also exhibit a broad resonance or peak when plotted versus $H_{//}$.

All of these features can be seen to follow from consideration of equation 6-2. Firstly we note that no magnetization appears perpendicularly to the applied magnetic field when $H_{//} = 0$ since $b_z(x)$ then remains at zero. This is in accord with the observations reported by Mattes (Mattes 1970) and Timms (Timms 1974) and in this thesis. Next we visualize that H_s has been increased with $H_{//}$ fixed and finite. Under these circumstances $B(x)$ decreases with depth into the slab and the detailed profile of the flux density can be obtained by solving the critical state equation. We encounter various situations depending on whether the change in H_s has been less or greater than H_s^*, the value required for full penetration of the front of the flux profile into the slab. We denote the depth of penetration of the total flux profile $B(x)$ by x_1 and consider the salient qualitative features of the evolution of the components of the configuration of magnetic induction and the magnetic moment as H_s is increased for various $H_{//}$. We refer the reader to Figure 28 for aid in visualizing the main aspects of the sequence of events.

(i) Partial penetration. $B(x)$ decreases to $H_{//}$ at a depth $0 < x_1 \leq a$ where a is the half-width of the slab since $H_s \leq H_s^*$. In this case $b_z(x)$ increases from $H_{//}$ at the surface to a maximum value $b_z(x_o) = \sqrt{H_{//}H_s}$ at a distance $x_o < x_1$. In the region $x_o \leq x \leq a$ we find $b_y = 0$ and $B_z(x) = B(x)$. Here the vortices are directed along the z-direction ($\theta = 0$). The longitudinal component of the magnetic induction grows as H_s increases and is paramagnetic since $\langle b_z \rangle > H_{//}$. The transverse component of the magnetic moment is also increasing. Further if H_s is not too large so that the pinning force density which is being exploited is everywhere less than the maximum we expect that the magnitude of the transverse magnetization will be greater than that encountered for a corresponding H_s with $H_{//} = 0$. This can be most readily seen by writing the critical state equation for a slab in the form

$$\frac{db_y}{dx} = \frac{-\mu_o F_p(B) \quad b_z \dfrac{db_z}{dx}}{b_y} \qquad 6\text{-}3$$

and noting that the right hand side is made larger by the $b_z \dfrac{db_z}{dx}$ term since the slope of b_z is positive where $b_y \neq 0$. As a consequence the gradient of the transverse field profile is accentuated and the magnitude of the diamagnetic moment ($H_\perp - \langle b_y \rangle$) is enhanced when $H_{//} \neq 0$. This augmentation is an important feature of all the pertinent data.

A crucial feature of the present model is that the number of vortices longitudinally threading the region between x_o and a need not be equal to the number initially permeating the sample. Indeed since vortices are allowed to rotate this number may either increase or decrease depending on specific conditions.

(ii) Full penetration. $B(x)$ decreases to $B(a) > H_{//}$ at the center of the slab. Two situations need to be envisaged.

a) $b_z(x)$ increases from $H_{//}$ at the surface to a maximum value $b_z(x_o) = \sqrt{H_{//}H_s}$ where $x_o < a$. As before $b_y = 0$ and $b_z(x) = B(x)$ in the region $x_o \leq x \leq a$ where vortices are compressed and directed in the z-direction ($\theta = 0$).

b) $b_z(x)$ increases to a maximum at the mid-plane. $b_y(x) \neq 0$ and $\theta(x) \neq 0$ anywhere. All of the fluxons originally threading the slab have rotated to some degree and $b_y(x)$ does not decrease to zero. This is an important difference with the Campbell and Evetts model. In both situations (a) and (b) above, $\langle b_z(x) \rangle > H_{//}$ and a paramagnetic magnetization is encountered along the z-axis. We can see from the sketches that the longitudinal moment must diminish after attaining a maximum as $H_{\perp}$ (hence H_s) increases to a large value. This decrease also emerges from consideration of the expression for the magnetization in the z-direction.

$$\langle 4\pi M \rangle_{//} = \langle b_z \rangle - H_{//} = H_{//}(\langle \frac{H_s}{B(x)} \rangle - 1) \qquad 6\text{-}4$$

where we have introduced equation 6-2. Considering the last expression with $H_{//}$ constant we note that since $\langle B(x) \rangle$ approaches H_s as H_s approaches H_{c2}, the term in parentheses must eventually decrease monotonically.

Remembering that $\langle 4\pi M \rangle_{//} = 0$ when $H_{//} = 0$ and noting that $\langle b_z \rangle / H_{//} = H_s / \langle B(x) \rangle$ must deviate less and less from unity hence from $H_{//}$ as $H_{//}$ (hence H_s) approaches H_{c2} we also expect that $<4\pi M>_{//}$ for a given $H_{\perp}$ will also traverse a peak and eventually decrease and vanish when plotted versus $H_{//}$ (hence H_s).

We have focussed attention on the behaviour anticipated from equation 6-2 combined with the critical state concept when $H_{\perp}$ is increased from zero since this is perhaps a conceptually easier situation to examine that that where $H_{\perp}$ is removed after the slab has becoming superconducting in a "diagonally" applied field ($H_{\perp} \neq 0$, $H_{//} \neq 0$). Nevertheless most of the considerations developed above can be applied, mutans mutandis, to this situation. An important difference is that the magnitude of the components of the magnetization will both attain a maximum as $H_{\perp}$ reaches zero. We emphasize only one basic feature. Under the circumstances where $H_{\perp}$ is removed, since $B(x)$ increases with depth, it follows from equation 6-2 that $b_z(x)$ decreases with x. Thus we expect equation 6-2 to generate diamagnetic moments in the z-direction ($<b_z> < H_{//}$) in harmony with observations.

We conclude then that phenomenologically equation 6-2 leads to the correct behaviour in contrast with the predictions of the previous two models we have examined. In this chapter we will show in detail that this simple prescription yields results also in quantitative agreement with observations.

In the preceding general discussion we have established that the empirical expression (equation 6-2) we propose is capable of generating the observed phenomena. It is also of interest to attempt to derive this empirical equation or at least to relate it to more basic physical concepts. We now turn our attention to this exercise.

Firstly we note the similarity between equation 6-2 above and equation 5-15 of the preceeding chapter, namely

$$b_z(x) = \frac{H_{//}H_s}{H_c}$$

where H_c is the total field existing at the surface when the fluxons now found at a depth x were created. We recall that equation 15 (chapter 5) was derived for the situation where vortices are not allowed to rotate and no pinning is present to oppose their migration, hence B(x) the total flux density profile in the slab is uniform at all times (for any H_s). We are now considering the case where the progress of the vortices is hindered by pinning and they can rotate. Equation 6-2 taken in analogy with equation 5-15 may be viewed as stating that the vortices now at a depth x with a density $B(x)/\phi_o$ are oriented as if they had advanced without rotating and were created earlier at the surface with their present density.

We can obtain a more general form of equation 6-2 from another phenomenological approach. From an examination of the magnetic field profiles required to produce the observed phenomena (see sketches above) we note that in the region when the direction of the vortices varies, $b_z(x)$ increases (decreases) if B(x) decreases (increases). In other words, the gradient of the profile of the total magnetic induction dB/dx and of its longitudinal component db_z/dx are opposite in sign. We normalize each of these gradients to the local value of the corresponding field profile, (dB/B)a/dx

and $(db_z/b_z)(a/dx)$ and postulate that these quantities are proportional hence

$$\frac{db_z}{b_z\ d(x/a)} = - \frac{kdB}{B\ d(x/a)} \qquad 6\text{-}5$$

where the constant of proportionality $k > 0$ and is independent of position, magnetic induction but may vary from one material to another. Introducing the boundary conditions $B(o) = H_s$ and $b_z(0) = H_{//}$ we write the integrals

$$\int_{H_{//}}^{b_z} \frac{db_z}{b_z} = - k \int_{H_s}^{B} \frac{dB}{B}$$

which yields

$$b_z(x) = H_{//} \left(\frac{H_s}{B(x)} \right)^k \qquad 6\text{-}6$$

We will exploit this more general empirical equation to describe the change of orientation of the fluxons in the analysis of our results but limit our choice to two values of the exponent k namely 1 and 2.

Equation 6-6 (hence equation 6-2) can be explicitly written as a function of θ, the angle between the total magnetic field vector and the z-direction. Inserting the definition $b_z(x) = B(x)$ $\cos\theta(x)$ into equation 6-6 yields

$$\cos\theta = \frac{H_{//}H_s^k}{B(x)^{k+1}} \qquad 6\text{-}7$$

and differentiating with respect to x we obtain the gradient of the angular profile

$$\frac{d\theta}{dx} = \left[\frac{(k+1)H_{//}H_s^k}{B^{k+2}\sin\theta}\right]\frac{dB}{dx} \qquad 6\text{-}8$$

It is instructive to introduce the critical state equation for an infinite slab into the expression for the gradient of θ. Equation 6-8 can then be rewritten as

$$\frac{d\theta}{dx} = \left\{\frac{(k+1)\ H_{//}H_s{}^k}{B^{k+3}\sin\theta}\right\} F_p(B) \qquad 6\text{-}9$$

where $F_p(B) = \alpha(T)\ f_p(B)$ is the pinning function for the material.

This expression states that the gradient of the angular displacement of the fluxons depends linearly on the pinning force density. This result appears physically reasonable since the pinning sites presumably oppose the rotation of the vortices (azimuthal displacement) and their migration into or out of the sample with equal effectiveness. In the limit where there is no pinning ($F_p = 0$), this expression requires that the fluxons angle be constant throughout the sample. In the approximation where $B(o) = H_s$ this angle will correspond to the direction of the applied field and vary in "phase" with H_s provided that H_s changes orientation slowly. The form of the dependence on the magnetic flux density also appears reasonable. Equation 6-9 indicates that it is considerably harder to alter the orientation of the fluxons when they are densely packed. This is consistent with the observation in other contexts that the flux line lattice becomes appreciably more rigid at high densities. We note that this empirical equation has been obtained in the specific framework where the total applied field varies in magnitude and direction while its longitudinal component is maintained stationary. We believe that this is the reason why the gradient of θ contains the quantities $H_{//}$, H_s and sin θ explicitly. The presence of k as an exponent is puzzling. We note however that at high fields where $B/H_s \approx 1$ throughout the sample, the gradient becomes insensitive to this exponent. We may then regard the factor (k + 1) as just a constant of proportionality.

Finally we note that introducing equation 6-6 in equation 6-5 yields the expression

$$\frac{db_z}{dx} = -\frac{kH_{//}H_s^{\,k}}{B^{k+1}}\frac{dB}{dx} \qquad 6\text{-}10$$

for the gradient of the longitudinal field profile in terms of the boundary conditions and the profile of the total magnetic induction.

We note from inspection of equations 6-8 and 6-10 (or 6-5) that the sign of the gradient of $\theta(x)$ and $b_z(x)$ changes when the sign of the gradient of $B(x)$ changes. Depending on the previous magnetic history of the sample in the superconducting state, the gradient of $B(x)$ may undergo changes in sign at various depths in the slab. Thus corresponding changes in the sign of the gradient of $\theta(x)$ and $b_z(x)$ may occur. It is important to realize however that the existence of a gradient of $B(x)$ does not necessarily entail a variation in the direction of the fluxons. When we apply the basic equations to specific situations in the next sections we will encounter regions where the vortices have been compressed (or decompressed) at constant angle. Further we will encounter regions where, as a consequence of the variation of the magnitude and direction of the applied field, the vortices are compressed (or decompressed) while the existing profile of $\theta(x)$ although spatially varying remains unaltered. In other words detailed physical considerations lead us to envisage situations where modifications in the $B(x)$ profile occur without causing changes in the $\theta(x)$ profile. We now turn our attention to these important features in some detail.

Application of the Vortex Rotation Model

In the application of the basic expressions enunciated in the previous section to the analysis of our experimental observations we need to consider a variety of sequences of events in detail. We develop the simplest case first and then proceed to the progressively more complicated situations which are encountered in our work. The entire analysis is pursued in the context of infinite slab geometry since the samples we have studied are wide ribbons with the applied field directed along the flat faces of the slab.

In every case the slab is viewed as becoming superconducting in a uniform applied field H_{si} which may be directed at an angle θ_{si} with respect to the z-axis. We assume $B(x) = H_{si}$ after the slab has become superconducting and before H_s is varied. Also as in the previous chapters we assume that reversible surface shielding currents can be neglected hence $B(o) = H_s$ and take $\nabla \times B(x) = \nabla \times H(x)$. This is equivalent to letting $\mu = 1$ in the relation $B = \mu H$ and is a good approximation when κ is large or $B(x)$ is close to H_{c2}. We also emphasize that in our work, $H_{//}$, the z-component of the applied field remains fixed as $H_{\perp}$ the y-component is allowed to vary.

We need to consider three main types of variations of $H_{\perp}$ and consequently H_s: We refer the reader to figure 27 for aid in visualizing the variety of situations encountered in our work. (i) where $H_{\perp}$ (hence H_s) increases, (ii) where $H_{\perp}$ (hence H_s) decreases and (iii) where $H_{\perp}$ after an initial increase to a maximum value $H_{\perp max}$ is subsequently cycled between $H_{\perp max}$ and another value $H_{\perp min}$. Under the latter circumstances we need to

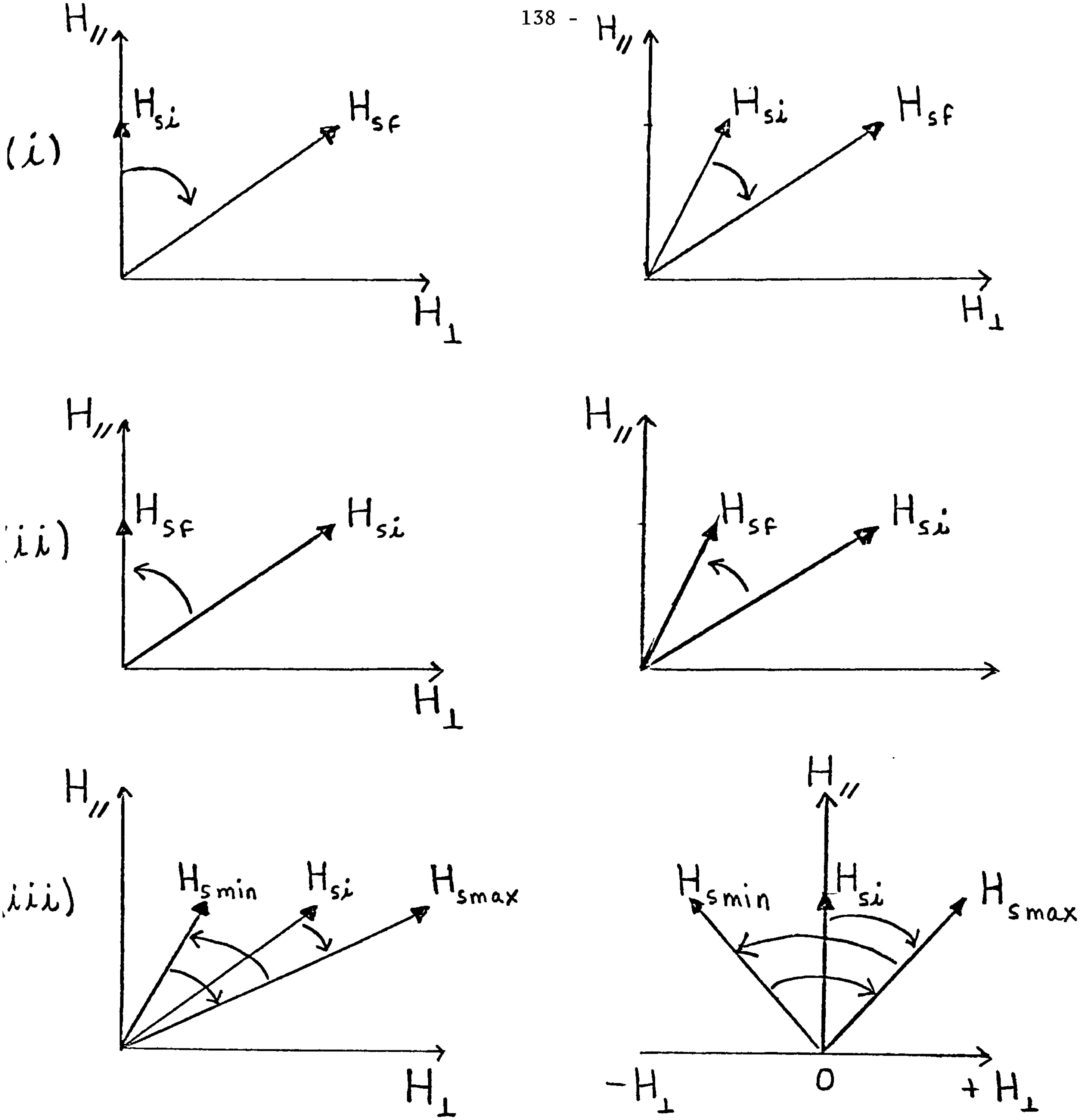

FIGURE 27: Sketch of the variations of $H_{\perp}$ encountered in our work.

focus attention on two distinct possibilities. (a) $H_{\perp min}$ is in the same direction as $H_{\perp max}$ and (b) $H_{\perp min}$ is directed oppositely to $H_{\perp max}$. Hence in (a) the polarity of $H_{\perp}$ does not change during the cycle whereas in (b) the polarity of $H_{\perp}$ alternates between + and -. We note that for (b), the magnitude of H_s varies at twice the frequency of $H_{\perp}$ and $H_{\perp min}$ may be chosen such that $|H_{\perp min}| = |H_{\perp max}|$. In situation (i) the initial transverse field may be zero ($H_{\perp i} = 0$) and in (ii) the final transverse field may be chosen zero ($H_{\perp f} = 0$).

In every case we need to establish the sequence of configurations of the magnitude and the direction of the total magnetic induction as a function of distance from the surface(s) of the slab. We first require a knowledge of B(x), the field or B profile. We then exploit this information to delineate the corresponding orientation θ(x), the angular or θ profile.

We determine the field profile by solving the critical state equation

$$B \frac{dB}{dx} = \pm F_p(B) \qquad \text{6-11}$$

where the choice of sign follows from whether B(x) is caused to increase or decrease. This in turn depends on the magnetic history to which the slab has been subjected. A specific form for the pinning function $F_p(B)$ is chosen so as to generate a magnetization curve with $H_{//} = 0$ which gives a good fit to the corresponding experimental curve.

In our analysis we have exploited two simple and similar analytic expressions of the generally accepted form

$$F_p = \alpha(T)\ B^n\ \{1 - (B/H_{c2})^{\ell}\}^m \qquad 6\text{-}12$$

to describe the magnetic behaviour of the two materials we have investigated. These pinning functions are presented in the table below which also lists the pinning parameter α and the critical field H_{c2} we have used in the calculations as well as other data on the samples.

TABLE III

Pinning Function	α	H_{c2}(kg)	k	Thickness (cm)	Width	Sample
$\alpha\ B(1 - B/H_{C2})^2$	6.5×10^5 G/cm	110	1	0.020	0.135	NbTi
$\alpha B^{\frac{1}{2}}(1 - B/H_{C2})^2$	1.0×10^5 $G^{3/2}$/cm	20	2	0.15	0.51	VTi

We have explored the curves generated for various other combinations of the exponents n, ℓ and m and compared these with the observed behaviour. In this survey we have restricted the choice of m and ℓ to 1/2, 1 and 2 for reasons of simplicity both physical and analytical. Further, allowing n to exceed unity appears difficult to justify physically. Such a choice also means that the critical current of the ribbon in a transverse applied field must increase as $H_{\perp}/H_{c2}$ increases in the range of weak and intermediate fields in contradiction with all available data. As indicated in the previous chapter, the values n = 0, 1/2 and 1 have been used extensively in the literature and some theoretical basis developped for each of these exponents. The predicted behaviour is very sensitive to the choice of this exponent. The selection of n = 1/2 and 1 we have made in each case are mandated by the need to obtain satisfactory overall agreement for a vast assortment of families of curves measured for each of our samples and not only to reproduce the magnetization curve for increasing $H_{\perp}$ with $H_{//} = 0$. The choice of the exponent of the factor $(1 - B/H_{c2})$ is also important (although less crucial than the power n) in the analysis of the data for the VTi ribbon since here our measurements span the range $0 < B/H_{c2} \lesssim 0.6$. It is however not too significant for the interpretation of the NbTi data because in this material we could only scan the range of B/H_{c2} extending to $\gtrsim 0.16$.

Once F_p is fixed, it is a relatively straightforward exercise to map out the sequences of B profiles as $H_{\perp}$ is swept upwards (or downwards) and subsequently cycled for various values of $H_{//}/H_{c2}$. We present the salient features of such sequences of B profiles in the following sections. For the case where n = 1, we can obtain analytic expressions for the various segments of the B-profile and the boundaries of the regions they occupy. Some of these expressions have already been developed in chapter 5. These derivations mainly involve some tedious algebraic manipulations and the results are not especially illuminating hence they will generally not be presented in this chapter. We have pursued some calculations using these analytic expressions for our edification and as a check that the method of attack we took leads to corresponding results. The case where n = 1/2 in particular and most of the other pinning functions we explored are not amenable to analytic development of the B profile. As a consequence we developed a flexible computer program to solve the critical state equation in its differential form (6-11) where the pinning function in its general form (equation 6-12) is introduced.

Once the B profile has been mapped out, clearly there are now several routes at our disposal to determine the corresponding $\theta(x)$, $b_z(x)$ and $b_y(x)$ profiles in the context of the phenomenological vortex rotation framework we have developed above. In most situations we have found it convenient to obtain cos θ (x) numerically using equations 6-7 (i.e. $\cos\theta(x) = H_{//}H_s^k/B(x)^{k+1}$). Here again a series of trial computations with k = 1, 3/2 and 2 led us to us to retain the values k = 1 and 2 as most suitable to reproduce the observations for the NbTi and VTi samples respectively.

We then use cos $\theta(x)$ to determine $b_z(x)$ and $b_y(x)$ since by definition

$$b_z(x) = B(x)\cos\theta(x),\quad b_y(x) = B(x)\sin\theta(x) \qquad 6\text{-}13$$

Finally the evolution of the components of the magnetization as $H_\perp$ is varied with different $H_{//}$ was calculated numerically from the definitions given earlier and repeated here for convenience.

$$<4\pi M>_\perp = \frac{1}{a} \int_0^a b_y(x)\ dx - H_\perp \qquad 6\text{-}14$$

$$<4\pi M>_{//} = \frac{1}{a} \int_0^a b_z(x) dx - H_{//} \qquad 6\text{-}15$$

We close this outline of our empirical computational approach by noting that in our analysis the grouping or stacking of the families of curves of $<4\pi M>_\perp$ vs $H_\perp$ increasing or decreasing for different $H_{//}$ are primarily sensitive to the choice of the power n in the pinning function. The main role of the factor $(1 - B/H_{c2})$ is to cause these curves to decrease continously to zero as H_S approaches H_{c2}. The exponents ℓ and m in $(1 - (B/H_{c2})^{\ell})^m$ of course determine the shape or rate of this decrease. The bunching and magnitude of the families of curves of $<4\pi M>_{//}$ vs $H_\perp$ increasing or decreasing for different $H_{//}$ are primarily sensitive to the choice of the power k in the expressions for the rotation of the flux lines (equations 6-7, and the equivalent equations 6-8, 6-9 and 6-10) although the pinning function is implicitly or explicitly contained in the latter expressions.

We now develop the salient features of the sequences of B, θ, b_z and b_y profiles encountered according to the vortex rotation model during the various sets of measurements exploited in our work and enumerated above (figure 27) namely I) increasing $H_{\perp}$, II) decreasing $H_{\perp}$ and III) cycling $H_{\perp}$.

I. <u>Increasing $H_{\perp}$</u>

a) $H_{\perp i} = 0$. We first consider the simple situation where the infinite slab becomes superconducting in $H_{\perp} = 0$, hence initially at the surface and throughout the sample $B(x) = H_s = H_{//} = b_z(x) = b_z(0)$ and $\theta(x) = \theta(0) = \theta_s = 0$ and also $b_y(x) = 0$. Subsequently, as $H_{\perp}$ is impressed, flux enters the sample adopting sequences of critical state profiles whose orientation is determined by the prescription that $b_z(x) = H_{//}(H_s/B(x))^k$ and $b_y(x) = \sqrt{B^2(x) - b_z^2(x)}$. As $H_{\perp}$ and H_s grow, the front of the B profile advances deeper and deeper into the slab eventually reaching the mid-plane when $H_{\perp}$ and the corresponding H_s attain values which we denote by $H^*_{\perp}$ and H^*_s respectively.

It follows from our prescription for the rotation of the vortices that the front of the advancing θ-profile lags behind the front of the B-profile, independently of the form of the pinning function which governs the latter, provided that $k \geq 1$. A proof of this is presented in appendix II for the case with $k = 1$, where the algebra is tractable. Let θ^*_s denote the direction of the applied field when $H_s = H^*_s$ and the leading edge of the B profile reaches the centre of the slab. After further increase of H_s to a value H_s^{**}, the front of the invading θ profile also attains the mid-plane and we denote its value at the surface by θ_s^{**}. In brief, the arrival of the front of the B profile at the centre and the subsequent arrival of the front of the θ profile at the centre are denoted by using one and two asterisks respectively as superscripts to the various quantities of interest. Also we let x_1 denote the front of the B profile and use the subscript 1 to characterize the various quantities at this position, i.e. $B_1 = B(x_1)$, $b_{z1} = b_z(x_1)$ etc. Finally we let x_o denote the leading edge of the θ profile and use the subscript o to label the various quantities at this position, i.e. $B_o = B(x_o)$, $b_{zo} = b_z(x_o)$ etc. We emphasize that $x_o \leq x_1$.

To follow the main features of the evolution of the profiles of magnetic induction as $H_\perp$ (hence H_s) is raised we need to consider the following three stages in the sequence of events, (i) $H_{//} < H_s \leq H_s^*$, (ii) $H_s^* \leq H_s \leq H_s^{**}$ and (iii) $H_s^{**} \leq H_s \leq H_{c2}$. For each range in the growth of H_s we examine the characteristics of the quantities of interest $B(x)$, $b_z(x)$, $b_y(x)$ and $\theta(x)$ and the migration of the boundaries of the various domains of these quantities. We do not present sketches of the configurations of current densities. These can be visualized from consideration of the appropriate field profiles and bearing in mind that Maxwell's equations for an infinite slab geometry gives

$$\mu_o j_z = \frac{db_y}{dx} \qquad \text{and} \quad \mu_o j_y = -\frac{db_z}{dx}$$

where $\mu_o = 4\pi/10$ in the practical system of units we are using and the total current density $j = \sqrt{j_z^2 + j_y^2}$. We refer the reader to figure 28 for aid in visualizing the development of the field and angular profiles.

(i) $H_{//} < H_s \leq H_s^*$

We can identify three different regions in the slab.

A) $0 < x \leq x_o$

This region is filled with induced currents attempting to shield the slab against the entry of the increasing transverse field $H_\perp$. Nevertheless, since the current densities are finite (except at a mathematical plane of zero width situated at x_o), the transverse component of the magnetic induction has entered to a depth x_o where $b_y(x_o) = 0$. In this region the direction of the vortices varies from θ_s at the surface to 0 at x_o. The fluxons occupying this region do not retain their angle of creation but rotate as they advance. In so doing they tend to align along the direction of the total current density. Alternatively we may say that the total current density $\vec{j}$ tends to flow in the direction of the total magnetic induction $\vec{B}$. Regardless of the viewpoint, the resulting configuration of $\vec{j}$ and $\vec{B}$ is partially force free in this volume since a component of $\vec{j}$ flows // to $\vec{B}$ and a component

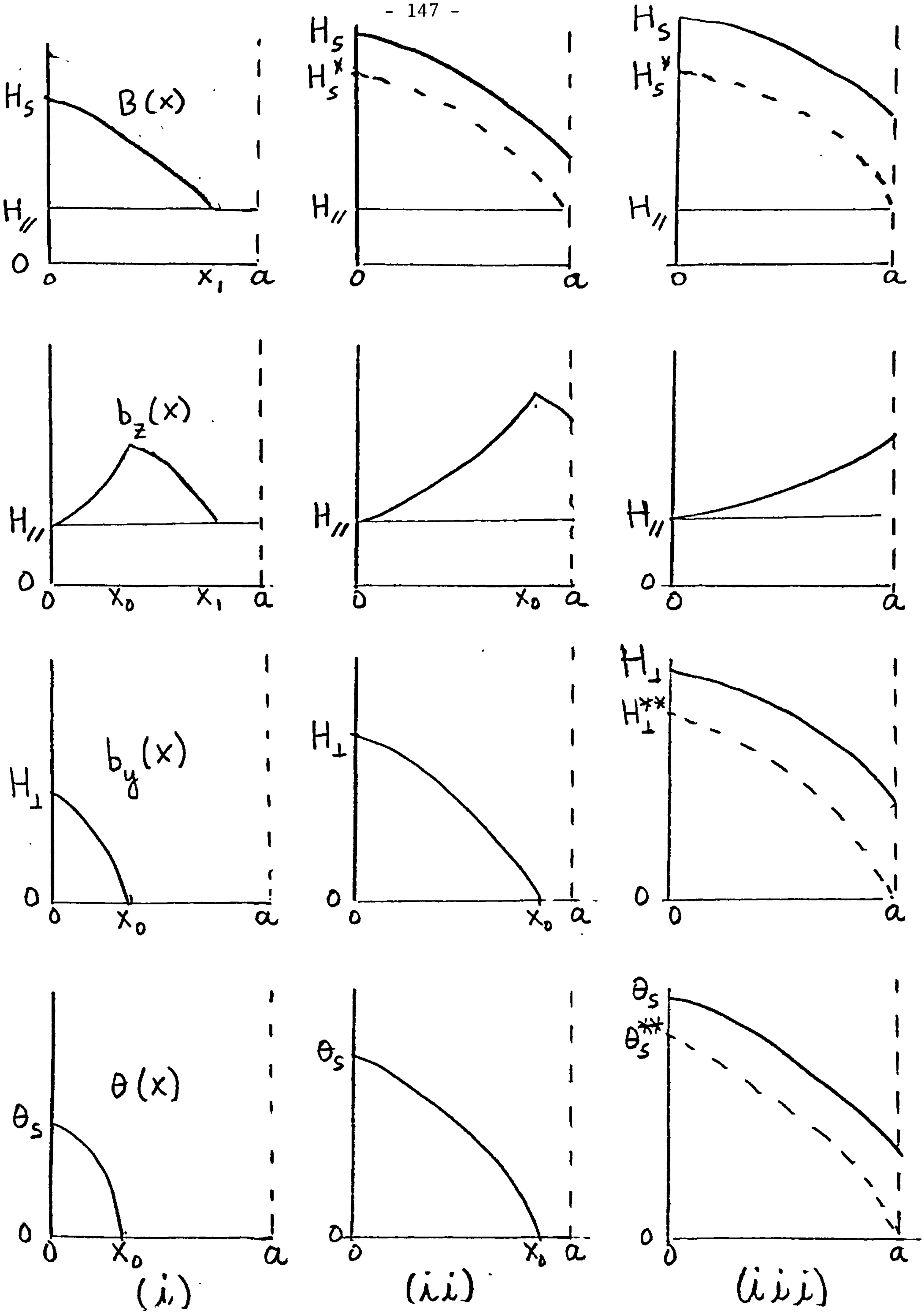

FIGURE 28: Sequence of field and angular profiles for $H_\perp$ increasing from $H_{\perp i} = 0$.

flows $\perp$ to $\vec{B}$. Since the current $\vec{j}$ occupying this region is flowing with a component // to $\vec{B}$, hence a force free component, the current densities existing in this volume can be considerably enhanced compared to that permitted if the currents $\vec{j}$ were entirely $\perp$ to $\vec{B}$. According to our basic prescription, the longitudinal field $b_z(x)$ increases from $H_{//}$ at the surface to $b_z^{k+1}(x_o) = H_{//}H_s^k$ and B(x) follows a critical state profile declining from H_s to $B(x_o) = b_z(x_o)$ since $b_y(x_o) = 0$.

B) $x_o \leq x \leq x_1$

In this region $B(x) = b_z(x)$ and both follow a critical state profile decreasing to $H_{//}$ at x. In this region the vortices are compressed at the same angle $\theta = 0$ and induced currents opposing the invasion of the magnetic induction flow perpendicularly to $\vec{B}$.

C) $x_1 \leq x \leq a$

No new vortices have entered this region and the initial profile $B(x) = b_z(x) = H_{//}$, $b_y(x) = 0$, $\theta(x) = 0$ remain undisturbed.

We emphasize that the total number of vortices threading the space between x_o and a, need not correspond to the number originally threading the half slab when it becomes superconducting since vortices are allowed to change their orientation. Following our prescription for describing the direction of the fluxons we find that the number of longitudinally oriented vortices has diminished.

ii) $H_s^* \leq H_s \leq H_s^{**}$

The B profile has penetrated to the mid-plane but the b_y profile has not yet reached the center of the slab. We recognize the existence of two regions.

A) $0 < x \leq x_o$

The features identified above for this region still apply.

B) $x_o \leq x \leq a$

The situation here is similar to that described above under B) except that $b_z(x)$ hence $B(x)$ decreases to a value $B(a) = b_z(a) \geq H_{//}$ at the mid plane. The vortices in this region are all compressed. Again we note that the flux in this region is not commensurate with $H_{//}\, a\ell_y$, the flux originally threading the entire half slab. Indeed in this space $\phi_z < H_{//}\, a\ell_y$.

iii) $H_s^{**} \leq H_s \leq H_{c2}$

The b_y profile has now also penetrated to the center of the slab and hence the b_z and θ profiles also. The other features indicated above under A) still apply except that now $b_y(x)$ decreases from $H_\perp$ at the surface to $b_y(a) \geq 0$ at the center whereas $b_z(x)$ increases from $H_{//}$ to $b_z = H_{//} H_s^k/B^k$ (a). Correspondingly $\theta(a) \geq 0$. We no longer find any vortices oriented along the z-axis. Thus all of the vortices originally present have rotated and are now aligned to some degree along H_s.

b) $H_{\perp i} \neq 0$.

The sequence of events we have just examined needs to be amended for the case where the superconducting slab becomes superconducting in a "diagonally" directed magnetic field where initially $H_{\perp i} \neq 0$. We now review the discussion just presented and note the features which are modified when H_s initially possesses a transverse component $H_{\perp i}$ which is subsequently increased. This basic situation is intrinsically interesting and is important in our later analysis of complete hysteresis loops or cycles. We refer the reader to figure 29 which schematically depicts the sequences of profiles.

Let $H_{si} = (H_{\perp i}^2 + H_{//}^2)^{\frac{1}{2}}$ and $\theta_{si} = \cos^{-1} H_{//}/H_{si}$ denote the magnitude and direction of the applied field when the sample becomes superconducting. In keeping with the simplifying assumptions indicated previously we visualize that initially $B(x) = H_{si}$ and $\theta(x) = \theta_{si}$, in other words, the flux in the slab has the same intensity and direction as the applied field. The main difference from the profiles encountered earlier as $H_{\perp}$ grows for the case where $H_{\perp i} = 0$ is that now at the depth x_o where the leading edge of the θ profile decreases to θ_{si}, the transverse field profile $b_y(x)$ has diminished to a value $b_y(x_o) > H_{\perp i}$. Consequently in the volume $x_o \leq x \leq x_1$ (the region referred to as (B) above), the vortices are compressed but do not rotate and maintain their original orientation

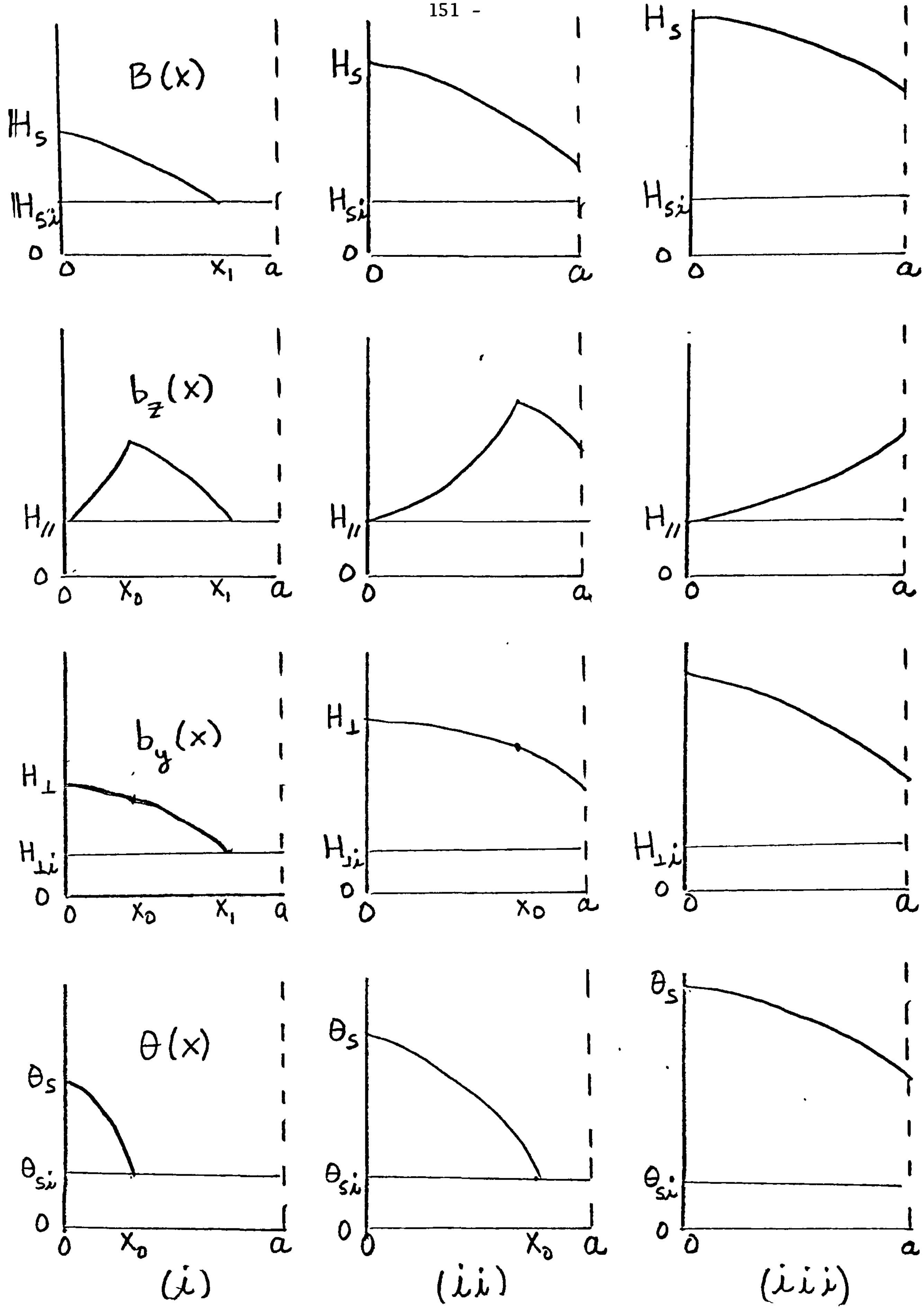

FIGURE 29: Sequence of field and angular profiles for $H_\perp$ increasing from $H_{\perp i} > 0$

$$\theta_{si} = \theta(x_o) = \cos^{-1} H_{//}/H_{si} = \cos^{-1} b_z(x_o)/B(x_o)$$

$$= \sin^{-1} b_y(x_o)/B(x_o) \qquad 6\text{-}17$$

Eventually when $H_s \geq H_s^{**}$, there are no longer any vortices present with this orientation and $\theta(x) \geq \theta(a) \geq \theta_{si}$.

Results and Discussion

We have carried out computer calculations of the behaviour predicted by the vortex rotation model just described where we used the two pinning functions and sets of parameters listed in table III. The pinning strength parameter α and the exponent n in the pinning function were selected to yield a good fit to the experimental magnetization curves of our NbTi and VTi samples with $H_\perp$ increasing from zero when $H_{//} = 0$. The values of H_{c2} introduced in each case correspond to the values accepted in the literature for these materials at 4.2^oK and are applicable to our samples. In the volume where the angular disturbance penetrates (region A of our discussion above) and where our empirical rule (equation 6-7) governing the angular variation of the flux lines applies, we have used the parameter k = 1 to achieve a comparison with our data on NbTi and k = 2 for the VTi sample. The values of $H_{//}$ introduced in the calculations were deliberately chosen to correspond to that employed in the measurements. We wish to point out that this procedure constitutes a severe test of the validity of the model. This approach means that not only are individual curves of a family required to rise and fall in qualitative and quantitative agreement with observation but we are also demanding that the relative "position" and distribution of all the members of a large family of curves correspond to the observations.

In the following pages (figures 30 through 33 and 37 through 44) we present the evolution of both the longitudinal and transverse components separately of the magnetization during the sweep of $H_{\perp}$ from zero for several values of $H_{//}$ up to the limiting values accessible with our orthogonal superconducting magnets. Each figure presenting a family of experimental curves is followed by a figure showing the corresponding series of curves generated by our model for immediate comparison. In the case of the VTi sample our measurements span a significant fraction of the range 0 to H_{c2}. Thus to avoid clutter we found it necessary to double the number of figures. The sketch below may aid in placing the data in perspective. The sketches show that a three-dimensional surface diagram can be constructed for each component of the magnetization from the various series of figures we present for each sample in the next pages.

The first requirement imposed on the model we have developed is that it must generate these two open surfaces satisfactorily

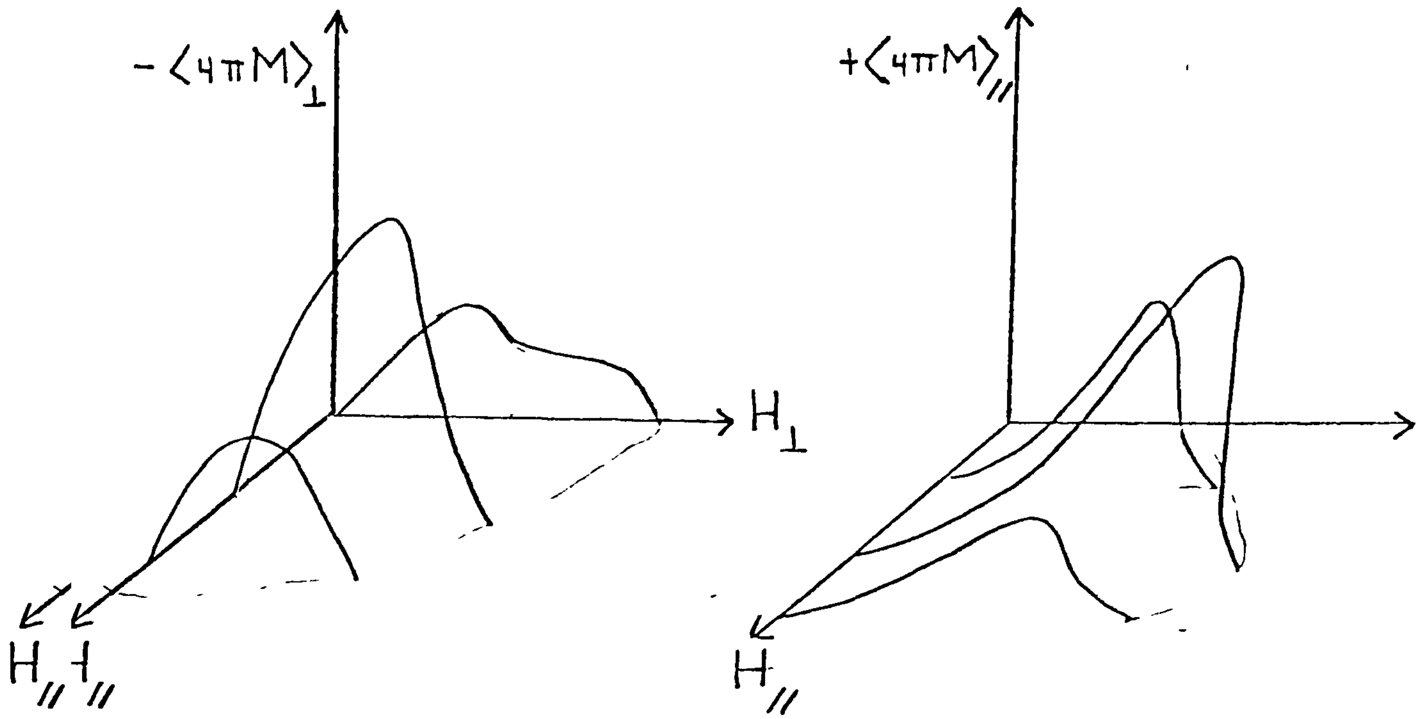

once the two adjustable parameters α and k are fixed for a given sample. We believe that inspection of the figures indicates that this objective is met. We will see below that the model must also produce other open and closed surfaces which correspond with observations on a given sample exploiting the two basic rules (equations 6-8 and the critical state equation) and the same two parameters.

For completeness we also present a sequence of profiles of B, b_y and b_z generated by our model during each set of calculations of the growth of the magnetic moments, namely n = 1, k = 1, figures 34 through 46 and n = 1/2, k = 2, figures 45 through

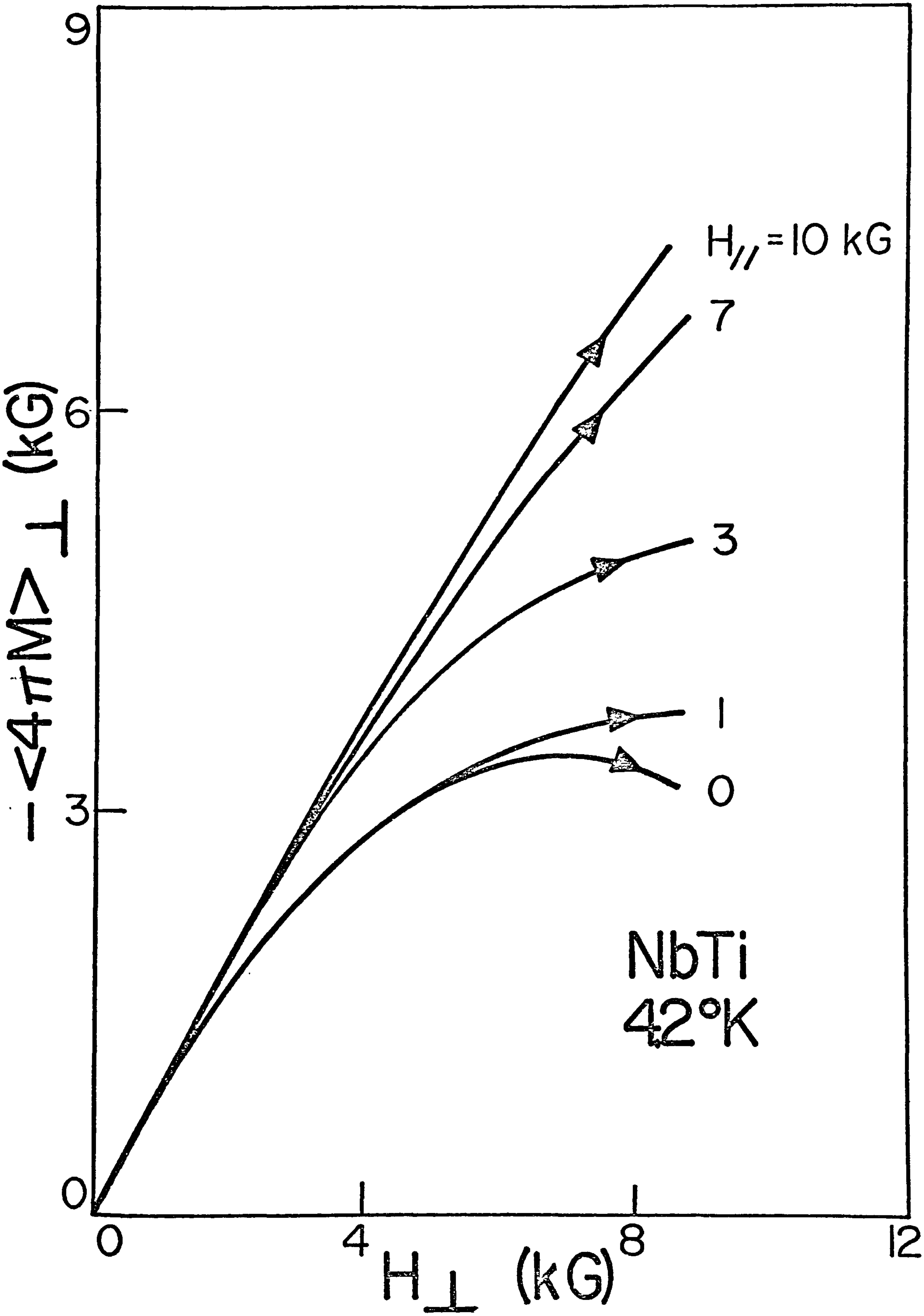

Figure 30: Experimental values of $\langle 4\pi M\rangle_{\perp}$ versus $H_{\perp}$ for NbTi ($H_{\perp}$ increasing).

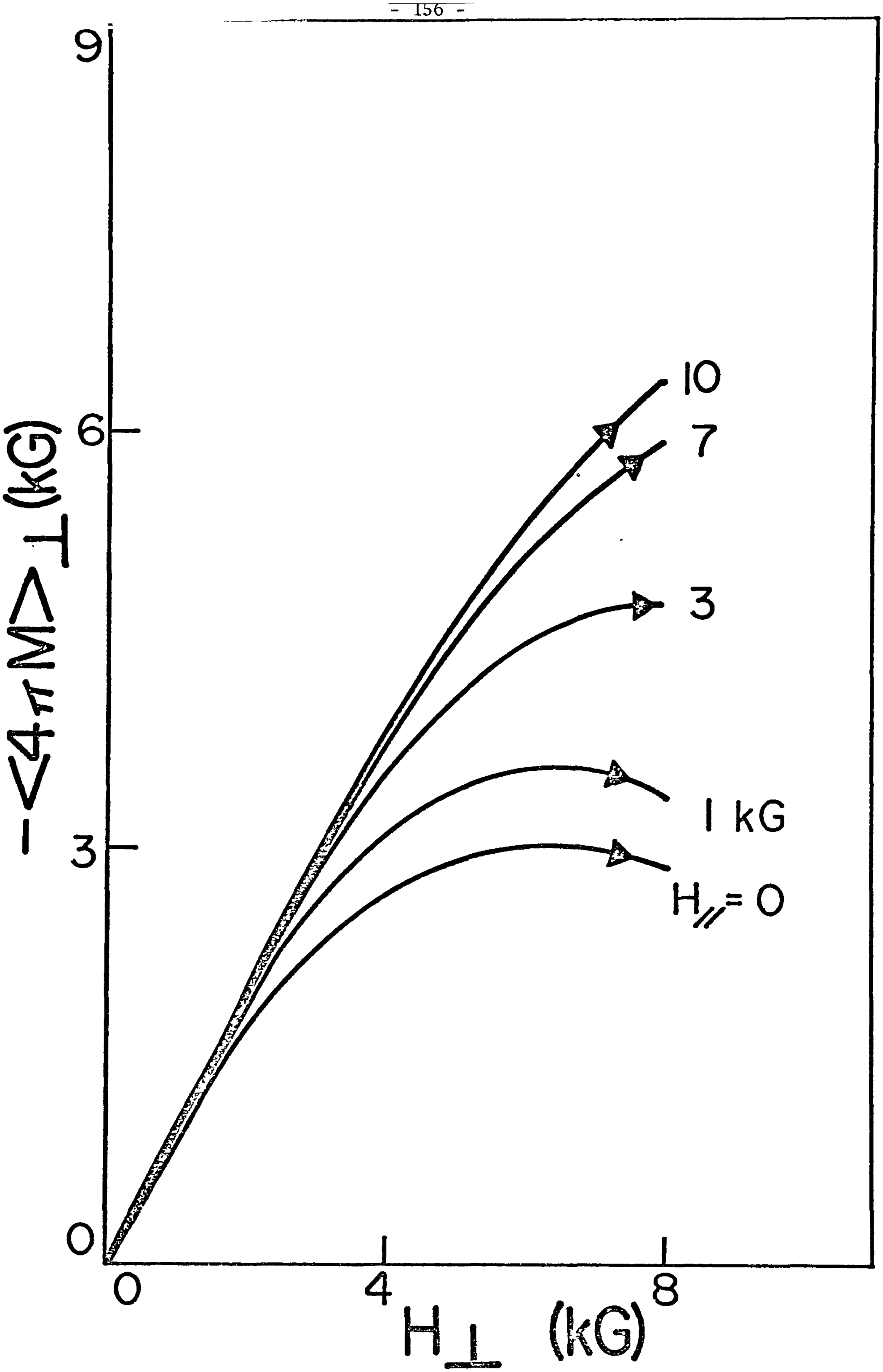

Figure 31: Values of $\langle 4\pi M\rangle_\perp$ versus $H_\perp$ calculated for NbTi according to vortex rotation model.

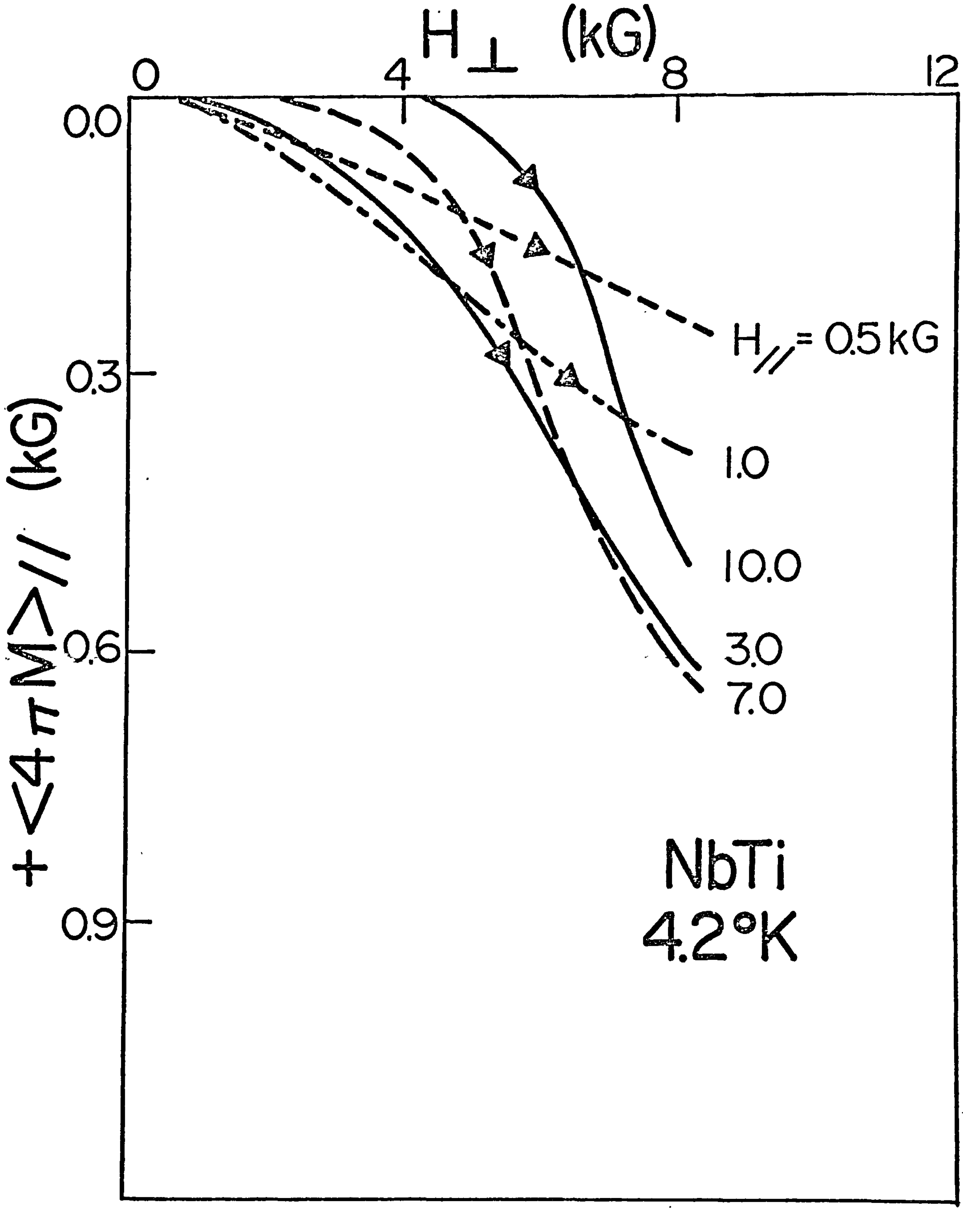

Figure 32: Experimental values of $\langle 4\pi M\rangle_{//}$ versus $H_{\perp}$ for NbTi ($H_{\perp}$ increasing).

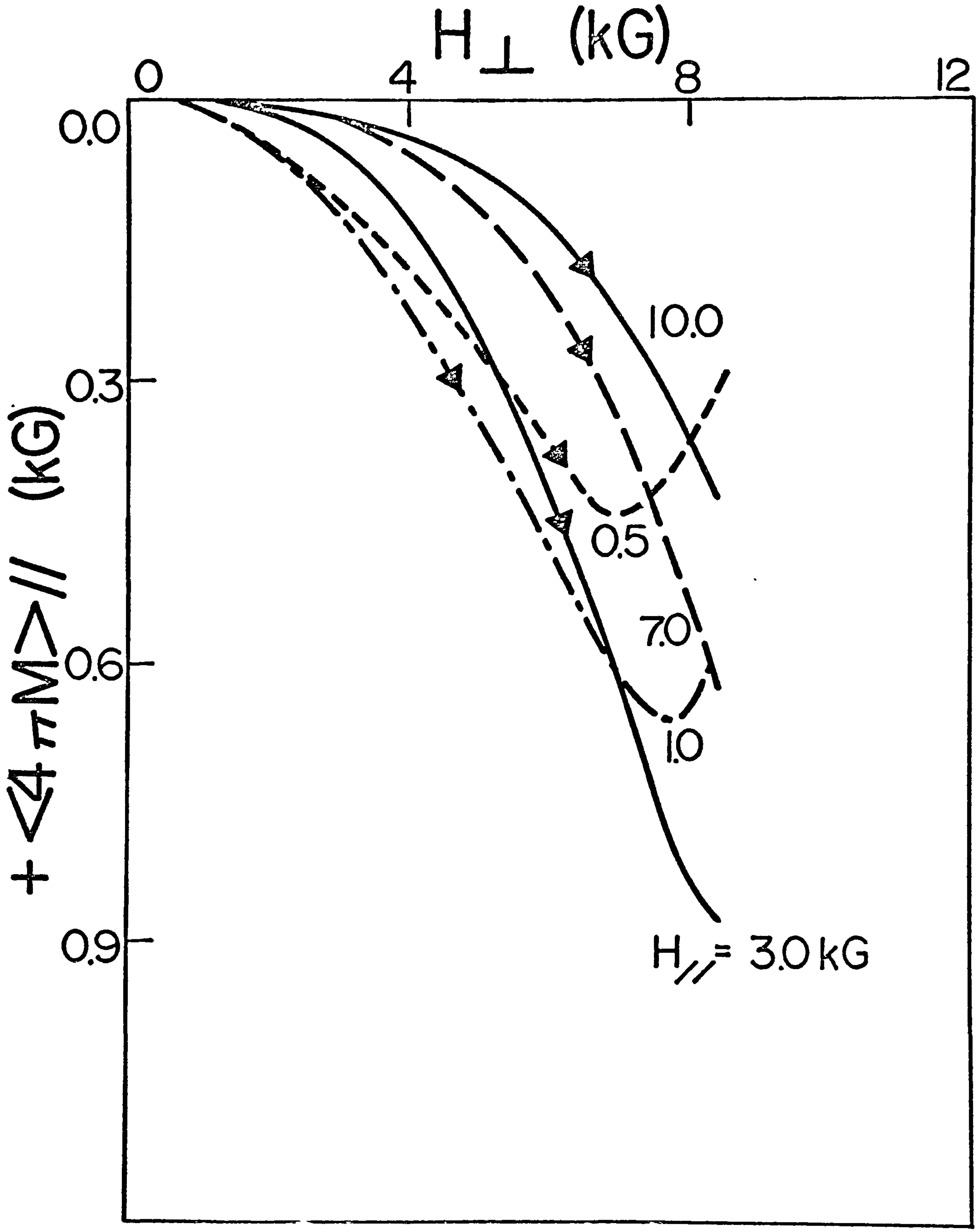

Figure 33: Values of $\langle 4\pi M\rangle_{//}$ versus $H_\perp$ calculated for NbTi according to vortex rotation model.

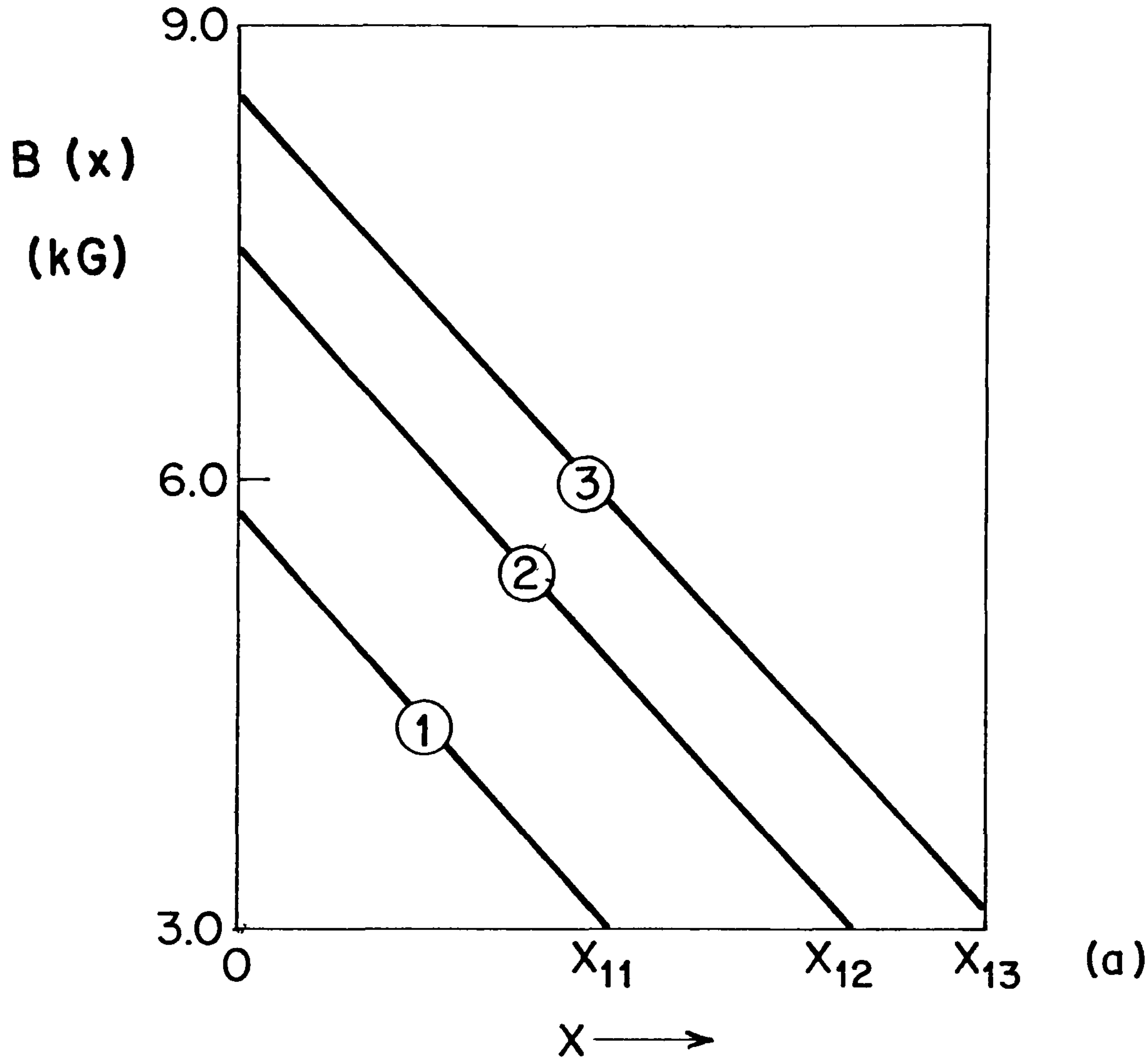

Figure 34: Calculated B(x) profiles for $H_{//}$ = 3kG in NbTi. $H_{\perp}$ = 5, 7 and 8kG for ①, ②, and ③ respectively.

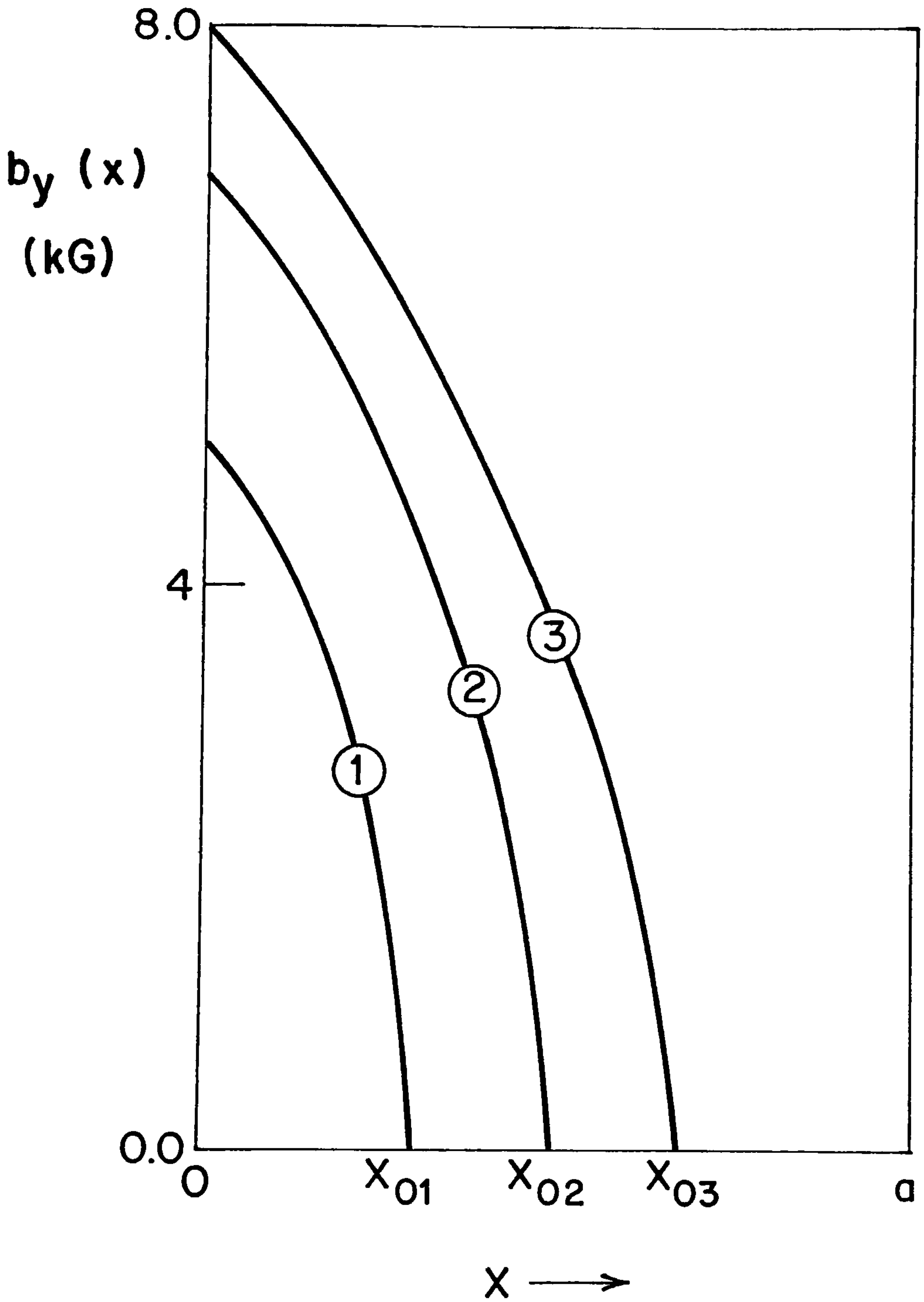

Figure 35: Calculated $b_y(x)$ profiles for $H_{//}$ = 3kG in NbTi. $H_{\perp}$ = 5, 7 and 8kG for 1, 2, and 3 respectively.

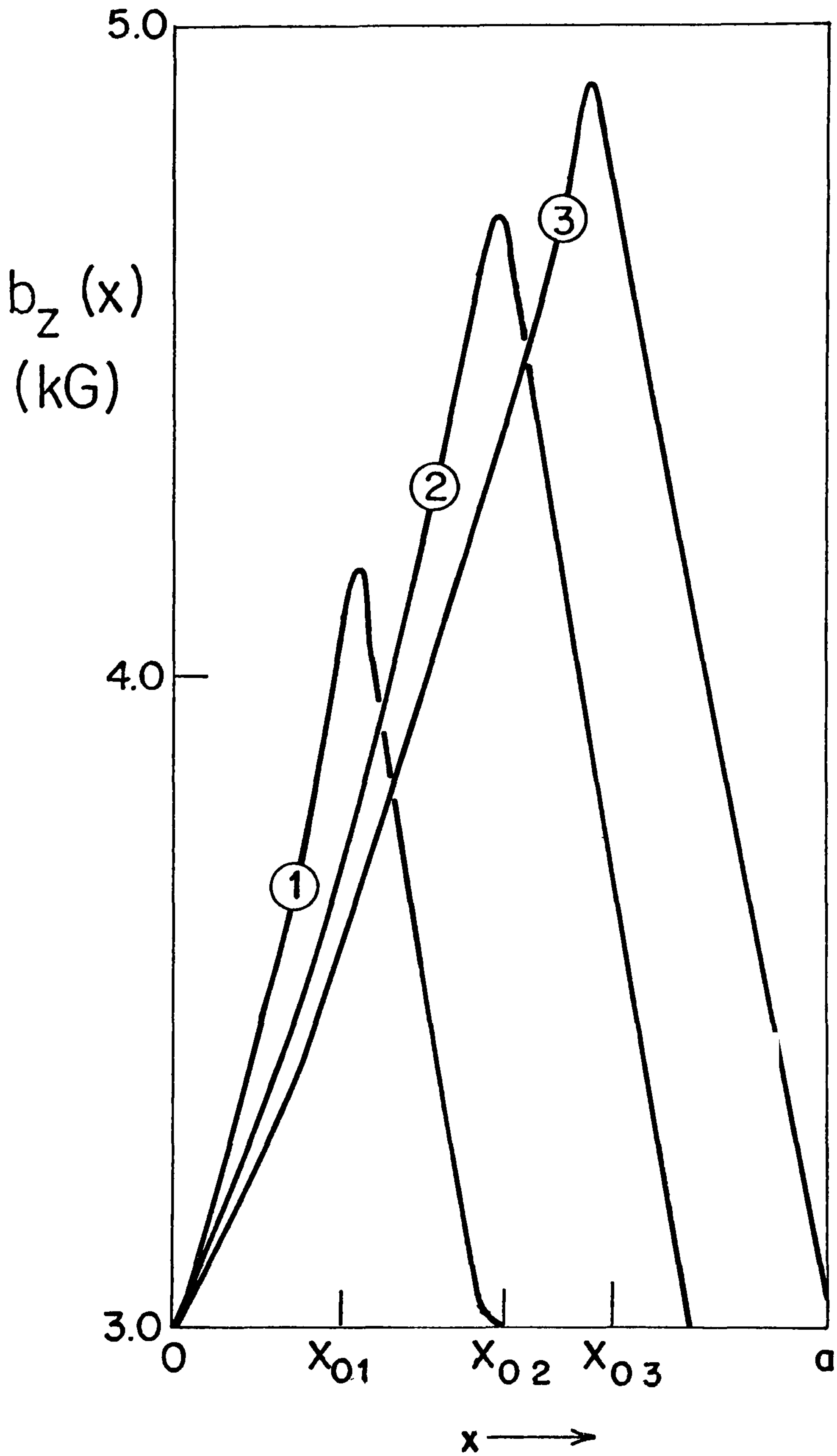

Figure 36: Calculated $b_z(x)$ profiles for $H_{//}$ = 3kG in NbTi. $H_{\perp}$ = 5, 7 and 8kG for ①, ②, and ③ respectively.

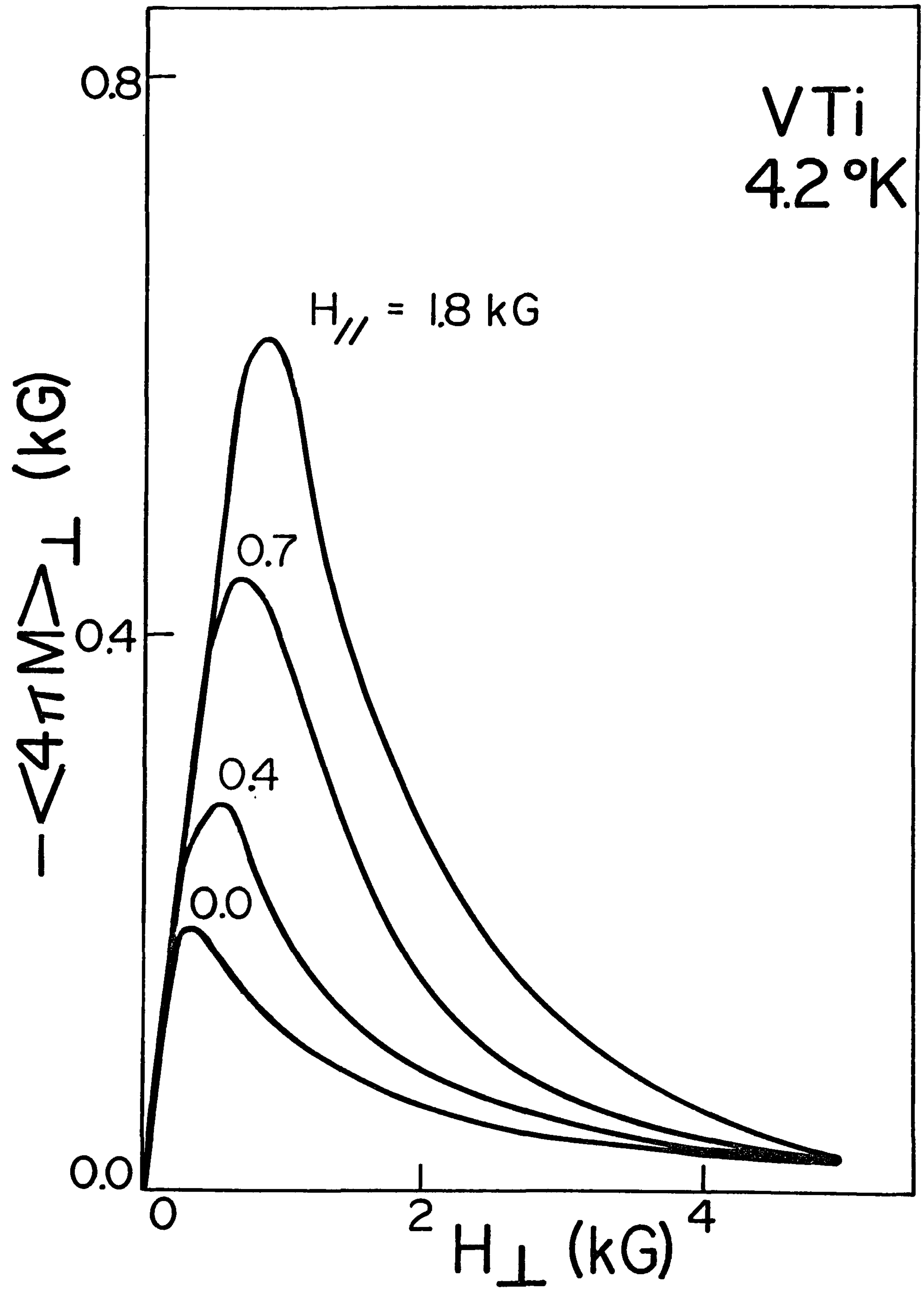

Figure 37: Experimental values of $\langle 4\pi M \rangle_{\perp}$ versus $H_{\perp}$ for VTi. ($H_{//}$ = 0 to 1.8kG) [$H_{\perp}$ increasing].

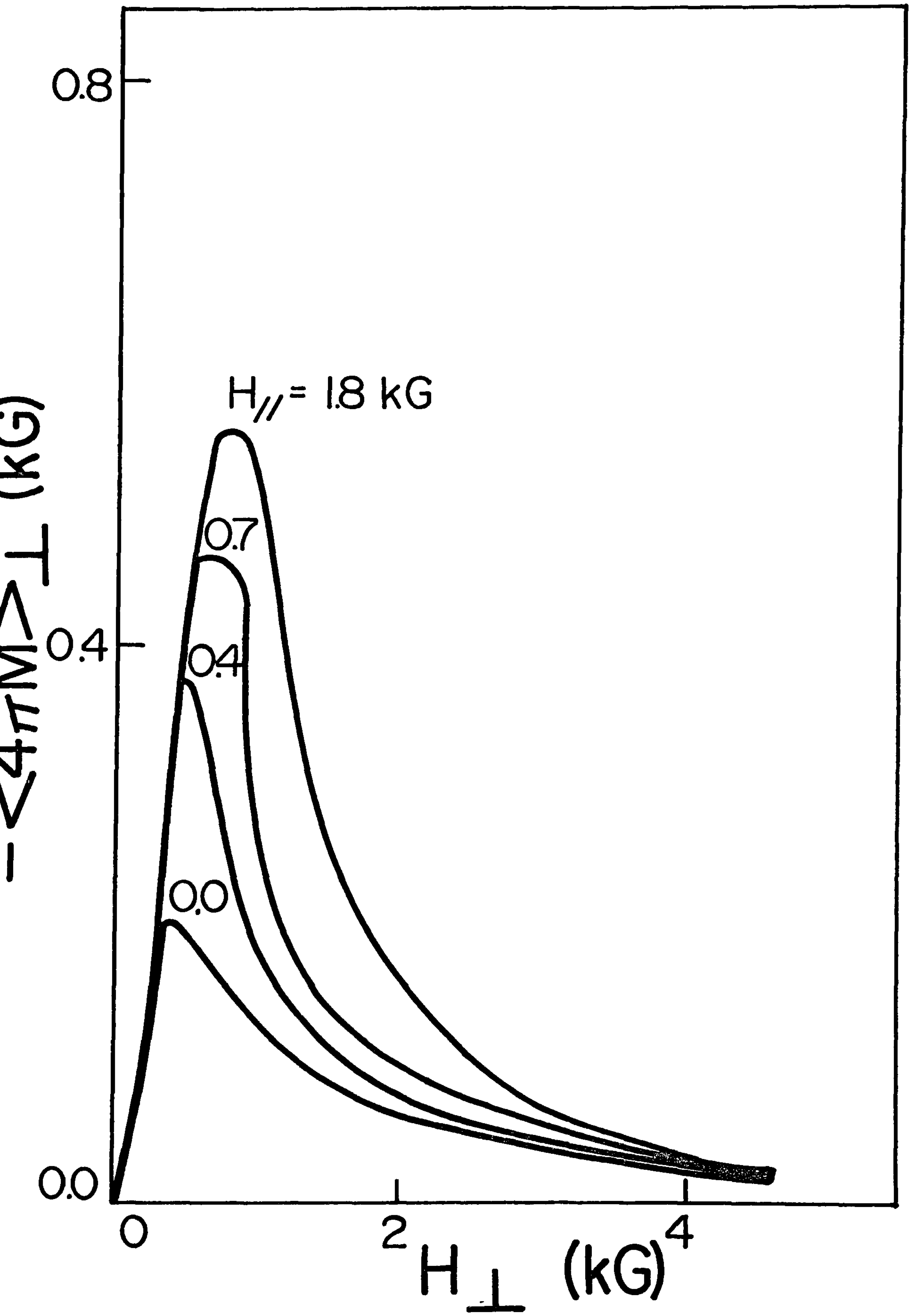

Figure 38: Values of $\langle 4\pi M\rangle_{\perp}$ versus $H_{\perp}$ calculated for VTi according to vortex rotation model ($H_{//}$ = 0 to 1.8kG).

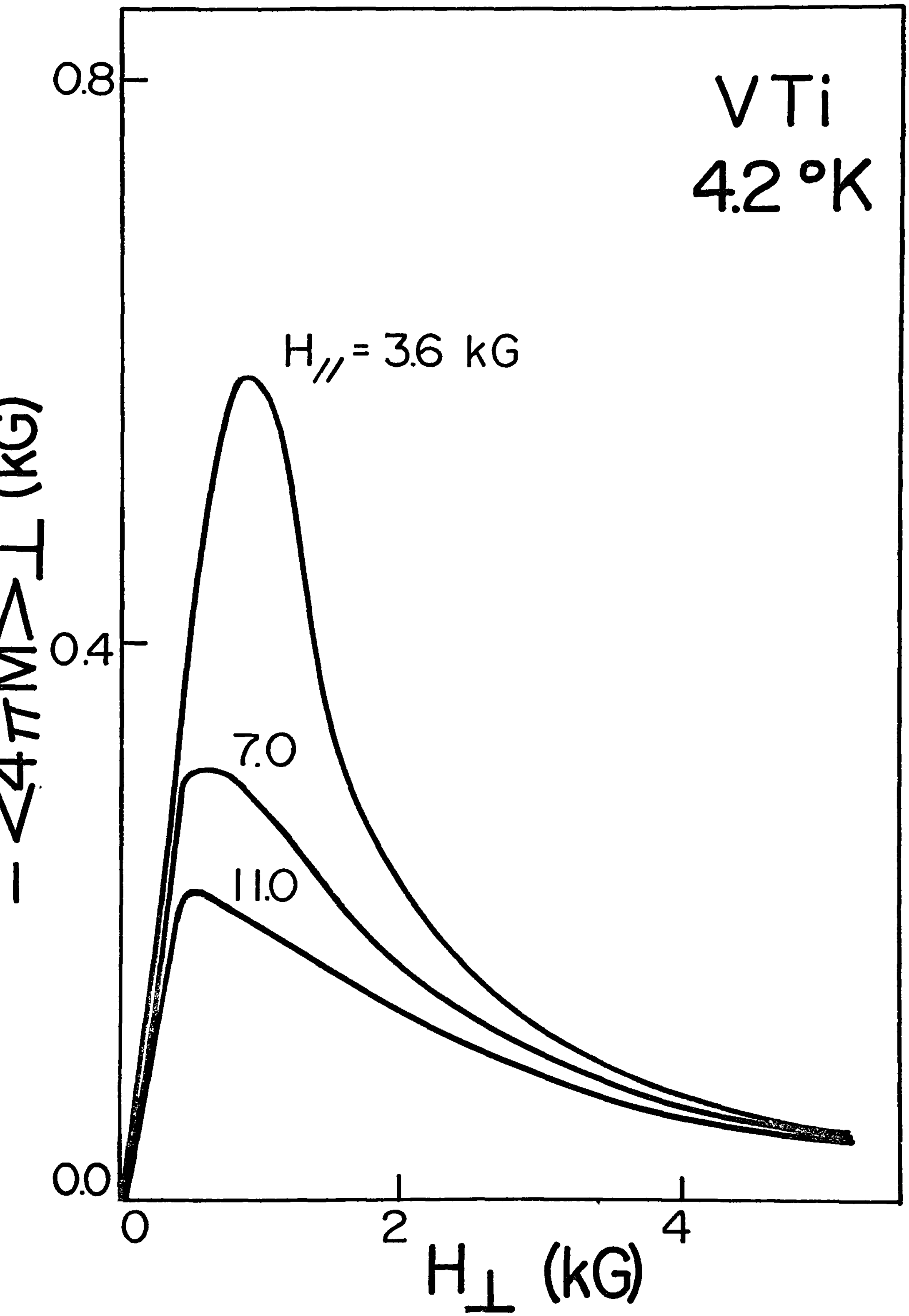

Figure 39: Experimental values of $\langle 4\pi M\rangle_\perp$ versus $H_\perp$ for VTi ($H_{//}$ = 3.6 to 11.0kG) [$H_\perp$ increasing].

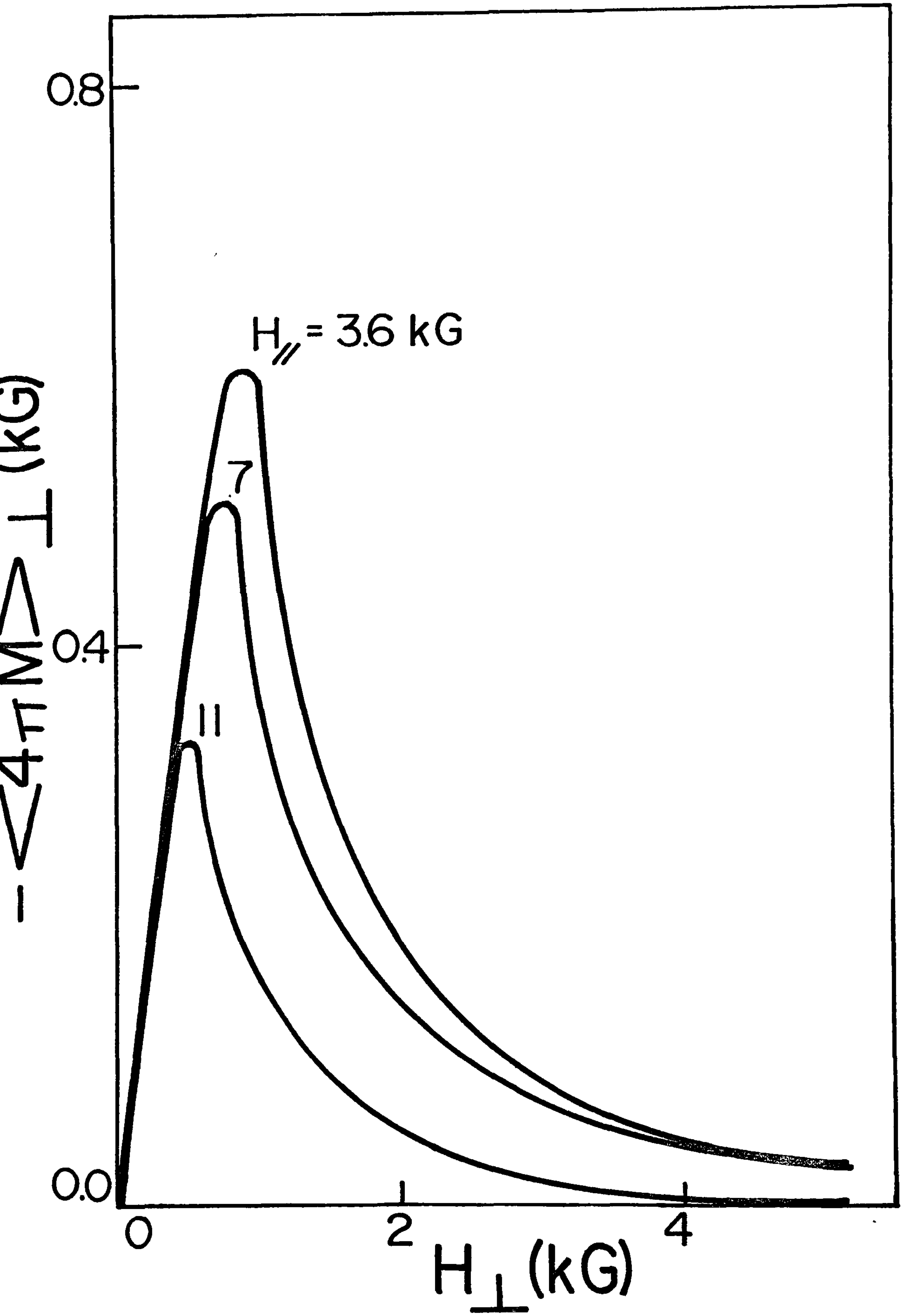

Figure 40: Values of $\langle 4\pi M\rangle_{\perp}$ versus $H_{\perp}$ calculated for VTi according to vortex rotation model ($H_{//}$ = 3.6 to 11.0kG).

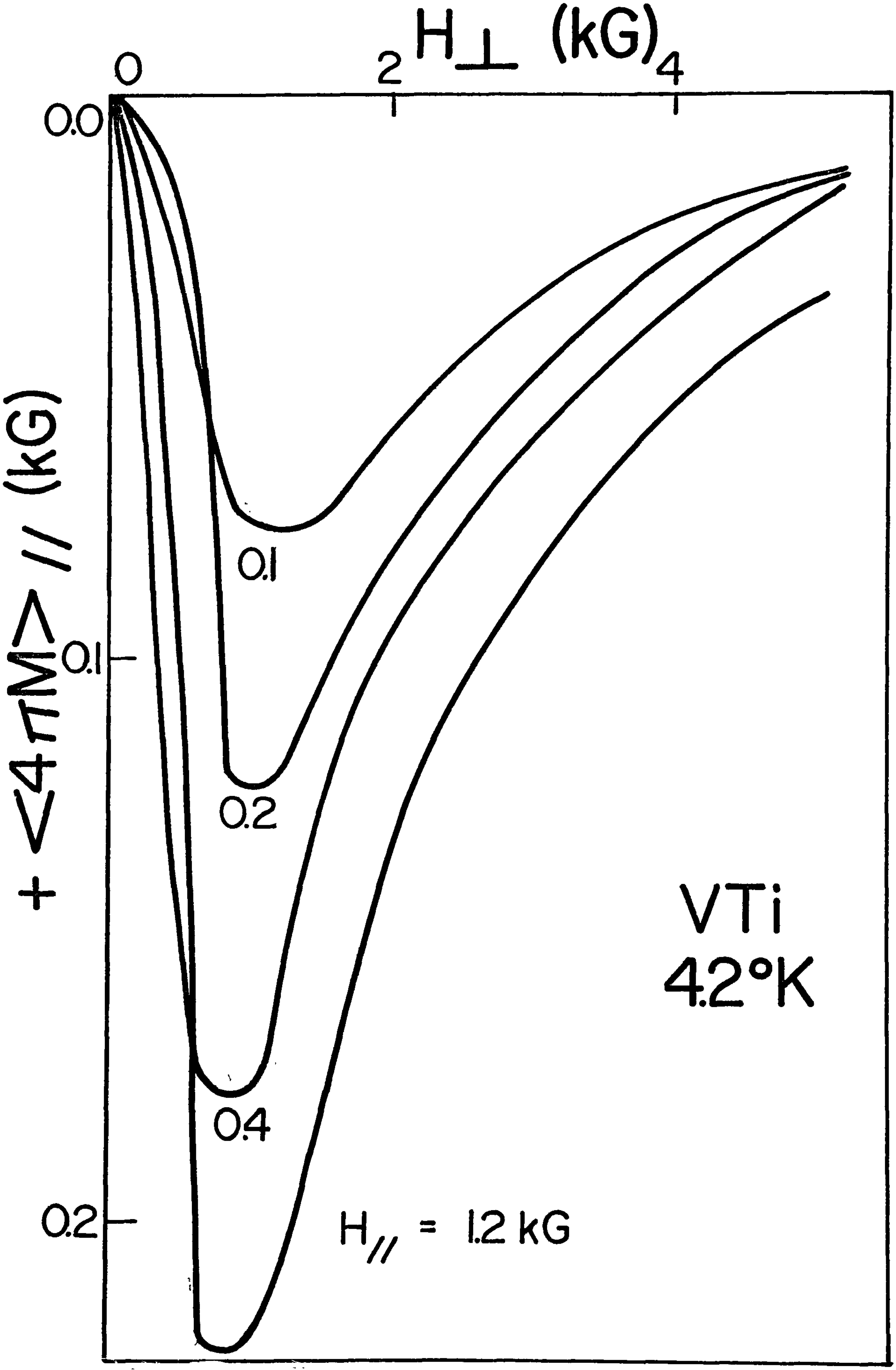

Figure 41: Experimental values of $\langle 4\pi M\rangle_{//}$ versus $H_\perp$ for VTi. ($H_{//}$ = 2kG) [$H_\perp$ increasing].

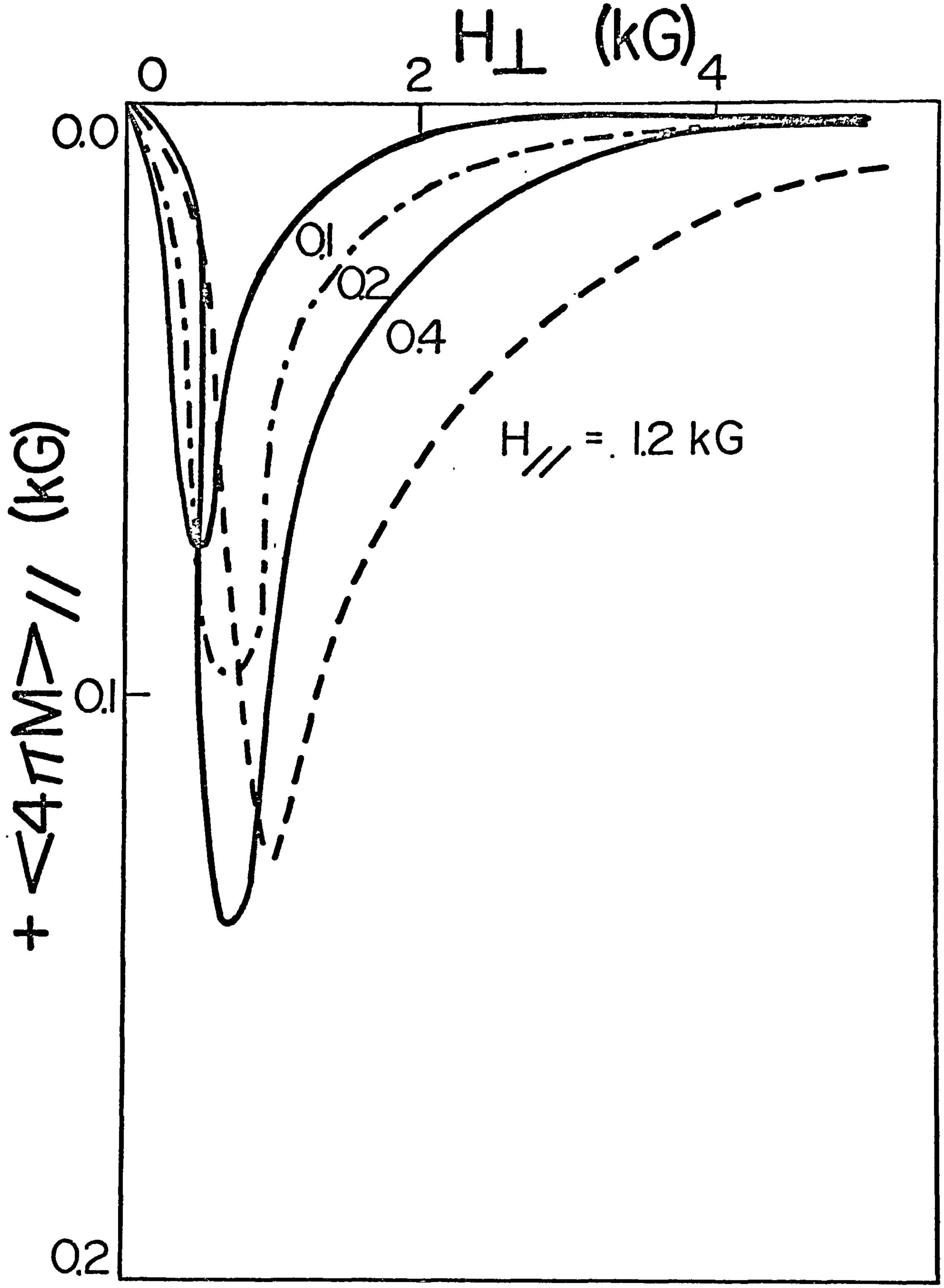

Figure 42: Values of $\langle 4\pi M \rangle_{//}$ versus $H_{\perp}$ calculated for VTi according to vortex rotation model ($H_{//}$ = 0.1kG to 1.2kG).

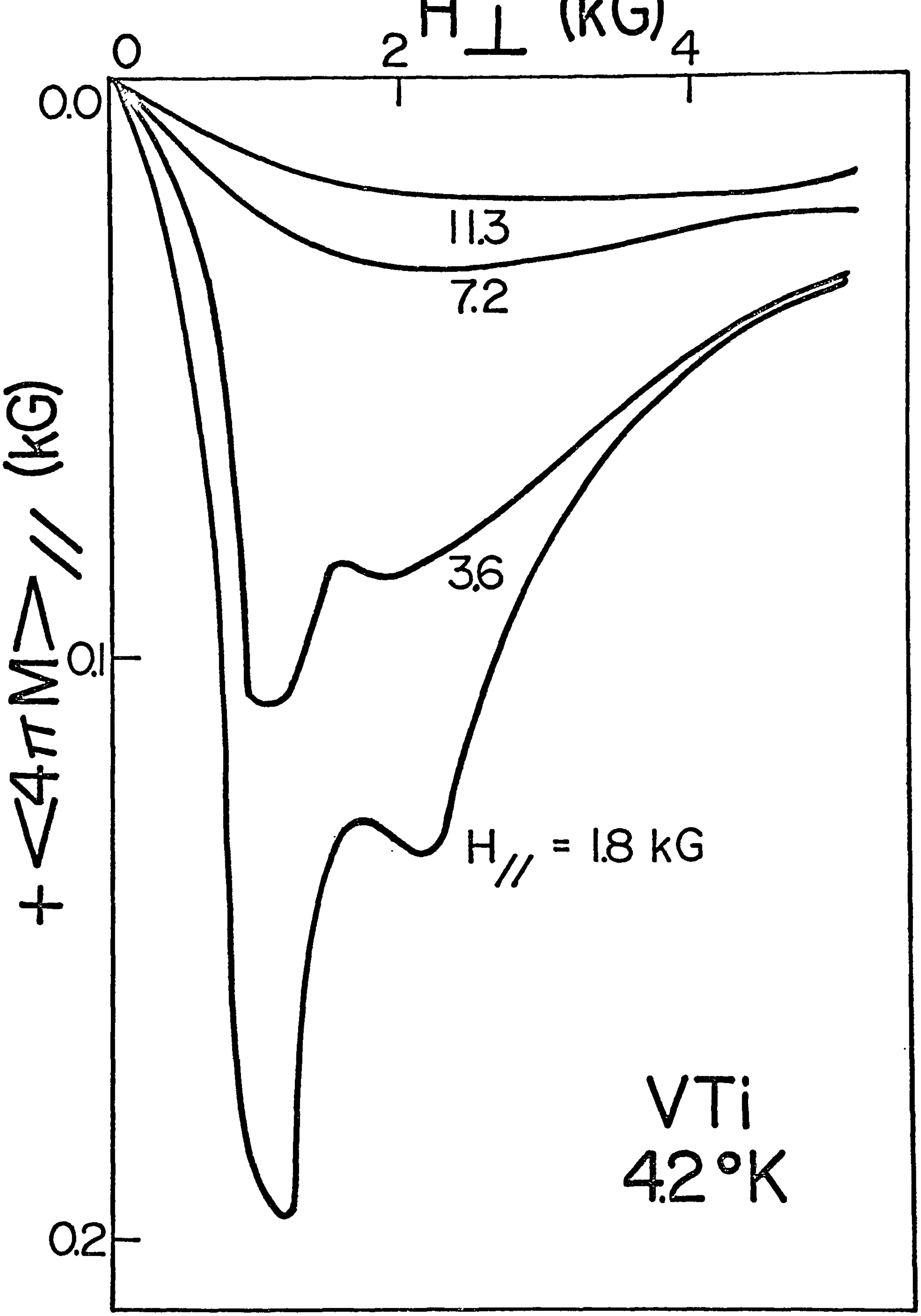

Figure 43: Experimental values of $\langle 4\pi M \rangle_{//}$ versus $H_\perp$ for VTi. ($H_{//}$ = 1.8 to 11.3kG) ($H_\perp$ increasing).

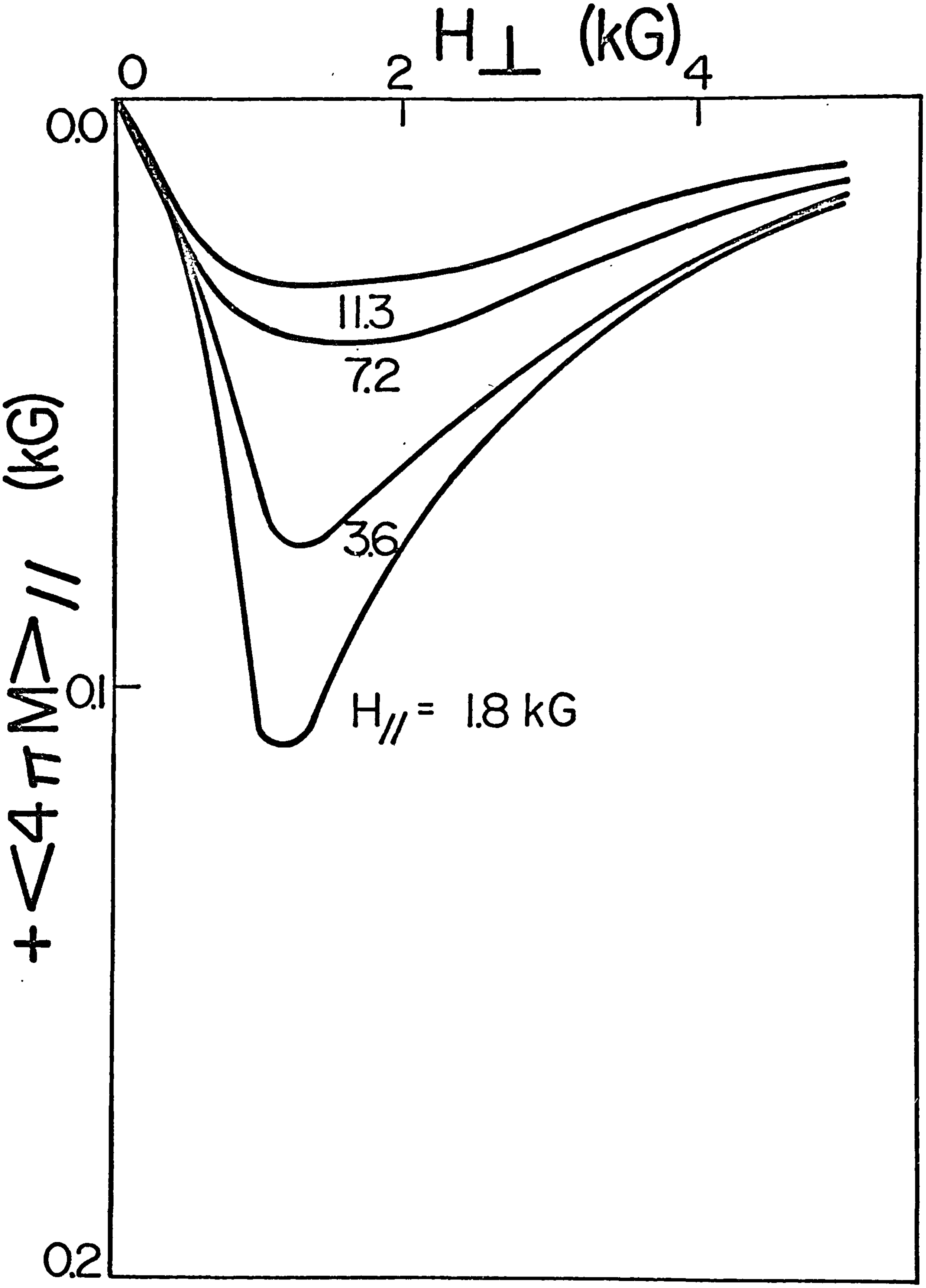

Figure 44: Values of $\langle 4\pi M \rangle_{//}$ versus $H_\perp$ calculated for VTi according to vortex rotation model ($H_{//}$ = 1.8 to 11.3kG).

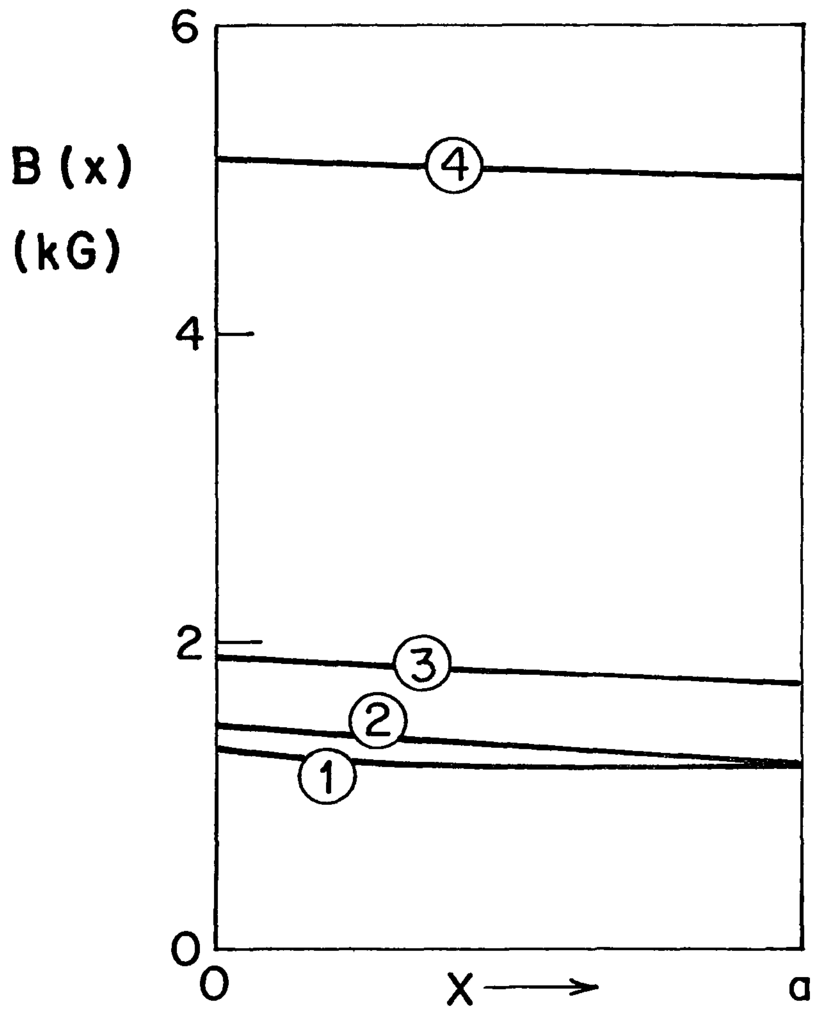

Figure 45: Calculated B(x) profiles for $H_{\parallel}$ = 1.2kG in VTi. $H_{\perp}$ = 0.5, 0.75, 1.5 and 5.0kG.

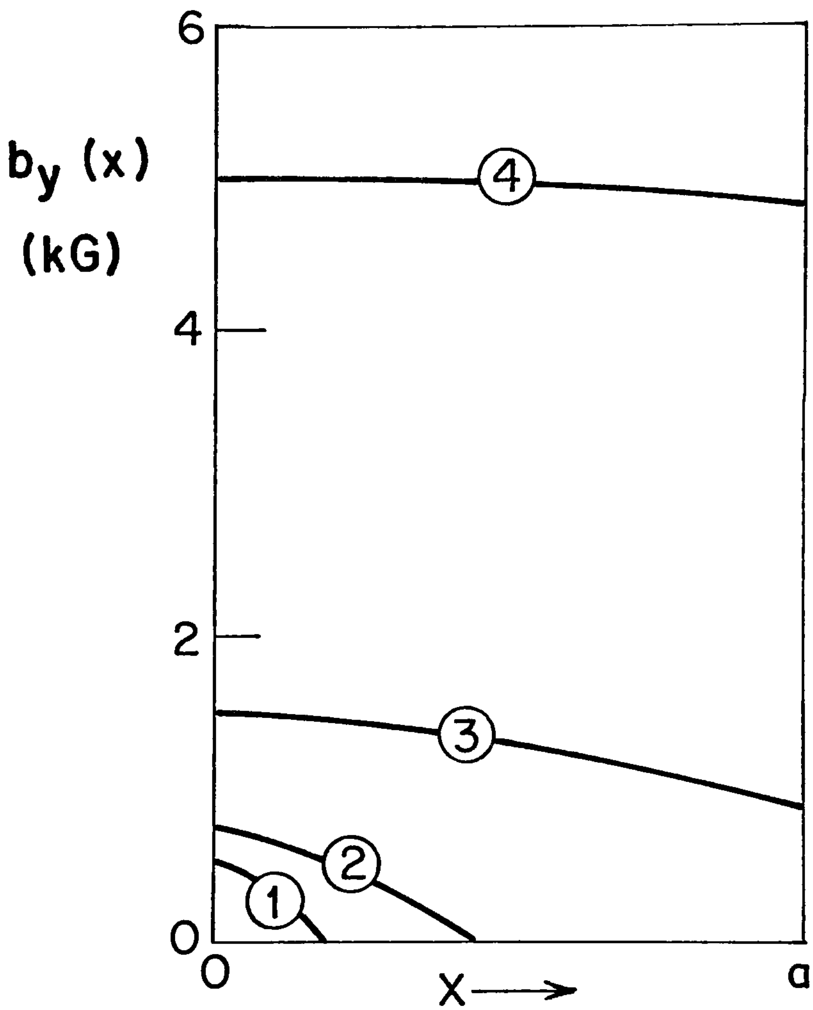

Figure 46: Calculated $b_y(x)$ profiles for $H_{//}$ = 1.2kG in VTi. $H_{\perp}$ = 0.5, 0.75, 1.5 and 5.0kG.

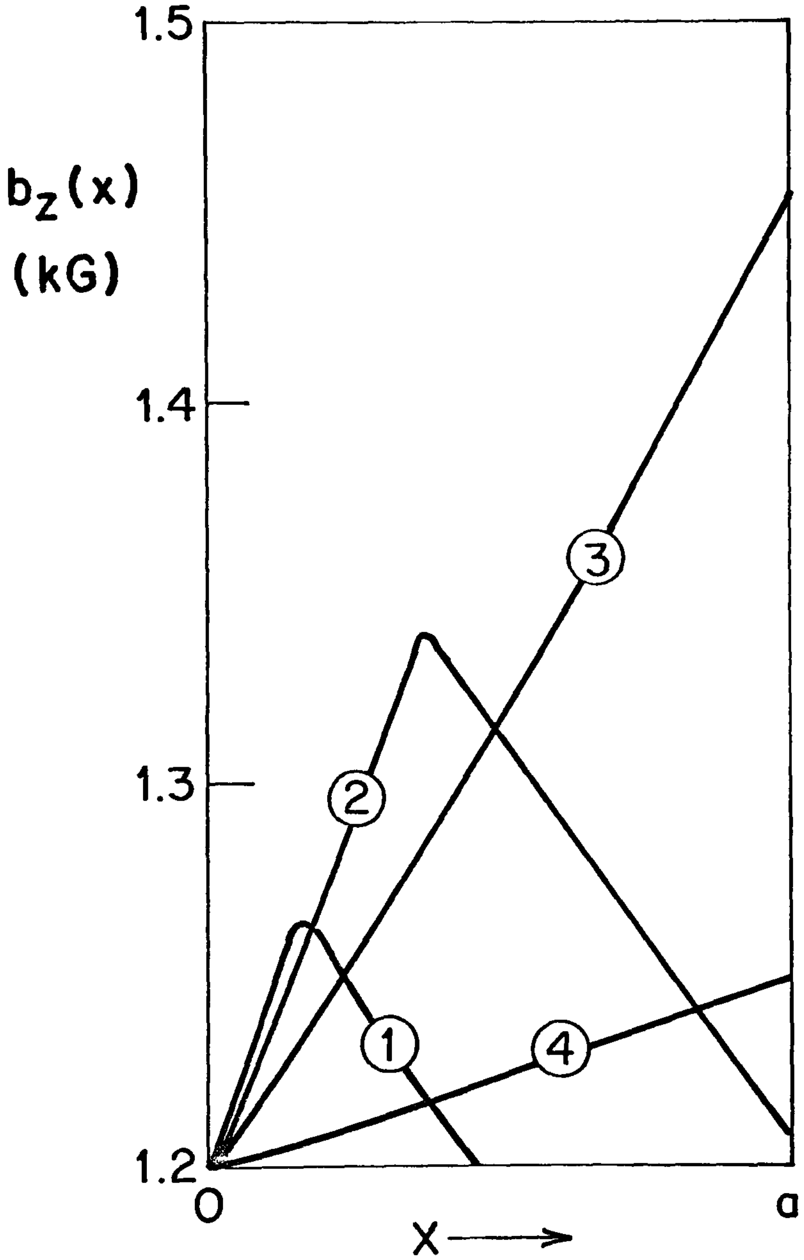

Figure 47: Calculated $b_z(x)$ profiles for $H_{//}$ = 1.2kG in VTi. $H_{\perp}$ = 0.5, 0.75, 1.5 and 5.0kG.

47 . We have examined a vast number of such profiles numerically generated in the course of the calculations and find that they confirm all the important features presented schematically in figures 28 and 29 . Unfortunately, to date there are no direct measurements available to verify whether these profiles are correct. The signals we register with our apparatus provide information only on the integrals of these profiles hence the detailed structure is hidden in the measurements. The kaleidoscopic structure and evolution of the profiles is nevertheless extremely interesting and contains a wealth of physical meaning which is indirectly probed by our investigations.

II Decreasing $H_{\perp}$

The slab becomes superconducting in a diagonally directed magnetic field i.e. initially $H_{\perp i} \neq 0$ and $H_{//} \neq 0$. The initial conditions are thus identical to that encountered above under I(b). The difference is that now $H_{\perp}$ is decreasing, usually down to zero, instead of being increased. The situation we now examine has expectedly many similarities with the former case. A logical extension of the situation we now examine is clearly the case where $H_{\perp}$ after being reduced to zero is then raised in the opposite direction. We will scrutinize this extension and other more complicated cases in the next section and in later sections.

We refer the reader to Figure 48 for aid in visualizing the sequence of events. In the present situation the magnitude of the applied field is being diminished, hence the B-profile rises from H_s at the surface to $H_{si} = (H_{\perp i}^2 + H_{//}^2)^{1/2}$ at a depth which we still denote by x_1. We continue to refer to this distance of penetration of the field disturbance as the front or leading edge of the B profile. In other words, at x_1, the region where $dB/dx \neq 0$ intersects with the region where $dB/dx = 0$.

Also in this case, the angle the applied field makes with the z axis is being reduced, hence the θ profile increases from θ_s at the surface to θ_{si} at a depth which we still denote by x_o. Again we refer to this distance of penetration of the angular disturbance as the front or leading edge of the θ-profile. In other words, at x_o, the region where $d\theta/dx \neq 0$ meets the region where $d\theta/dx = 0$.

As we have noted previously, $x_o < x_1$. Thus the front of the θ-profile "leads" the front of the B-profile with respect to the surface. This important feature is a consequence of the empirical prescription we exploit to describe the rotation of the vortices. This statement is proven rigorously for a specific case in appendix II and is verified throughout our detailed computations. We use the subscripts 1 and 0 to characterize the various quantities at the positions x_1 and x_o respectively.

It is still useful to introduce two benchmarks in the sequence of profiles: H_s^*, the applied field when the field disturbance

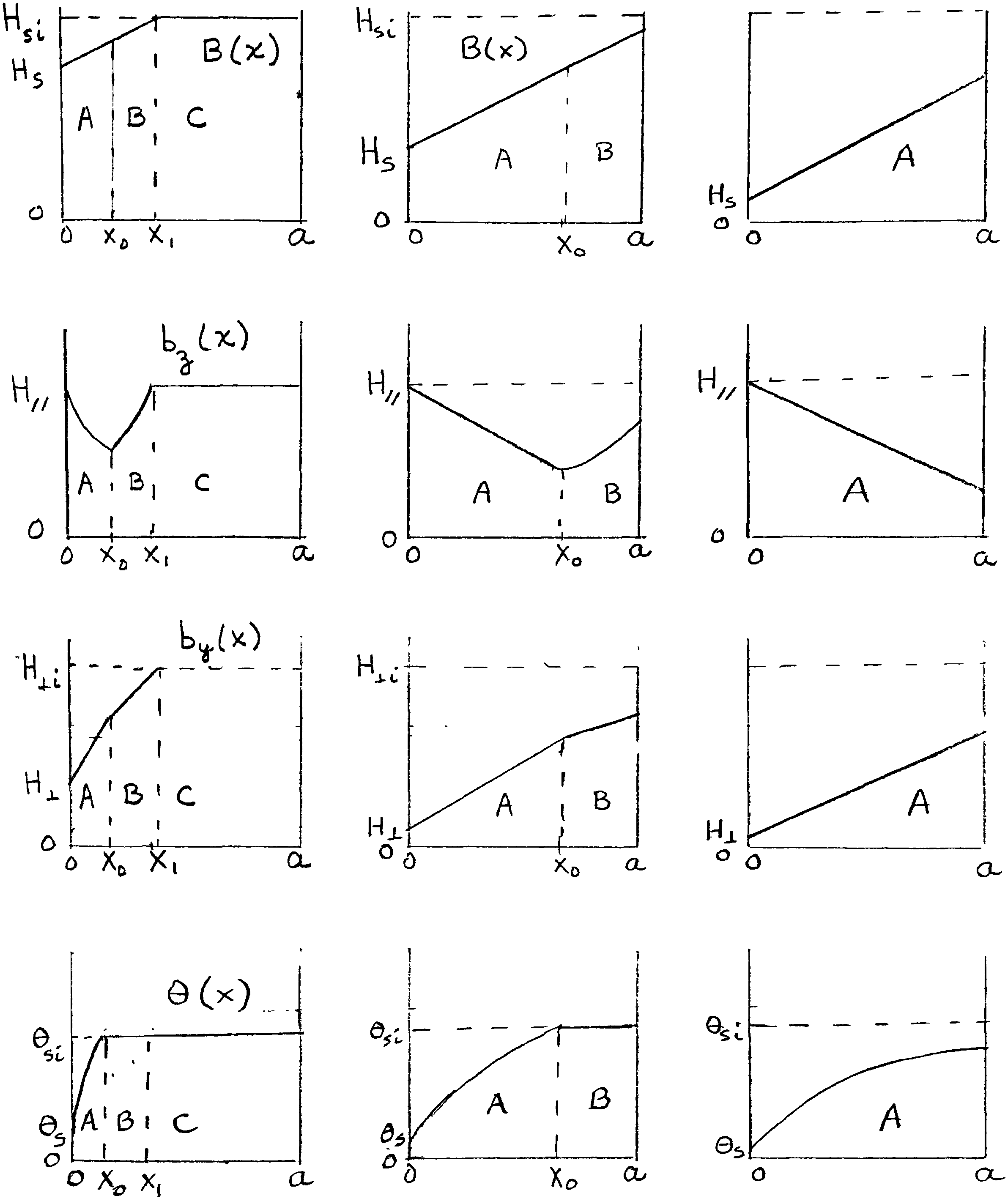

Figure 48: Sequence of magnetic induction and angular profiles as $H_{\perp}$ is reduced from $H_{\perp i} > 0$.

arrives at the mid-plane and θ^{**}_s , the direction of the applied field when the angular disturbance reaches the center of the slab. In brief, the arrival of the front of the B profile at the center and the subsequent arrival of the front of the θ profile are denoted by using one and two asterisks respectively as superscripts to the various quantities of interest.

The sequence of the B, b_z, b_y and θ profiles we now encounter as H_s is reduced are essentially mirror images of the corresponding profiles when H_s was increased with $H_{\perp i} \neq 0$ provided that $H_{\perp i}$ is sufficiently large so that $H_{\perp}$ can be decreased below $H^{**}_{\perp}$ without reaching the value zero (i.e. $0 \leq H^{**}_{\perp} < H_{\perp i}$ or $H_{//} \leq H^{**}_s < H_{si}$). The mirror in each case consists of the initial profile of the particular quantity. This similarity emerges from a comparison of Figures 29 and 48 . Thus as H_s is swept through H^*_s and then H^{**}_s , the regions discussed in section I(ii) above evolve in a completely analogous manner: region A grows continuously until $H_s = H^{**}_s$, region B grows until $H_s = H^*_s$ then diminishes to zero when $H_s = H^{**}_s$ whereas region C shrinks continuously and vanishes when $H_s = H^*_s$.

It is helpful to examine briefly the salient features of these three regions by considering the first stage of the sequence of events where $H^*_s \leq H_s < H_{si}$.

A) $0 < x \leq x_o$

In this region the direction of the vortices varies from θ_s at the surface to θ_{si} at x_o and presumably their orientation is governed by the empirical rule we have proposed (equation 6-8). This region is filled with induced currents attempting to oppose the exit of the flux lines as H_s is decreased. The configuration of $\vec{j}$ and $\vec{B}$ here is partially force free since the angle between $\vec{j}$ and $\vec{B}$ lies between 0 and $\pi/2$. As a consequence of this arrangement, the profile of b_y is steeper and the corresponding current density is greater than would occur in the critical state with $H_{//} = 0$ for a comparable range of B. This state of affairs is responsible for the enhancements in the transverse component of the magnetization which are observed.

Looking at the situation in the light of the expression $b_z(x) = H_{//}(H_s/B(x))^k$ and noting that $B(x) > H_s$ we see that the b_z profile decreases from $H_{//}$ at the surface to a minimum at x_o. This minimum is greater than zero since $H_s > H_{//} \neq 0$ and $B(x) < \infty$. We also indicate an interesting feature in the sequence of b_z profiles. In both the situations where H_s is decreasing or increasing, successive b_z profiles fall below the preceding one as x_o penetrates to the mid plane and as H_s is varied beyond H_s^{**}. This feature emerges from a careful consideration of the expression $b_z(x) = H_{//}(H_s/B(x))^k$ and the convex upwards critical state behaviour of B(x). It is a consequence of this feature in the sequence of b_z profiles that the longitudinal magnetization generated by our model exhibits a "resonance" for H_s increasing and displays a monotonic increase to a maximum as $H_\perp$ is lowered to zero.

This region expands until it occupies the entire half slab at $H_s = H_s^{**}$. At this stage and subsequently as H_s is decreased further, none of the vortices threading the slab are oriented in the original direction θ_{si}.

B) $x_o \leq x \leq x_1$

In this region as H_s decreased the vortices have been "decompressed" i.e.($B(x) < H_{si}$) while retaining the original orientation θ_{si}. As a consequence of the decompression $b_z(x) < H_{//}$ and $b_y(x) < H_{\perp i}$. Because the initial orientation is preserved $b_y(x) / b_z(x) = H_{\perp i}/H_{//}$. The induced currents generated to oppose the exit of the flux flow perpendicularly to $\vec{B}$. This region moves inward and expands until $H_s = H_s^*$ then shrinks as H_s decreases further and vanishes when $H_s = H_s^{**}$.

C) $x_1 \leq x \leq a$

This is an "inert" region where the density and the direction of the vortices is undisturbed from the original configuration. No currents flow in this volume and its domain contracts as x_1 advances to disappear when $H_s = H_s^*$.

Results and Discussion

Proceeding as outlined in section I above we have carried out computer calculations of the evolution of both the longitudinal and transverse components of the magnetization as the transverse component of the applied field is reduced to zero for several values of $H_{//}$ chosen to correspond to that used in our measurements. The results of these computations and the corresponding experimental curves for both our NbTi and VTi samples are presented in the next pages in a manner which permits a detailed comparison yet avoids cluttering up the various figures.

Again we note that an open surface can be constructed from a

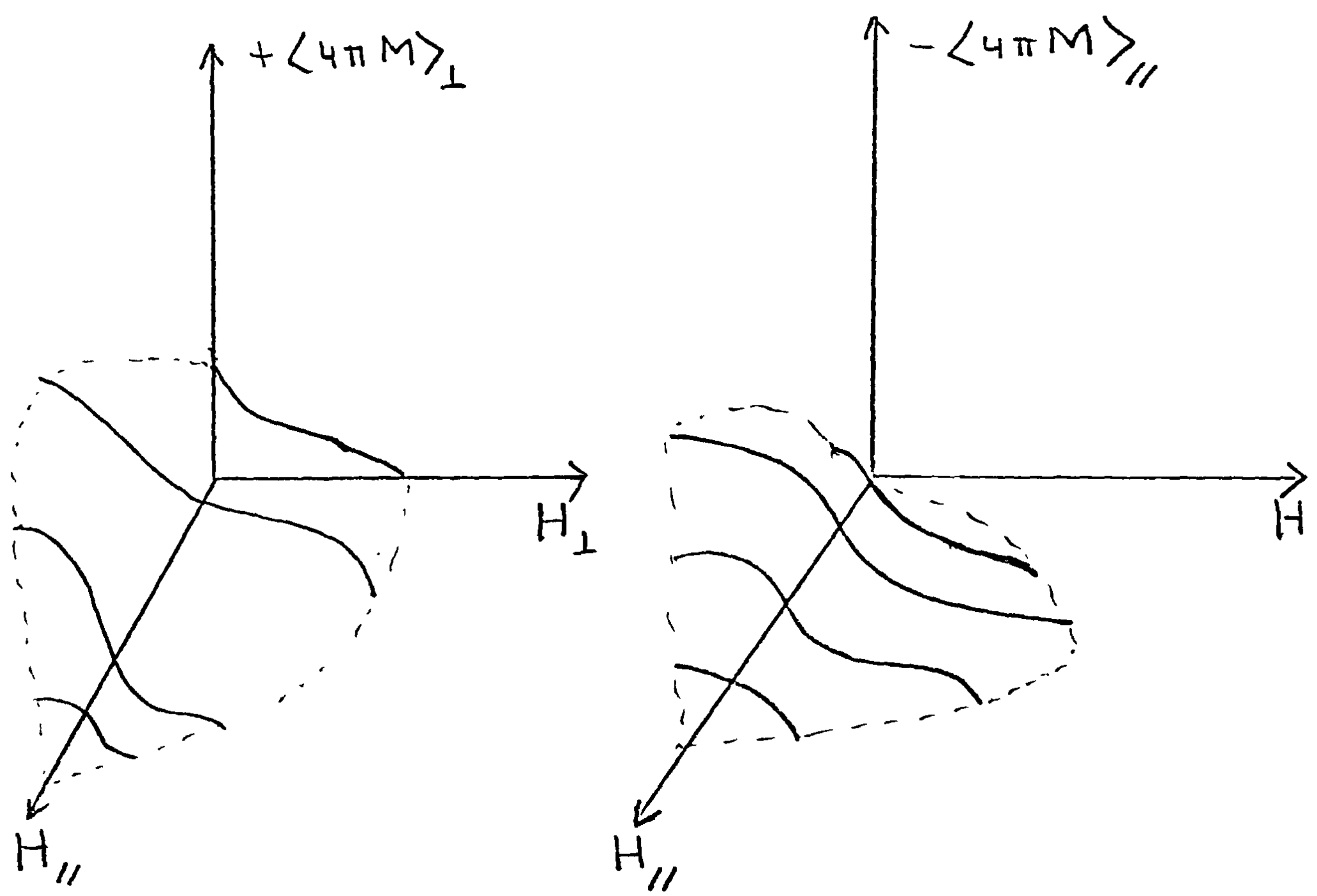

juxtaposition of the experimental or calculated curves for each component of the magnetization in the $H_{//}$ - $H_{\perp}$ plane. The two surfaces mapped out with $H_{\perp}$ decreasing are sketched schematically above.

The figures presented in the following pages (Figures 49 through 52 for the NbTi sample and Figures 57 through 64 for the VTi sample) test the ability of the vortex rotation model we propose to generate surfaces in $M_{\perp}$ - $H_{\perp}$ - $H_{//}$ and $M_{//}$ - $H_{\perp}$ - $H_{//}$ spaces (where $H_{\perp}$ is decreasing) which overlap or match those observed for each specimen. These two additional surfaces are related to but nevertheless physically different from the surfaces generated with $H_{\perp}$ increasing discussed in the previous section.

To illustrate typical sequences of profiles quantitatively we present two sets of series of computed profiles in Figures 53-56 and 65-68. These calculated profiles corroborate the schematic sketches presented in Figure 48 and are included for completeness. Myriads of such profiles are generated and integrated in the computer calculations of the families of curves (surfaces) spawned by the model as presented in the following pages.

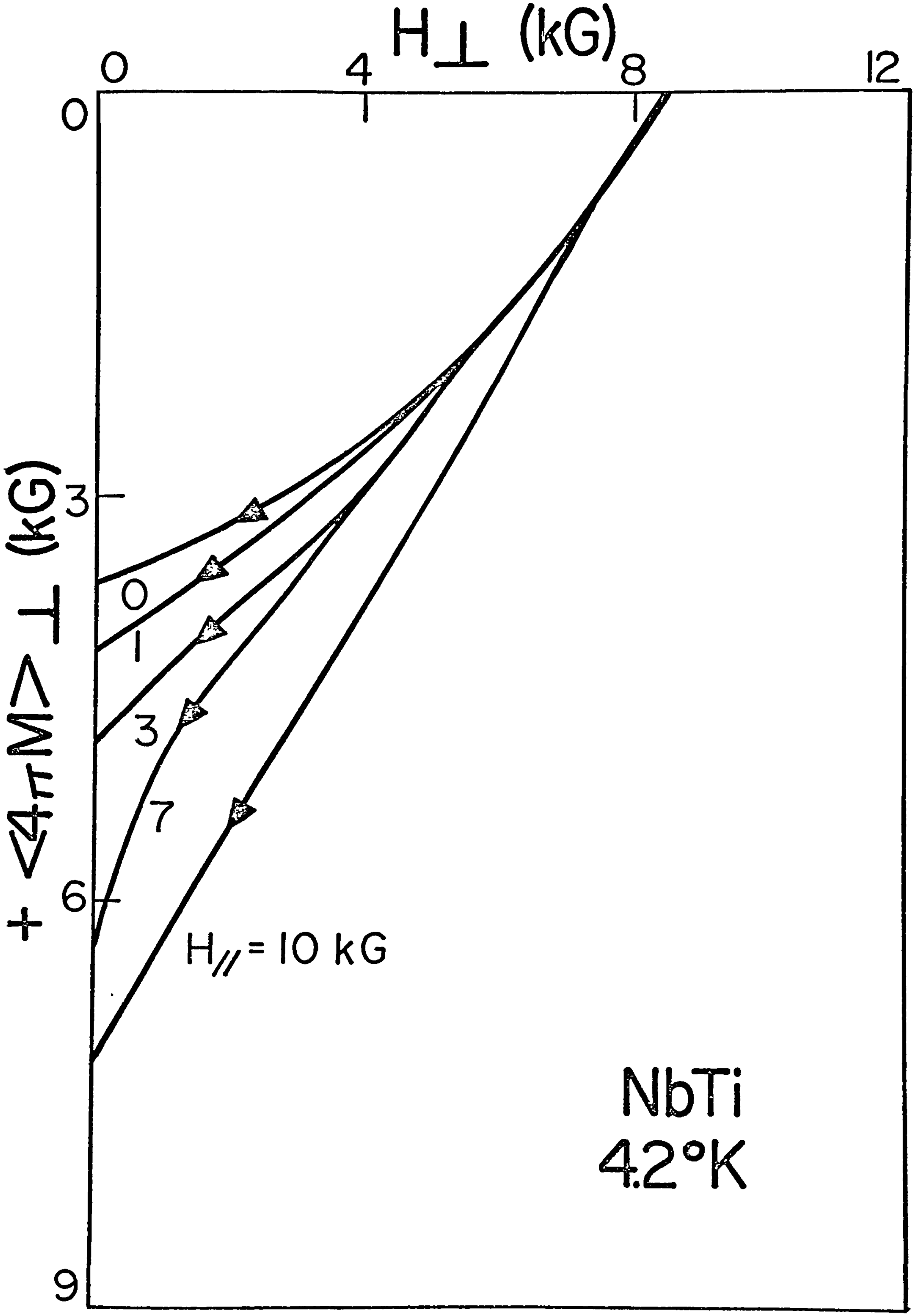

Figure 49: Experimental values for $<4\pi M>_{\perp}$ versus $H_{\perp}$ for NbTi. ($H_{\perp}$ decreasing).

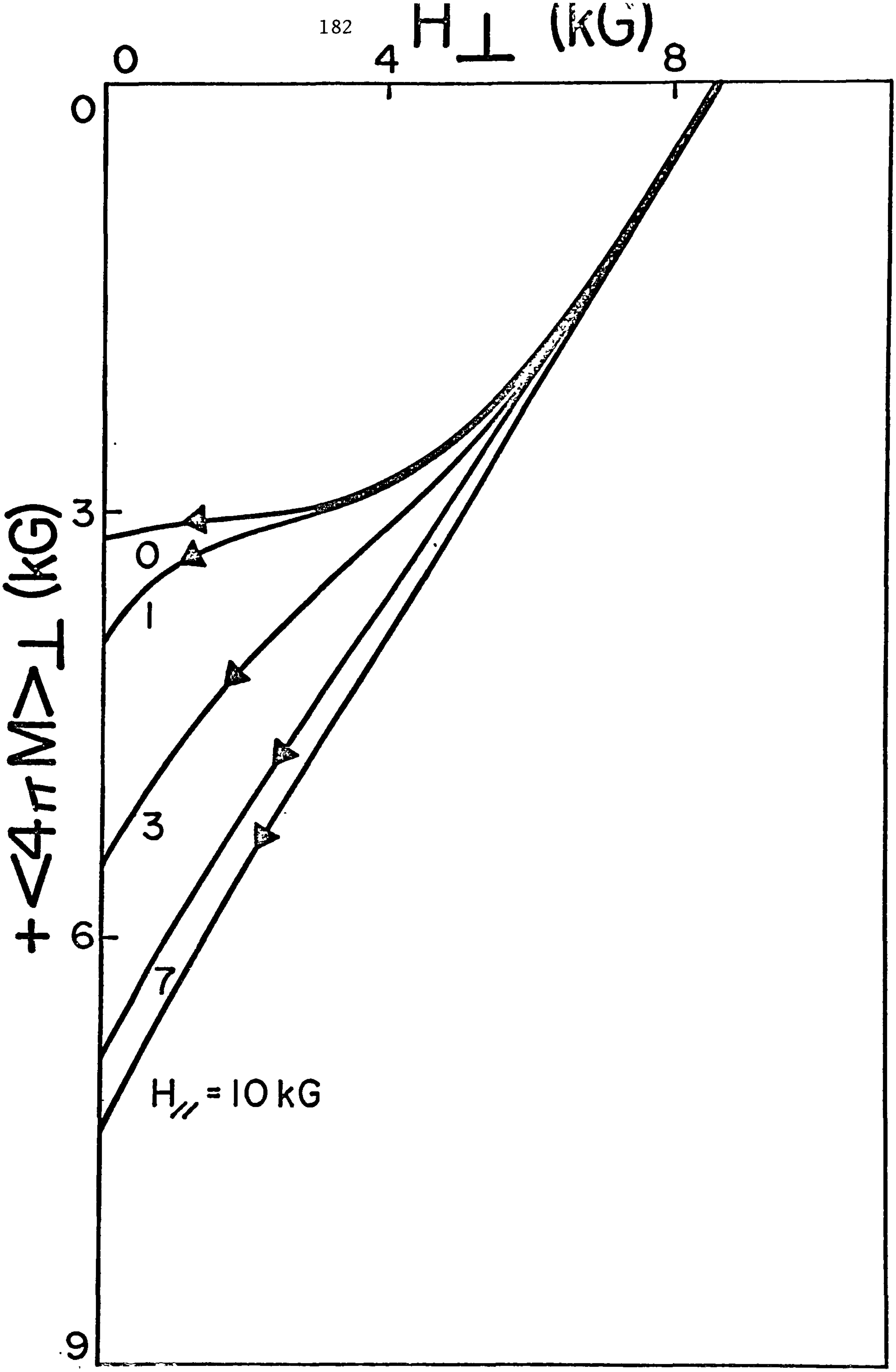

Figure 50: Values of $\langle 4\pi M\rangle_\perp$ versus $H_\perp$ calculated for NbTi according to vortex rotation model.

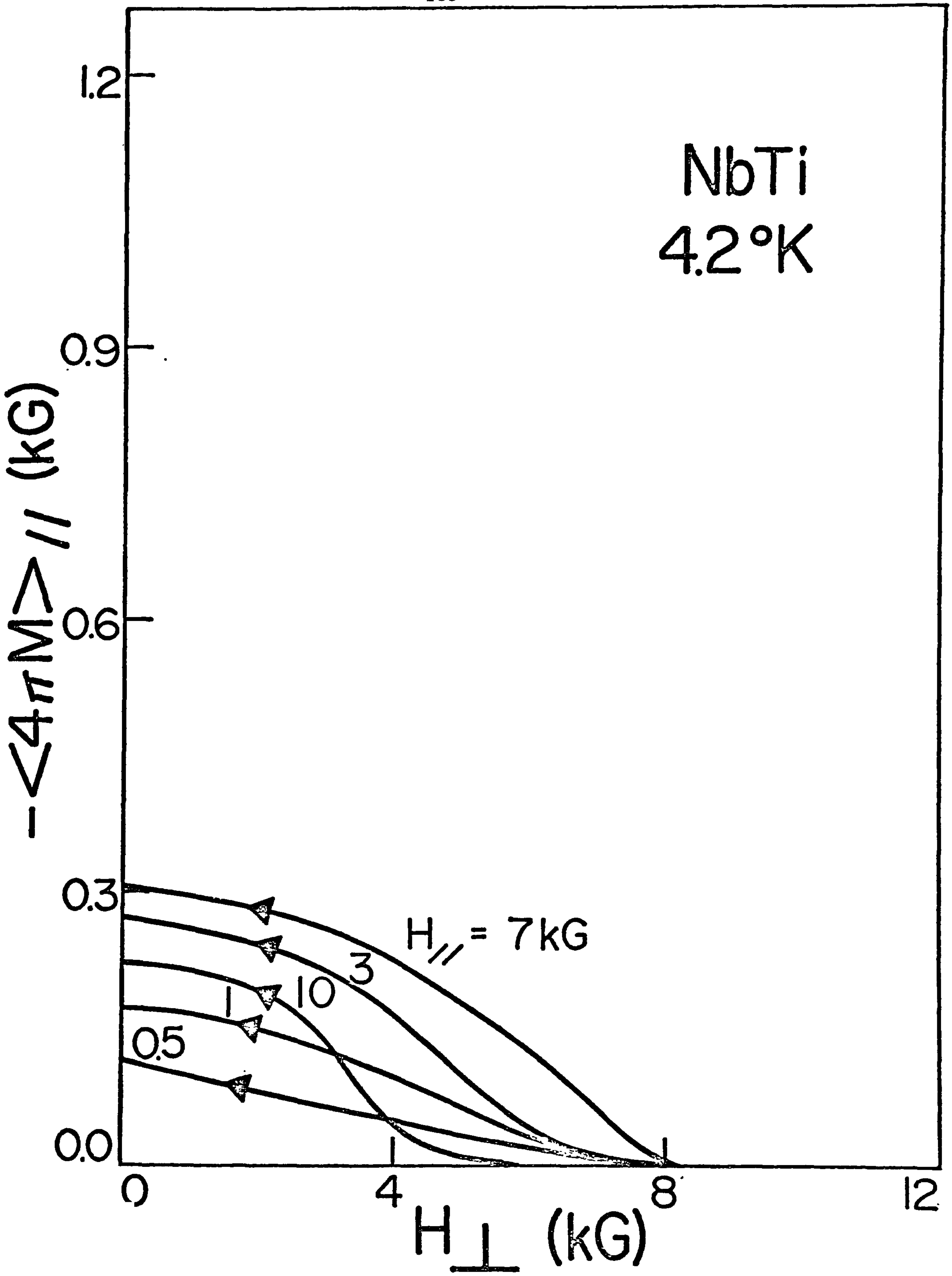

Figure 51: Experimental values of $\langle 4\pi M\rangle_{//}$ versus $H_\perp$ for NbTi. ($H_\perp$ decreasing).

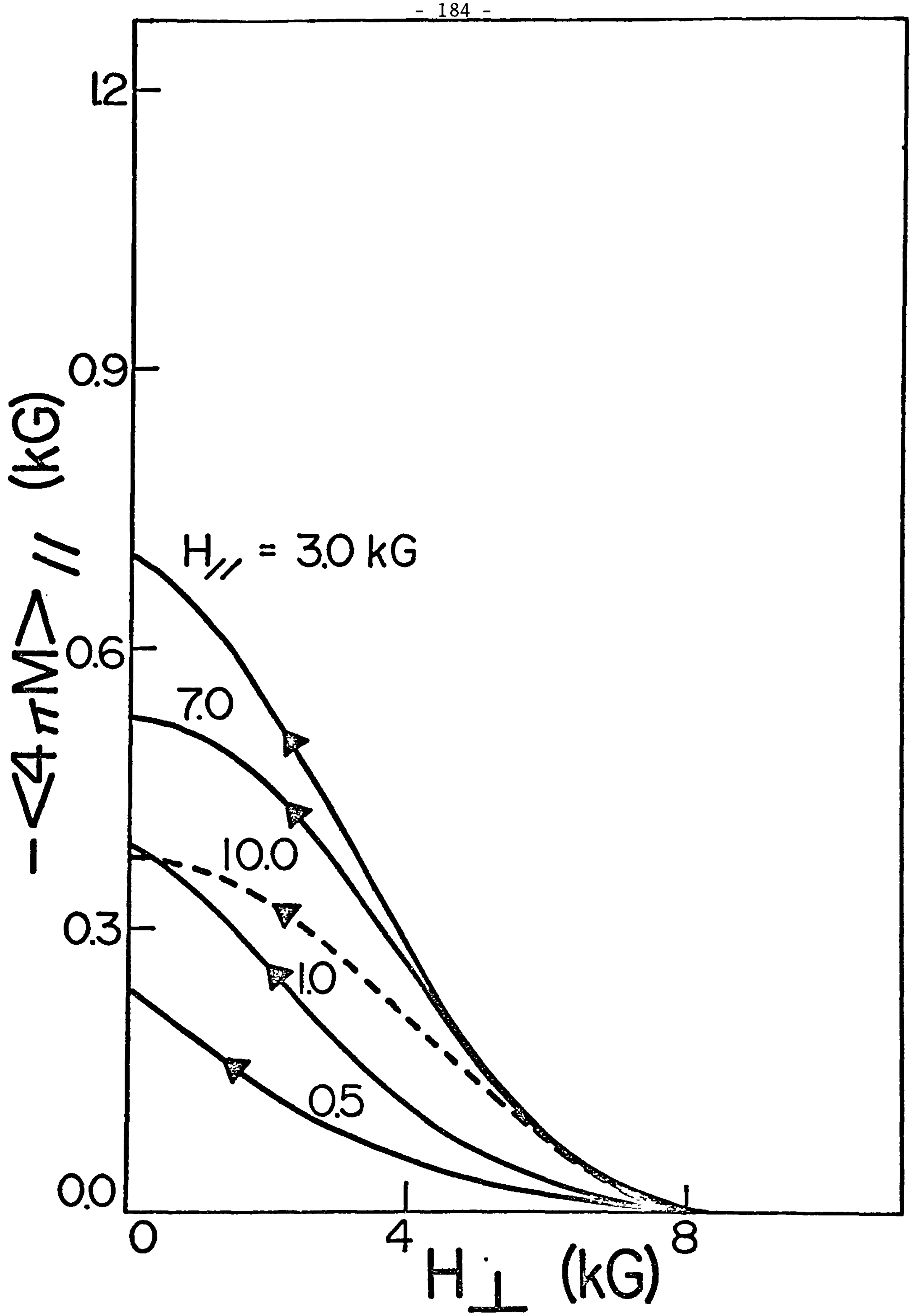

Figure 52: Values of $\langle 4\pi M\rangle_{//}$ versus $H_{\perp}$ calculated for NbTi according to vortex rotation model.

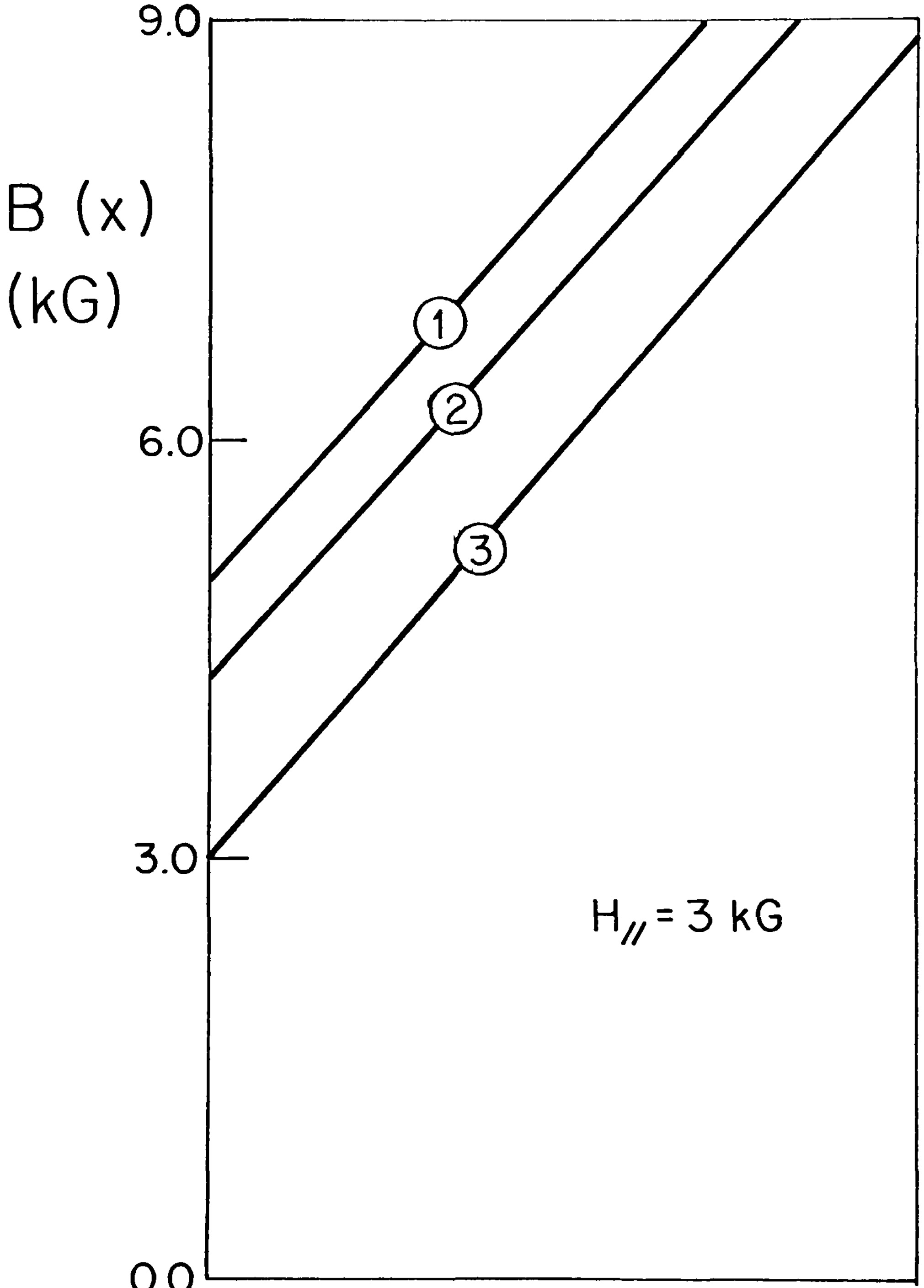

Figure 53: Calculated B(x) profiles for $H_{//}$ = 3kG in NbTi. $H_{\perp}$ = 4, 3 and 0kG for 1, 2 and 3 respectively.

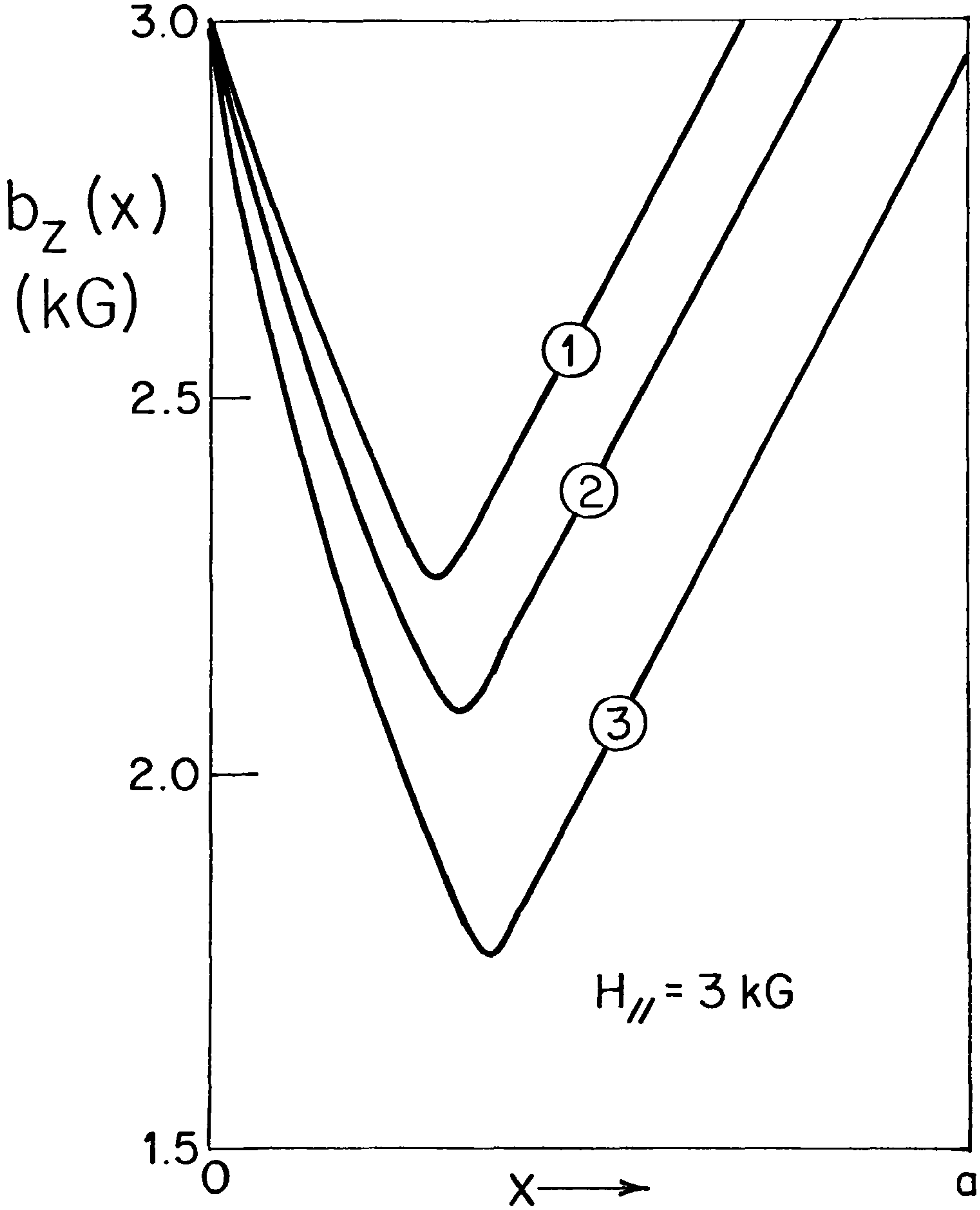

Figure 54: Calculated $b_z(x)$ profiles for $H_{//} = 3$kG in NbTi. $H_{\perp} = 4$, 3 and 0kG for 1, 2 and 3 respectively.

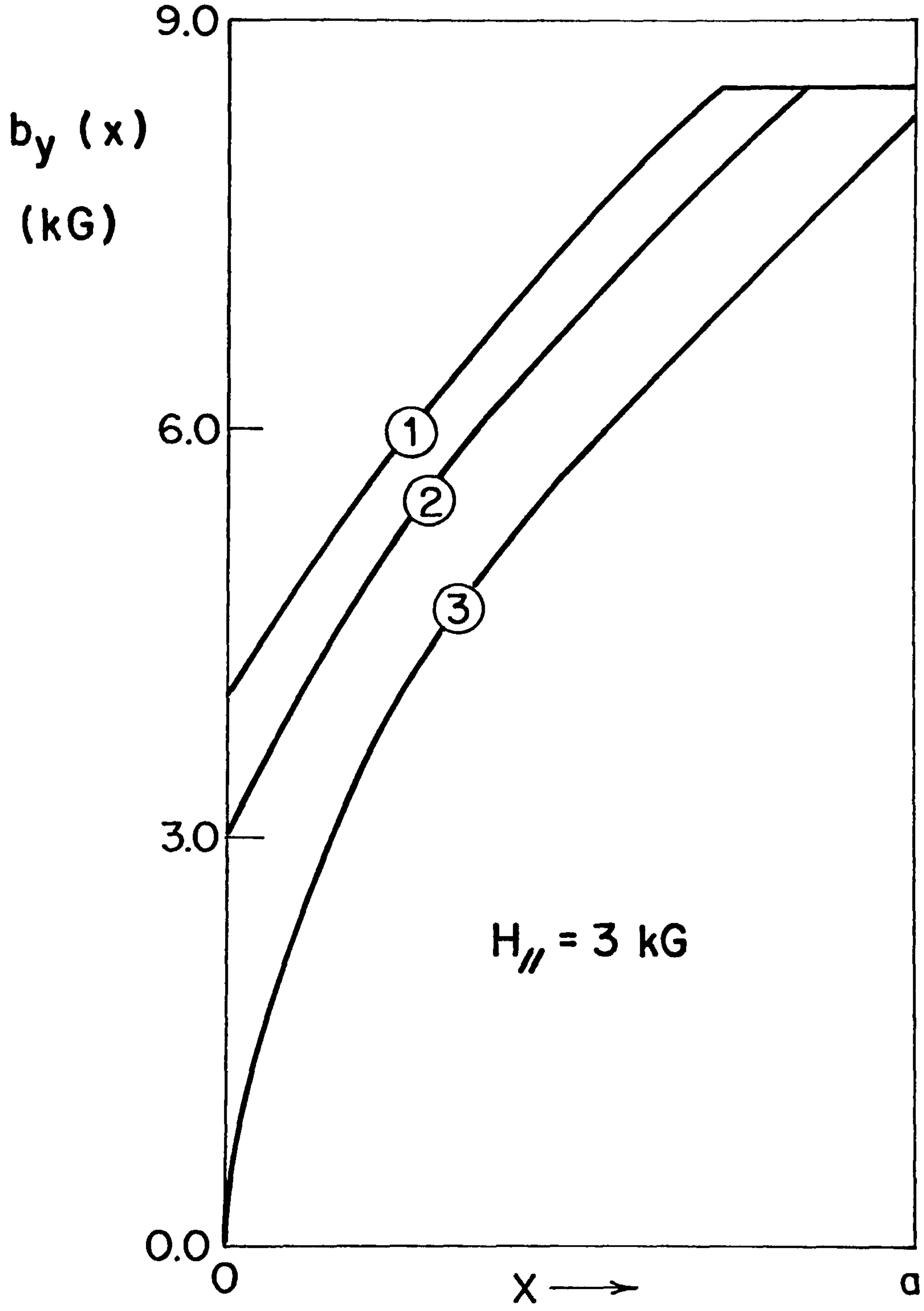

Figure 55: Calculated $b_y(x)$ profiles for $H_{//}$ = 3kG in NbTi. $H_{\perp}$ = 4, 3 and 0kG for ①, ② and ③ respectively.

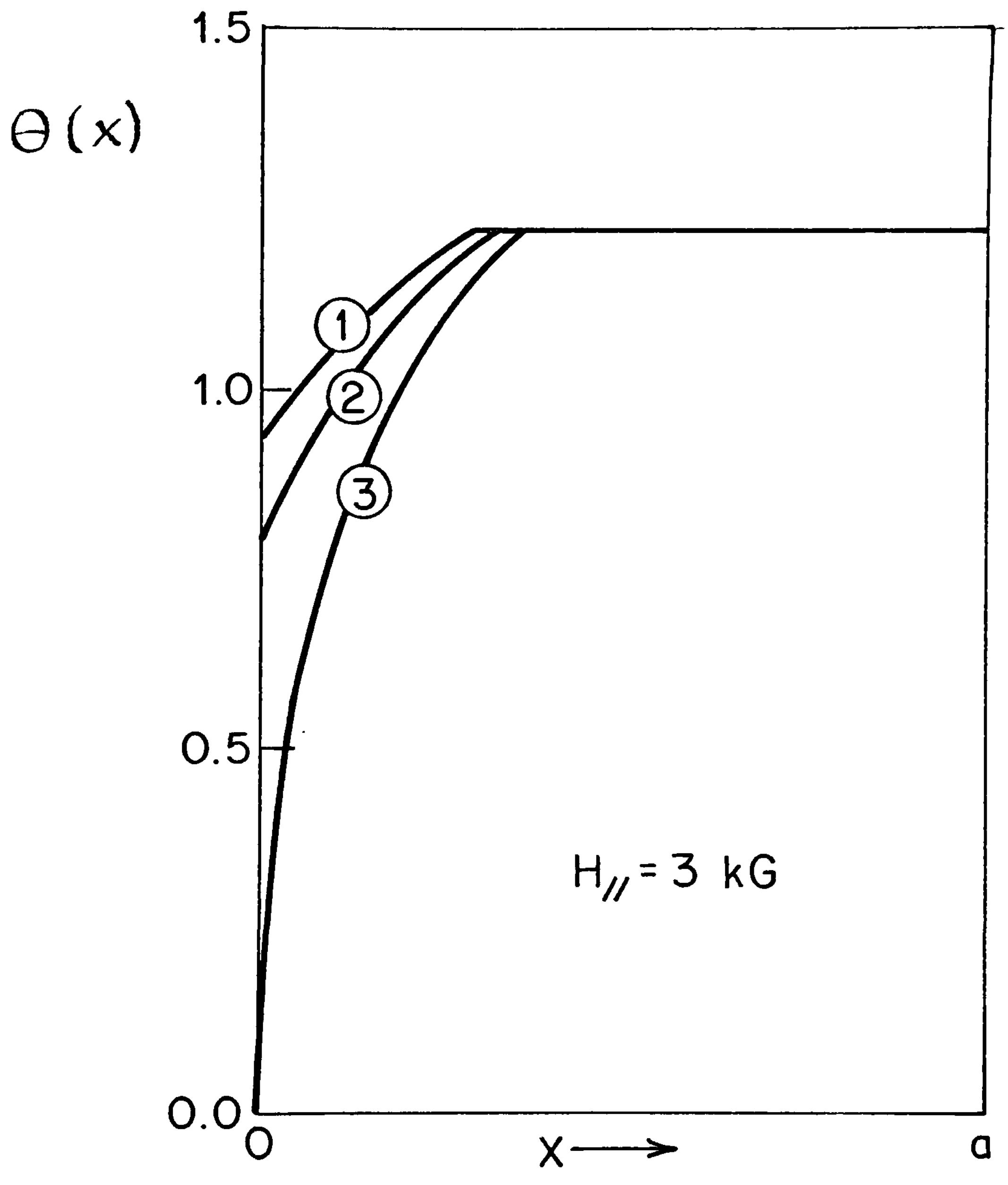

Figure 56: Calculated $\theta(x)$ profiles for $H_{//}$ = 3kG in NbTi. $H_{\perp}$ = 4, 3 and 0kG for ①, ② and ③ respectively.

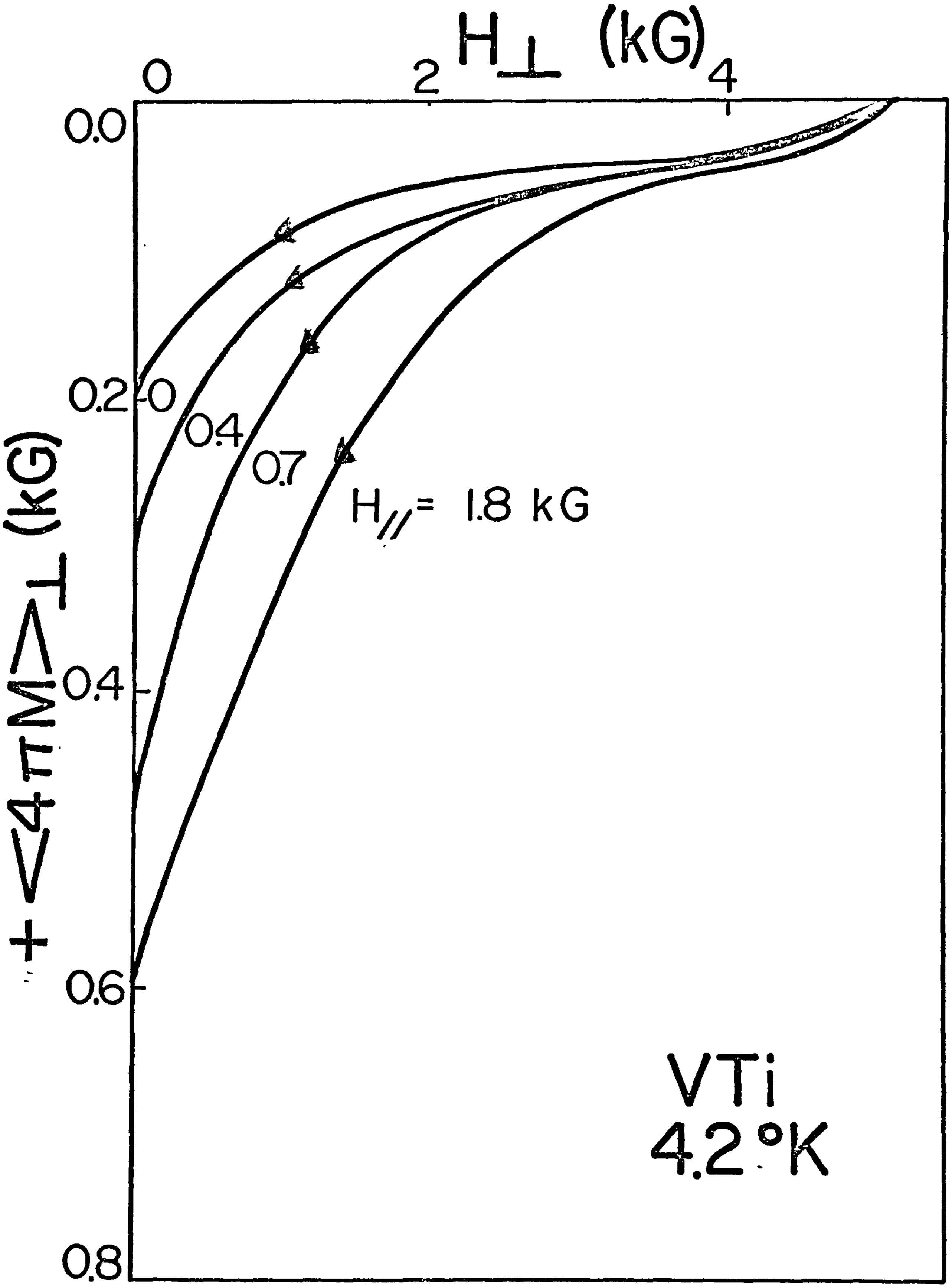

Figure 57: Experimental values of $\langle 4\pi M\rangle_\perp$ versus $H_\perp$ for VTi. ($H_\perp$ decreasing).

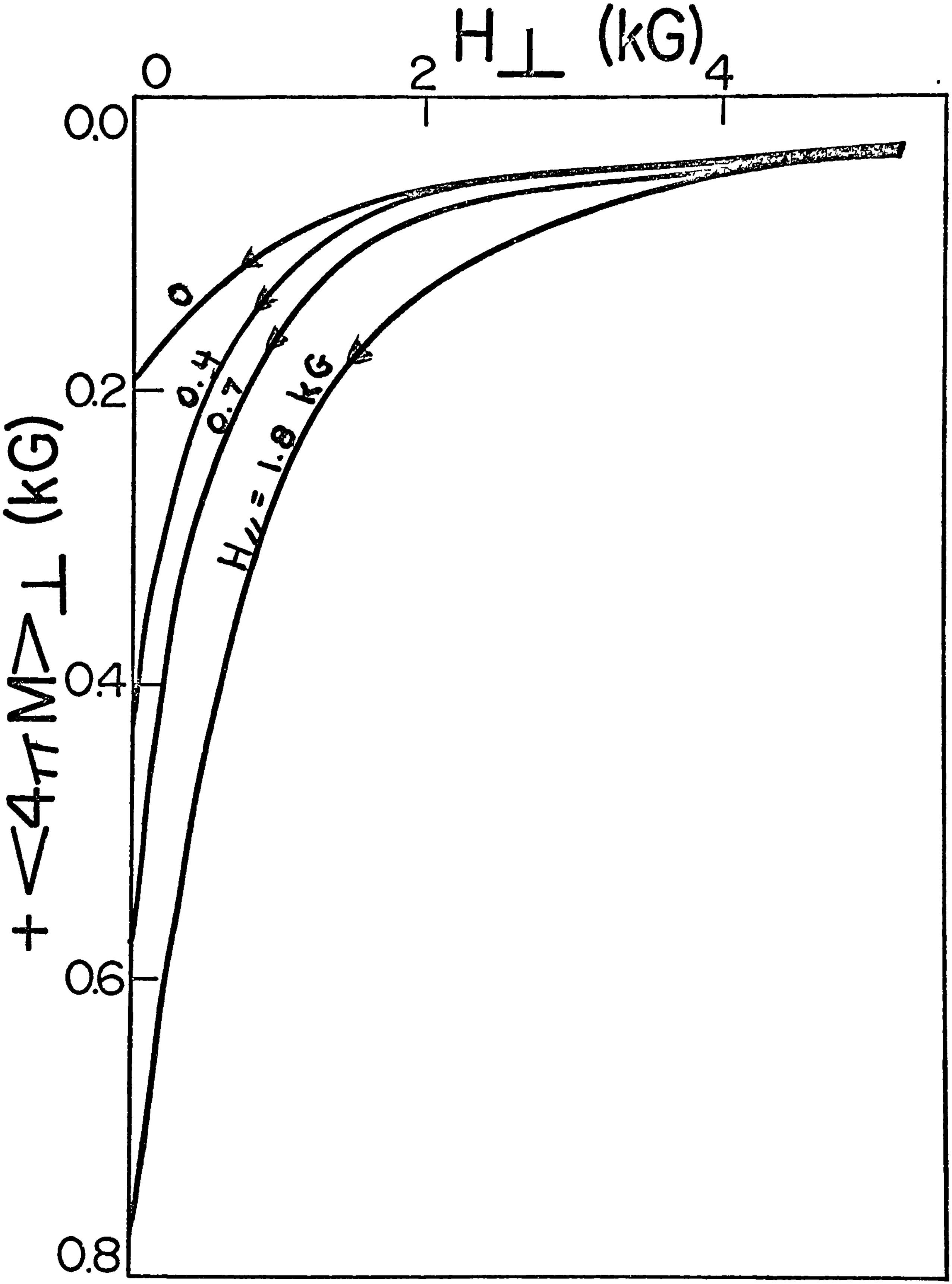

Figure 58: Values of $\langle 4\pi M\rangle_{\perp}$ versus $H_{\perp}$ calculated for VTi according to vortex rotation model.

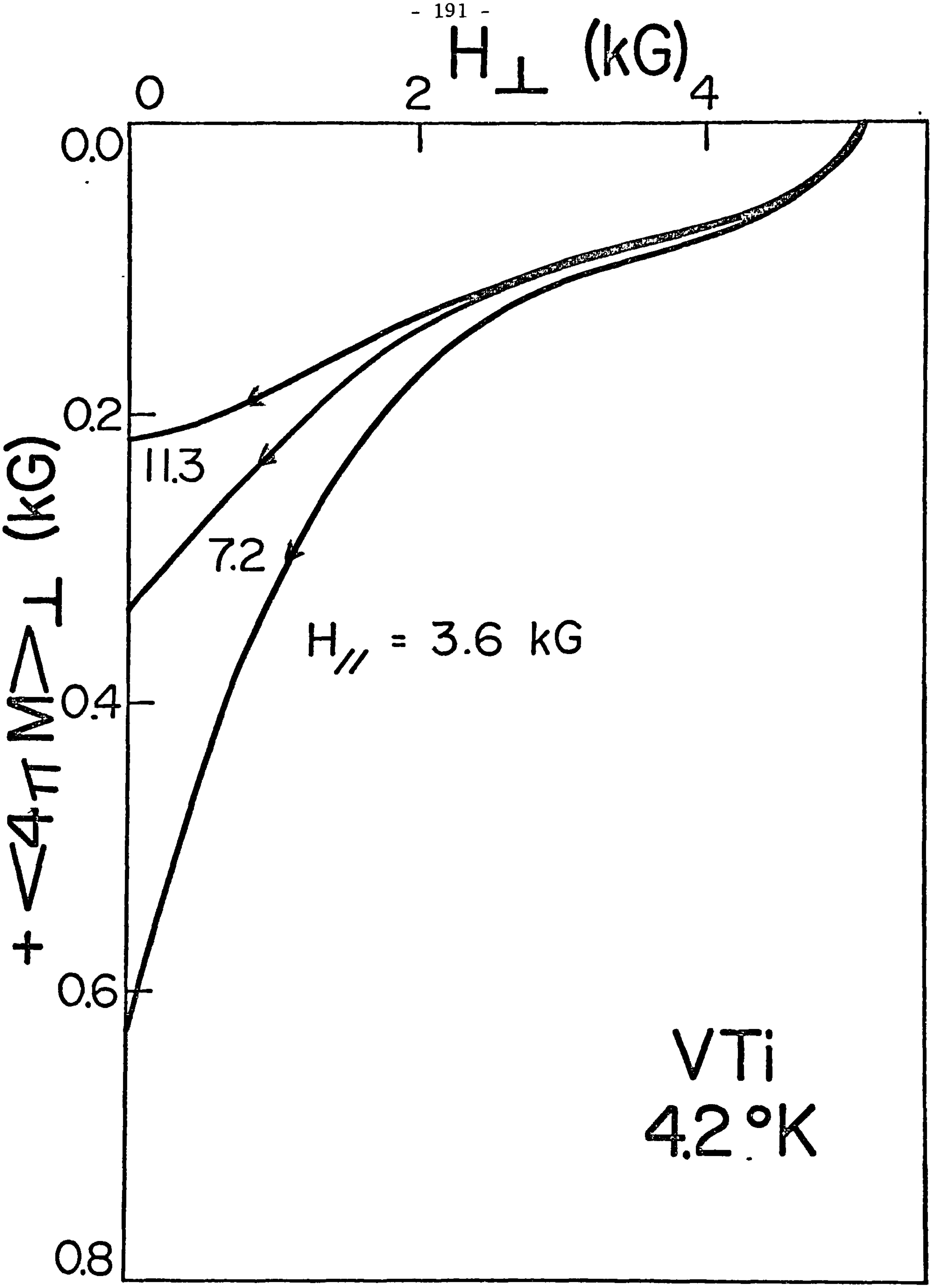

Figure 59: Experimental values of $\langle 4\pi M\rangle_\perp$ versus $H_\perp$ for VTi. ($H_\perp$ decreasing).

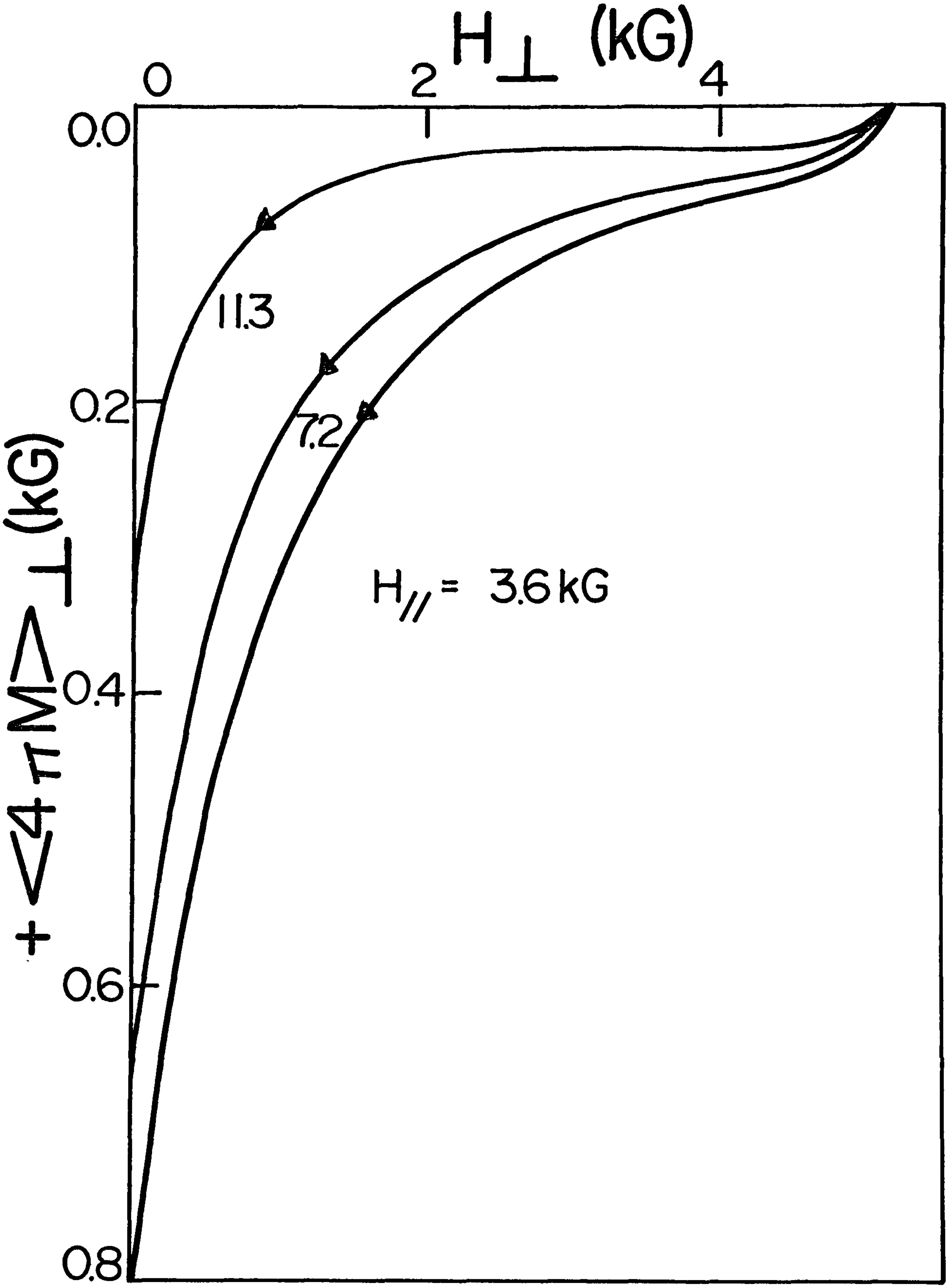

Figure 60: Values of $<4\pi M>_{\perp}$ versus $H_{\perp}$ calculated for VTi according to vortex rotation model.

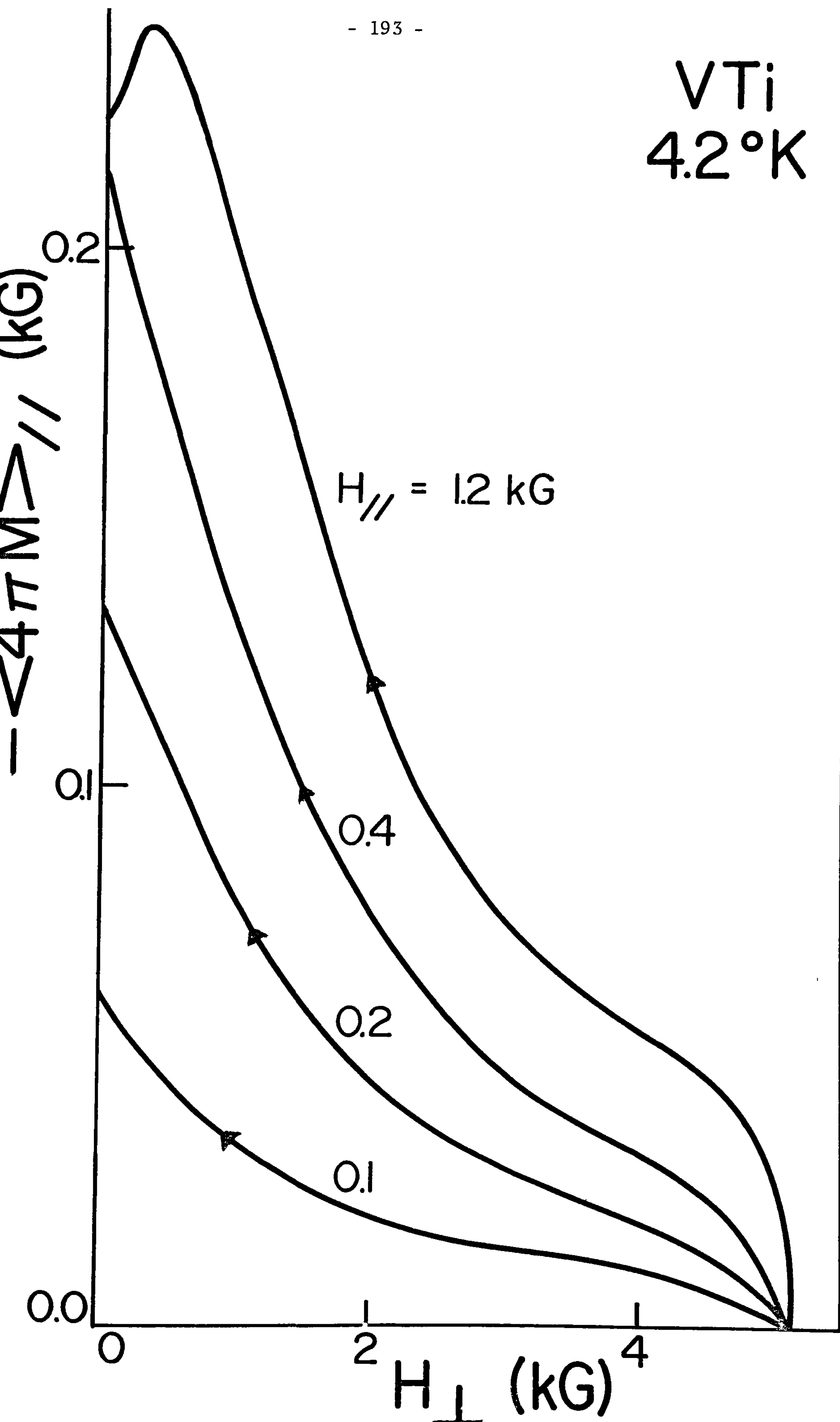

Figure 61: Experimental values of $\langle 4\pi M \rangle_{//}$ versus $H_{\perp}$ for VTi

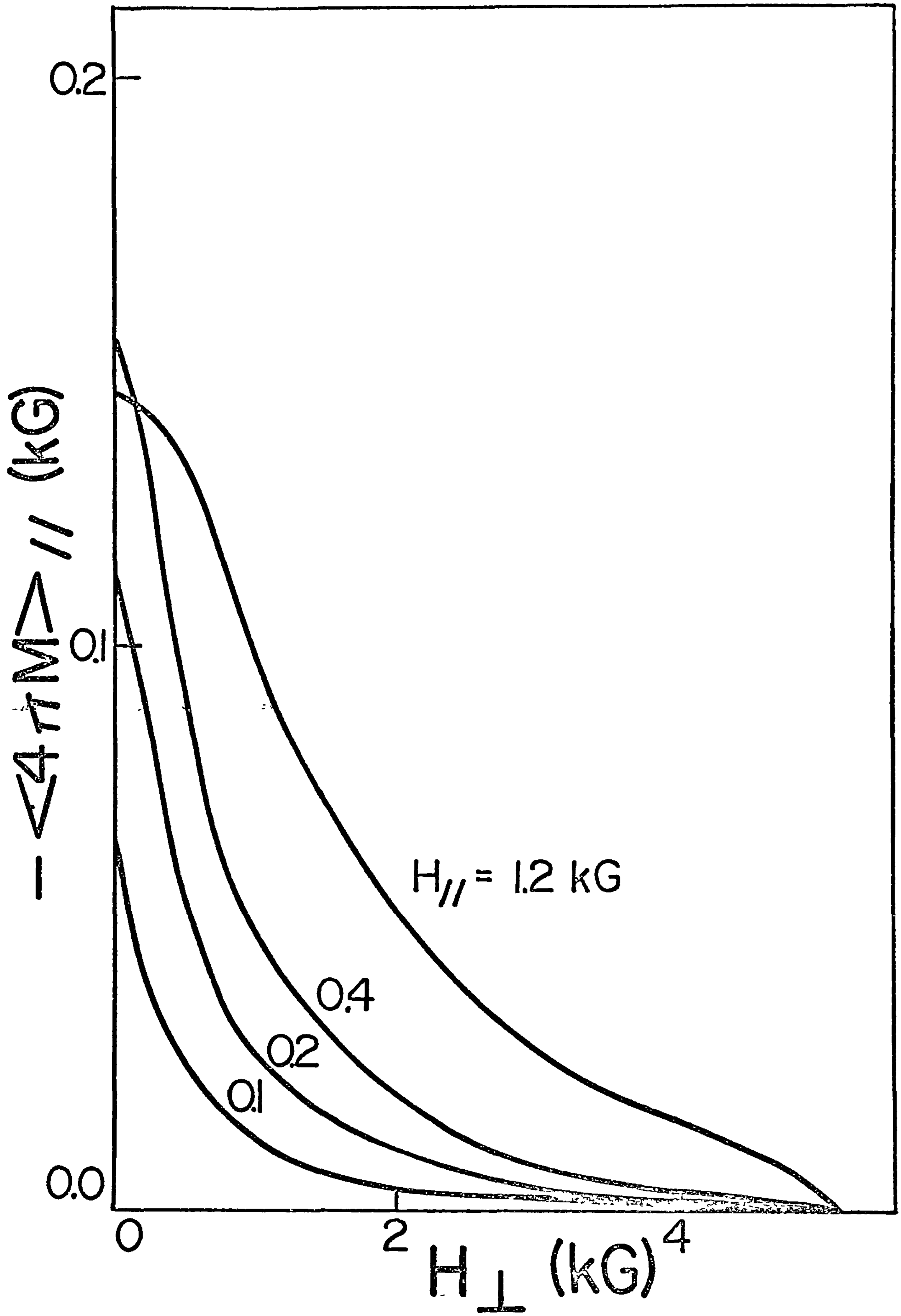

Figure 62: Values of $\langle 4\pi M\rangle_{//}$ versus $H_{\perp}$ calculated for VTi according to vortex rotation model.

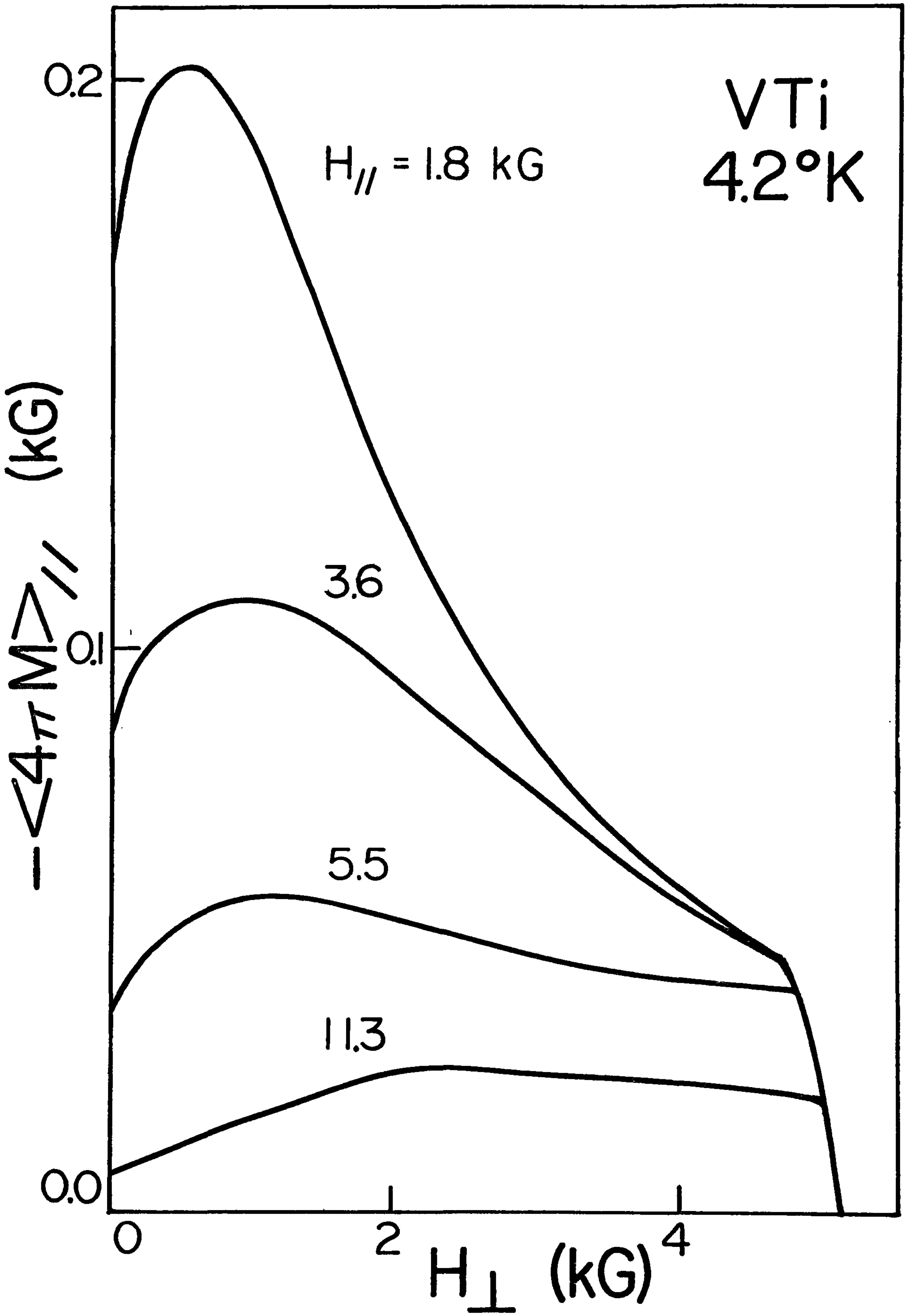

Figure 63: Experimental values of $\langle 4\pi M \rangle_{//}$ versus $H_\perp$ for VTi ($H_\perp$ decreasing).

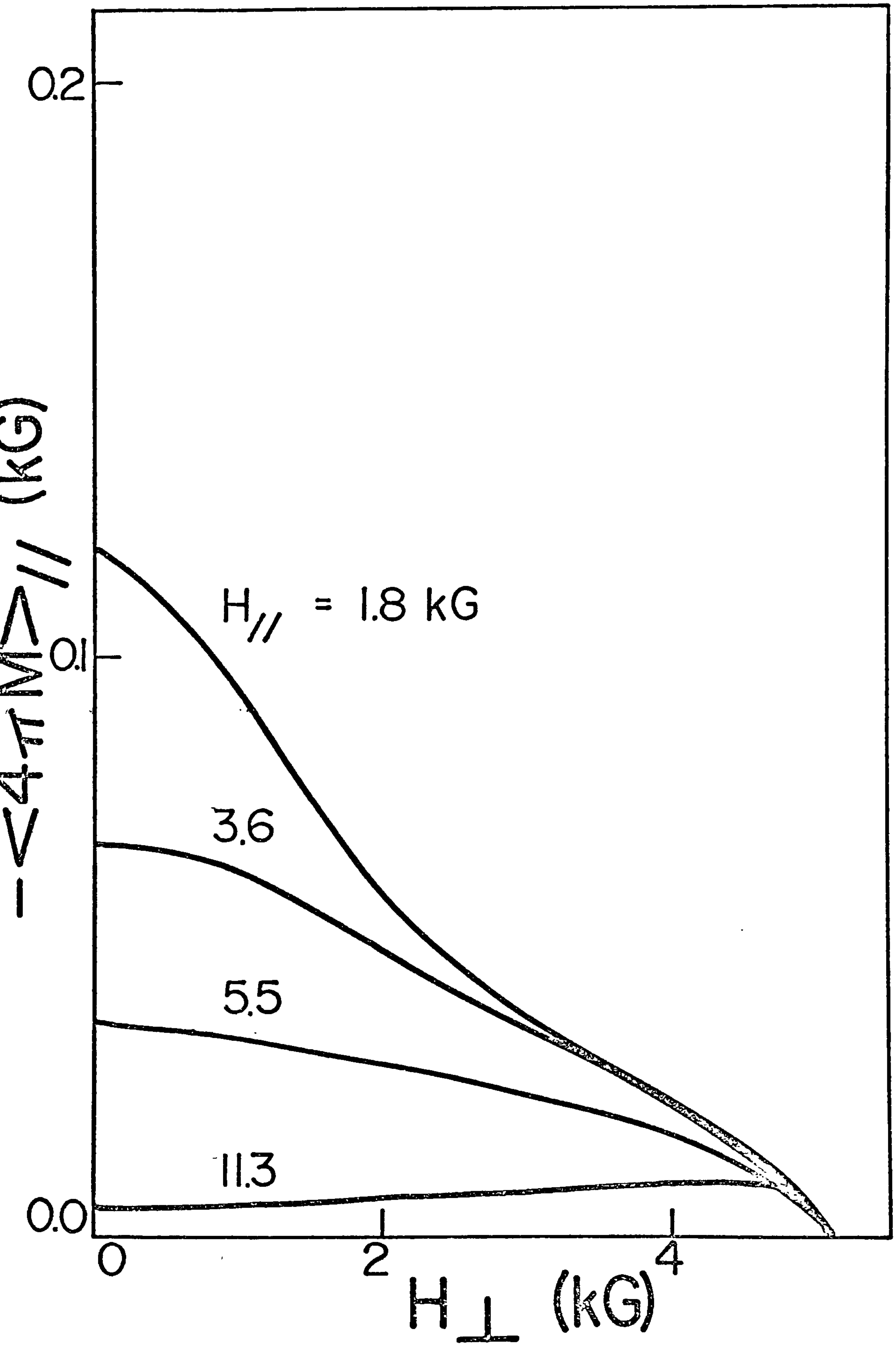

Figure 64: Values of $\langle 4\pi M \rangle_{//}$ versus $H_{\perp}$ for VTi according to vortex rotation model.

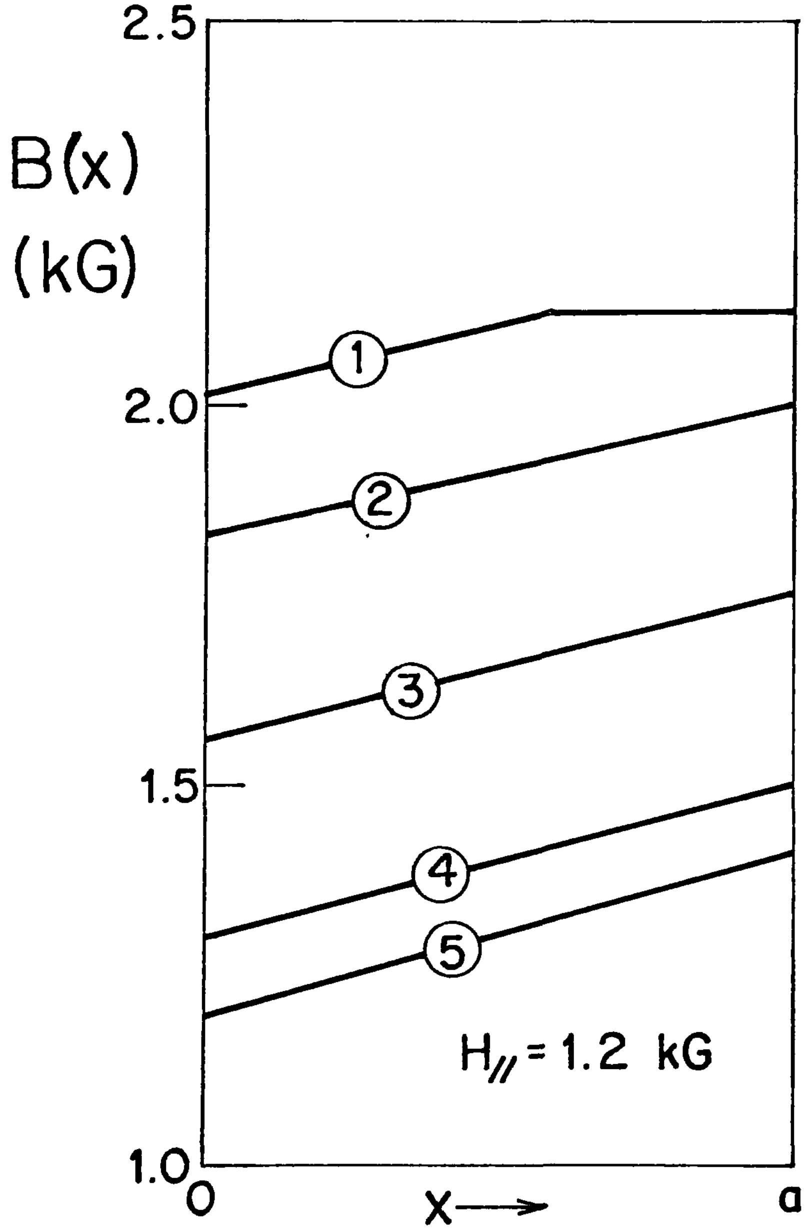

Figure 65: Calculated B(x) profiles for $H_{//}$ = 1.2kG in VTi. $H_{\perp}$ = 1.6, 1.4, 1.0, 0.5 and 0kG for ①, ②, ③, ④ and ⑤ respectively.

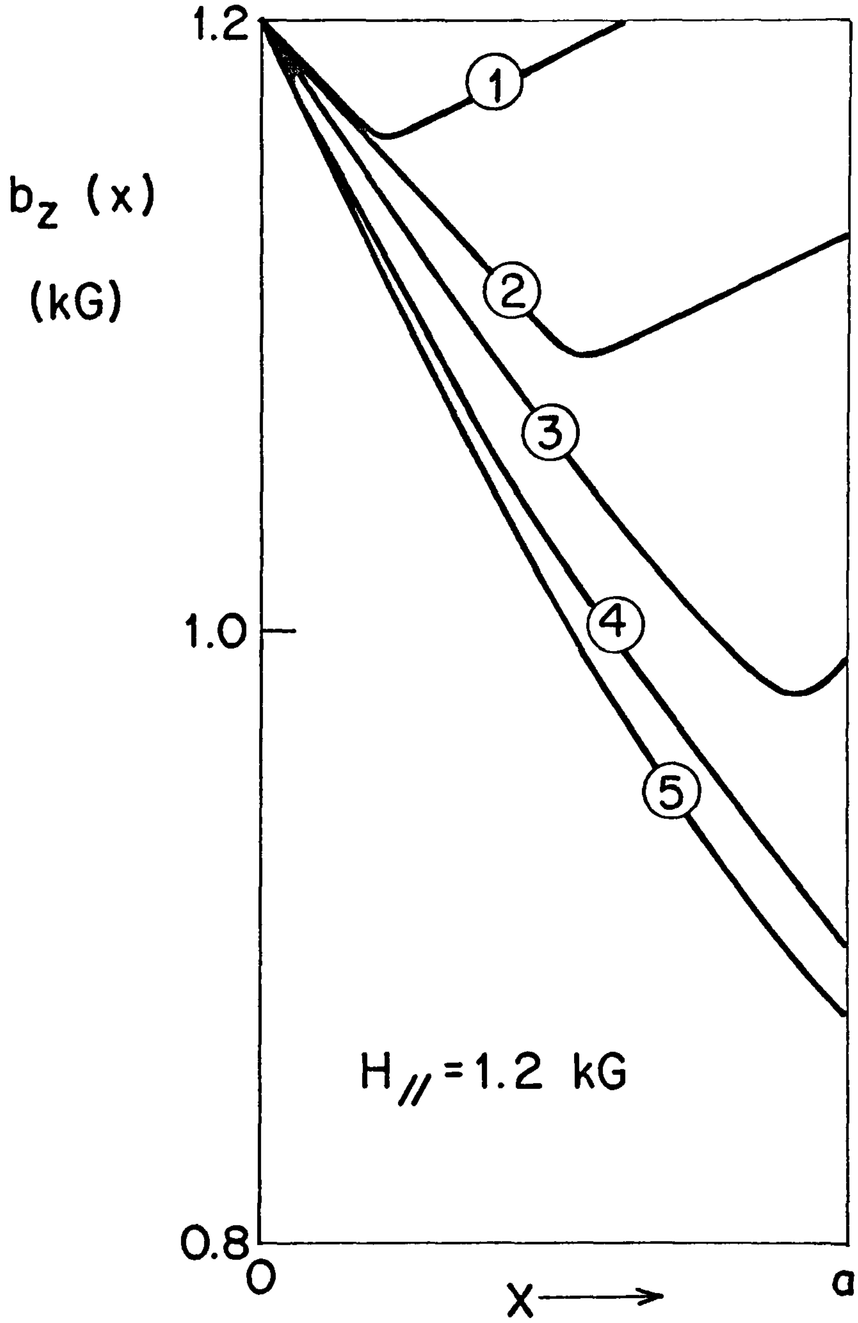

Figure 66: Calculated $b_z(x)$ profiles for $H_{//}$ = 1.2kG in VTi. $H_{\perp}$ = 1.6, 1.4, 1.0, 0.5 and 0kG for 1, 2, 3, 4 and 5 respectively.

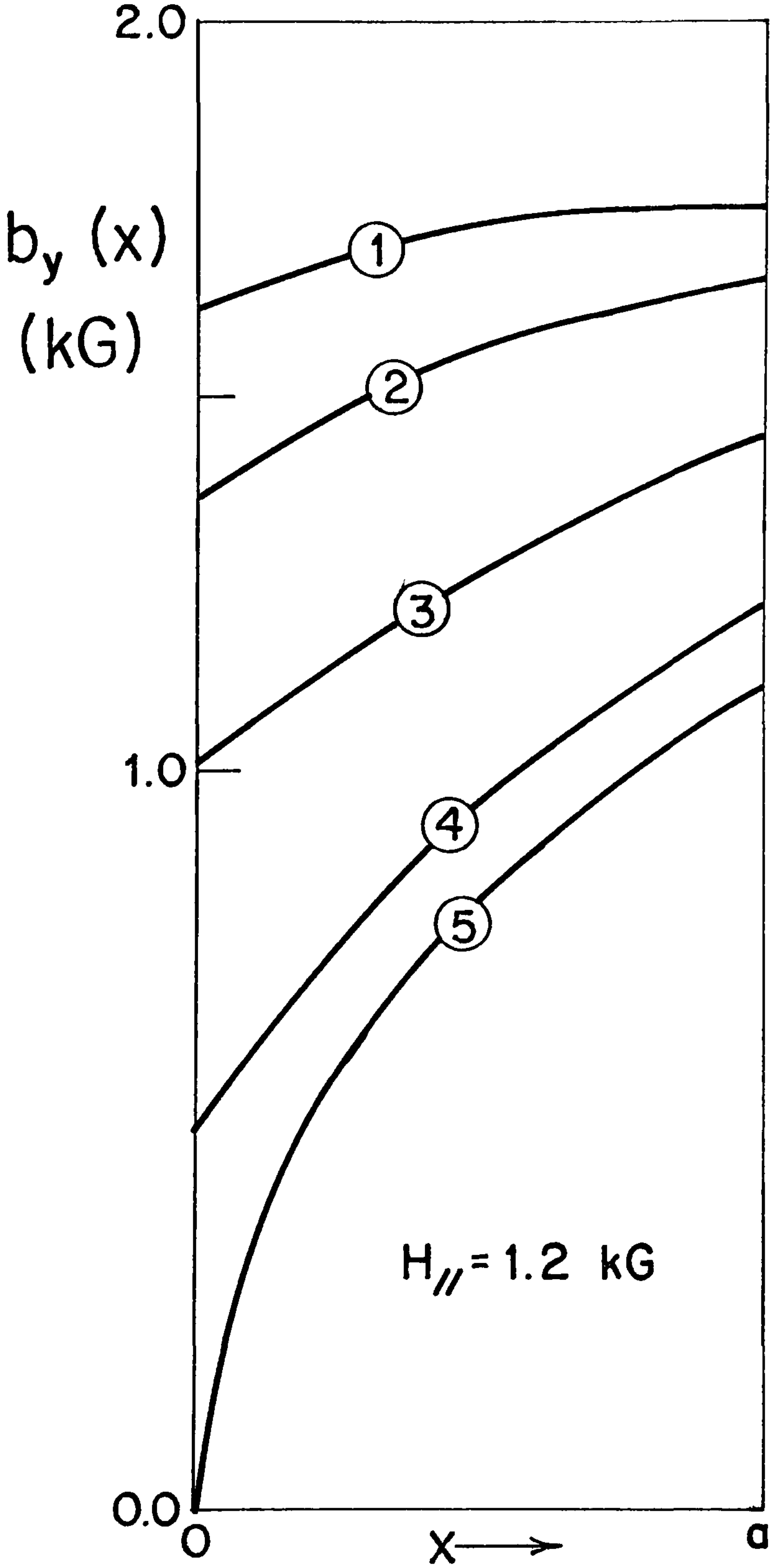

Figure 67: Calculated $b_y(x)$ profiles for $H_{//}$ = 1.2kG in VTi. $H_{\perp}$ = 1.6, 1.4, 1.0, 0.5 and 0kG for ①, ②, ③, ④ and ⑤ respectively.

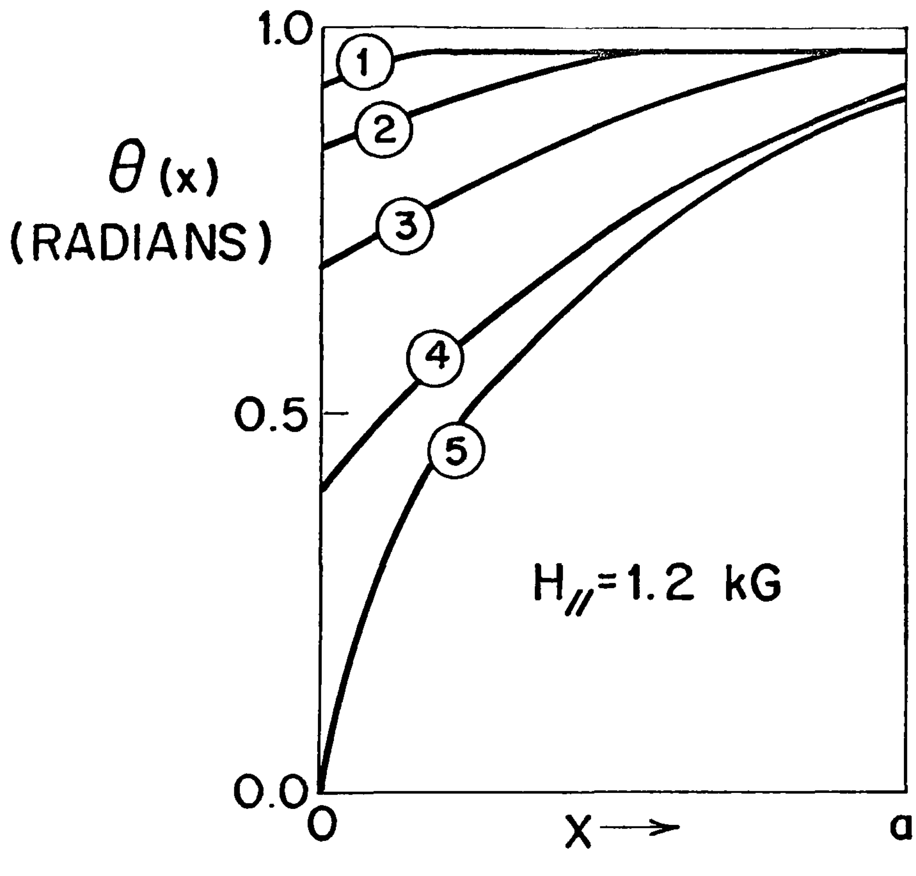

Figure 68: Calculated $\theta(x)$ profiles for $H_{//} = 1.2$kG in VTi. $H_{\perp} \doteq 1.6$, 1.4, 1.0, 0.5 and 0kG for 1 , 2 , 3 , 4 and 5 respectively.

III. Cycling $H_\perp$

The sample becomes superconducting in a "diagonal" field $H_{si} = (H_{\perp i}^2 + H_{//}^2)^{\frac{1}{2}}$ whose magnitude is subsequently varied through successive complete cycles. There are two distinct possibilities (see figure 27). (i) The transverse component does not change direction during the cycle ($H_\perp$ and θ_s always remain positive as they oscillate) or (ii) the transverse component traverses zero and changes sign during the cycle. The latter case involves certain complications and will be considered last. In both cases the initial quarter cycle only serves to establish the effective initial conditions of the cyclical variation and is thus not an integral part of the hysteresis loop. We analyze the two cases separately and present experimental and theoretical results for each situation.

i) $H_\perp$ does not change direction

We need to consider three different phases in the sequence of events; namely 1) the effective initial conditions are established, 2) the first half cycle is traversed and 3) the second half cycle is traversed.

Phase 1

For convenience we consider that in phase 1) $H_\perp$ is increased from $H_{\perp i}$ to a maximum value $H_{\perp max}$, hence H_s is varied from

H_{si} to $H_{s\,max}$. This excursion establishes an upper boundary for the profiles of B, θ, b_y and b_z which will be denoted by the subscript max. For simplicity and brevity, we restrict our analysis to the situation where the profile B_{max} has not penetrated to the mid plane ($x_1 \leq a$) and thus the front of the θ_{max} profile is situated some distance from the center (recall that $x_o < x_1$). We have discussed this first stage in some detail in Section I(ii) above and depict the end of phase 1 in Figure 73 .

In phase 2, H_s varies from $H_{s\,max}$ through H_{si} to a minimum value $H_{s\ min}$ and in phase 3 the magnetic field is swept back to $H_{s\ max}$. We refer the reader to Figure 27 for a schematic representation of the situation. Clearly the choice we have made for the excursion of the magnetic field is arbitrary and an alternative but equivalent order is possible, namely, the reverse or opposite order, where in phase (1) $H_{si} \rightarrow H_{s\ min}$, phase (2) $H_{s\ min} \rightarrow H_{s\ max}$ and phase (3) $H_{s\ max} \rightarrow H_{s\ min}$. It is a straightforward matter to adapt the development of the profiles we now present to this alternate sequence.

Phase 2

The next four figures in this chapter show typical sequences of B, θ, b_y and b_z profiles during the sweep from H_{max} to H_{min} hence from $H_{s\ max}$ to $H_{s\ min}$. The profiles shown were computed using the parameters listed in table III which are applicable to the analysis of the NbTi sample and where we took $H_{//} = 3\text{kG}$, $H_{\perp i} = 3$ kG, $H_{\perp max} = 6$ kG, $H_{\perp min} = 0$ hence $H_{s\ max} = (H_{\perp max}^2 + H_{//}^2)^{\frac{1}{2}} = 6.7$ kG, $H_{si} = (H_{\perp i}^2 + H_{//}^2) = 4.24$ kG $H_{s\ min} = (H_{\perp min}^2 + H_{//}^2)^{\frac{1}{2}} = 3$ kG.

It is evident that the profiles are becoming more and more complicated. This is to be expected since as the magnitude and direction of the applied field progresses through each phase of the cycle, a new B and θ disturbance propagates inwards while deeper inside the slab the profiles tend to retain the imprint of all the previous magnetic disturbance to which the slab has been subjected with respect to both intensity and orientation.

The b_y and b_z profiles in particular become very complicated. Physically, however, the entire behaviour is relatively straightforward and is governed by the critical state which determines the B profile and the rotation of the vortices which dictates the θ profile according to the simple empirical rule we expound (equation 6-8). The intricate structure of the b_y and b_z profiles follows from the detailed application of these simple principles with the previous history being carefully taken into account at every step of the excursion. We introduce a labelling system for the boundaries which is an extension of the scheme used earlier. Let $x_{o\ max}$ and $x_{1\ max}$ denote the maximum depth of penetration of the initial θ and B disturbances applied during phase 1 when H_s

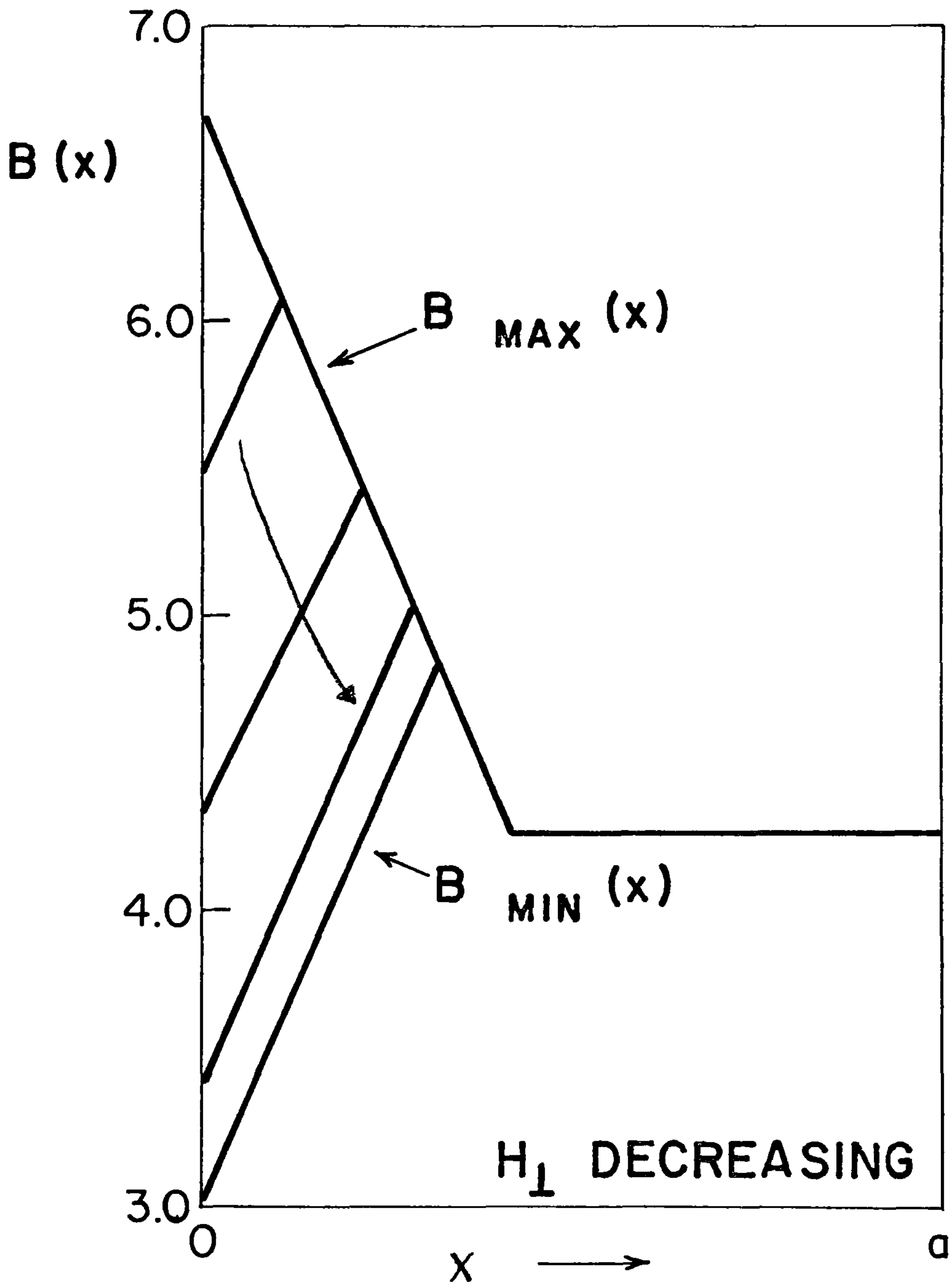

Figure 69: Sequence of B(x) profiles in phase 2 (cycling $H_{\perp}$) calculated from votex rotation model for NbTi.

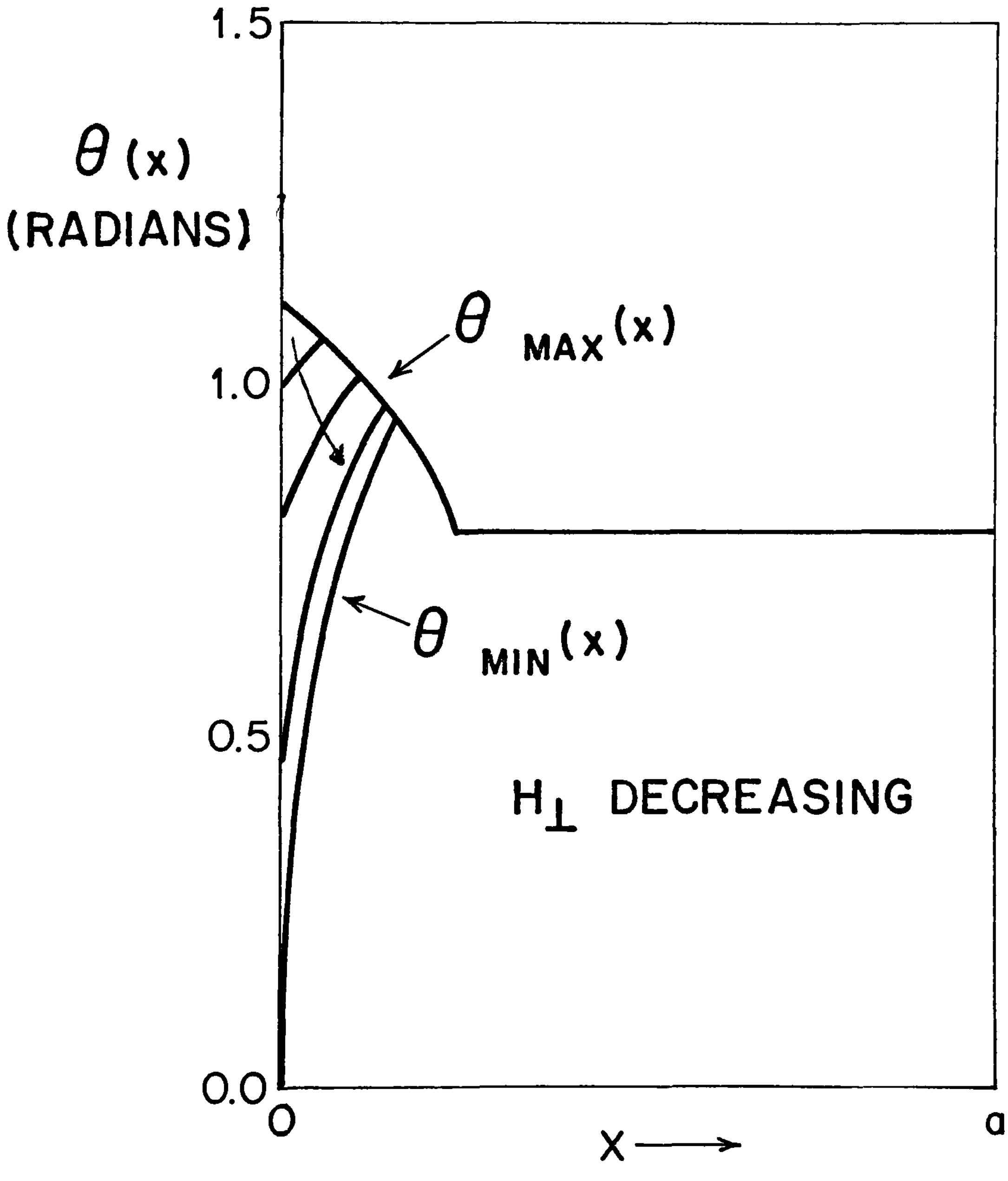

Figure 70: Sequence of $\theta(x)$ profiles in phase 2 (cycling $H_\perp$) calculated from vortex rotation model for NbTi.

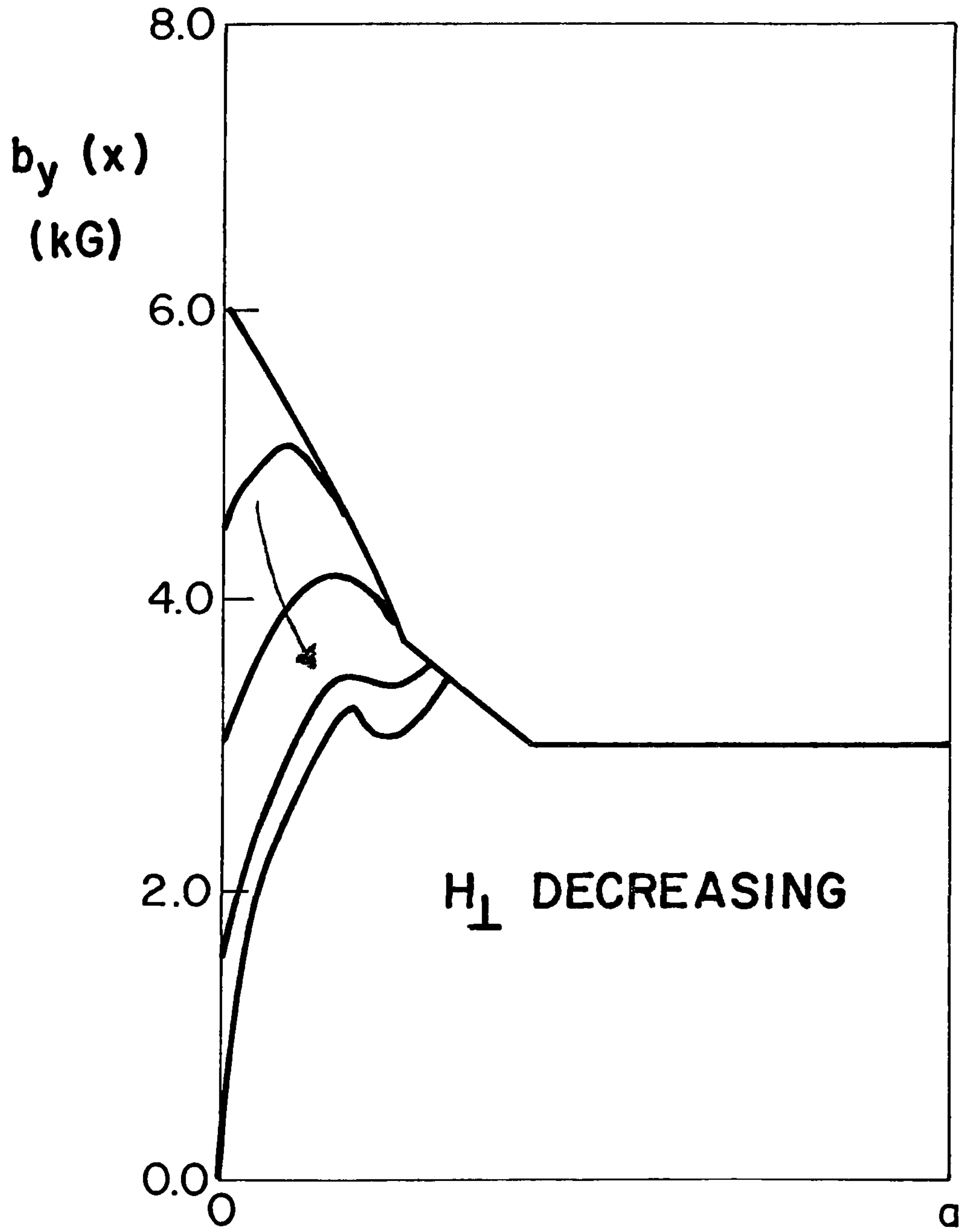

Figure 71: Sequence of $b_y(x)$ profiles in phase 2 (cycling $H_\perp$) calculated from vortex rotation model for NbTi.

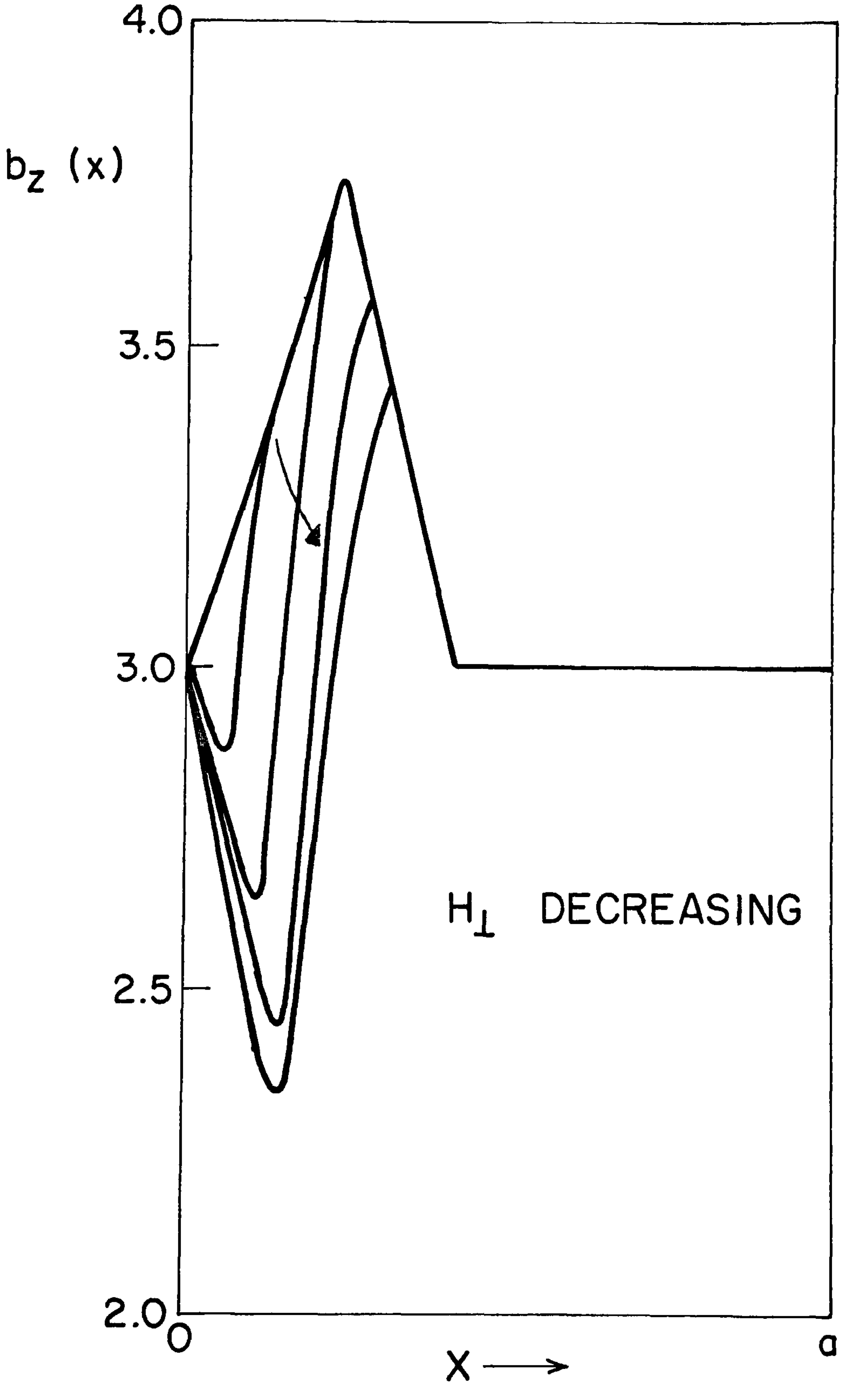

Figure 72: Sequence of $b_z(x)$ profiles in phase 2 (cycling $H_\perp$) calculated from vortex rotation model for NbTi.

END OF PHASE 1

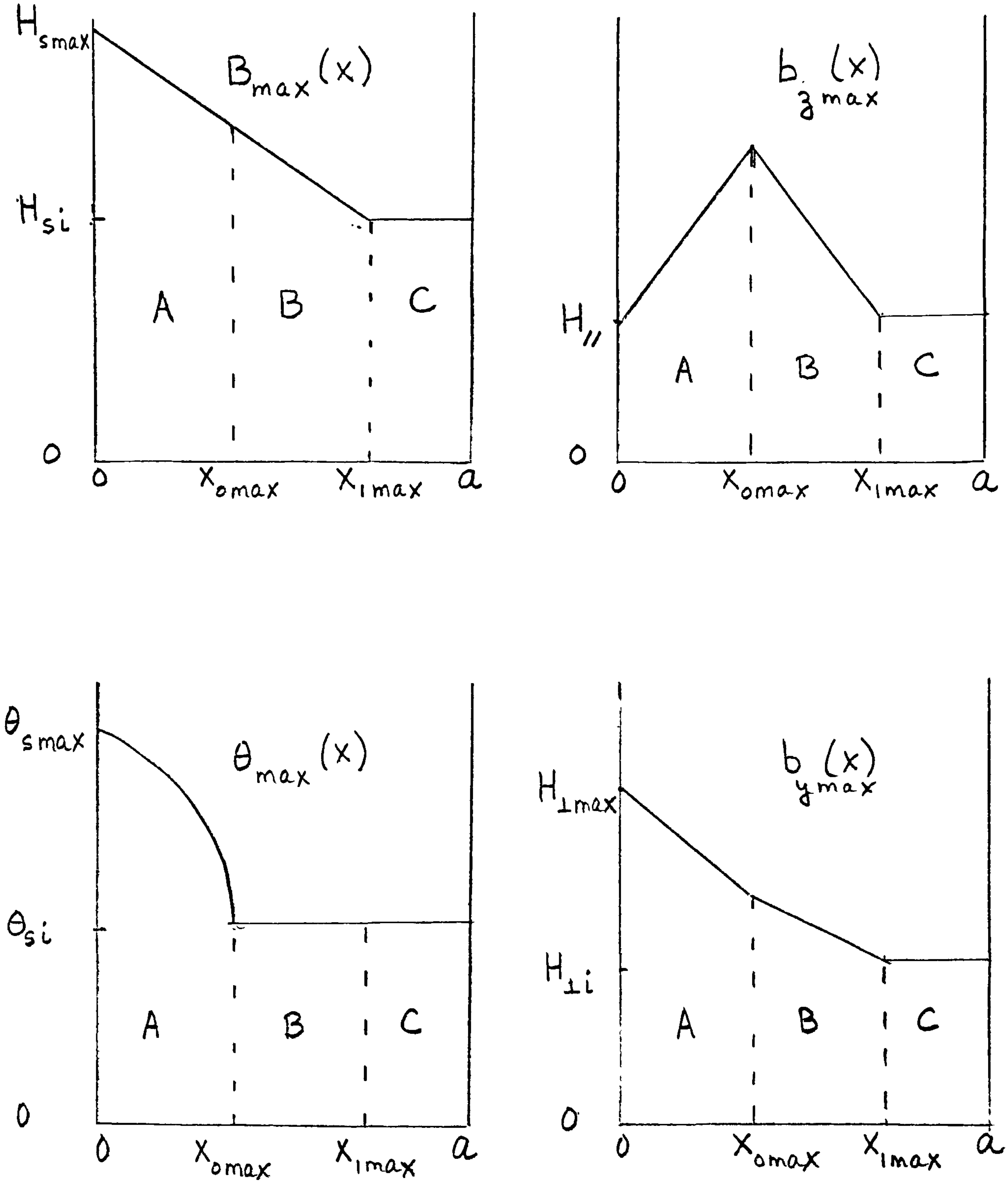

Figure 73: Schematic of magnetic induction and angular profiles at end of phase 1 (cycling $H_{\perp}$).

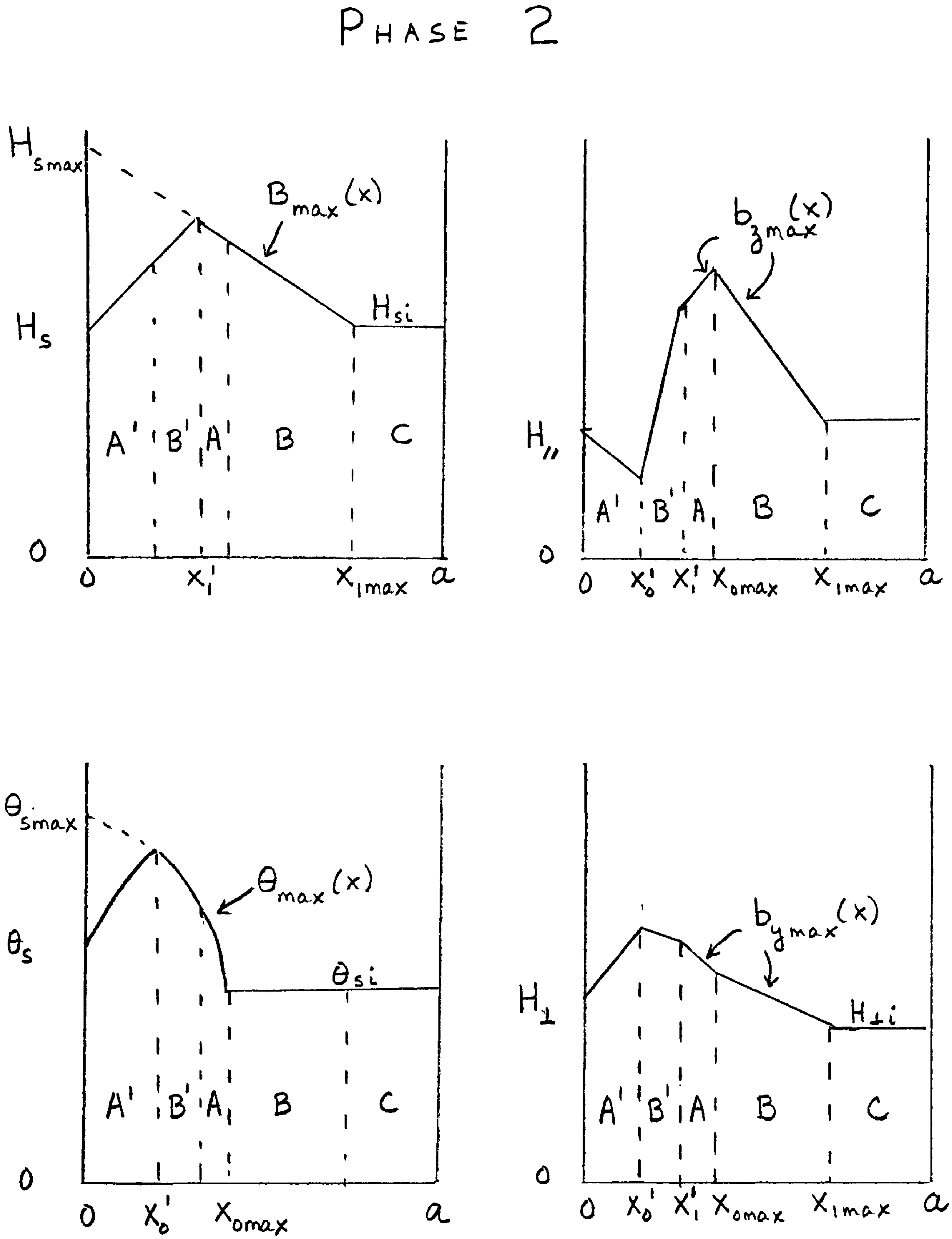

Figure 74: Schematic of magnetic induction and angular profiles during phase 2 (cycling $H_{\perp}$).

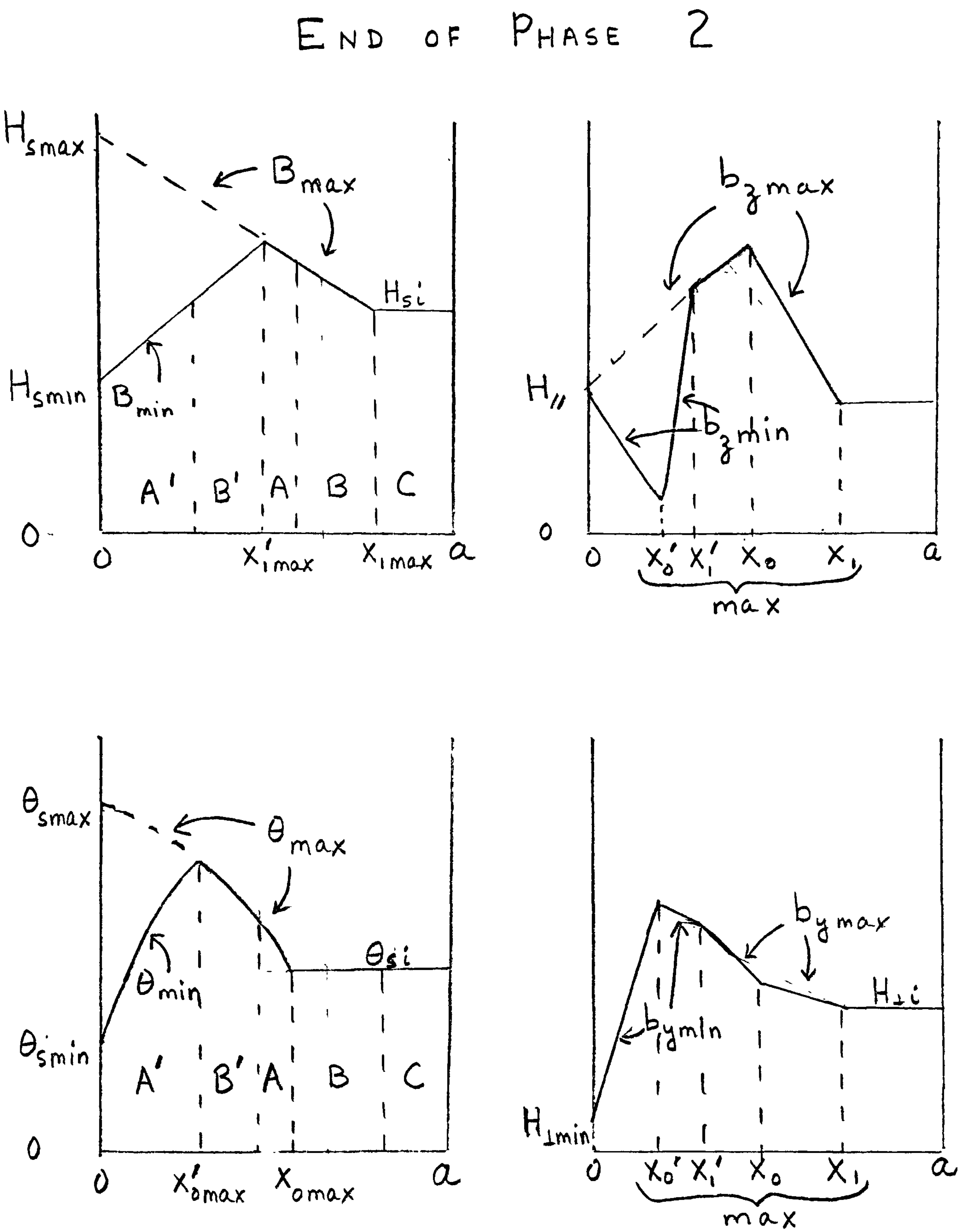

Figure 75: Schematic of magnetic induction and angular profiles at end of phase 2 (cycling $H_{\perp}$).

PHASE 3

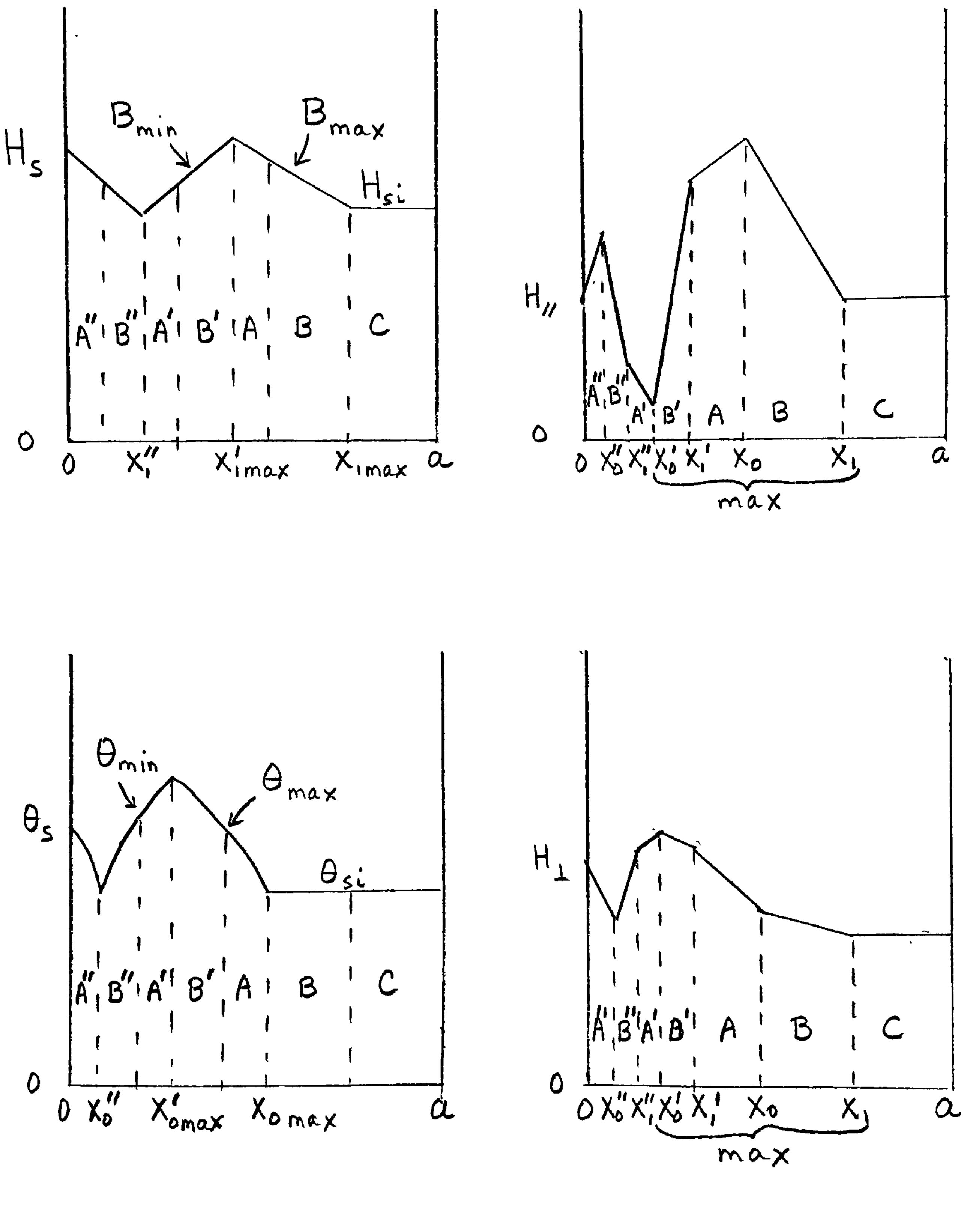

Figure 76: Schematic of magnetic induction and angular profiles during phase 3 (cycling $H_\perp$).

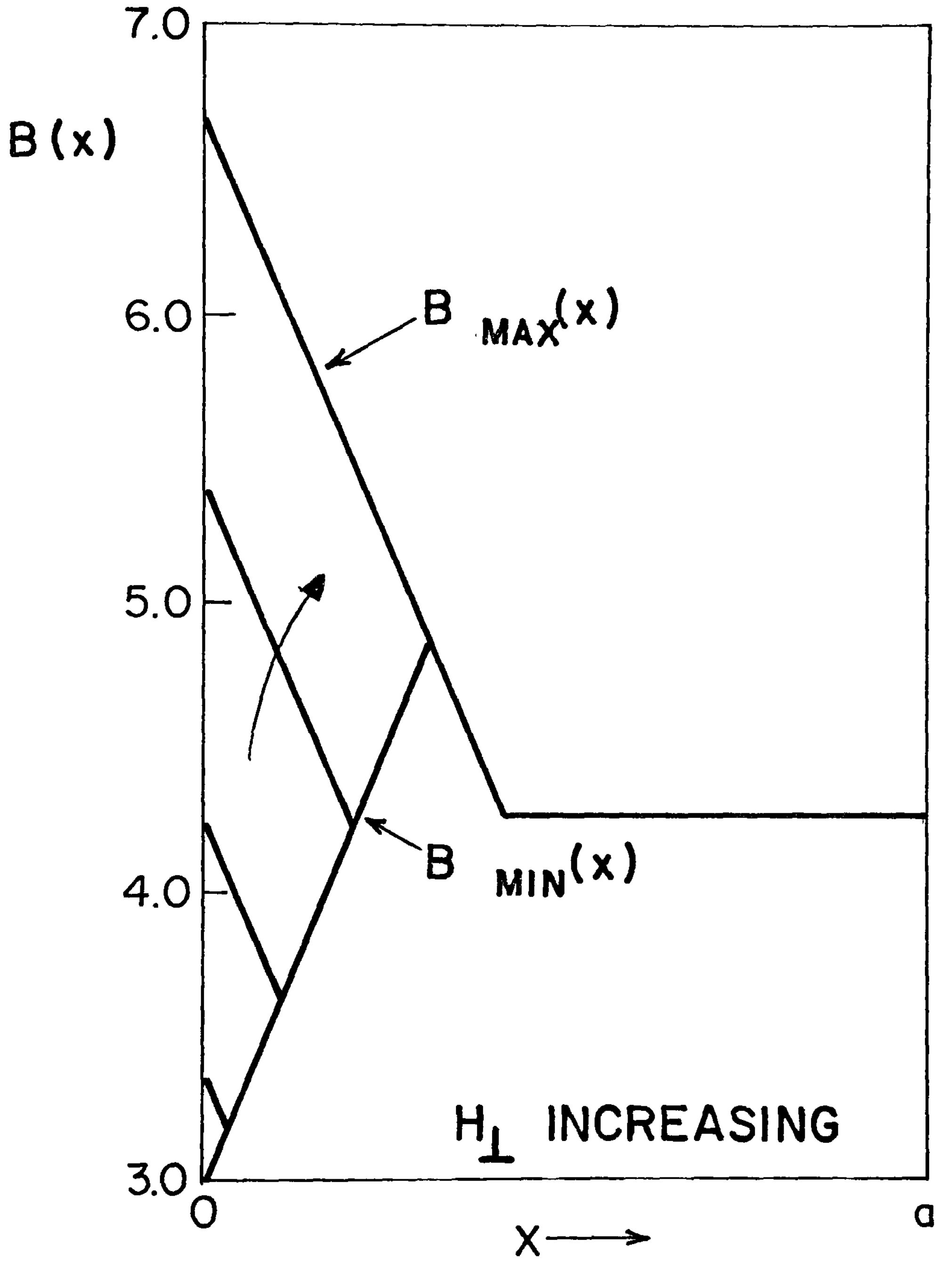

Figure 77: Sequence of B(x) profiles in phase 3 (cycling $H_{\perp}$) calculated from vortex rotation model for NbTi.

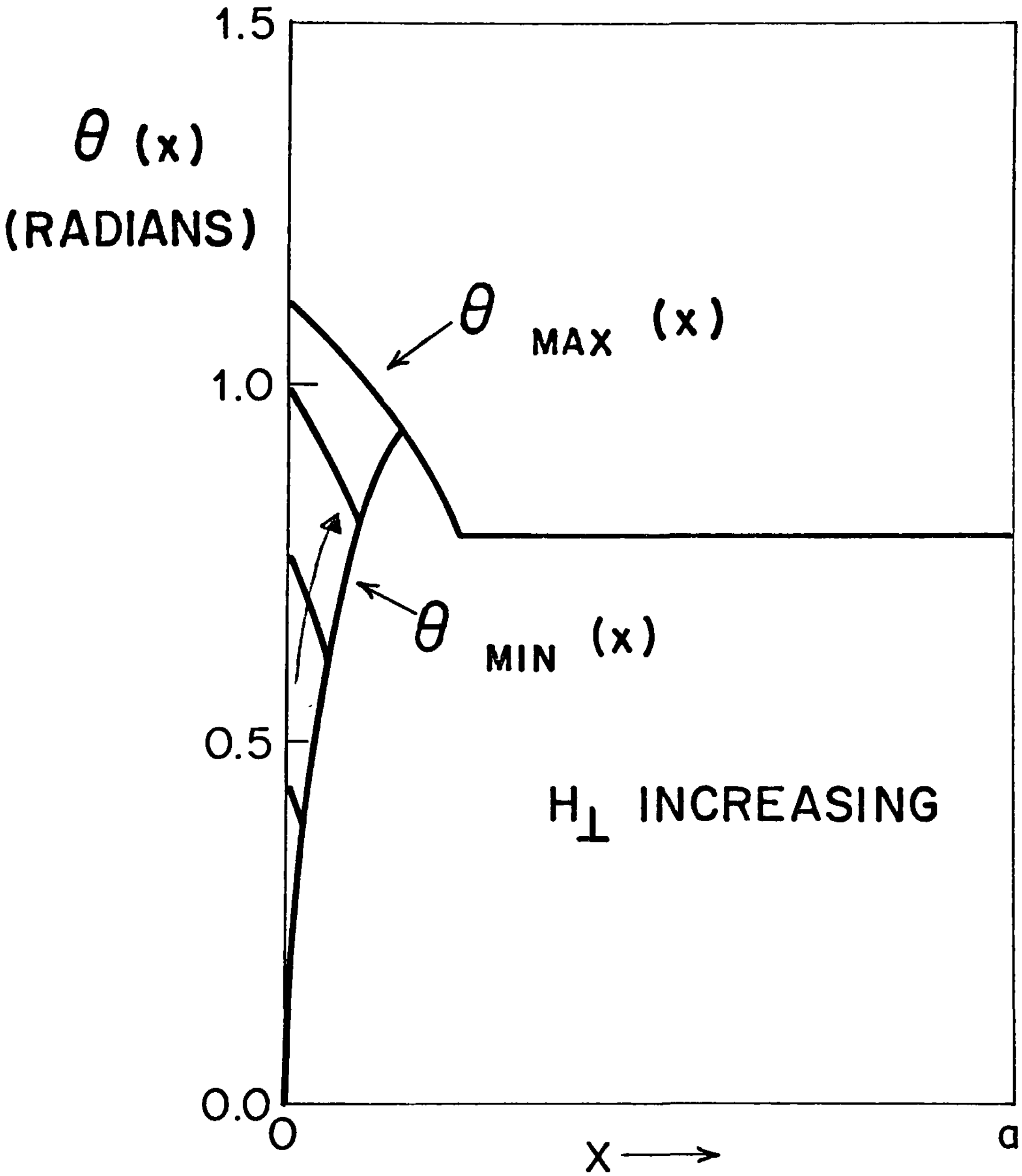

Figure 78: Sequence of $\theta(x)$ profiles in phase 3 (cycling $H_\perp$) calculated from vortex rotation model for NbTi.

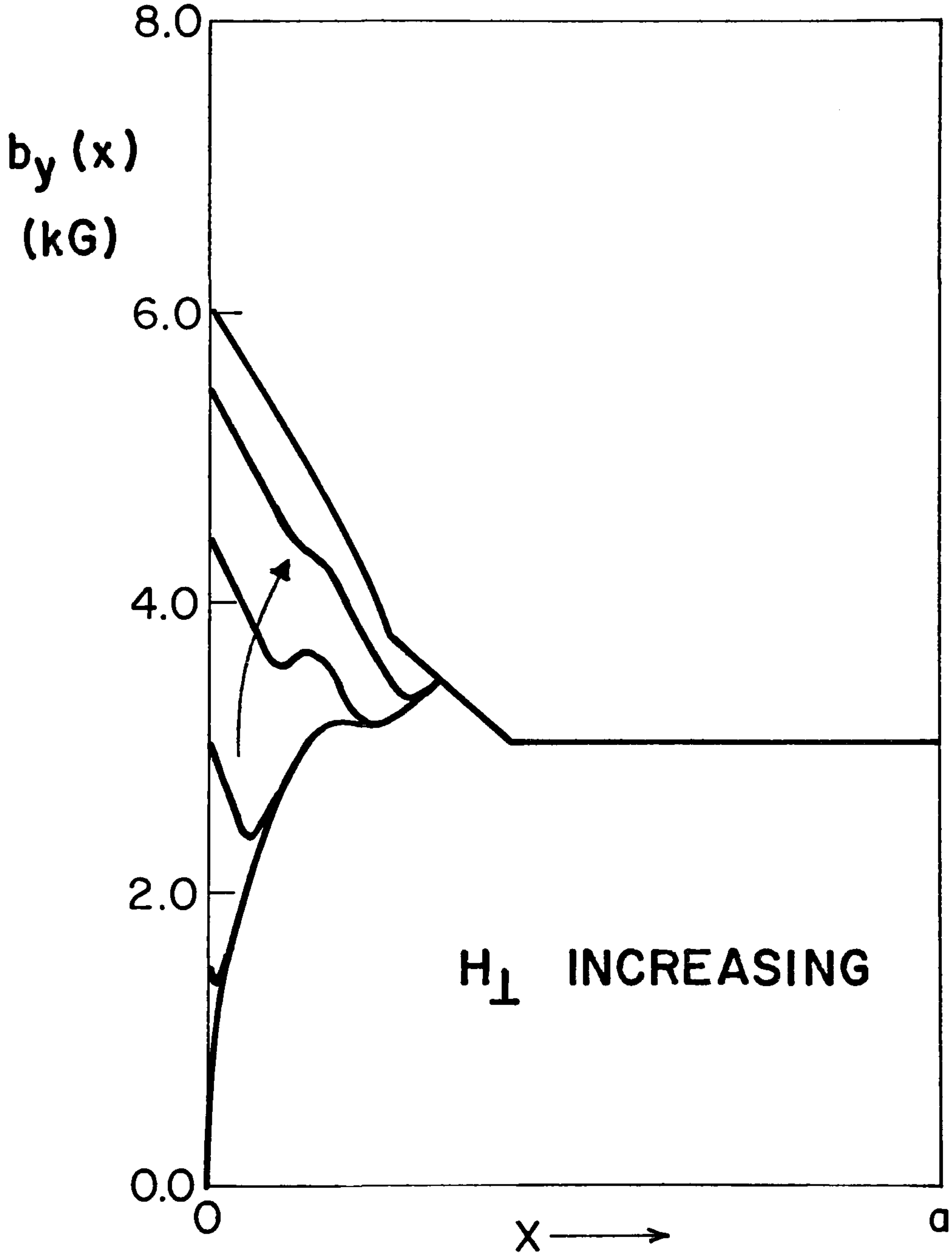

Figure 79: Sequence of $b_y(x)$ profiles in phase 3 (cycling $H_\perp$) calculated from vortex rotation model for NbTi.

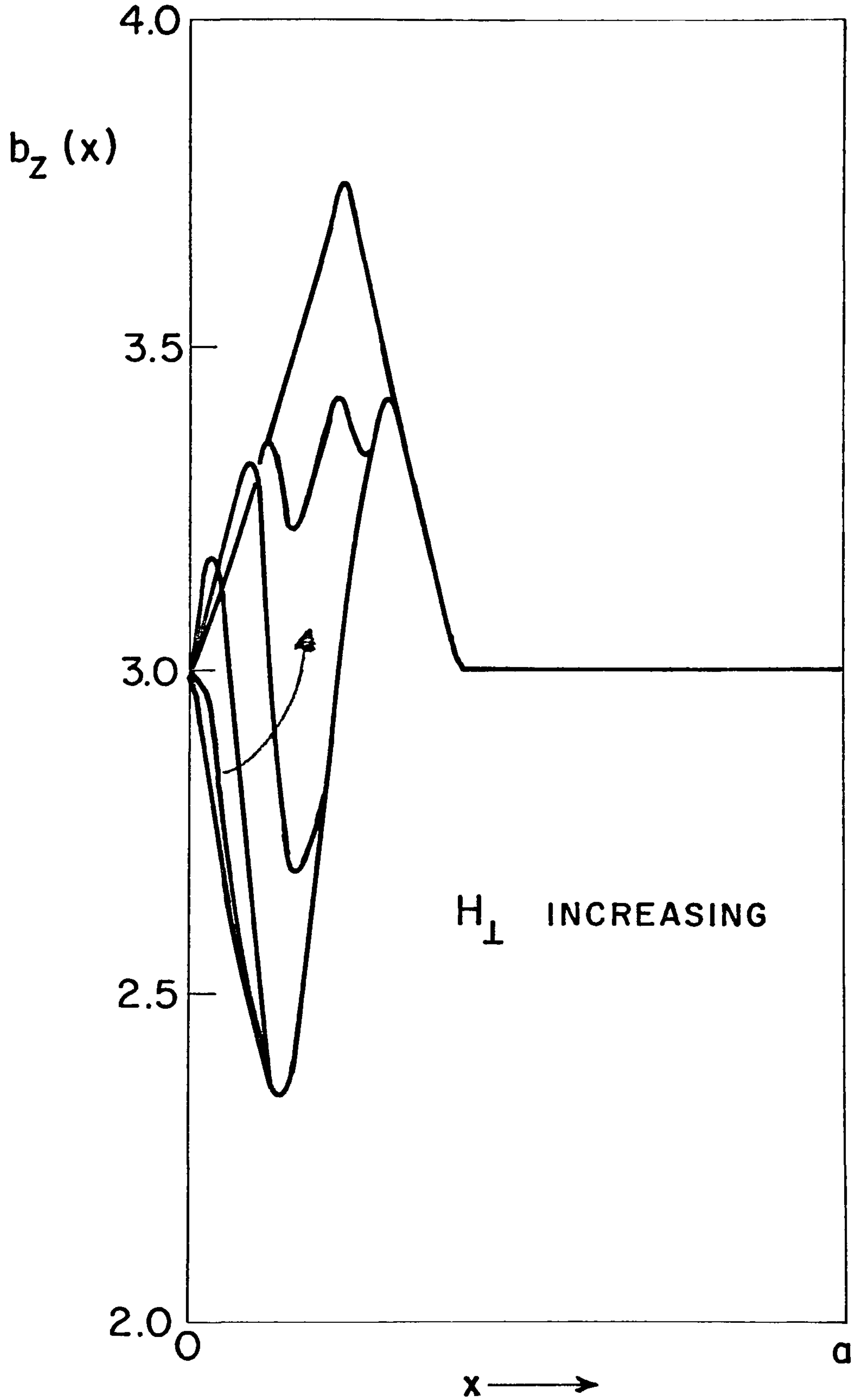

Figure 80: Sequence of $b_z(x)$ profiles in phase 3 (cycling $H_\perp$) calculated from vortex rotation model for NbTi.

was increased from H_{si} to $H_{s\ max}$. We recall that $x_{o\ max} < x_{1\ max}$. These two boundaries remain fixed as H_s is subsequently cycled.

Let x_o' and x_1' denote the depth of penetration of the θ and B disturbances as H_s is swept from $H_{s\ max}$ to $H_{s\ min}$ during phase 2. These two boundaries migrate inwards as H_s is varied. Again we note that $x_o' < x_1'$. Further, in order that the full cycle be complete or closed the limiting or maximum depth of penetration of each disturbance in phase 2 must be smaller than in phase 1, i.e. $x'_{o\ max} < x_{o\ max}$ and $x'_{1max} < x_{1\ max}$.

During the initial part of phase 2, $x_1' < x_{o\ max}$. As phase 2 progresses, however, and H_s approaches $H_{s\ min}$, x_1' may advance beyond x'_{omax}. In Figure 74 we present schematically a set of profiles at an intermediate stage in the sweep of H_s from $H_{s\ max}$ to $H_{s\ min}$ for the case where $x_1' < x_{o\ max}$. We can identify 5 regions in the slab hence 4 frontiers or dividing planes in addition to the surface and the mid-plane.

Region A'; $0 < x \leq x_o'$

This region is penetrated by both of the "new" angular and field disturbances. Thus $\theta(x)$ increases from θ_s to θ_{max} at x_o'. Also B and b_y increase with depth in this region. $b_z(x)$ however decreases to a minimum at x_o' since $\theta(x)$ increases proportionately more rapidly than $B(x)$.

Region B'; $x'_o \leq x \leq x'_1$

$\theta(x)$ follows the θ_{max} profile established at the end of phase 1 but the B profile continues to rise since the field disturbance extends throughout this region with its leading edge located at x'_1. Thus in this region the vortices are being decompressed while maintaining the orientation $\theta_{max}(x)$ established at the end of phase 1.

Regions A, B and C; $x'_1 \leq x \leq x_{o\ max}$, $x_{o\ max} \leq x \leq x_{1\ max}$, $x_{1\ max} \leq x \leq a$ respectively.

The vortices in these three regions retain the configuration of orientation and density established at the end of phase 1. From $x_{o\ max}$ to the mid-plane the direction of the vortices corresponds to θ_i, that existing when the sample became superconducting. These three regions have been discussed in detail under section I (ii) above.

Depending on the relative amplitude of the variations of θ_s and H_s during phase 1 and 2, the front of the new field disturbance, x'_1, may penetrate beyond $x_{o\ max}$. Even if this occurs, the characteristics of region A' remain unchanged. Region B', however, may be viewed as consisting now of two sub-regions, extending from x'_o to $x_{o\ max}$ and from $x_{o\ max}$ to x'_1 respectively. In the first sub-region the vortices are decompressed while maintaining the orientation $\theta_{max}(x)$ established at the end of phase 1 while in the second sub-region, the vortices are decompressed while maintaining the orientation θ_i existing when the slab became superconducting. This difference in the nature of the two sub-regions manifests itself in changes of slope in the b_z and b_y profiles (see Figures 72 and 71). Region A vanishes when x_1' reaches $x_{o\ max}$ and the width of region B shrinks as x_1' advances beyond x_o max.

We note that whether $x'_{1\ max}$ progresses beyond $x_{o\ max}$ or not, the configuration of the magnetic induction in the volume between x'_{max} and the mid-plane remains "inert" as H_s is subsequently cycled. Hence this volume and the detailed configuration of flux threading it plays no further role in the locus of the magnetization and its components and thus in the determination of hysteresis (A.C.) losses.

Phase 3

H_s is swept from $H_{s\ min}$ back to $H_{s\ max}$ thereby closing the full cycle. At the end of phase 2, the θ and B disturbances had penetrated to a distance $x'_{o\ max}$ and $x'_{1\ max}$ respectively where $x'_{o\ max} < x'_{1\ max}$. Earlier, at the end of phase 1 which established the initial conditions for the full cycle, the θ and B disturbances had penetrated to a depth $x_{o\ max}$ and $x_{1\ max}$ respectively where $x_{1\ max} > x'_{1\ max}$. We envisaged two possibilities; the second B disturbance progressed less or more deeply than the first θ

disturbance, i.e. $x'_{1\,max} \lesseqgtr x_{o\,max}$. We first focus on the situation where $x'_{1\,max} < x_{o\,max}$.

As H_s is now increased from $H_{s\,min}$ to $H_{s\,max}$ a third set of θ and B disturbances penetrate into the slab. Let x''_o and x''_1 denote the front of these new "wave fronts" respectively where $x''_o < x''_1$. At the beginning of the sweep of H_s from $H_{s\,min}$, the depth of penetration of the third B disturbance, x''_1 is smaller than $x'_{o\,max}$, the maximum penetration of the θ disturbance during phase 2. We refer the reader to Figure 76 which shows schematically the various profiles and boundaries at this juncture. Eventually x''_1 reaches $x'_{o\,max}$. Later, phase 3, hence the complete cycle, terminate when x''_o reaches $x'_{o\,max}$ and simultaneously x''_1 reaches $x'_{1\,max}$.

Clearly the sequences of intermediate profiles will be increasingly complex since these involve 3 separate sets of boundaries in addition to the surface and the mid plane. Two of these boundaries are advancing and ultimately encroach upon some of the others. Nevertheless, we claim that the basic physics of the problem is relatively uncomplicated since the two guiding principles, the critical state and the rotation of the vortices are conceptually simple.

The initial penetration of the new θ and B "wave fronts" gives rise to 2 new regions labelled A" and B" respectively. These simultaneously invade, but with x''_1 ahead of x''_o, the area initially occupied by region A'. This is the situation shown schematically in Figure 76 . We can thus identify 7 separate regions: the new regions A" and B", the surviving portion of region A', and the regions B', A, B, C which are undisturbed at this juncture,

Region A"; $o < x \leq x_o''$

The region has been penetrated by both of the new θ and B disturbances. Since flux is entering this region at an angle which is increasing with time, the B, b_y and θ profiles are all growing with time. In response to the increase in density of the magnetic flux, the b_z profile rises with depth to a local maximum at x_o'', the limit of the penetration of the angular disturbance.

Region B"; $x_o'' \leq x \leq x_1''$

The region is penetrated by the new flux density disturbance only. Thus in this region the vortices are compressed while maintaining the orientation $\theta_{min}(x)$ existing at the end of phase 2. This increase in flux density with time at fixed orientation is reflected in the growth of the slopes of the b_z and b_y profiles.

Subsequently as H_s is increased further, region A' dwindles to disappear when $x_1'' = x_o'$. Then as x_1'', the leading edge of the B disturbance penetrates beyond $x'_{o\,max}$, the flux density in a growing portion of section B' is compressed while retaining the orientation established at the end of phase 2.

We now consider the case where region B' (the region where flux has been decompressed without rotating during phase 2) consists of two sub-regions, an outer one where $\theta_{max}(x)$ prevails and an inner one where θ_i prevails. The only difference or new complication is that two sub-regions instead of a single region must be taken into account during phase 3. The B disturbance traverses the outer and then enters and fills the inner sub-region. As the B wave front advances the vortices are compressed without rotating, hence while maintaining the orientation existing in each sub-region. The fact that the direction of the vortices differs for each sub-region leads to corresponding structure in the b_z and b_y profiles.

We emphasize that regardless of which case is encountered physically ($x'_{1\ max} \gtrless x_{o\ max}$), the cycle closes and phase 3 must then terminate when the third set of B and θ disturbances reach (simultaneously) the position attained earlier by the B and θ disturbances respectively at the end of phase 2. (i.e. $x''_1 = x'_{1\ max}$ and $x''_o = x'_{o\ max}$). We also indicate again that the volume beyond $x'_{1\ max}$ plays no role in the cycle or hysteresis loop hence has no effect on the hysteresis (A.C.) losses. This means that the mid plane could be located at x'_1 without affecting the pertinent physical results.

A typical sequence of profiles for the entire phase 3 is presented in Figures 77 through 80 . These profiles were calculated using the parameters applicable to the analysis of the NbTi sample (table III). We note also that for the series shown here, the condition $x'_{1\ max} > x_{0\ max}$ applies at the end of phase 2.

Results and Discussion

We have examined in detail the sequence of the structure of the profiles of b_z and b_y as $H_\perp$ is cycled without changing polarity when the slab is immersed in a static longitudinal field $H_{//}$. The integration of each profile yields the average of the corresponding component of the magnetic induction,
$\langle b_z \rangle = H_{//} + \langle 4\pi M \rangle_{//} = \int b_z\ dx/a$, $\langle b_y \rangle = H_\perp + \langle 4\pi M \rangle_\perp = \int b_y\ dx/a$.
The locus of $\langle b_z \rangle$ and $\langle b_y \rangle$ as $H_\perp$ is swept through complete cycles trace out "hysteresis" loops. We find it more convenient to continue presenting the contour of $\langle 4\pi M \rangle_{//}$ and $\langle 4\pi M \rangle_\perp$ instead of $\langle b_z \rangle$ and $\langle b_y \rangle$ as $H_\perp$ is varied.

In the next pages we present closed contours of the longitudinal component of the magnetization as $H_\perp$ is cycled without changing direction between $H_{\perp\ min}$ and $H_{\perp max}$ for the case where $H_{\perp min} = 0$. The sequence of closed contours illustrates the complicated variations in the form of the closed loops as the range in the sweep of $H_\perp$, hence $H_{\perp\ max}$ is made greater and greater for a selected value of $H_{//}$. The first group of figures are experimental results obtained with the VTi sample (Figures 81 through 87). The second group of figures have been computed using our model and taking the parameters we have found applicable to the analysis of this material (see table III).

We remark that the behaviour of the specimen when $H_\perp$ is cycled between $H_{\perp min} = 0$ and $H_{\perp max}$ is equivalent to that encountered when a half-wave alternating current is caused to flow along the length of the ribbon from an external current supply which provides a peak current $I_p = (2H_{\perp max}/\mu_o)\ell_y$ where I is in amperes/, H_{max} in Gauss, ℓ_y in cm and $\mu_o = 4\pi/10$. This situation where the current is fed into the specimen is of considerable technical interest. The transverse field generated by the conduction current I is positive along one surface of the slab and negative along the other. In our experimental set up where the currents are established by induction, the transverse field has the same polarity along both surfaces of the ribbon. This difference in the symmetry or image of the magnetic induction in the two halves of the slab becomes physically significant when the front of the two b_y profiles reach the mid-plane. The conduction current then attains a critical value I_c which, if exceeded, leads to a flux flow state and a possible collapse of superconductivity by thermal runaway. It is possible, however, to raise the external magnetic field further and establish a succession of stable critical states when the currents are generated by induction as in our work.

The contours of the hysteresis loops traced out by the transverse component of the magnetization as $H_{\perp}$ is cycled with and also without a change of polarity will be discussed together at the end of this chapter under the sub-heading of hysteresis (A.C.) losses.

The structure of the hysteresis loops traced out by the longitudinal component of the magnetization where a change of polarity in $H_{\perp}$ occurs as it is swept between its limiting or extreme values is very different from that encountered when no change of polarity takes place and will be examined separately in the next section.

The juxtaposition in $M_{//}$ - $H_{//}$ - $H_{\perp}$ space of the observed contours which are presented in Figures 81 through 87 maps out a closed surface. An acceptable model must reproduce all of the major features of this intricate convoluted three dimensional closed surface. An inspection of the sequence of calculated curves presented in Figures 88 through 95 reveals that our model accomplishes this formidable task quite successfully.

Firstly we note that when $H_{\perp}$ is swept through small amplitudes the locus of $\langle 4\pi M \rangle_{//}$ travels clockwise and the left hand extremum of the contour terminates below the horizontal zero line, hence in the paramagnetic quadrant. With increasing amplitude this end point is gradually displaced upwards and eventually rises above the zero line and to a comparable height in the diamagnetic quadrant. As this displacement takes place, the sausage shaped loop becomes narrower and finally the sides touch and then intersect. Consequently, the locus of $\langle 4\pi M\rangle_{//}$ then travels counterclockwise as it traces out the area located to the right of the cross over point. This area subsequently becomes fatter and eventually occupies most of the surface embraced by the contour. Upon further increase of the amplitude of the oscillation of $H_{\perp}$, this segment of the loop progressively develops a pronounced downward bulge.

Inspection and comparison of the group of observed and calculated loops reveals that they are remarkably similar. The model successfully generates almost all of the major features of the intricate contours as well as the correct sequence in the evolution of their progressively more complicated structure with increasing amplitude of the sweep of $H_{\perp}$. A careful consideration of the features we have just enumerated shows that these are associated with and a consequence of specific characteristics in the sequence of configurations of the b_z profiles generated by our model.

We draw the attention of the reader to the valley adjoining the surface and the adjacent promontory deeper inside the slab in the b_z profile established at the end of phase 2 (see figure 75).

The area gouged out by the valley compared to that of the neighbouring hill determines the position of the left hand extremum of the loops. Both the valley and the hill grow in size with increasing amplitude of $H_{\perp}$. The valley, however, is enlarged at a faster rate, hence this end point of the loop is displaced from the paramagnetic to the diamagnetic quadrant. As $H_{\perp}$ is swept up from zero during its oscillation, this valley fills up. The rate of filling is proportionately greater when the valley is deep and wide. This is the reason for the change in the sense of circulation of the locus of $\langle 4\pi M\rangle_{//}$. Finally we remark that the appearance of the downward bulge in the contours has been encountered earlier in this chapter under section (i) ($H_{\perp}$ increasing from zero). At high amplitudes, the b_z profile first penetrates to the mid plane and eventually the summit of the hill advances to the midplane (see Figures 28 and 47). At this juncture the longitudinal magnetization traverses a paramagnetic peak or maximum.
It is gratifying to see that the sequence of events can be related to basic features of our model.

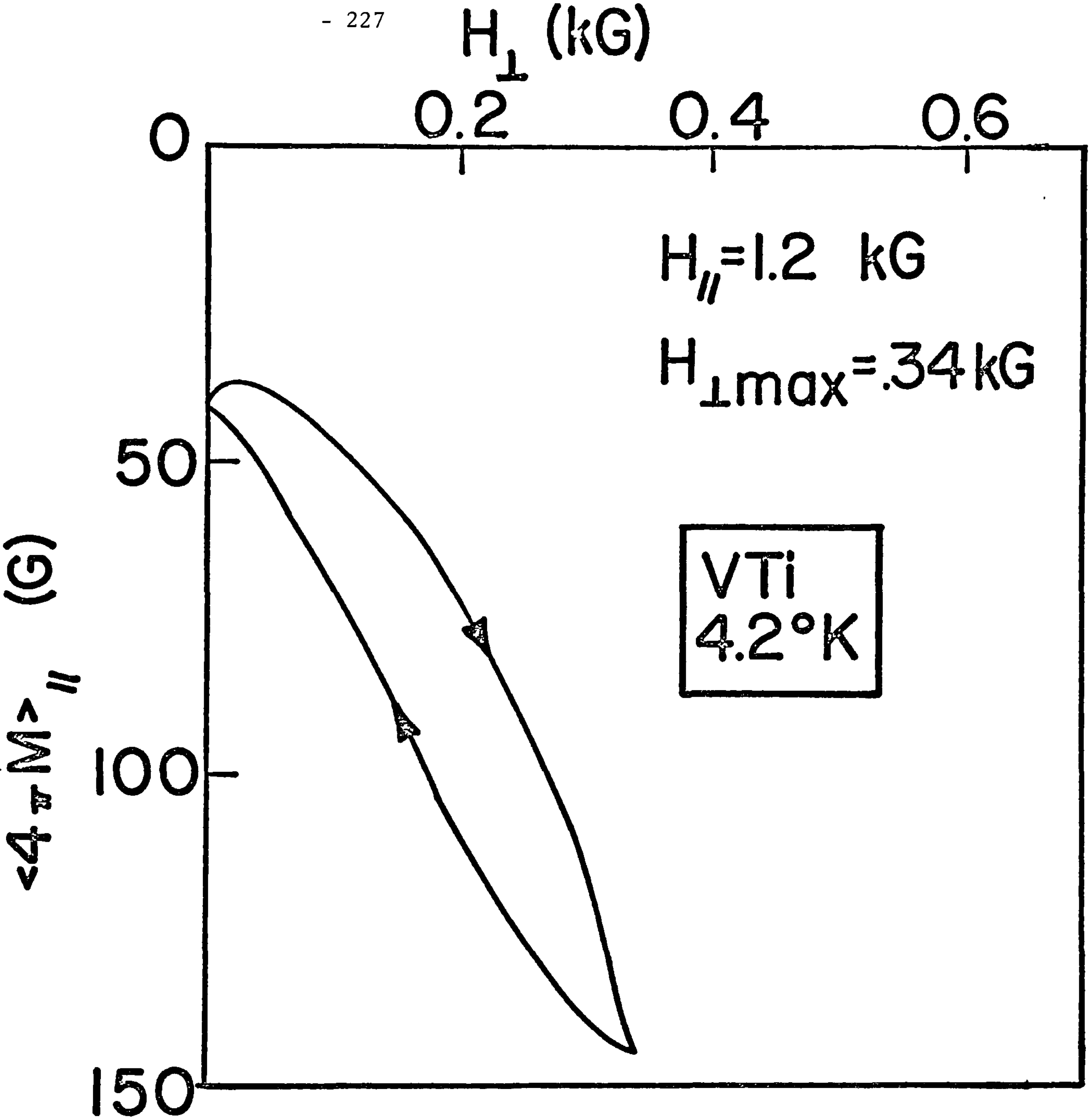

Figure 81: Experimental values of $\langle 4\pi M \rangle_{//}$ versus cycling $H_{\perp}$ for VTi. $H_{//} = 1.2$kG, $H_{\perp\,max} = 0.34$kG.

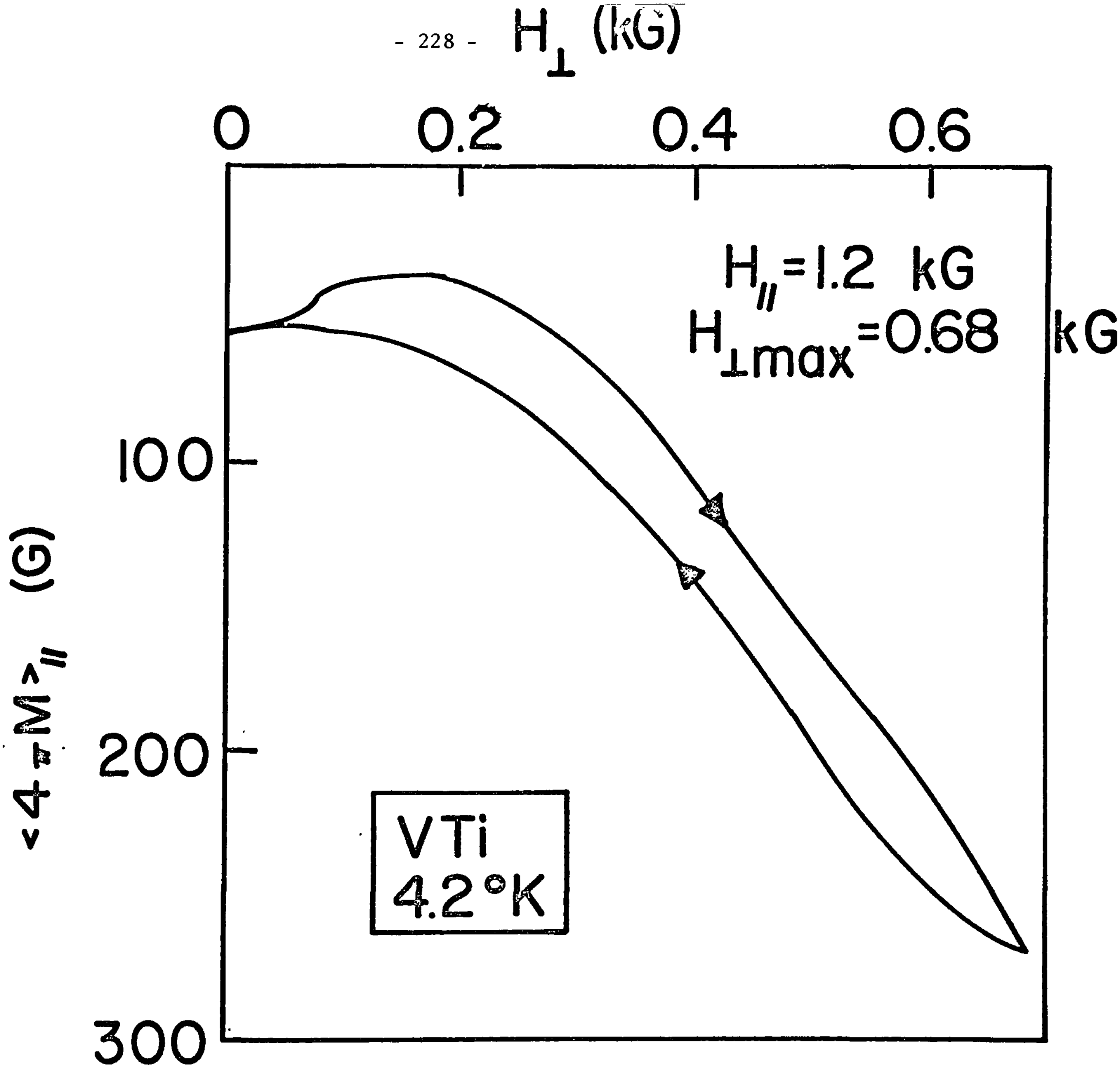

Figure 82: Experimental values of $<4\pi M>_{/\!/}$ versus cycling $H_\perp$ for VTi. $H_{/\!/}$ = 1.2kG, $H_{\perp max}$ = 0.68kG.

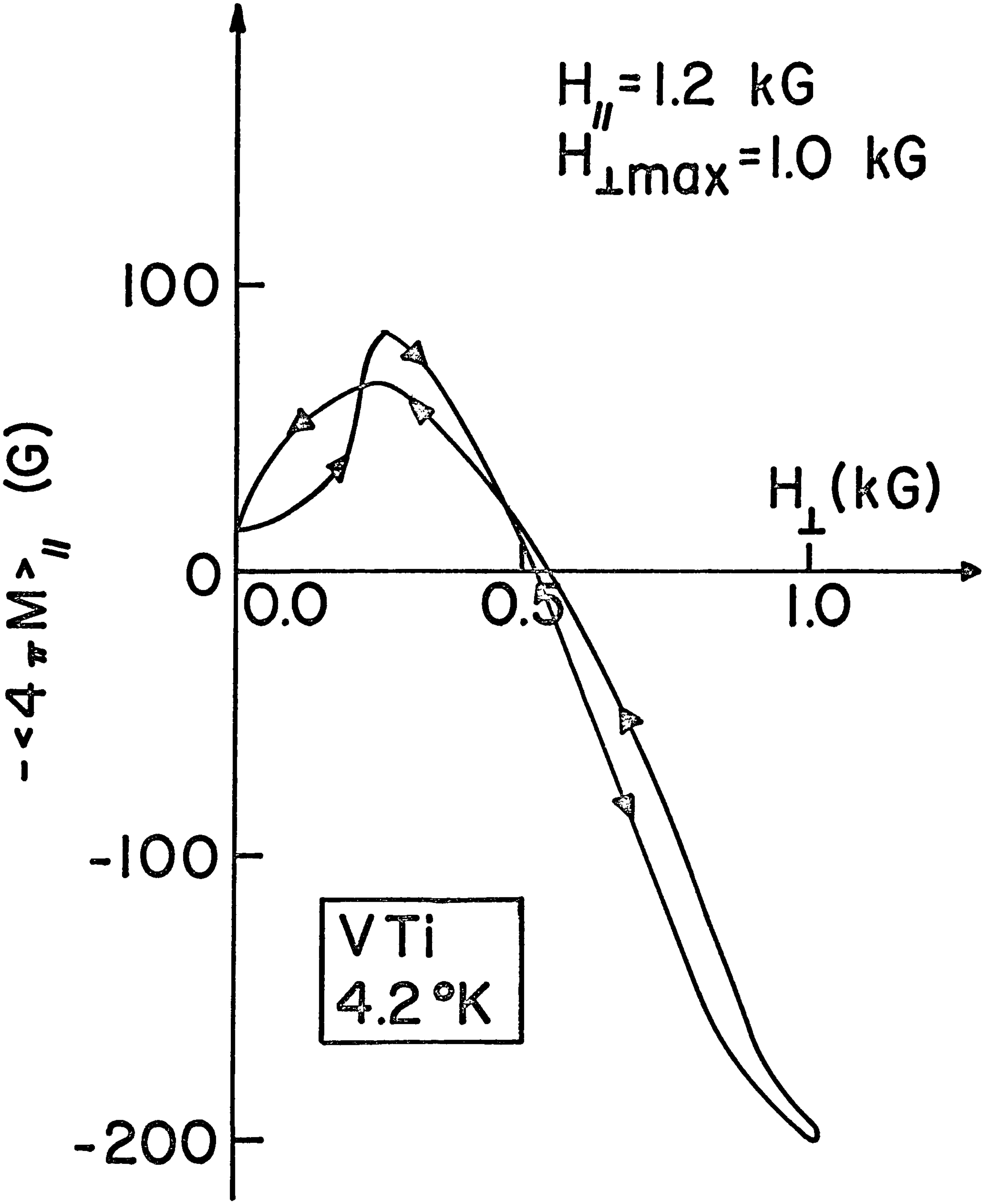

Figure 83: Experimental values of $\langle 4\pi M\rangle_{//}$ versus cycling $H_{\perp}$ for VTi. $H_{//} = 1.2kG$, $H_{\perp max} = 1.0kG$.

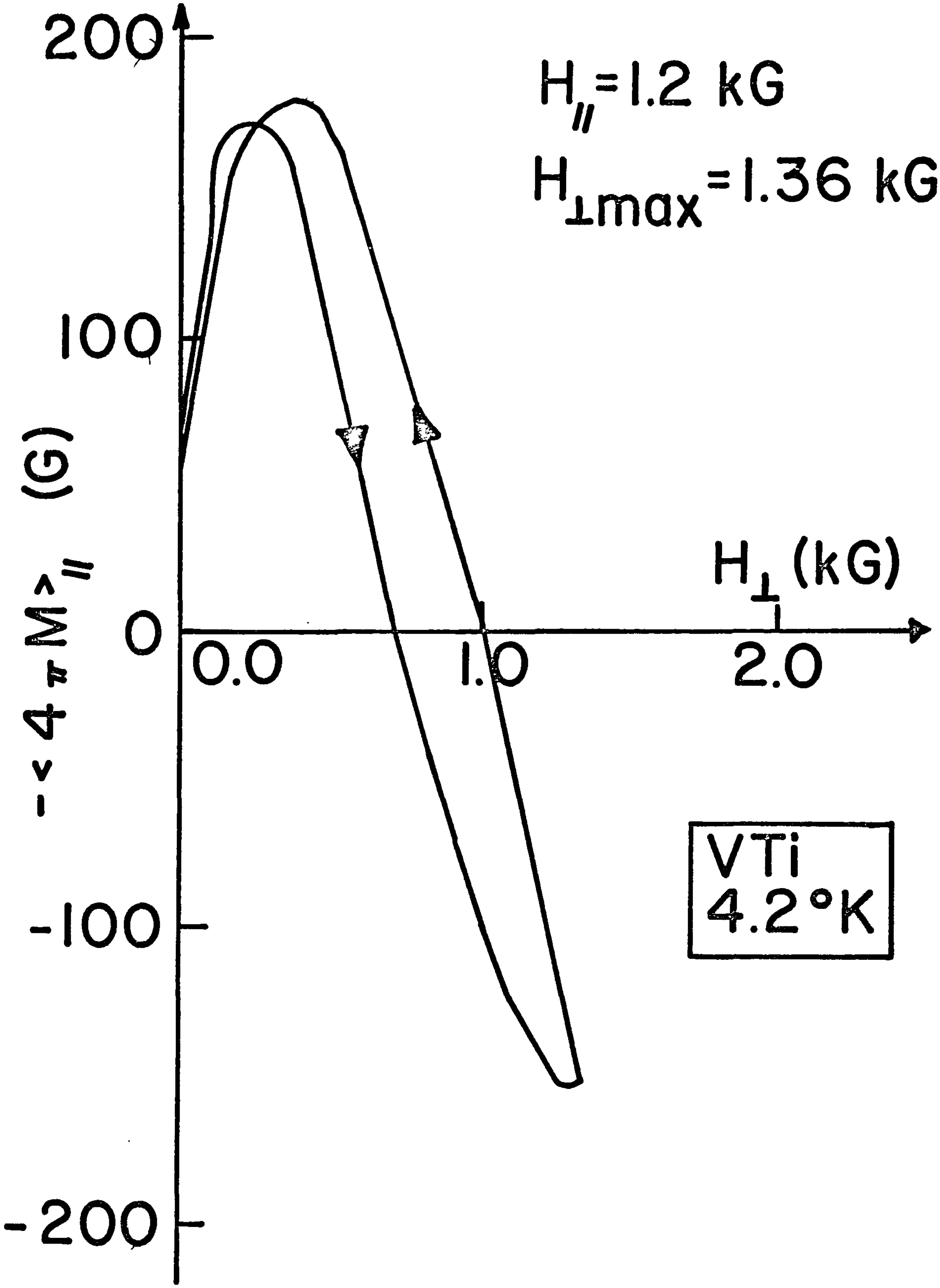

Figure 84: Experimental values of $\langle 4\pi M\rangle_{//}$ versus cycling $H_{\perp}$ for VTi. $H_{//} = 1.2$kG, $H_{\perp max} = 1.36$kG.

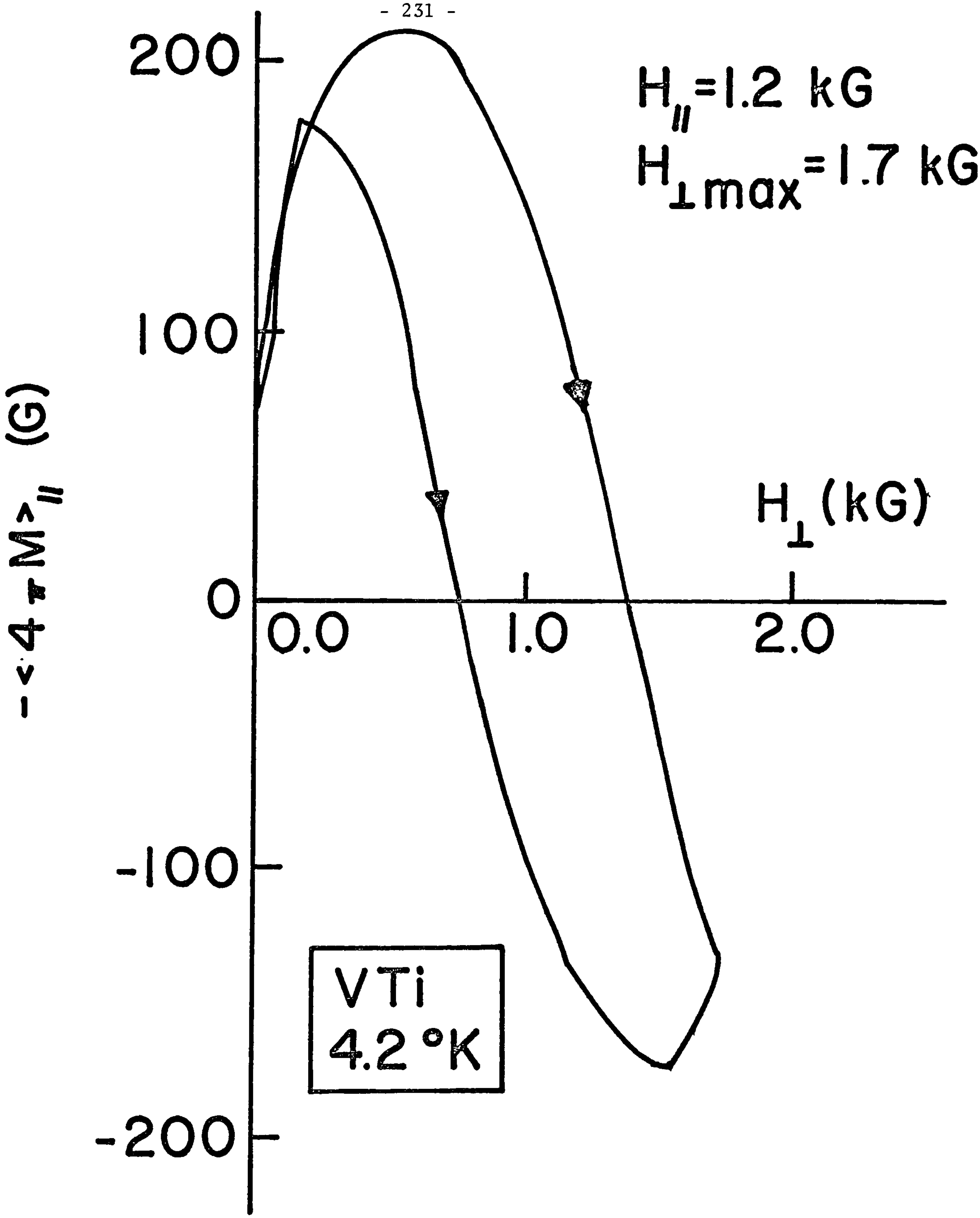

Figure 85: Experimental values of $\langle 4\pi M \rangle_{\parallel}$ versus cycling $H_{\perp}$ for VTi. $H_{\parallel}$ = 1.2kG, $H_{\perp\, max}$ = 1.7kG.

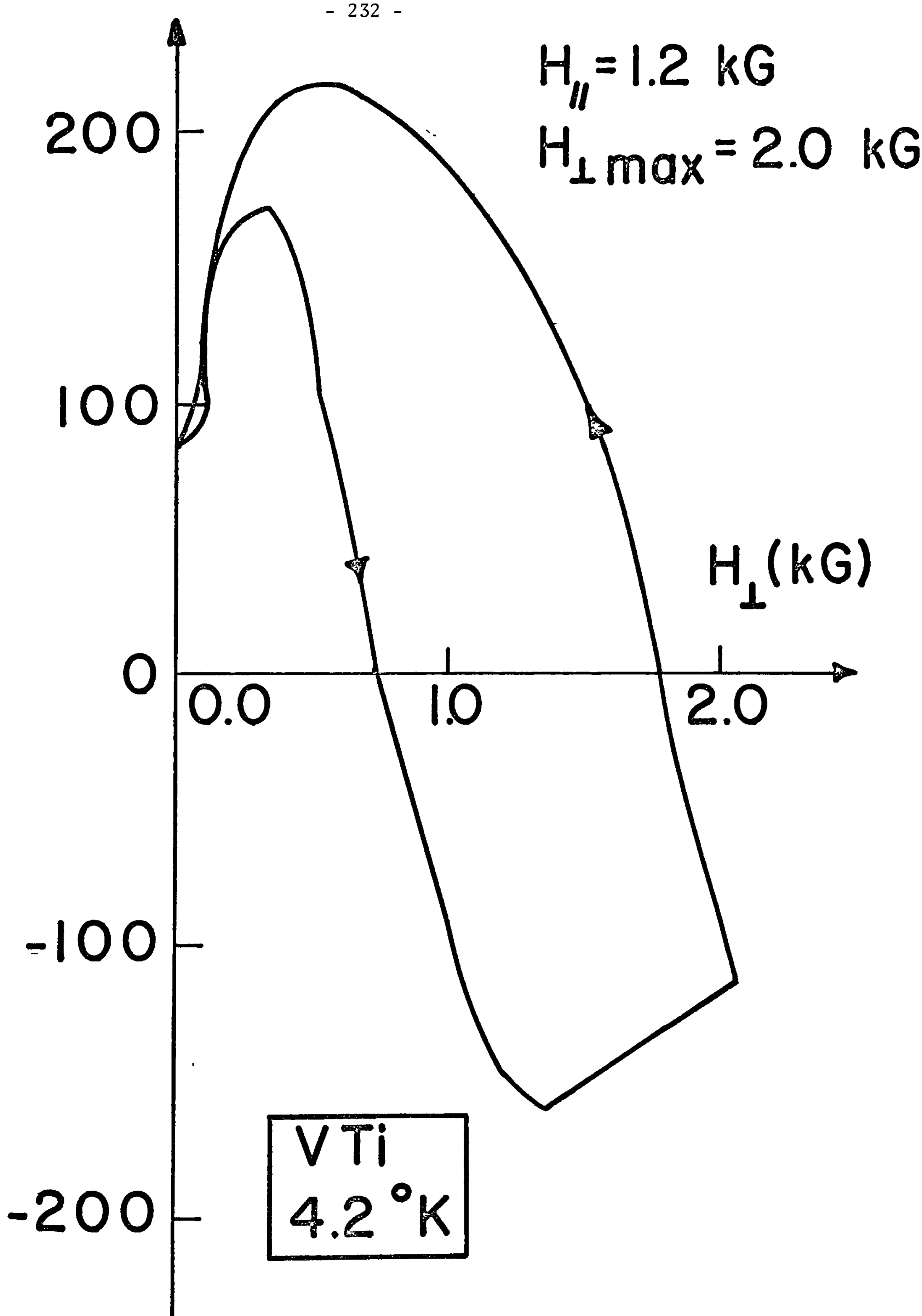

Figure 86: Experimental values of $\langle 4\pi M\rangle_{//}$ versus cycling $H_{\perp}$ for VTi. $H_{//} = 1.2$kG, $H_{\perp max} = 2.0$kG.

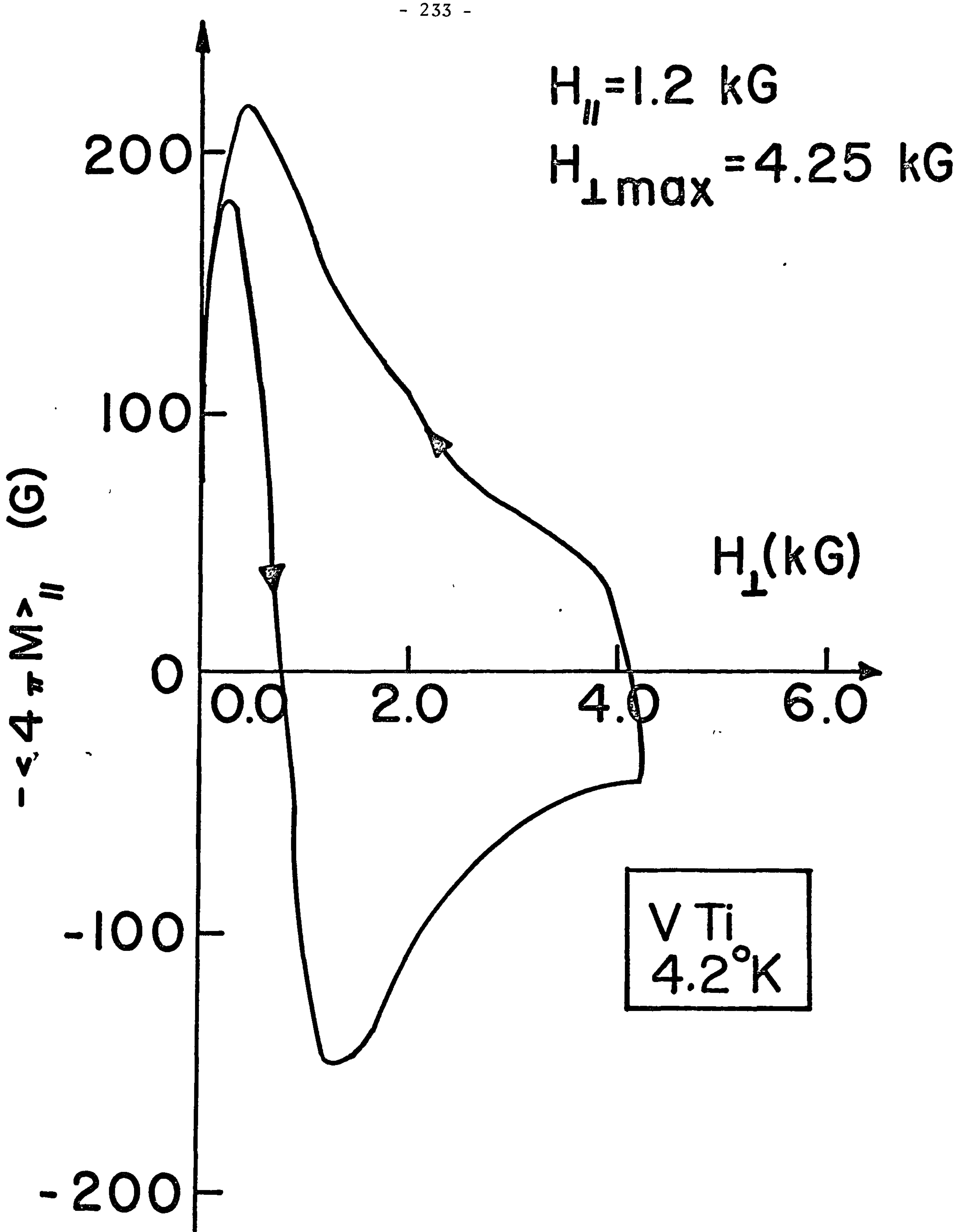

Figure 87: Experimental values of $\langle 4\pi M\rangle_{//}$ versus cycling $H_\perp$ for VTi. $H_{//}$ = 1.2kG, $H_{\perp max}$ = 4.25kG.

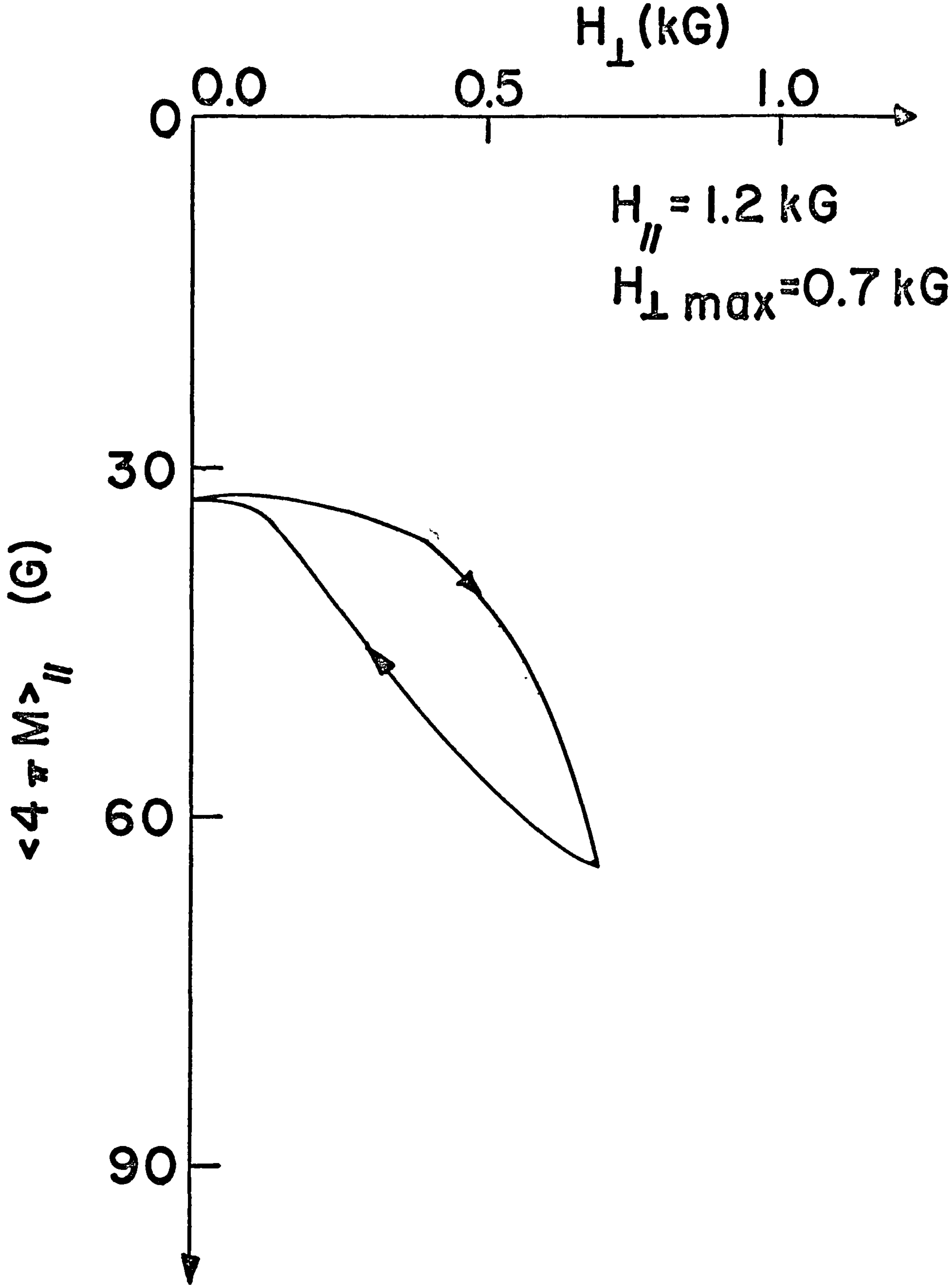

Figure 88: Calculated values of $\langle 4\pi M\rangle_{//}$ versus cycling $H_\perp$ for VTi. (V.R. model).

$H_{//}$ = 1.2kG, $H_{\perp max}$ = 0.7kG.

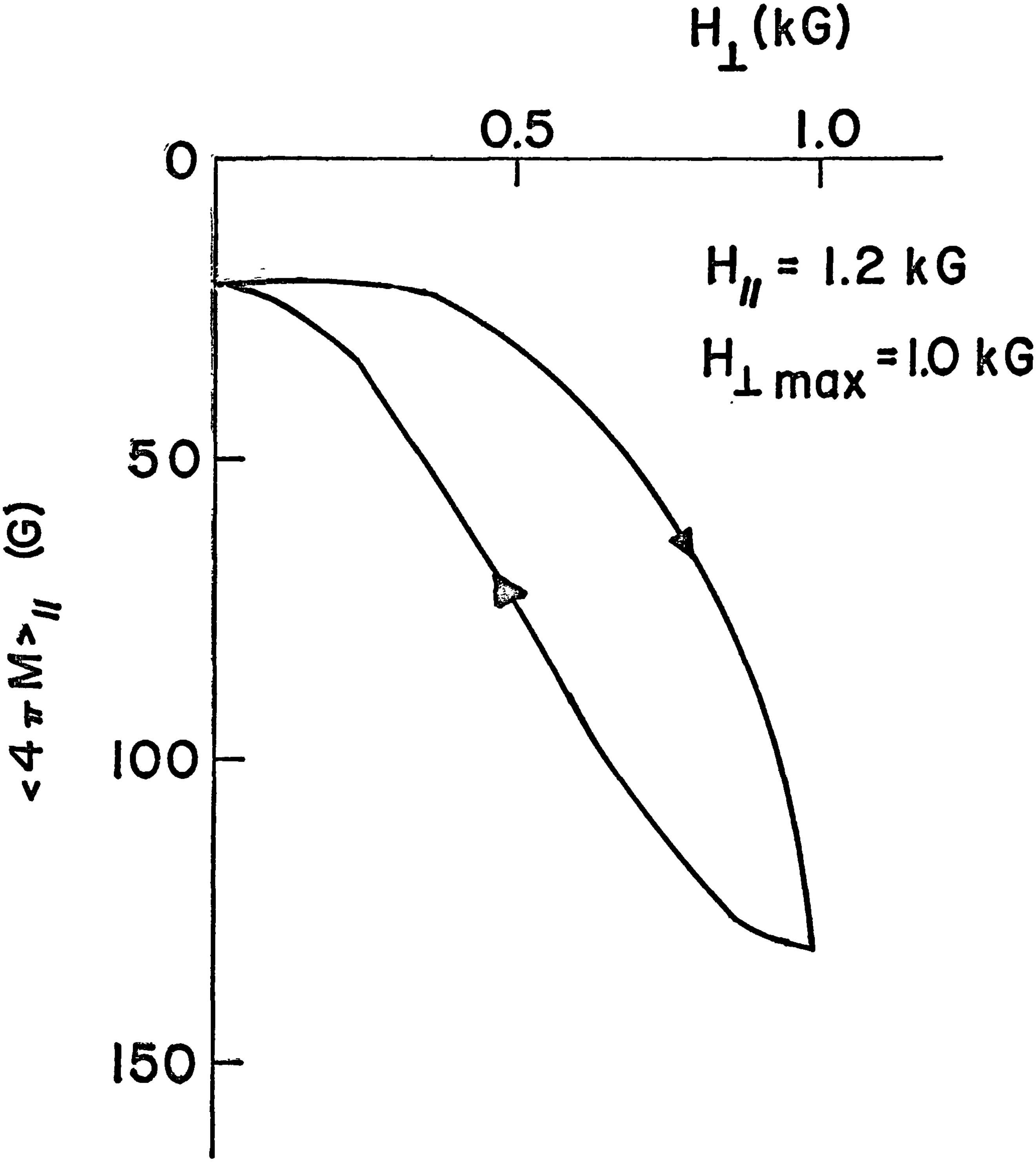

Figure 89: Calculated values of $<4\pi M>_{//}$ versus cycling $H_{\perp}$ for VTi (V.R. model).

$H_{//} = 1.2$kG, $H_{\perp max} = 1.0$kG.

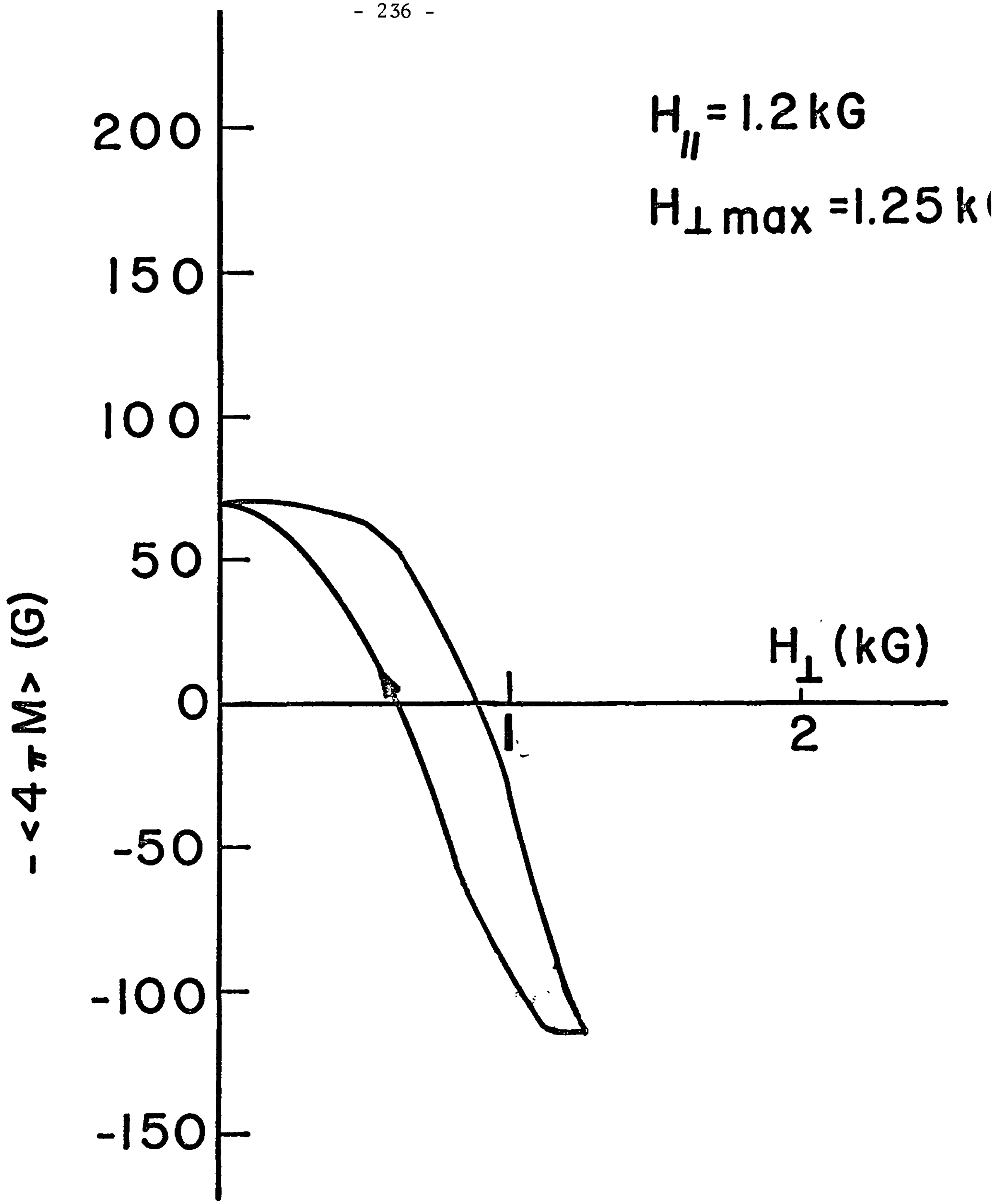

Figure 90: Calculated values of $\langle 4\pi M \rangle_{//}$ versus cycling $H_{\perp}$ for VTi (V.R. model).

$H_{//} = 1.2\text{kG}$, $H_{\perp max} = 1.25\text{kG}$.

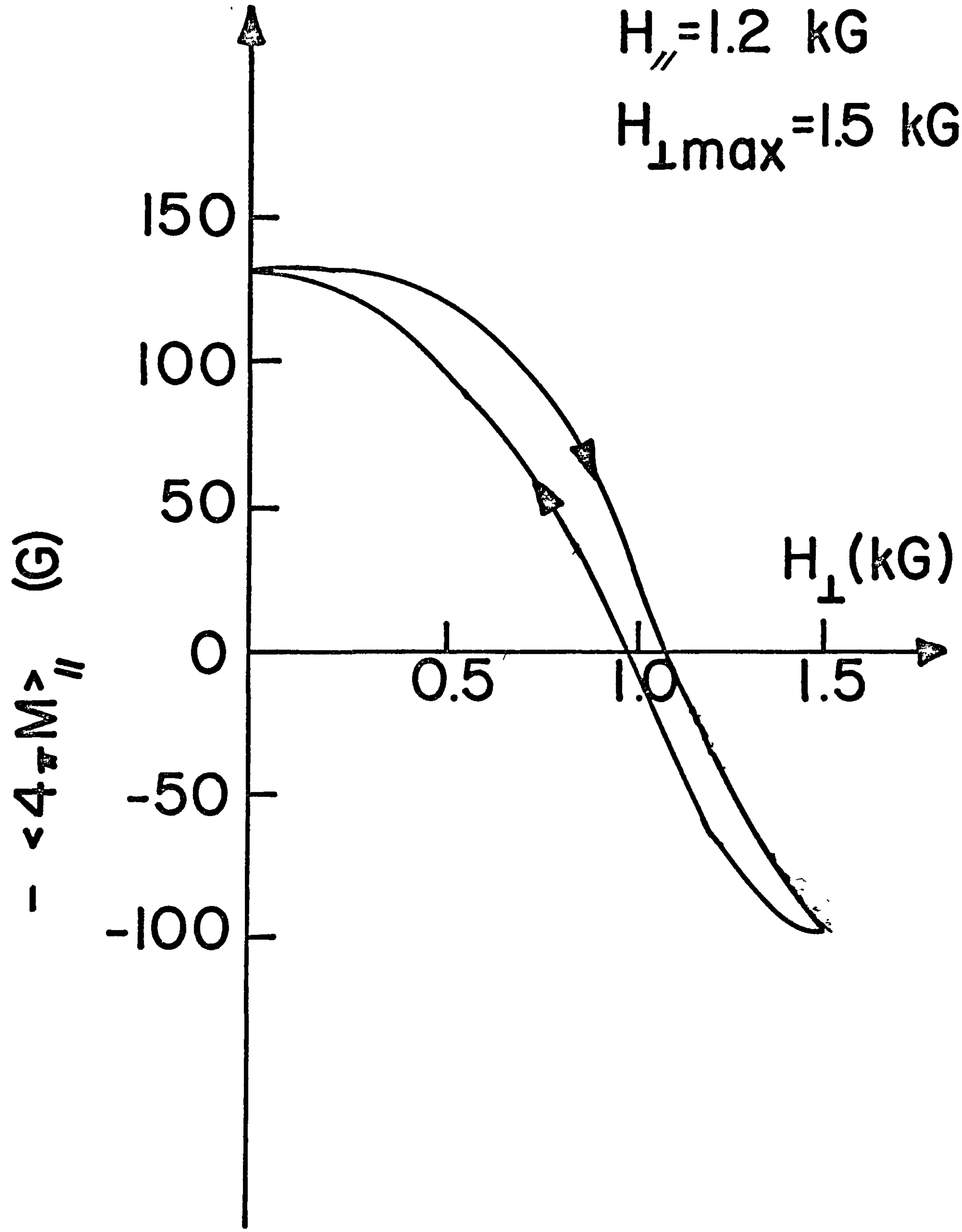

Figure 91: Calculated values of $\langle 4\pi M\rangle_{//}$ versus cycling $H_{\perp}$ for VTi (V.R. model).

$H_{//} = 1.2$kG, $H_{\perp max} = 1.5$kG.

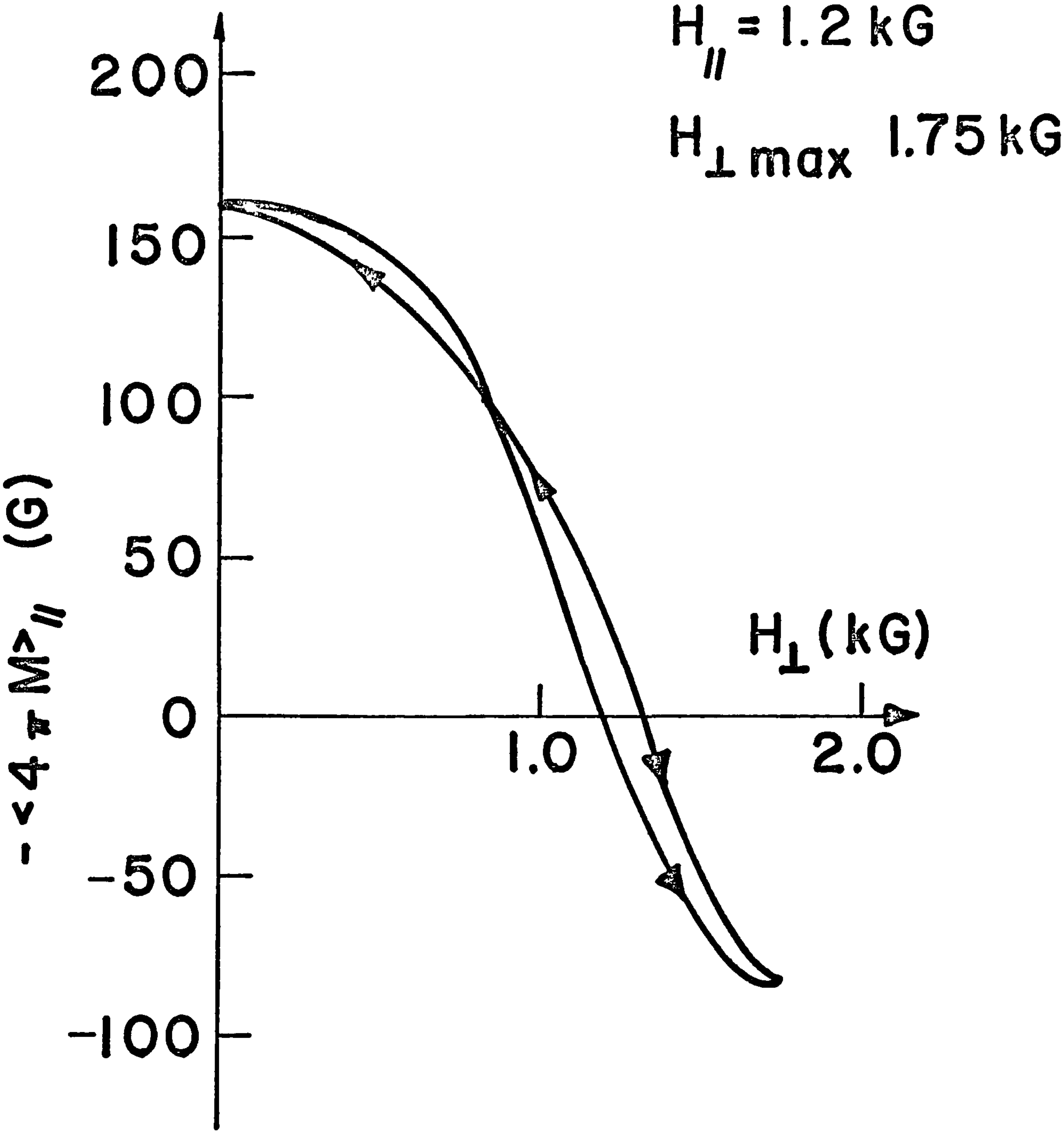

Figure 92: Calculated values of $\langle 4\pi M\rangle_{//}$ versus cycling $H_{\perp}$ for VTi (V.R. model).

$H_{//} = 1.2$kG, $H_{\perp max} = 1.75$kG.

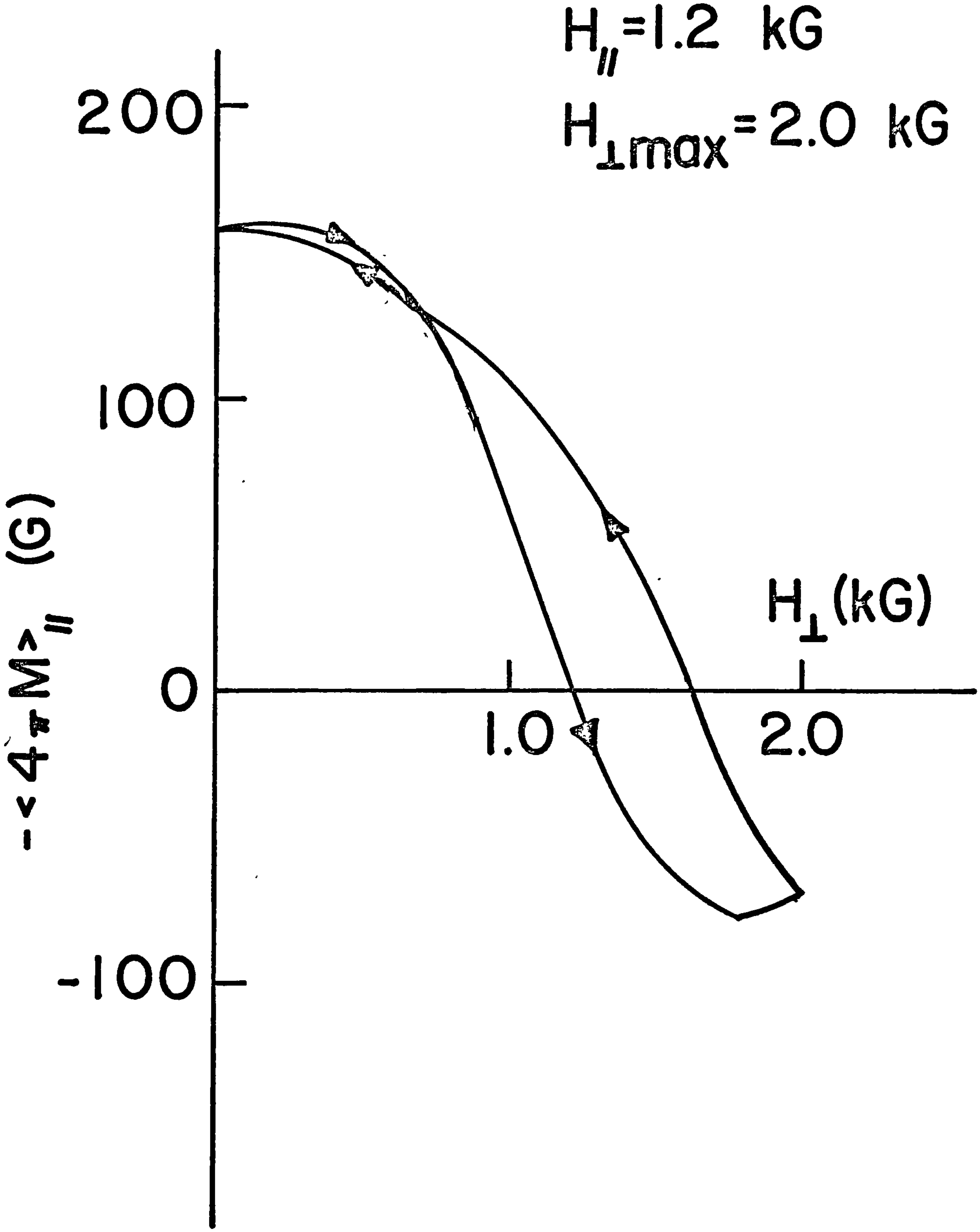

Figure 93: Calculated values of $\langle 4\pi M \rangle_{//}$ versus cycling $H_{\perp}$ for VTi (V.R. model).

$H_{//}$ = 1.2kG, $H_{\perp max}$ = 2.0kG.

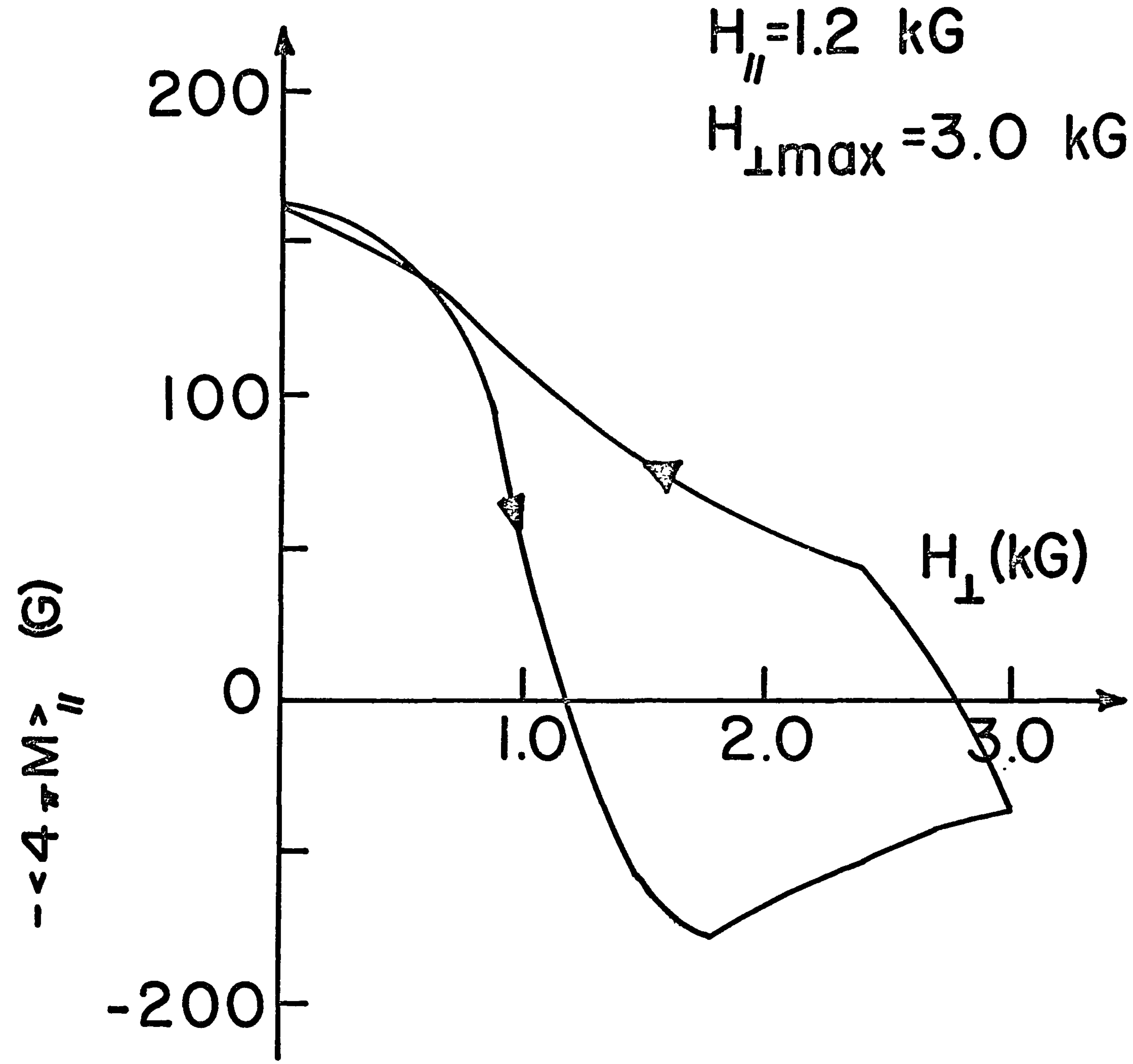

Figure 94: Calculated values of $\langle 4\pi M\rangle_{//}$ versus cycling $H_\perp$ for VTi (V.R. model).

$H_{//}$ = 1.2kG, $H_{\perp max}$ = 3.0kG.

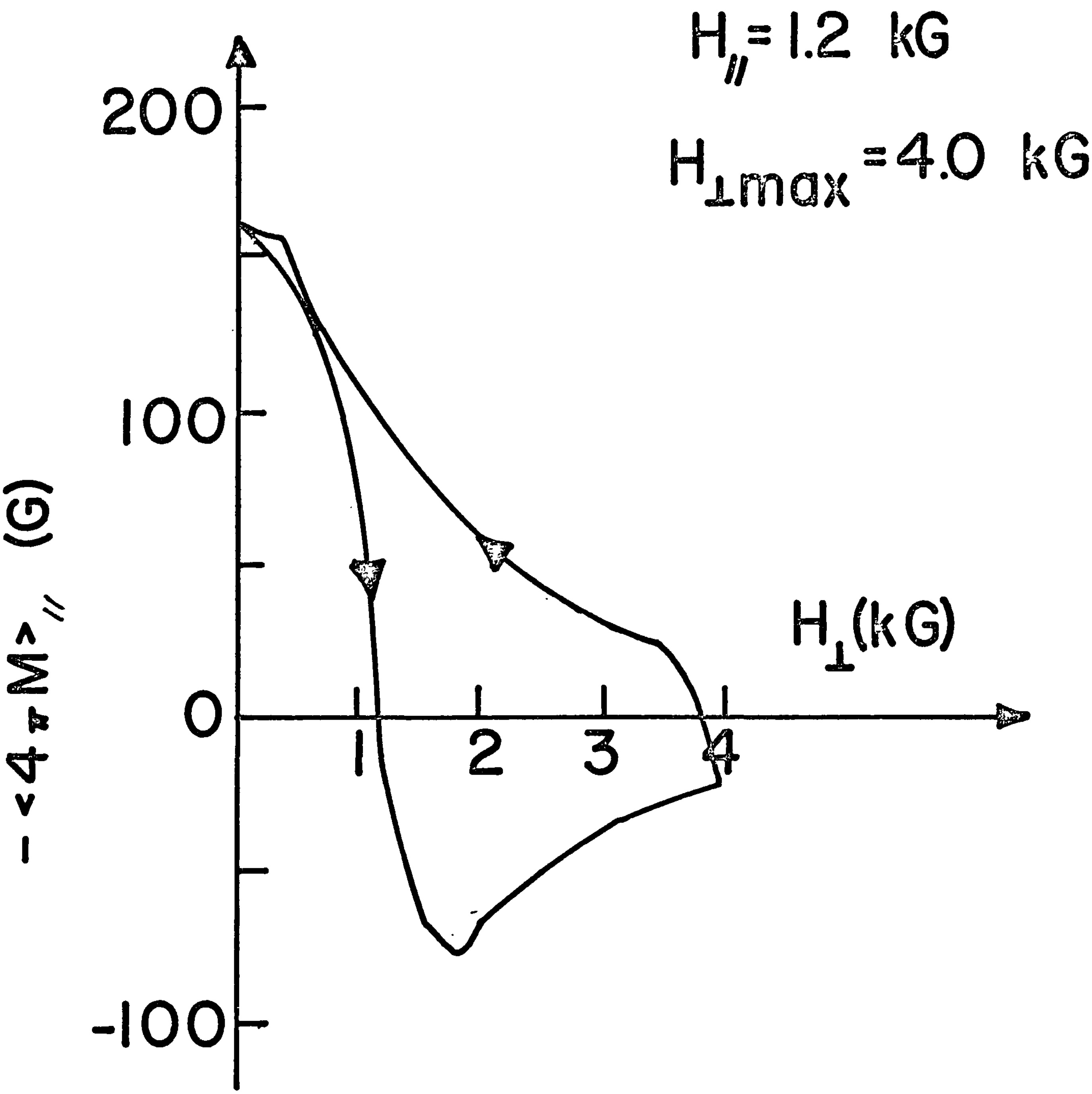

Figure 95: Calculated values of $\langle 4\pi M \rangle_{//}$ versus cycling $H_{\perp}$ for VTi (V.R.model).

$H_{//}$ = 1.2kG, $H_{\perp max}$ = 4.0kG.

(ii) $H_{\perp}$ changes direction (cycling through zero)

We now examine the magnetic response of the slab when the transverse field $H_{\perp}$ traverses the zero value and alternates in polarity as it is made to oscillate between $H_{\perp max}$ and $H_{\perp min}$ (see Figure 27). In other words, $H_{\perp max}$ and $H_{\perp min}$ are oppositely directed hence differ in sign. These extrema may also differ in magnitude. The symmetric case where $|H_{\perp max}| = |H_{\perp min}|$ is of particular interest. We wish to point out again that the response of the specimen to a symmetric driving field is equivalent to that obtained in the circumstances where a full wave alternating conduction current is fed along the length of the ribbon from an external supply. The amplitude of the driving transport current is related to the amplitude of the driving transverse field by the expression $I_{max} = 2\ H_{\perp max}\ \ell_y/\mu_o$ with I_{max} in amperes, $H_{\perp max}$ in Gauss, ℓ_y in cm and $\mu_o = 4\pi/10$ (practical system of units). We will only examine the symmetric case, $|H_{\perp max}| = |H_{\perp min}|$ in our discussion below since this situation is easier to visualize. Our analysis however can be readily extended to the general case where $|H_{\perp max}| \neq |H_{\perp min}|$.

We need to consider three different phases in the sequence of events, namely, (1) $H_{\perp max}$ is applied from zero thereby establishing the initial conditions for the cycle, (2) $H_{\perp}$ is reduced from $H_{\perp max}$ to 0 and (3) $H_{\perp}$ is varied from 0 to $-H_{max}$. In order to complete the cycle, $H_{\perp}$ must be swept back from $-H_{\perp max}$ through 0 to $+H_{\perp max}$. This "second" half of the full cycle, however, merely repeats the behaviour encountered during phases 2 and 3 with appropriate changes of sign hence contains no new features. Phases 1 and 2 have already been considered in detail in the previous section and need to be reexamined here again. We suggest that the reader return to Figures 73, 74 and 75 for a review of the sequences of profiles generated during these two phases.

We focus mainly on the new features which emerge during phase 3 as $H_{\perp}$ is varied from 0 to $-H_{\perp max}$. To simplify the discussion we take it that at the beginning of phase 1, $H_{\perp i} = 0$, hence $\theta_i = 0$. Also we consider only the situation where at the end of phase 2, the leading edge of the second B disturbance has advanced deeper than the front of the first θ disturbance (i.e. $x_1' > x_o$). These two stipulations not only simplify the analysis but also correspond to the situation encountered in our measurements and our calculations for the VTi sample.

Since $H_s = ((-H_{\perp})^2 + H_{//}^2)^{\frac{1}{2}}$, the applied magnetic field increases in magnitude from $H_{//}$ to H_{max} as $H_{\perp}$ is varied from 0 to $-H_{\perp max}$. Thus a "compressional" B disturbance penetrates deeper and deeper into the slab as phase 3 progresses. Consequently, also, H_s varies through two complete cycles for each full cycle traversed by $H_{\perp}$.

The crucial difference with the situation considered in the previous section lies in the spatial variation of the θ disturbance which now changes with depth from $-\theta_s$ through zero to positive values eventually reaching and following the θ profile existing at the end of phase 2. Let x''_{oo} denote the depth where θ crosses the zero axis. There are two possibilities: the θ-profile goes through zero before or after the depth where the new or third B disturbance reaches the B-profile existing at the end of phase 2. (i.e. $x''_{oo} \gtrless x''_1$). We examine the conditions under which $x''_{oo} \lessgtr x''_1$ in appendix III. We consider only the former possibility here since it is more frequently encountered and corresponds to the situation we meet in the analysis of our observations on the VTi sample. We have however, studied the second possibility and it does not contain any basically new features besides more or equally complicated b_z and b_y profiles. We refer the reader to Figures 96 and 97 which schematically present the various profiles at the end of phase 2 and some intermediate stage during phase 3 respectively for the specific situation under scrutiny.

Since for the situation under study, the second B disturbance has penetrated deeper than the first θ disturbance, i.e. $x'_1 > x_o$, region B' then consists of two sub-regions denoted B'_I and B'_{II} which differ in the following respect. In both sub-regions the flux has been decompressed while retaining the existing θ profile which in sub-region B'_I is not uniform and was established during

- 245 -

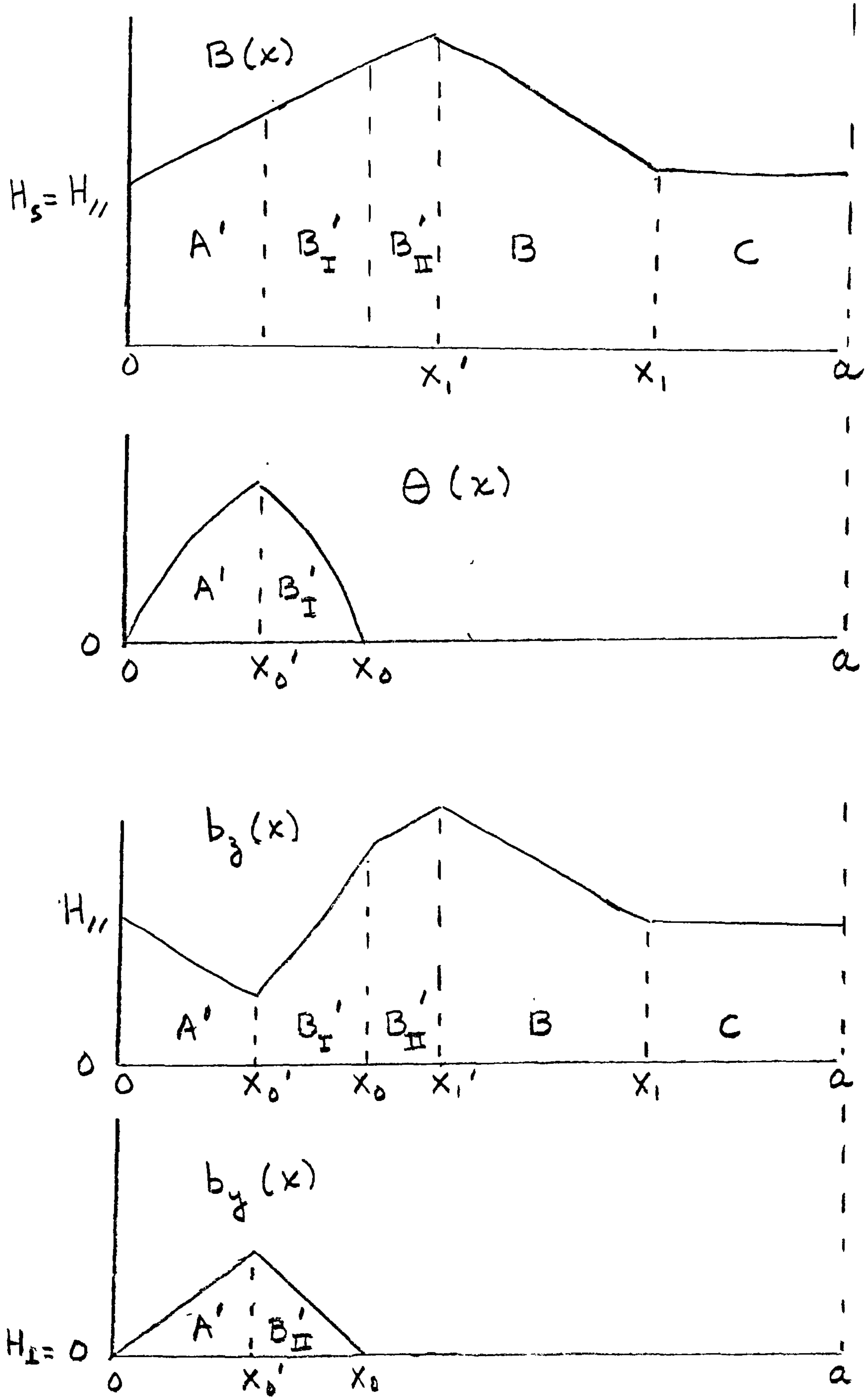

Figure 96: Schematic of magnetic induction and angular profiles at end of phase 2 ($H_\perp$ cycling through zero).

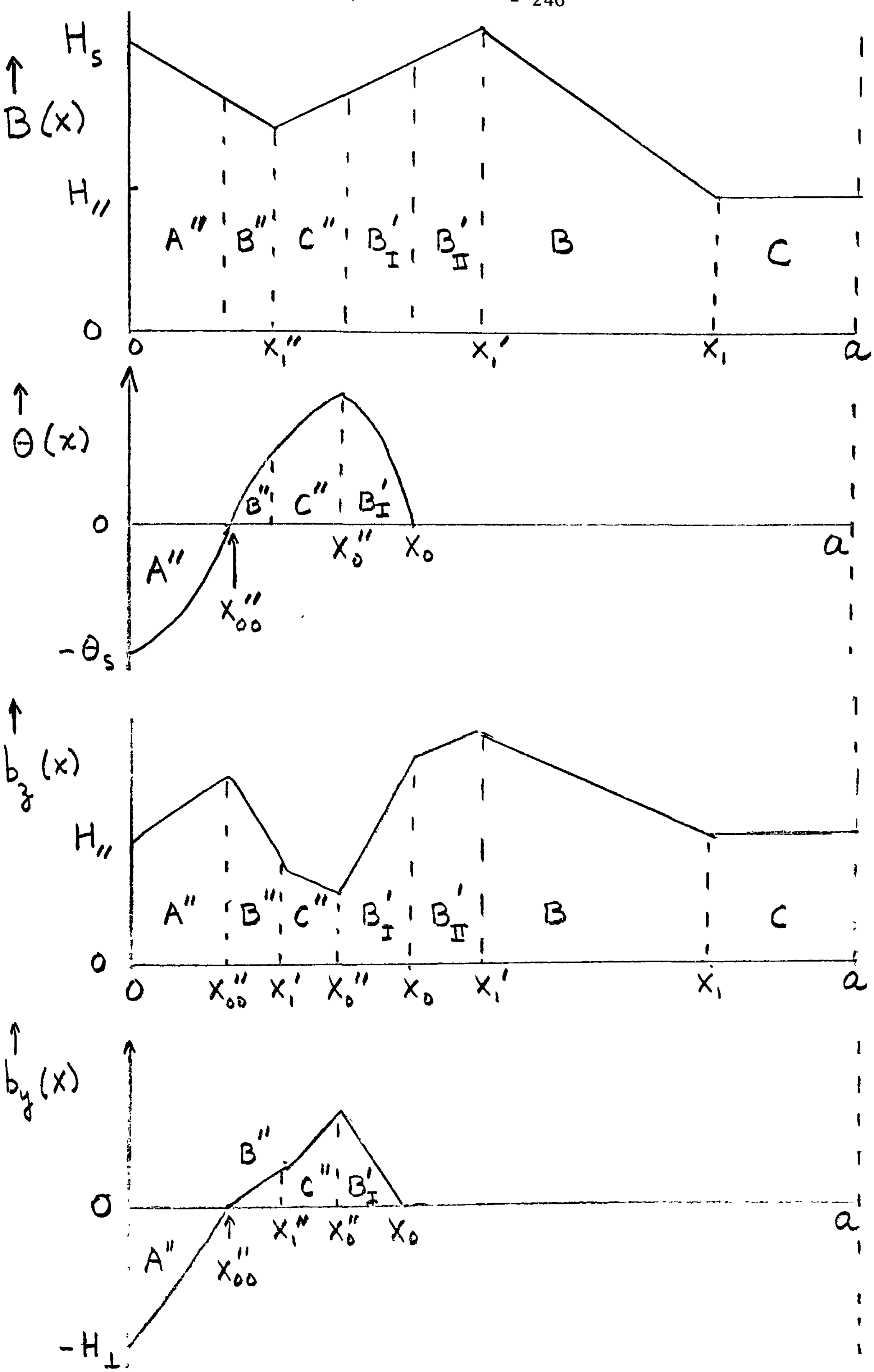

Figure 97: Schematic of magnetic induction and angular profiles during phase 3 ($H_\perp$ cycling through zero).

phase 1 whereas in sub-region B'_{II}, this profile is uniform and was established before phase I began (here $\theta(x) = \theta_i = 0$). The existence of these two sub-regions was indicated previously. We pause to point them out here because they have not been presented schematically in the earlier discussion.

We can identify 3 distinct new regions as $H_\perp$ is swept from 0 to $- H_{max}$, hence as θ at the surface varies from 0 to $-\theta_{s\ max}$.

Region A", $0 < x \leq x''_{oo}$

This region is penetrated by both the B and θ disturbances. The angle θ decreases in magnitude from θ_s at the surface to 0 at x''_{oo}.

Region B", $x''_{oo} \leq x \leq x''_1$

This region is also penetrated by both the B and θ disturbances. It differs from region A" only in that the angle θ <u>increases</u> in magnitude with depth, whereas the flux density <u>decreases</u> with depth. We have not encountered this behaviour before. This constitutes a crucial new feature. In order to describe the θ, b_z and b_y profiles in this region we must reassess the basic prescription we have been exploiting so far. We return to this important aspect shortly.

Region C", $x''_{oo} \leq x \leq x''_o$

This region is penetrated by the new θ disturbance only. The flux lines then have undergone a change in orientation while retaining the existing density configuration (B profile). We have not encountered this behaviour previously either. The reason this did not occur in the situations examined so far is that our basic prescription for the rotation of the flux lines causes the θ profile to vary more rapidly than the B profile. As a consequence, the B disturbance generally penetrated deeper than the accompanying θ disturbance. For the first time in this thesis we confront a situation where due to special circumstances, the opposite occurs and the new θ disturbance penetrates further than the new B disturbance. We will see below how our basic rule is applied to this situation.

It is useful at this juncture to review the essential features of our analysis of the response of the slab to changes in the magnitude and direction of the applied field H_s. Firstly we determine the B profile and the profile of its gradient dB/dx from the application of the critical state concept taking previous magnetic history into account. After this is accomplished we have several options at our disposal to determine the orientation of the vortices hence map out the θ, b_z and b_y profiles, namely equations 6-5, through 6-10. The choice among these equations is entirely a matter of convenience since they are different formulations of the same basic empirical rule. We have frequently exploited equation 6-6 in our discussion since to our mind it provides a particularly transparent description of the b_z profiles. In constructing our computer program we elected to use equation 6-7 together with the definitions $b_z = B \cos\theta$ and $b_y = B \sin\theta$. Other choices would have been equally satisfactory.

We note however that equations 6-6 through 6-10 are derived from equation 6-5 hence this expression should be regarded as our basic empirical postulate. We now point out that this expression and thus the others that flow from it apply when the gradients of B and $|\theta|$ have the same sign but are inadequate to describe the variation in the orientation of the vortices in situations where $|\theta|$ increases (decreases) while B decreases (increases) in magnitude. We are confronted by such a situation in region B" discussed above since here the magnetic induction B decreases but the angle of the vortices' θ increases from x''_{oo} to x''_1. Noting that $b_z = B$ since $\theta = 0$ ($\cos\theta = 1$) at x''_{oo} then clearly the expression $db_z/d_x = -k\, dB/dx$ and the relation immediately obtained from this, $b_z = H_{//}\,(H_s/B)^k$, if applied rigorously to this region lead to $b_z > B$ which is physically nonsensical since $B = (b_z^2 + b_y^2)^{\frac{1}{2}}$.

We can resolve the difficulty and retain some of the important features of our phenomenological starting point by introducing a modified form of equation 6-5, namely.

$$\frac{1}{b_z}\,\frac{db_z}{dx} = \frac{k'}{B}\,\frac{dB}{dx} \qquad \text{6-18}$$

applicable to situations where the gradient of B and the gradient of the magnitude of θ are of opposite sign. We retain the prescription $db_z/b_z dx = -k\ dB/B\ dx$ to govern the change in direction of the vortices in all other situations i.e. where the gradient of B and the gradient of the magnitude of θ have the same sign. We will see below that a single expression for the gradient of θ can be obtained provided that $k' = k + 2$. This choice of two different although analogous starting points depending on the physical circumstances seems artificial and arbitrary. These two prescriptions or routes however lead to one specific operational formula to which we can ascribe physical meaning. We develop this feature below.

If we wish to utilize the integral form of equation 6-18 (and of its analogue 6-5 as we have done already) we must be careful to introduce the appropriate boundary values for the integrals of db_x and dB. By way of illustration we apply equation 6-18 to region B".

$$\int_{b_z(x)}^{b_z(x''_{oo})} \frac{db_z}{b_z} = k' \int_{B(x)}^{B(x''_{oo})} \frac{dB}{B} \qquad 6\text{-}19$$

This yields

$$\frac{b_z(x''_{oo})}{b_z(x)} = \left\{\frac{B(x''_{oo})}{B(x)}\right\}^{k'} \qquad 6\text{-}20$$

where $x''_{oo} \leq x \leq x''_1$

However from integration of equation 6-5 over region A'' (hence where equation 6-6 is valid) we obtain

$$b_z\,(x''_{oo}) \;=\; B(x''_{oo}) \;=\; (H_{//}H_s^{\;k})^{\frac{1}{k+1}} \qquad 6\text{-}21$$

Introducing this result in equation 6-20 leads to a relation between between b_z and B valid for region B'',

$$b_z = \frac{B^{k'}}{(H_{//}H_s^{\;k})^{\frac{k'-1}{k+1}}} \qquad 6\text{-}22$$

this expression although cumbersome in appearance nevertheless states clearly that b_z decreases rapidly with distance into region B'' where B is diminishing.

Clearly from a knowledge of B at x''_1 we can determine b_z at that plane. We can then use these boundary values in the integration of equation 6-5 valid for region C'' in order to obtain an explicit relation between b_z and B there. It is obvious however that these expressions will become increasingly complicated and thus lose their usefulness. These considerations also carry over in the value of rewriting $\cos\,\theta = b_z/B$ explicitly in terms of B(x) i.e. eliminating b_z.

It is interesting and worthwhile however to introduce equation 6-18 in the expression

$$\frac{d\theta}{dx} = \frac{1}{B\,\sin\,\theta}\,\left(\frac{b_z}{B}\,\frac{dB}{dx} - \frac{db_z}{dx}\right) \qquad 6\text{-}23$$

obtained by differentiating $b_z = B\,\cos\,\theta$ with respect to x. This yields

$$\frac{d\theta}{dx} = \frac{(1 - k')}{B^2 \sin\theta} b_z \frac{dB}{dx} \qquad 6\text{-}24$$

If, however we introduce equation 6-5 in equation 6-23 we obtain

$$\frac{d\theta}{dx} = \frac{(1 + k)\, b_z}{B^2 \sin \theta} \frac{dB}{dx} \qquad 6\text{-}25$$

Letting $k' = k + 2$ we can combine equations 6-24 and 6-25 as follows

$$\frac{d\theta}{dx} = \pm \frac{(1 + k)\, b_z}{B^2 \sin \theta} \frac{db}{dx} \qquad 6\text{-}26$$

where the + sign applies to situations where the gradients of B and $|\theta|$ have the same sign and the - sign when the gradients of B and $|\theta|$ differ in sign.

Introducing the critical state equation in the form $dB/dx = F_p(B)/B$ in equation 6-26 we obtain

$$\frac{d\theta}{dx} = \pm \frac{(1 + k)\, b_z}{B^3 \sin \theta} F_p (B) \qquad 6\text{-}27$$

and $$\frac{d\theta}{dx} = \pm \frac{(1 + k)\, F_p(B)}{B^2 \tan \theta} \qquad 6\text{-}28$$

where we have used the definition $b_z/B = \cos \theta$. This last expression in particular enables us to appreciate the physical content of our empirical rule for the variation of the orientation of the vortices. This formulation states that the pinning force density linearly opposes the rotation of the vortices. Also it shows a high density (close packing) of flux lines facilitates the degree of rotation which can be achieved per unit of distance along the rows of vortices. These two features seem physically reasonable and provide the basis for a derivation of the critical gradient of θ from first principles. The tan θ term in the denominator indicates that the rotation of planes of vortices becomes progressively considerably more difficult as their orientation approaches the z axis. This term assigns a privileged status to the z-axis. Presumably it is a consequence of the fact that in our experiment this direction indeed has a special physical significance. It is generally along this axis that the flux lines are oriented when the ribbon becomes superconducting. Further in our work we maintain $H_z \equiv H_{//}$ fixed while $H_{\perp}$ varies. Presumably in the analysis of phenomena where both H_z and H_y are made to vary simultaneously (although not necessarily at the same rate) such as in rotating fields the tan θ term should not be present. Finally we note that the coefficient k is a constant of proportionality or adjustable parameter which may be temperature dependent.

Results and Discussion

In the next pages (Figures 99 through 102) we present a series of loops calculated for the longitudinal component of the magnetization as $H_{\perp}$ is cycled through zero over larger and larger amplitudes in a chosen static longitudinal field $H_{//}$. The parameters used in the computation are those chosen earlier for the VTi sample and are listed in table III. Figure 103 shows a magnetization loop measured at large amplitude for this material. Due to technical difficulties, experimentally reliable loops for smaller amplitudes were not available at the time of submission of this thesis.

The b_z profiles for the calculation of the loops were computed using equations 6-5 and 6-18 and numerically integrated to give $\langle 4\pi M\rangle_{//}$. Figure 99 shows sequences of computed b_z profiles during phases 2 and 3 of the cycle.

We note from inspection of Figures 99 through 102 that at low amplitudes, the loop is entirely located in the lower quadrants i.e. the locus of $\langle 4\pi M\rangle_{//}$ remains paramagnetic throughout the cycle. At larger amplitudes the locus of the z-magnetization travels through both upper and lower quadrants, i.e. $\langle 4\pi M\rangle_{//}$ swings between diamagnetic to paramagnetic as $H_{\perp}$ is swept back and forth. This migration of the loop and its straddling of the upper and lower quadrants at large amplitude was also encountered in the previous section for magnetization contours where $H_{\perp}$ did not reverse polarity during the cycle. The explanation presented there in terms of features of the b_z profile (depth and width of the valley, height and spread of the adjoining hill) also fully applies to the curves now under scrutiny.

Again we note that the juxtaposition of these loops in

$M_{//} - H_{\perp} - H_{//}$ space traces out a convoluted closed three dimensional surface or object. It appears that our model is again successful in generating the contours of an object in this space which corresponds in shape and size to that observed.

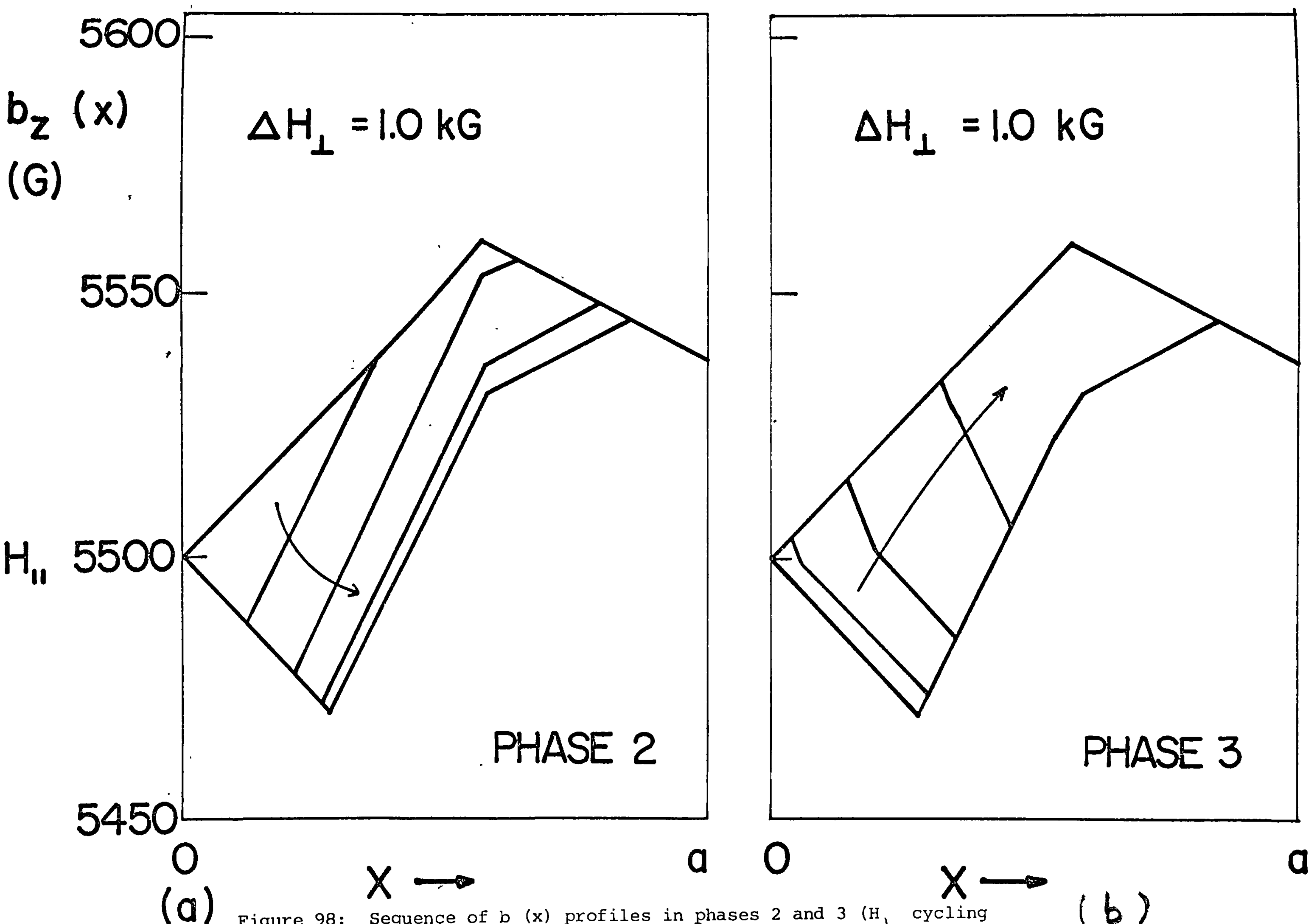

Figure 98: Sequence of $b_z(x)$ profiles in phases 2 and 3 ($H_{\perp}$ cycling through zero) calculated from the V.R. model for VTi.

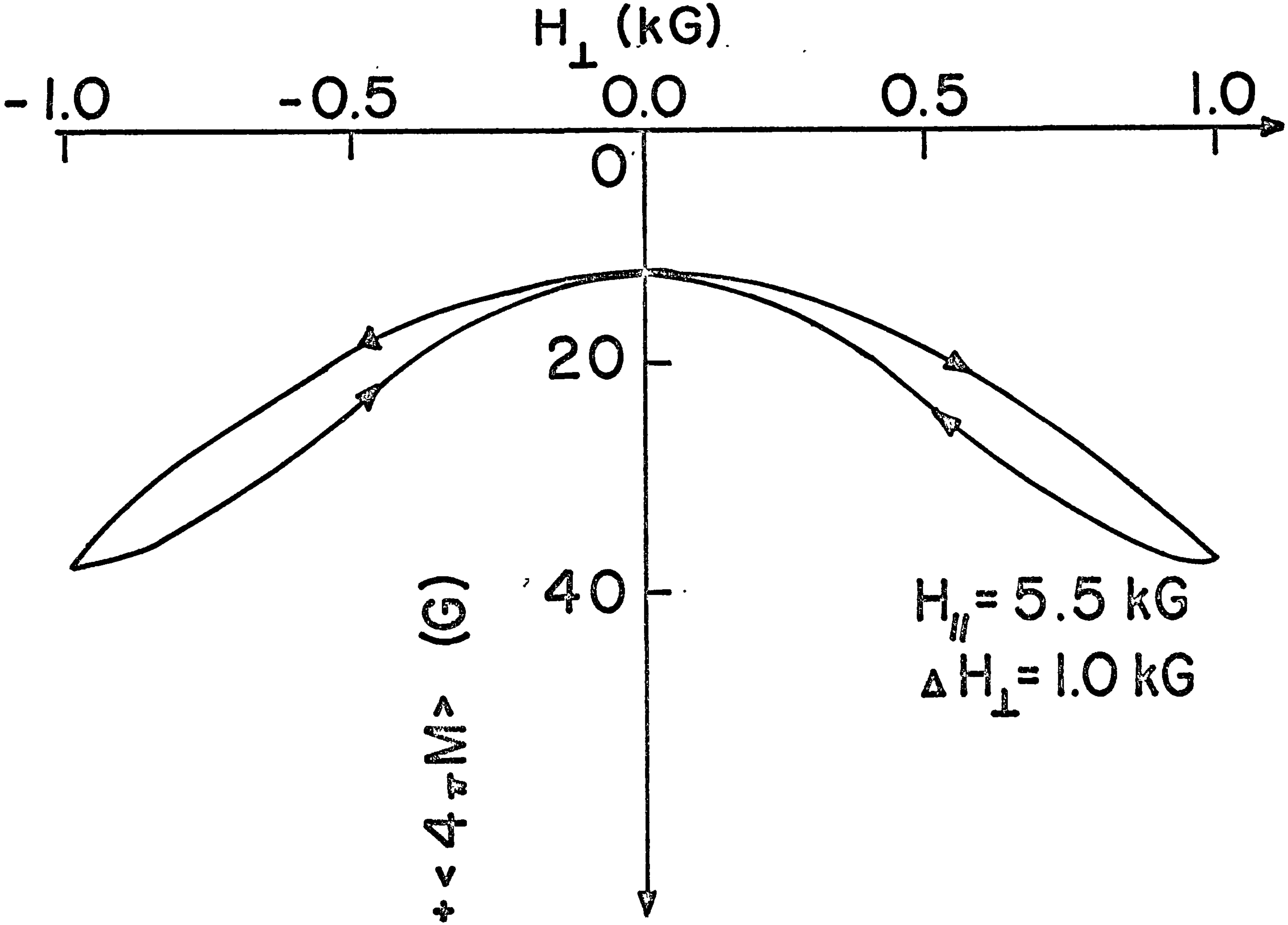

Figure 99: Calculated values of $<4\pi M>_{//}$ versus $H_\perp$ (cycling through zero).

$H_{//}$ = 5.5kG, $\Delta H_\perp$ = 1.0kG

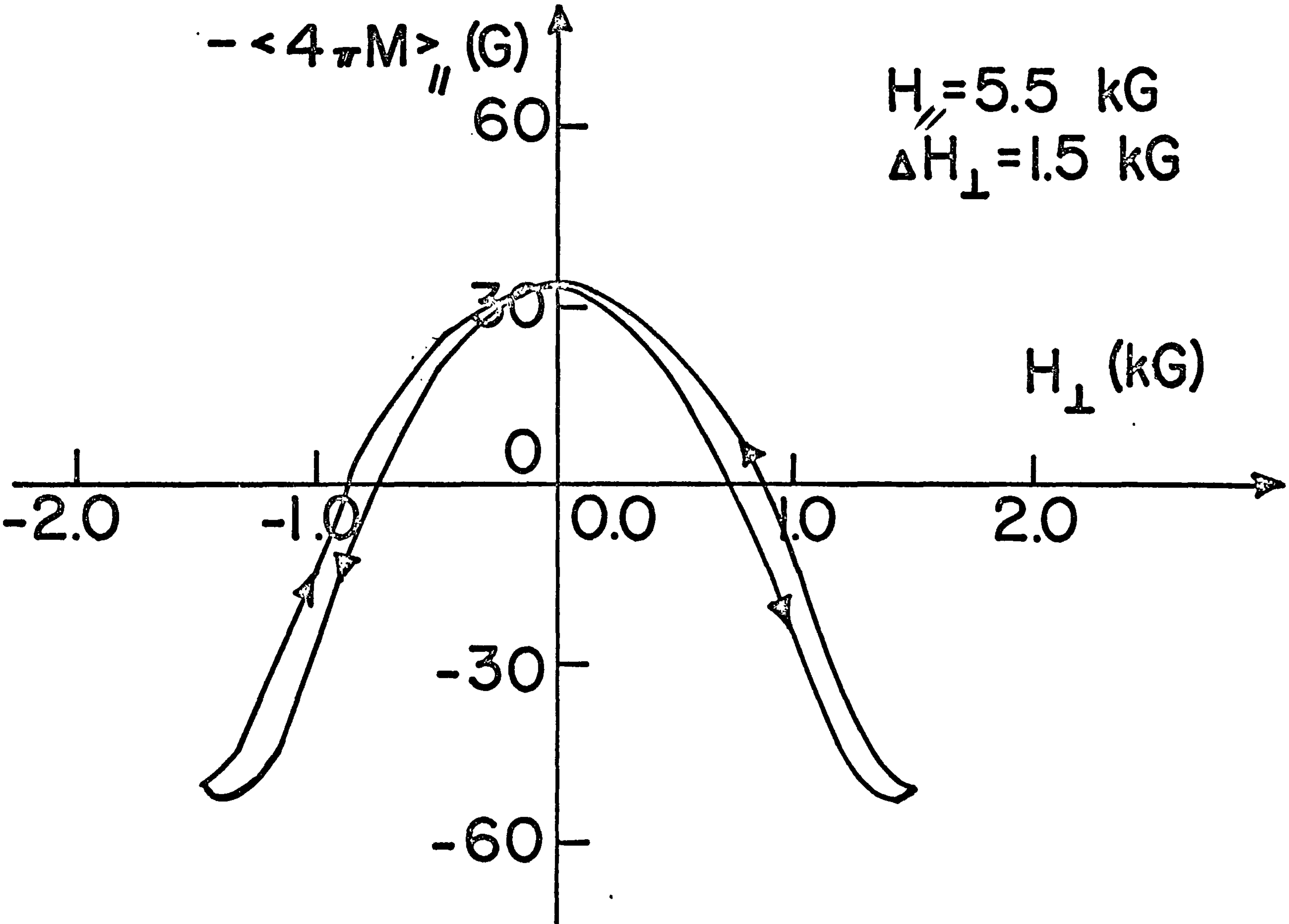

Figure 100: Calculated values of $\langle 4\pi M\rangle_{//}$ versus $H_{\perp}$ (cycling through zero).

$H_{//}$ = 5.5kG, $\Delta H_{\perp}$ = 1.5kG

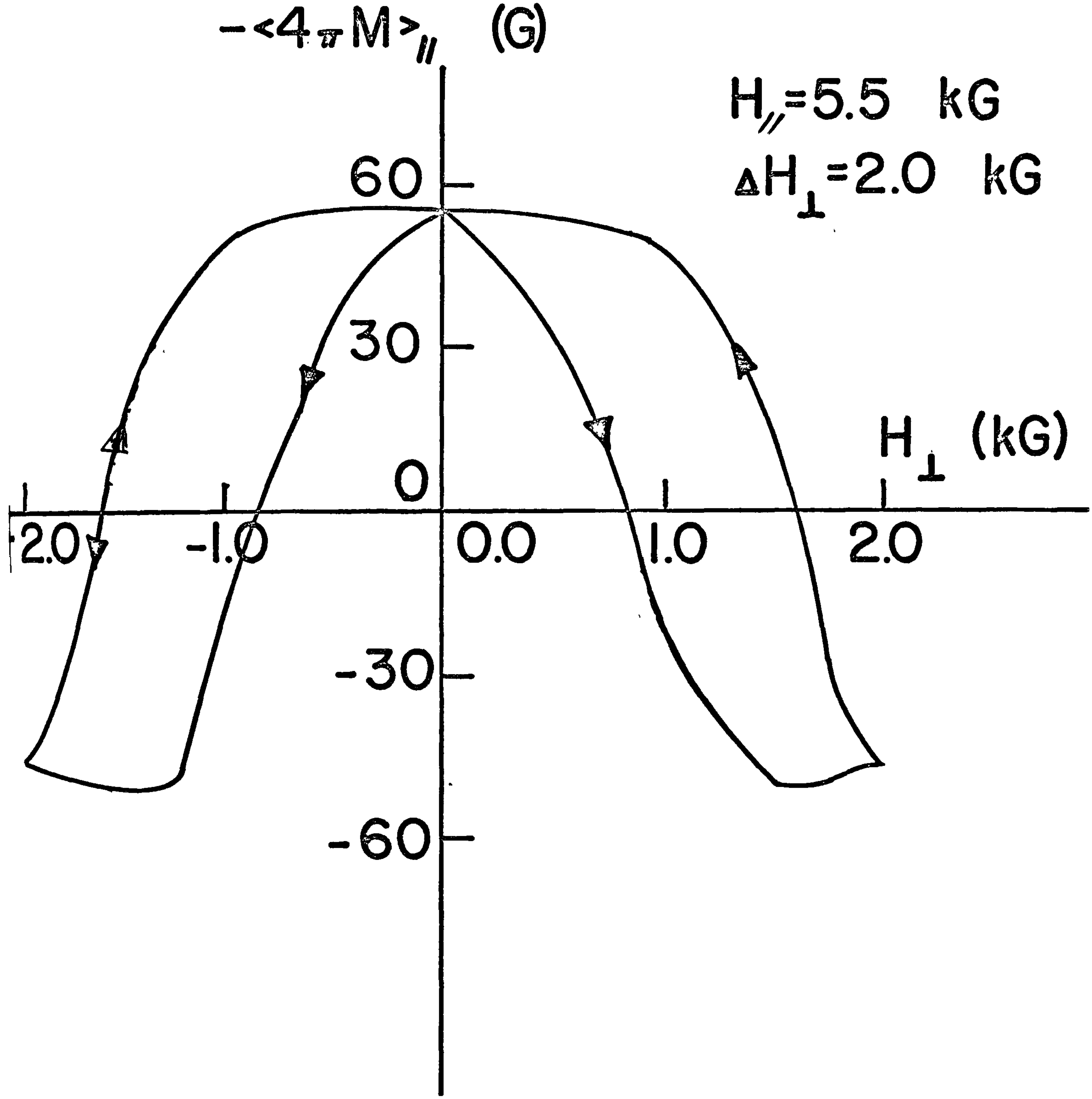

Figure 101: Calculated values of $\langle 4\pi M\rangle_{//}$ versus $H_{\perp}$ (cycling through zero).

$H_{//}$ = 5.5kG, $\Delta H_{\perp}$ = 2.0kG

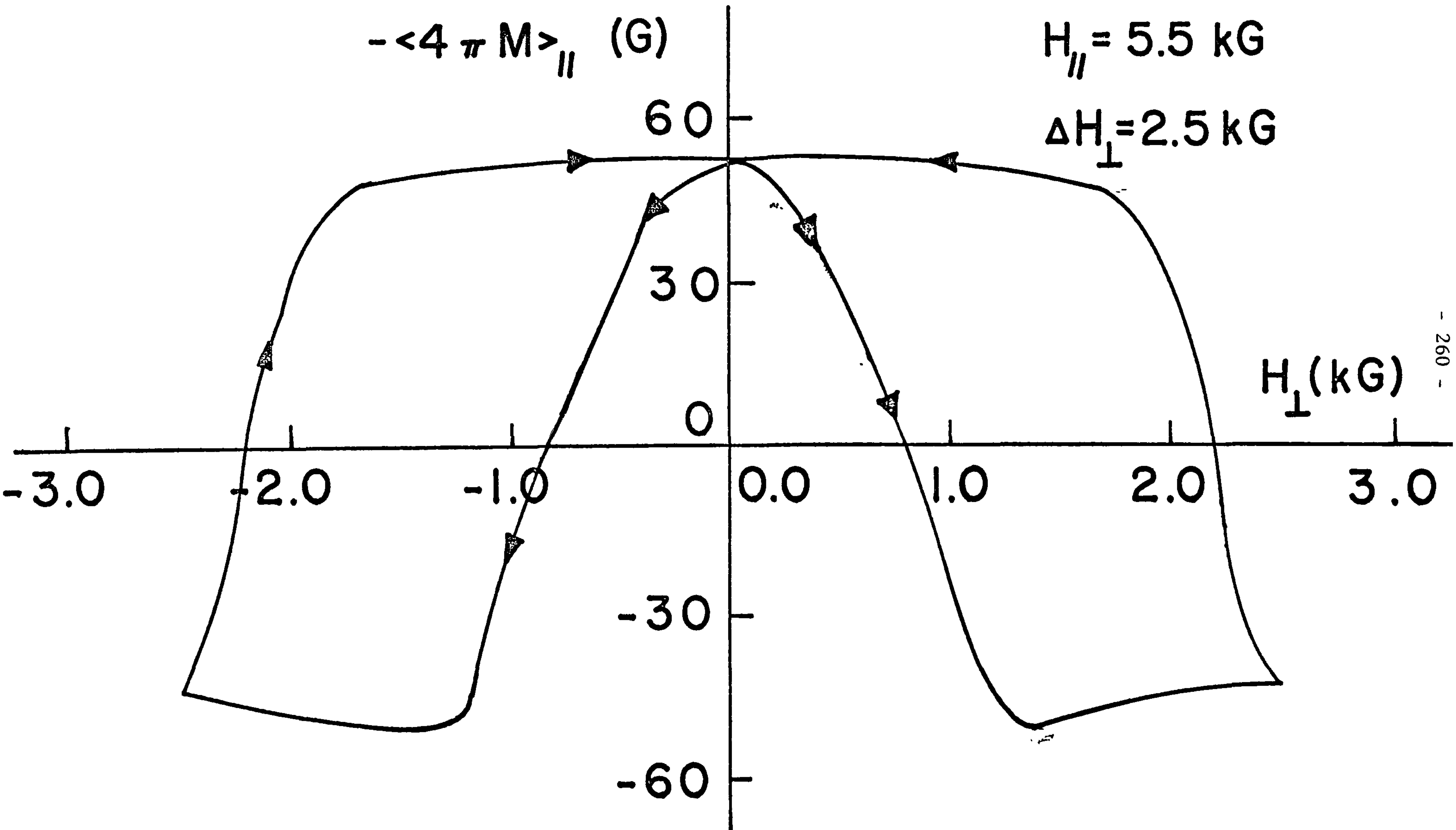

Figure 102: Calculated values of $\langle 4\pi M \rangle_{//}$ versus $H_{\perp}$ (cycling through zero).

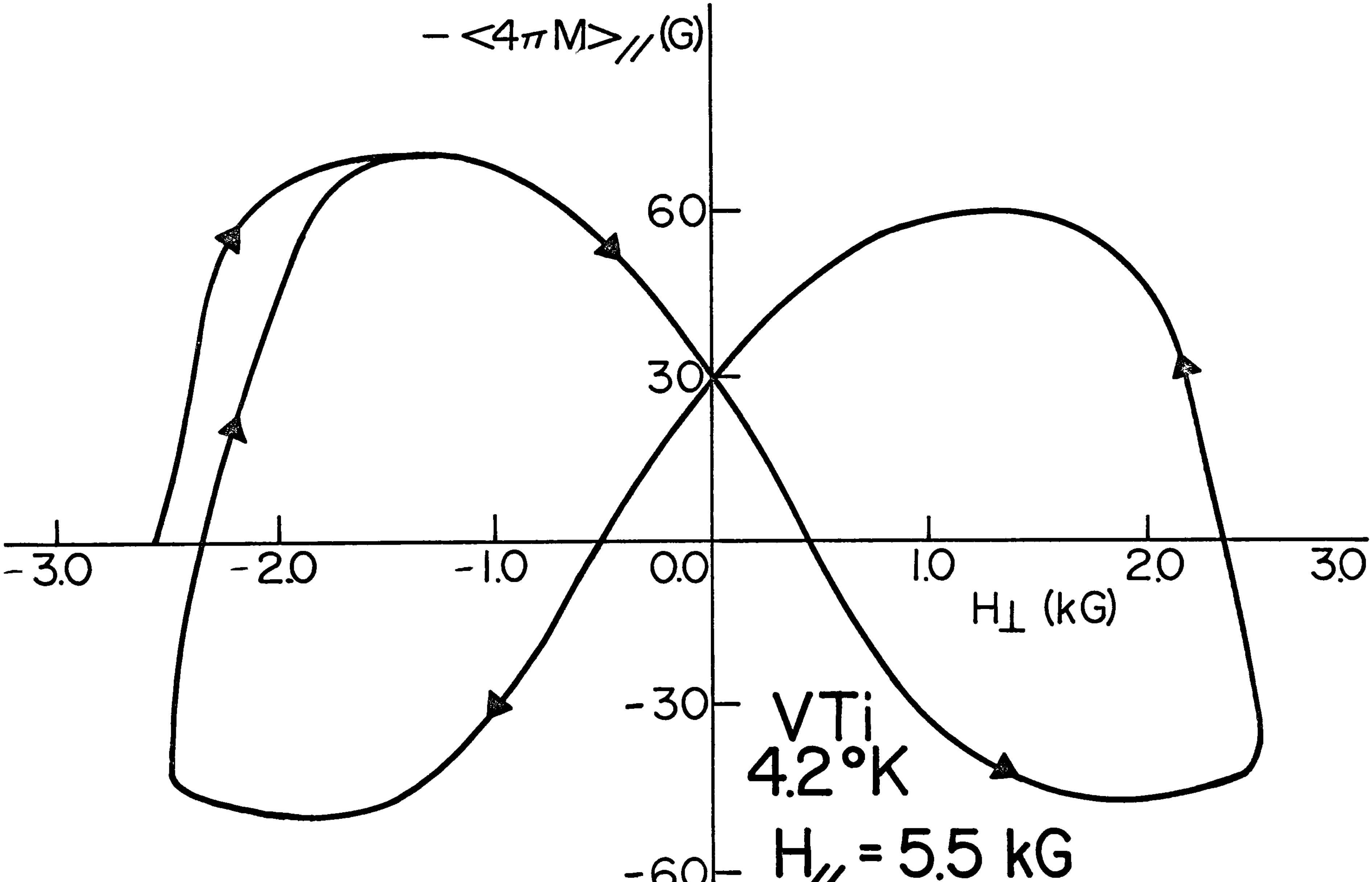

Figure 103: Experimental values of $\langle 4\pi M\rangle_{//}$ versus $H_\perp$ (cycling through zero)

$H_{//} = 5.5\text{kG}$, $\Delta H_\perp = 2.5\text{kG}$

IV Hysteresis Losses

Throughout the discussion of the previous section on the response of the ribbon samples to an oscillating transverse magnetic field in static longitudinal fields we have focussed attention on the locus of the longitudinal component of the magnetic moment $<4\pi M>_{//}$. We now turn our attention specifically to the loops traced out by $<4\pi M>_{\perp}$, the transverse component of the magnetization as $H_{\perp}$ is cycled. All the details needed however to determine $<4\pi M>_{\perp}$ and the contours it traces as $H_{\perp}$ is swept between $H_{\perp max}$ and $H_{\perp min}$ with and without reversal of polarity, have already been developed in the preceding section. Now that we have delineated the sequences of θ and b_z profiles, it is a straightforward matter to establish the corresponding b_y profiles from the definition $b_y = (B^2 - b_z^2)^{\frac{1}{2}}$ or $b_y = B \cos \theta$ and then to integrate these profiles numerically over the width of the slab to obtain $<B_y> = H_{\perp} + <4\pi M>_{\perp} = \int b_y \, d(x/a)$.

The loops of $<B_y>$ (or equivalently $<4\pi M>_{\perp}$) vs $H_{\perp}$ which we observe and calculate exhibit relatively uncomplicated "banana" silhouettes. A comparison between theory and experiment of the variation of the shape and location in the $M_{\perp} - H_{\perp}$ plane of these hysteresis loops as a function of the amplitude $\Delta H_{\perp}$ of the oscillation of $H_{\perp}$ and of the strength of the orthogonal bias field $H_{//}$ is not particularly illuminating. Nevertheless we note again for the sake of completeness that all of these results can be visualized in a three dimensional framework. A tracing out or juxtaposition of a complete group of hysteresis loops for a given amplitude $\Delta H_{\perp}$ in $M_{\perp}$ - $H_{\perp}$ - $H_{//}$ space defines a three dimensional closed surface hence the contours of a singly connected object. We also note that the particular choice of the central or mid value about which $H_{\perp}$ oscillates fixes the location of the spine of such a three dimensional body. Finally a family of such bodies similar in appearance but differing in girth and volume can be created in this space by choosing a different value in the series of possible amplitudes $\Delta H_{\perp}$. Clearly the presentation of this variety of three dimensional objects on paper is an arduous artistic enterprise. We could construct plaster models of these bodies and display photographs of these objects taken from various angles. We could then compare such a body as measured experimentally with its counterpart generated by our model. We partially achieve the same objective in the next pages by presenting graphs of the area enclosed by individual hysteresis loops vs. amplitude for several fixed $H_{//}$ and at various fixed amplitude and mid-values of $H_{\perp}$ vs. $H_{//}$.

We emphasize that the area embraced by a closed loop or complete contour of $\langle 4\pi M\rangle_{\perp}$ vs. $H_{\perp}$ constitutes a measure of the average energy density dissipated in the sample per cycle. This is generally referred to as hysteresis or A.C. losses. This identification can readily be seen by applying the Poynting vector formulation of energy dissipation to these loops. According to the Poynting approach, W the net energy dissipated per cycle and per unit volume can be written,

$$W = \frac{1}{V} \oint \int (\vec{E} \times \vec{H}) \cdot d\vec{S}\, dt \qquad 6\text{-}29$$

where $V = a\ell_y\ell_z$ is the volume and $S = \ell_y\ell_z$ is the surface of interest for the infinite slab geometry we exploit. Since $\vec{H}$ and $\vec{B}$ are parallel to the y-z plane we obtain,

$$\vec{E} \times \vec{H} = \hat{x}\,(E_yH_z - E_zH_y)$$

Further, noting that (see chapter 5, page)

$$E_y = -\,a \frac{d}{dt} \langle B_z \rangle \quad \text{and} \quad E_z = a \frac{d}{dt} \langle B_y \rangle$$

equation 6-29 can be rewritten

$$W = \oint H_z\, d\langle B_z \rangle + \oint H_y\, d\langle B_y \rangle \qquad 6\text{-}30$$

In our work $H_z \equiv H_{//}$ is stationary hence can be placed in front of the integration sign. Consequently this term does not contribute to the energy dissipation (hysteresis losses) since $\oint d\langle B_z \rangle = \langle B_z \rangle$ initial $- \langle B_z \rangle$ final $= 0$ for a closed or complete cycle. We stress that in the previous section we presented contours of $\langle 4\pi M \rangle_{//}$ vs. $H_{\perp}$ at constant $H_{//}$. These loops embrace a finite area with the dimensions of energy but do not represent any dissipation of energy. Graphs of $\langle 4\pi M \rangle_{//}$ vs $H_{//}$ as $H_{\perp}$ is cycled for a static $H_{//}$ constitute "hysteresis loops". These trace out vertical straight lines of various lengths starting and terminating at the same point and enclose no area. The energy dissipated per cycle and per unit volume is then in our work given by

$$W = \oint H_{\perp} d \langle B_y \rangle = \oint H_{\perp} d\langle 4\pi M\rangle_{\perp} \qquad 6\text{-}31$$

Results and Discussion

In Figures 104 through 106 we present experimental and theoretical results on energy dissipation per cycle per unit volume (hysteresis losses) in ribbons of NbTi and VTi as $H_{\perp}$ oscillates at extremely low frequencies in static longitudinal fields. In this work, although the amplitudes used are appreciable, we deliberately chose these not too large. The reason for this is that we wanted to make sure that the maximum penetration of the θ and b_y profiles did not reach the mid plane. In other words we wish to ensure that the induced longitudinally flowing currents did not fill the entire slab, hence $\mu_o j_z (a) = db_y(a)/dx = 0$. The reason for introducing this constraint is twofold. We are especially interested in exploring the response of the ribbon in the regime where the behaviour is equivalent to that encountered when an alternating conduction current of amplitude $\Delta I = (2\Delta H/\mu_o)\ell_y$ is fed in from an external current supply. In the latter situation ΔI cannot exceed the critical current I_c otherwise flux flow losses and often thermal runaway occur. Further, hysteresis

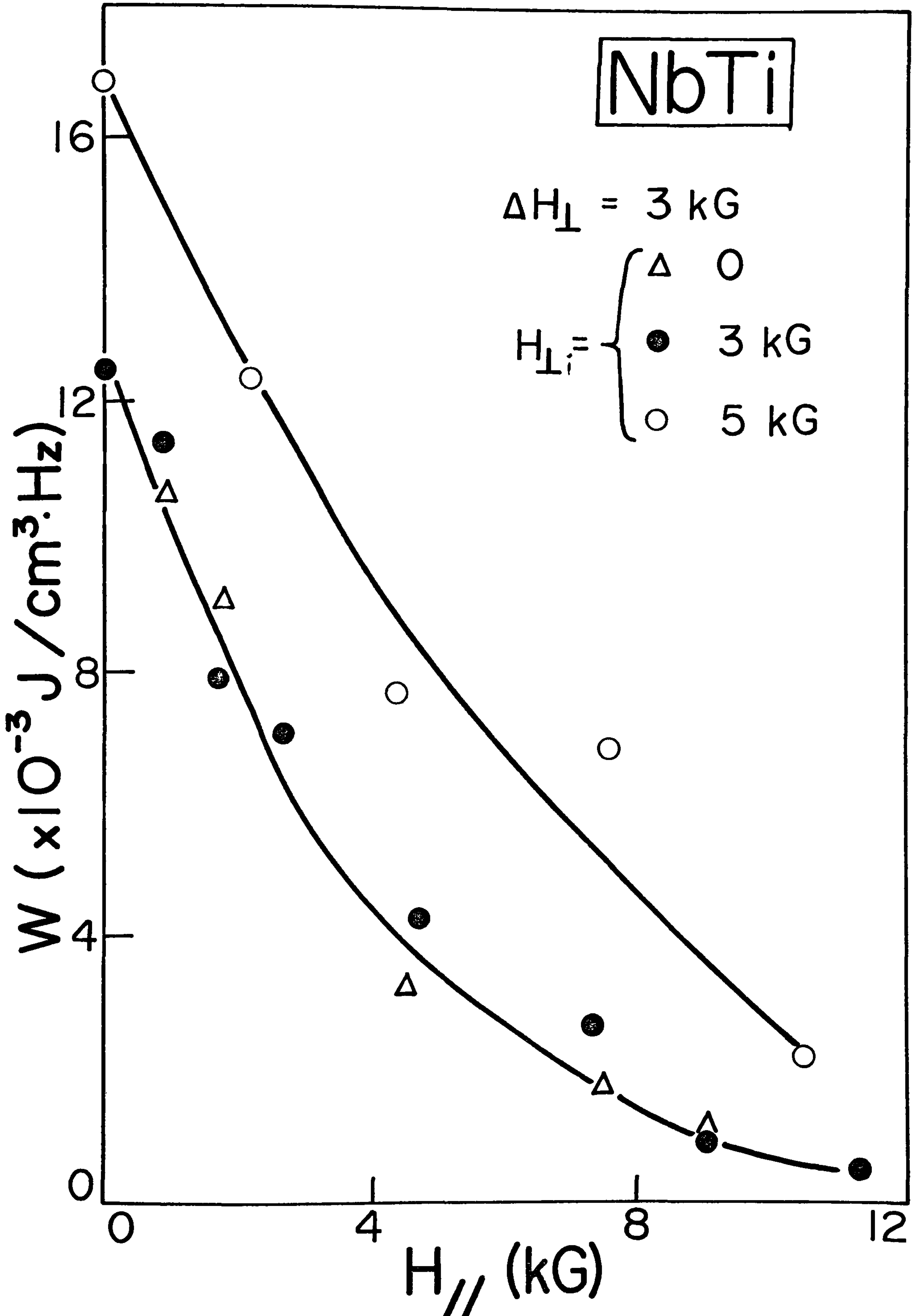

Figure 104: Experimental hysteresis losses as a function of $H_{//}$ for NbTi. ($\Delta H_{\perp}$ = 3kG).

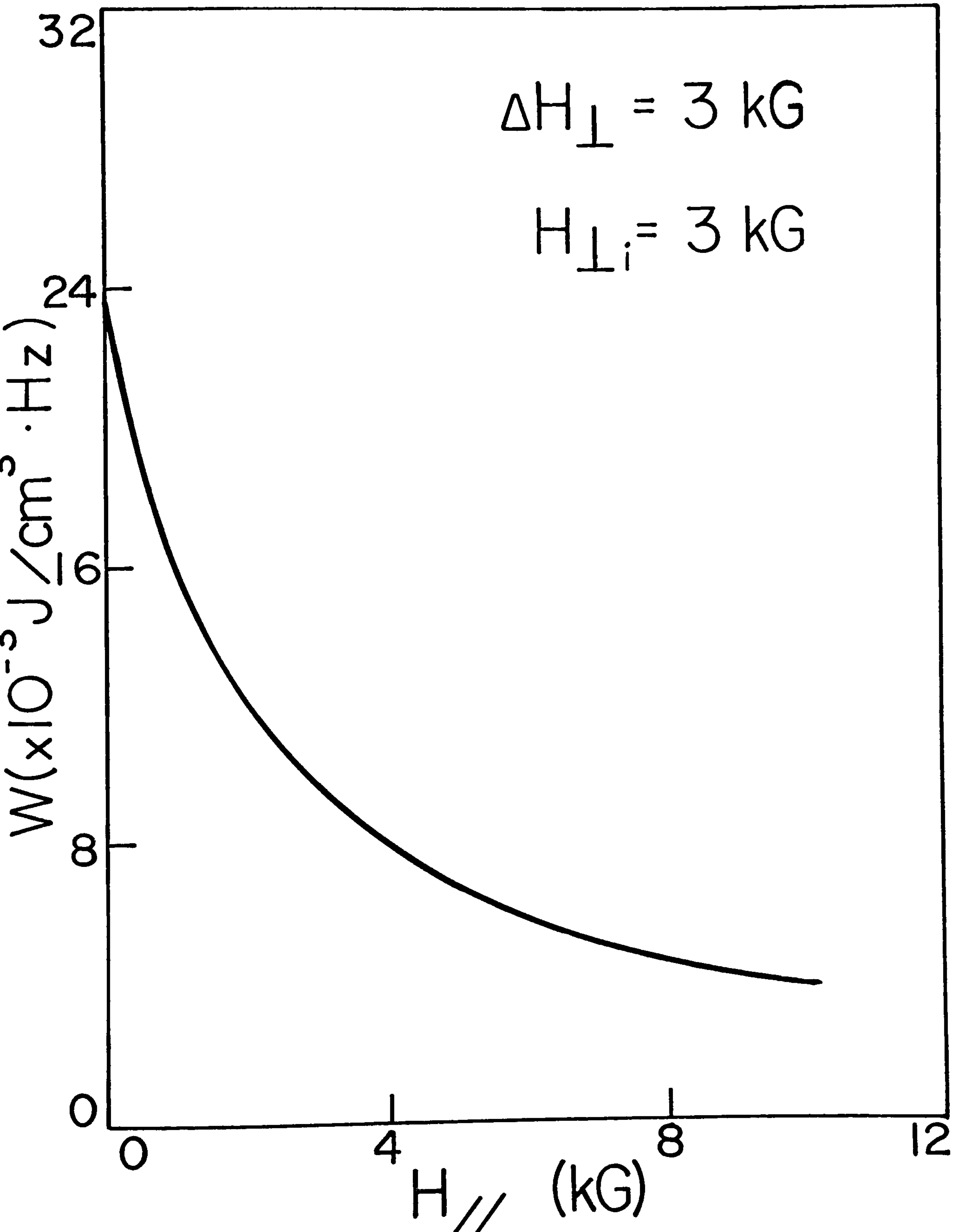

Figure 105: Hysteresis losses as a function of $H_{//}$ for NbTi calculated according to V.R. model. $H_{\perp i}$ = 3kG, $\Delta H_{\perp}$ = 3kG.

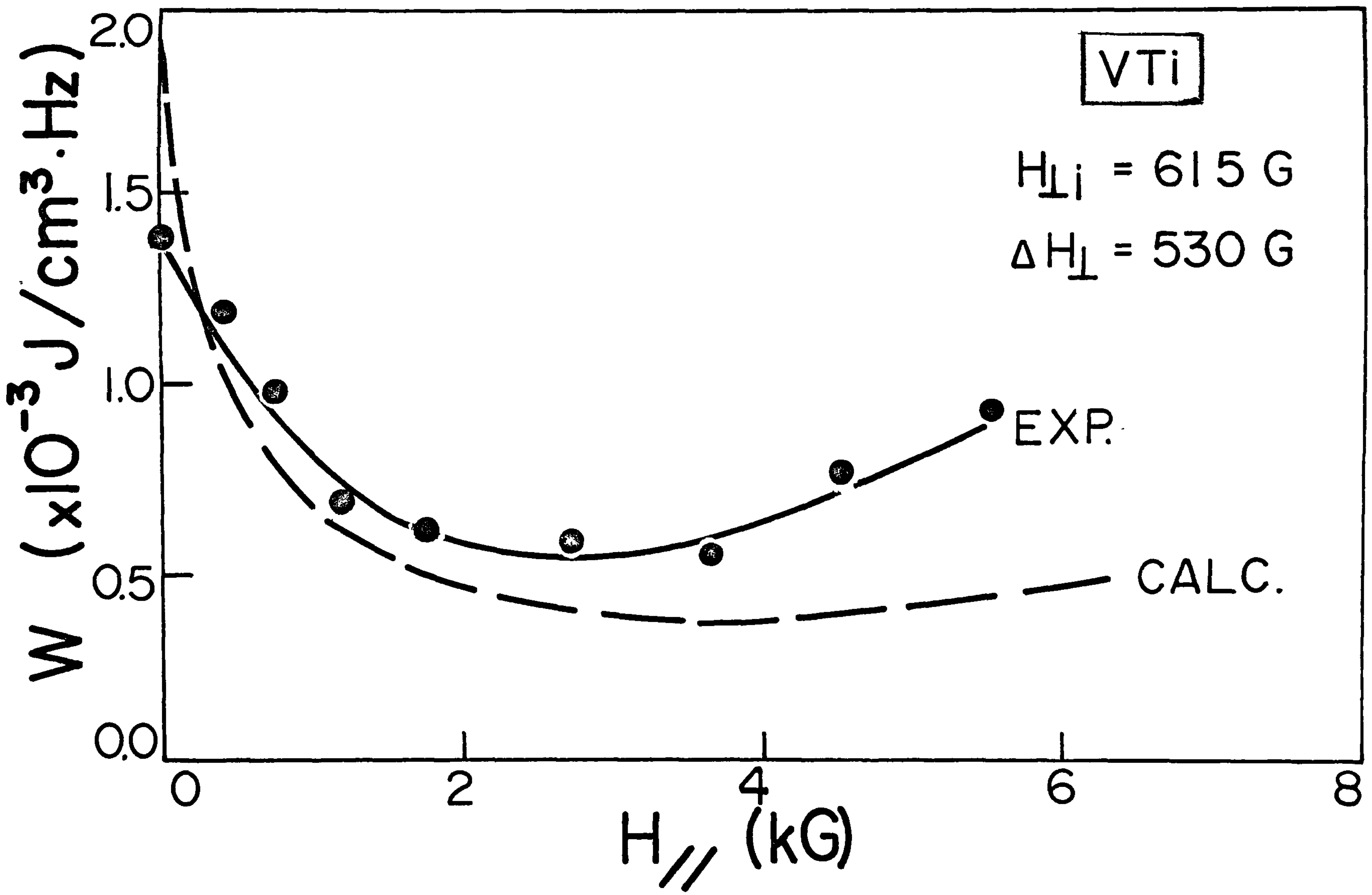

Figure 106: Experimental and calculated hysteresis losses as a function of $H_{//}$ for VTi.

losses at amplitudes $\Delta H \geq \mu_o I_c/2\ell_y$ although these can be readily measured with our set up, do not appear physically meaningful to us. (Ohmer and Heinrich 1973).

In Figure 104 we present data on hysteresis losses in NbTi as a function of $H_{//}$, for a fixed amplitude $\Delta H_{\perp} = 3$kG. The three different curves correspond to different choices for the central or mid transverse field $H_{\perp i}$. We note the dramatic reduction in losses over the range of $H_{//}$ studied. Figure 105 shows W vs $H_{//}$ calculated with our model for the same amplitude and for $H_{\perp i} = 3$ kG. In Figure 106 we compare the energy dissipation observed and calculated for the VTi sample as a function of $H_{//}$ where $\Delta H_{\perp} = 530$ G and $H_{\perp i} = 615$ G. We note that the locus of the losses both calculated and observed traverses a minimum. We return to this important feature shortly.

The initial decrease in hysteresis losses with increasing $H_{//}$ (at fixed $\Delta H_{\perp}$) occurs because the ribbon can support higher average critical currents as $H_{//}/H_{c2}$ is initially made larger. In other words, the disturbance in the b_y profile as $H_{\perp}$ oscillates through a chosen range penetrates less deeply the stronger we make $H_{//}$. This diminution in the depth of penetration of b_y (hence of j_z, of the transverse flux and also E_z) arises for two reasons. Firstly due to the resonance form of the pinning function, the effective average pinning force density initially increases as $H_{//}/H_{c2}$ increases. Secondly, the flux lines as they migrate in and out of the slab rotate in such a way that the configurations of $\vec{j}$ and $\vec{B}$ tend to be more force free than would occur if $j_y(x)$ remained zero, hence if the b_z profile stayed constant and uniform at $b_z(x) = H_{//}$. These partially force-free patterns of current permit higher densities of currents to flow before the Lorentz forces exceed the pinning forces. The rise in energy dissipation as $H_{//}/H_{c2}$ becomes large occurs because in this range of fields the pinning function has reached and passed its resonance peak and is now declining.

We show the behaviour of the losses as a function of amplitude in Figure 107 for three different values of $H_{//}$. Curves of log W versus log $\Delta H_{\perp}$ are linear within experimental accuracy and exhibit a slope p = 2.7 indicating that $W \alpha (\Delta H_{\perp})^p$. For induced currents circulating longitudinally only we expect p = 3 (Hancox 1966).

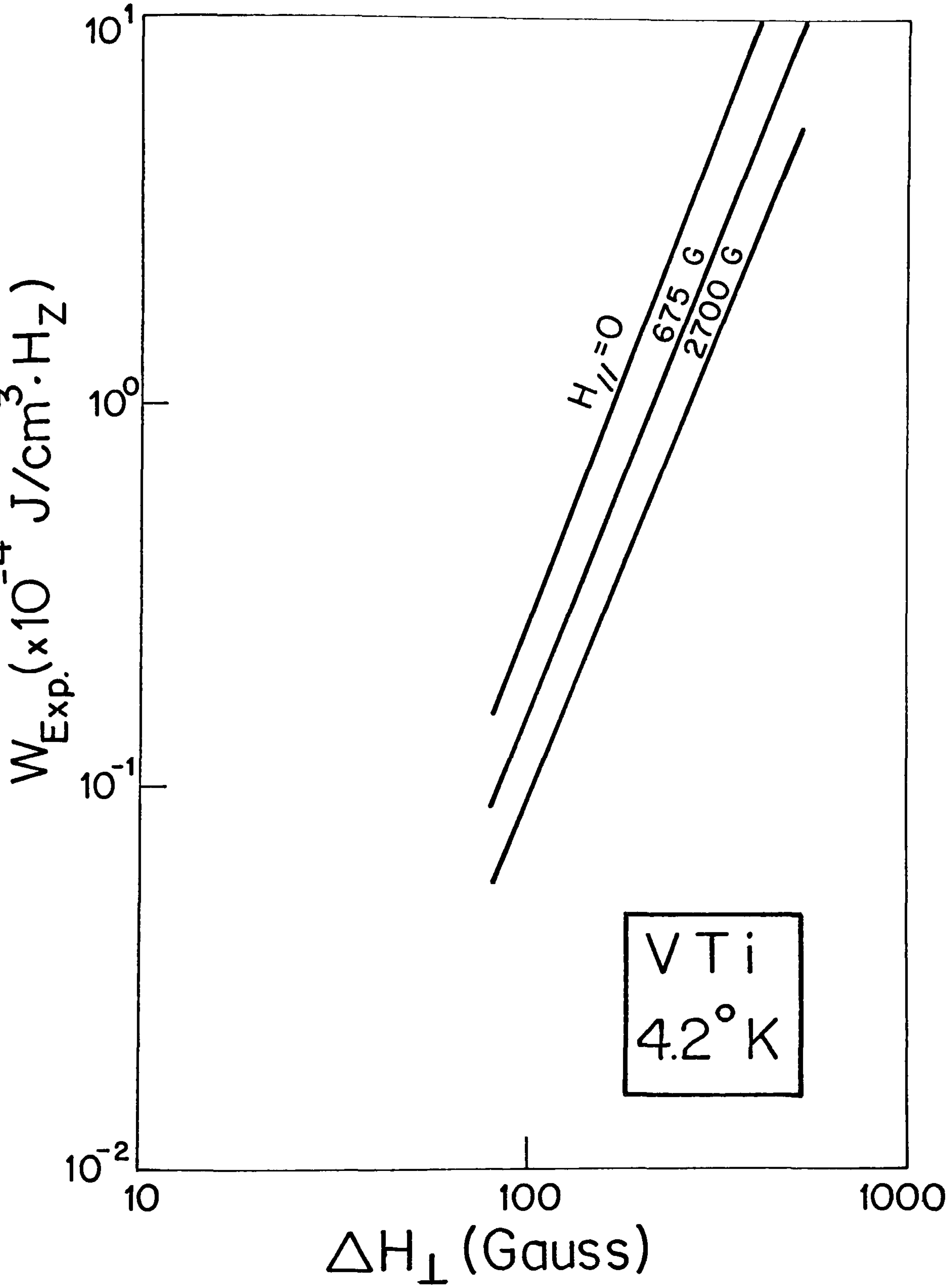

Figure 107: Experimental hysteresis losses as a function of amplitude, $\Delta H_\perp$, for fixed values of $H_{//}$, for VTi.

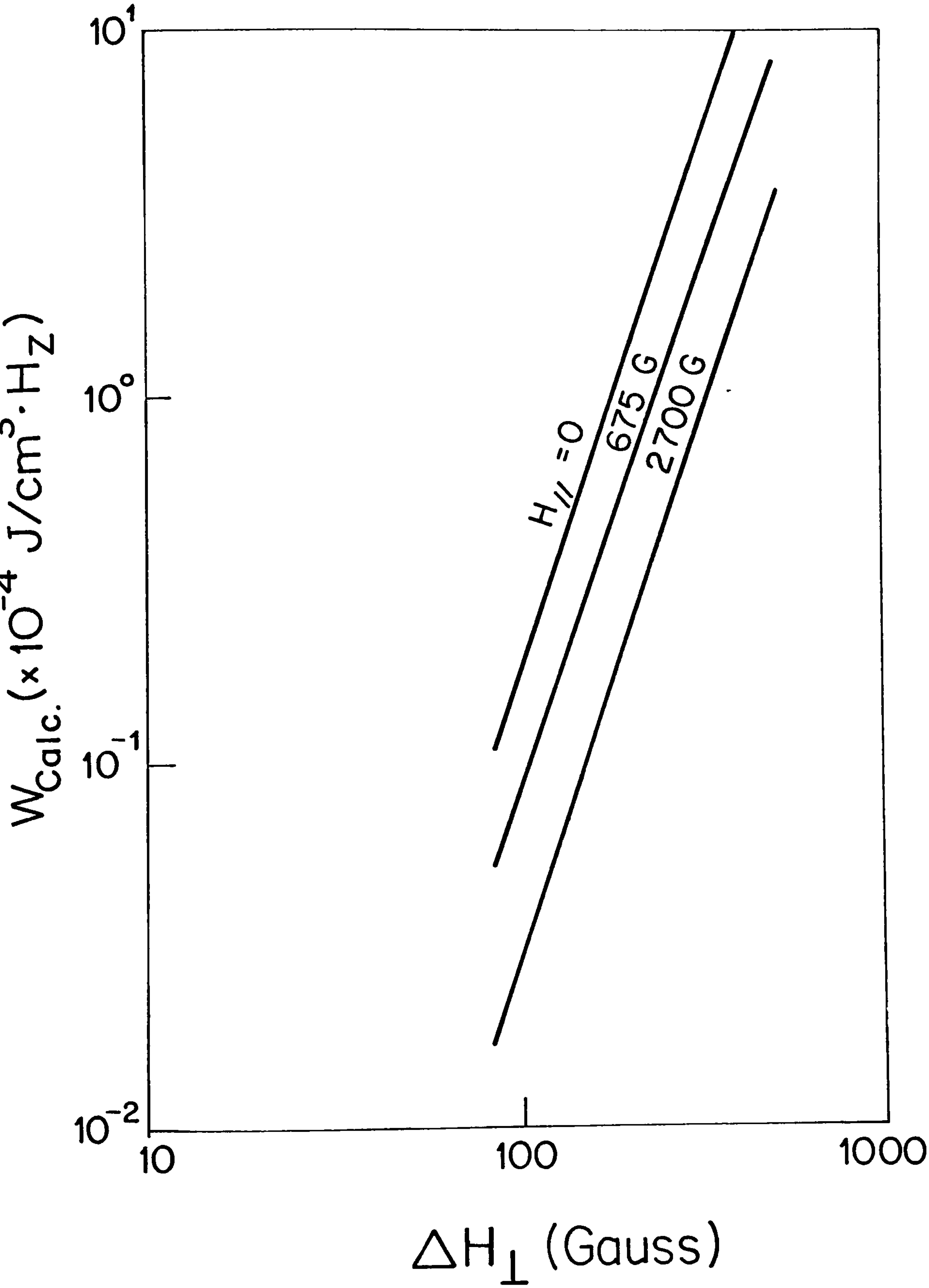

Figure 108: Calculated hysteresis losses as a function of amplitude, $\Delta H_{\perp}$, for fixed values of $H_{//}$, for VTi.

Conclusion

Our empirical vortex rotation model, which is a compromise between the two contrasting models of Bergeron (free rotation of fluxons) and Campbell-Evetts (no rotation), is rather successful in describing the magnetic behaviour of our samples over a wide variety of magnetic histories where $H_\perp$ is i) increased ii) decreased from an initial value and iii) cycled about an initial value with $H_{//}$ stationary.

The essential new feature of the model is the introduction of a critical state concept for the spatial variation of the orientation of the vortices to complement the critical state concept for the spatial variation of flux density. Specifically we put forward the simple prescription

$$\frac{d\theta}{dx} = \pm \gamma \frac{F_p(B)}{B^2 \tan \theta}$$

to govern the θ profile. The exploitation of this rule, in tandem with the appropriate critical state equation to determine the B profile, provides a satisfactory description of the response of slabs of hysteretic type II superconductors to simultaneous changes in the strength and direction of a magnetic field applied parallel to the surface of the slab. We apply these two concepts only in the framework where $B(x) \approx H(x)$, hence our results are valid for very irreversible type II superconductors and materials with high Ginzburg-Landau parameter κ.

The model we have developed gives us some insight into the phenomenon of vortex rotation and the interaction of non parallel planes of vortices with each other and with pinning sites. The model accounts quite satisfactorily for a) the increases in $<4\pi M>_{\perp}$, hence the enhancement of the longitudinal critical current densities, b) the degree of "tilt" as reflected in the measurements of $<4\pi M>_{//}$ and c) the dramatic decrease in hysteresis losses when the samples are immersed in a static longitudinal magnetic field, $H_{//}$. Presumably, reversible contributions to the local and average magnetization can be introduced into the model without affecting its basic structure. Such an extension of our work is in progress.

APPENDIX I

The equation of continuity or conservation of vortices for infinite slab geometry can be written in the form

$$\frac{dv}{dx} + \frac{1}{B}\frac{dB}{dx}v = -\frac{I}{B}\frac{dB}{dt}$$

Recalling that differential equations of the form

$$\frac{dy}{dx} + P(x)\,y = Q(x) \qquad \text{I-1}$$

have a solution of the form

$$y = \left(\int Q(x)e^{\int P\,dx}dx + C\right)e^{-\int P dx}$$

we let $P = \frac{1}{B}\frac{dB}{dx}$ and $Q = -\frac{I}{B}\frac{dB}{dt}$

Substituting v for y we obtain

$$v(x) = \left(-\int \frac{\dot{B}}{B}e^{\int \frac{1}{B}\frac{dB}{dx}dx}dx + C\right)e^{-\int \frac{1}{B}\frac{dB}{dx}dx}$$

$$= \left(-\int \frac{\dot{B}}{B}e^{\ell nB}dx + C\right)e^{-\ell nB}$$

$$= \left(-\int \frac{\dot{B}}{B}B\,dx + C\right)\frac{1}{B}$$

$$= \frac{C}{B} - \frac{1}{B}\int \dot{B}\,dx \qquad \text{I-2}$$

where C is a constant of integration.

We note that this result can also be obtained directly from integration of the equation of continuity $d(vB)/dx = -dB/dt$ with respect to x, thus we obtain

$$(vB)_x - (vB)_{x=0} = -\int_0^x \dot{B}\,dx \qquad \text{I-3}$$

where

$$(vB)_{x=0} = C$$

Since B depends on time through H_s only we may write

$$\dot{B} = \frac{dB}{dH_s} \dot{H}_s \qquad \text{I-4}$$

The critical state equation for infinite slab geometry

$$B \frac{dB}{dx} = \pm F (B) \qquad \text{I-5}$$

yields after differentiation with respect to time and some manipulation

$$\frac{d\dot{B}}{dx} + \frac{1}{B} \left(\frac{dB}{dx} \pm \frac{dF}{dB} \right) \dot{B} = 0$$

which is similar to equation I-1. Letting $y = \dot{B}$,

$P(x) = \frac{1}{B} \left(\frac{dB}{dx} \pm \frac{dF}{dB} \right)$, $Q(x) = 0$ we obtain

$$\dot{B} (x) = C' e^{- \int \frac{dB}{B} \pm \int \frac{1}{B} \frac{dF}{dB} dx} = \frac{C'}{B} e^{\pm \int \frac{1}{B} \frac{dF}{dB} \frac{dx}{dB} dB}$$

Introducing the critical state equation in the form

$dx/dB = \pm B/F(B)$ into the exponent yields

$$\dot{B}(x) = \frac{C'}{B} e^{\int \frac{dF}{F}} = C' \frac{F}{B} \qquad \text{I-6}$$

at the surface $\dot{B} = \dot{H}_s$ hence

$C' = H_s \dot{H}_s / F(H_s)$ and equation I-6 becomes

$$\dot{B} = \frac{H_s \dot{H}_s F(B)}{B \; F(H_s)} = \pm \frac{H_s \dot{H}_s}{F \; (H_s)} \frac{dB}{dx}$$

where we have again introduced the critical state equation. We can now integrate the right hand side of equation I-2 and obtain

$$(vB)_x - (vB)_o = \pm \frac{H_s \dot{H}_s}{F(H_s)} (B - H_s) \qquad \text{I-7}$$

Since $v = 0$ at the depth where $B = H_{//}$ we obtain

$$v_s = v(0) = \pm \frac{\dot{H}_s (H_{//} \quad H_s)}{F(H_s)}$$

Alternatively after full penetration $v = 0$ at the center of the slab where $B = B(a)$ and equation I-5 then yields

$$v_s = \pm \frac{\dot{H}_s}{F(H_s)} (B(a) - H_s) \qquad \text{I-8}$$

We are indebted to Dr. R.C. Smith for providing us with this general derivation.

APPENDIX II

We wish to prove that the empirical expression

$$b_z(x) = H_{//} \left(\frac{H_s}{B(x)} \right)^k \tag{II-1}$$

for the rotation of the vortices means that the B disturbance penetrates more deeply than the θ disturbance whether the transverse field is increased or decreased from some initial value $H_{\perp i}$ while $H_{//}$ is maintained constant. To show this it is sufficient to determine whether the ratio B/H_{si} is greater or less than unity at the position where the direction of the vortices coincides with θ_i, that existing initially when the slab became superconducting.

Introducing equation II-1 into the definition $\cos\theta = b_z/B$ for the orientation of the vortices yields

$$\cos\theta = \frac{H_{//} H_s^k}{B^{k+1}} \tag{II-2}$$

Initially we had

$$\cos\theta_i = \frac{H_{//}}{H_{si}} \tag{II-3}$$

At a depth x_o, $\theta = \theta_i$ hence

$$\cos\theta(x_o) = \frac{H_{//} H_s^k}{B(x_o)^{k+1}} = \cos\theta_i = \frac{H_{//}}{H_{si}} \tag{II-4}$$

This leads after some manipulation to the relation

$$\frac{B(x_o)}{H_{si}} = \left(\frac{H_s}{H_{si}} \right)^{k/k+1} \tag{II-5}$$

where $k > 1$, hence $1/2 \leq k/(k+1) < 1$.

We recall that $H_s = (H^2_\perp + H^2_{//})^{\frac{1}{2}}$ and $H_{si} = (H^2_{\perp i} + H^2_{//})^{\frac{1}{2}}$. A consequence of the critical state concept is that B varies monotonically from H_s at the surface $(x = 0)$ to H_{si} at a depth x_1, the distance of penetration of the B-disturbance regardless of the choice of pinning function. We see from inspection of equation II-5 that $B(x_o) > H_{si}$ if $H_s > H_{si}$ or alternatively that $B(x_o) < H_{si}$ if $H_s < H_{si}$ hence $x_o < x_1$ since the θ disturbance has "terminated" but the B disturbance is not yet "completed" at the depth x_o.

Appendix III

We examine whether during phase 3 of a cycle with reversal of polarity of $H_\perp$, the distance x''_{oo} (from the surface) where the θ disturbance crosses the zero axis is greater or less than x''_1, the depth at which the concomitant B disturbance reaches the B profile existing at the end of phase 2. The two possibilities are presented schematically below.

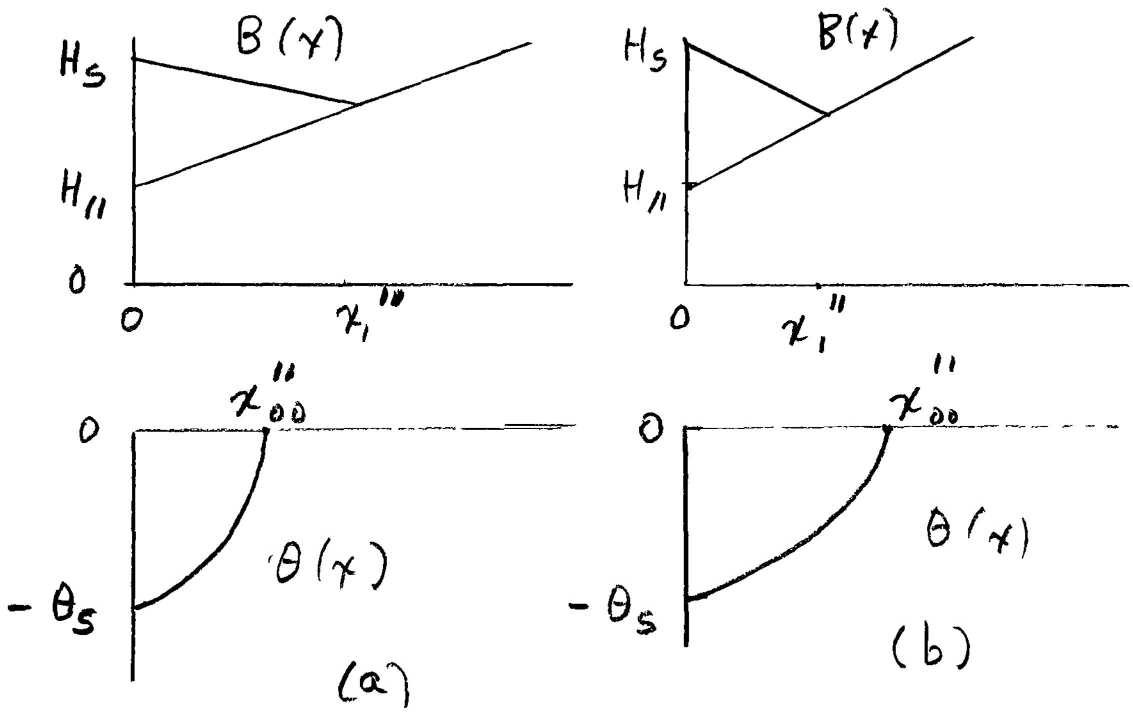

We explore this question within the framework of pinning functions of the form $F_p = \alpha B^n$ where $0 \leq n \leq 1$. Integrating the critical state function $BdB/dx = \pm F_p = \pm \alpha B^n$ we obtain

$$B(x) = \{H_{//}^{2-n} + (2 - n)\ \alpha x\}^{1/(2 - n)} \qquad \text{III-1}$$

for the B-profile near the surface at the end of phase 2 and

$$B(x) = \{H_s^{2-n} - (2 - n)\ \alpha x\}^{1/(2 - n)} \qquad \text{III-2}$$

for the profile of the new B disturbance in phase 3 where III-2 is valid for $x \leq x_1''$. Exploiting equations III-1 and III-2 we determine the value of B at x_1'' to be

$$B\ (x_1'') = \left(\frac{H_{//}^{2-n} + H_s^{2-n}}{2}\right)^{1/(2 - n)} \qquad \text{III-3a}$$

From equation 6-5 and its integral 6-6 which apply in the region $0 \leq x \leq x_{oo}''$ in sketch (a) we determine the value of B at x_{oo}'' to be

$$B(x_{oo}'') = (H_{//}H_s^k)^{1/(k + 1)} \qquad \text{III-4a}$$

since here $B = b_z$ because $\theta = 0$.

We can now establish whether $x_{oo}'' \leq x_1''$ by determining whether $B(x_{oo}'') > B(x_1'')$ for common values of $H_{//}$ and H_s. We write $H_s = H_{//} + \Delta$. Introducing this in equations III-3 and III-4 and after some manipulation we obtain

$$\frac{B(x_1'')}{H_{//}} = \left\{\frac{1 + (1 + y)^{2-n}}{2}\right\}^{1/(2 - n)} \qquad \text{III-3b}$$

and $$\frac{B(x_{oo}'')}{H_{//}} = (1 + y)^{k/(k + 1)} \qquad \text{III-4b}$$

where $y = \Delta/H_{//} = \{1 + (H_{\perp}/H_{//})^2\}^{\frac{1}{2}} - 1$. Figure 109 shows graphs of these two quantities computed for k = 1, 2 and n = 0, 1/2 and 1 respectively. We note that for the case of special interest in our work (k = 2, n = 1/2), $x_{oo}'' < x_1$ in the range of fields used.

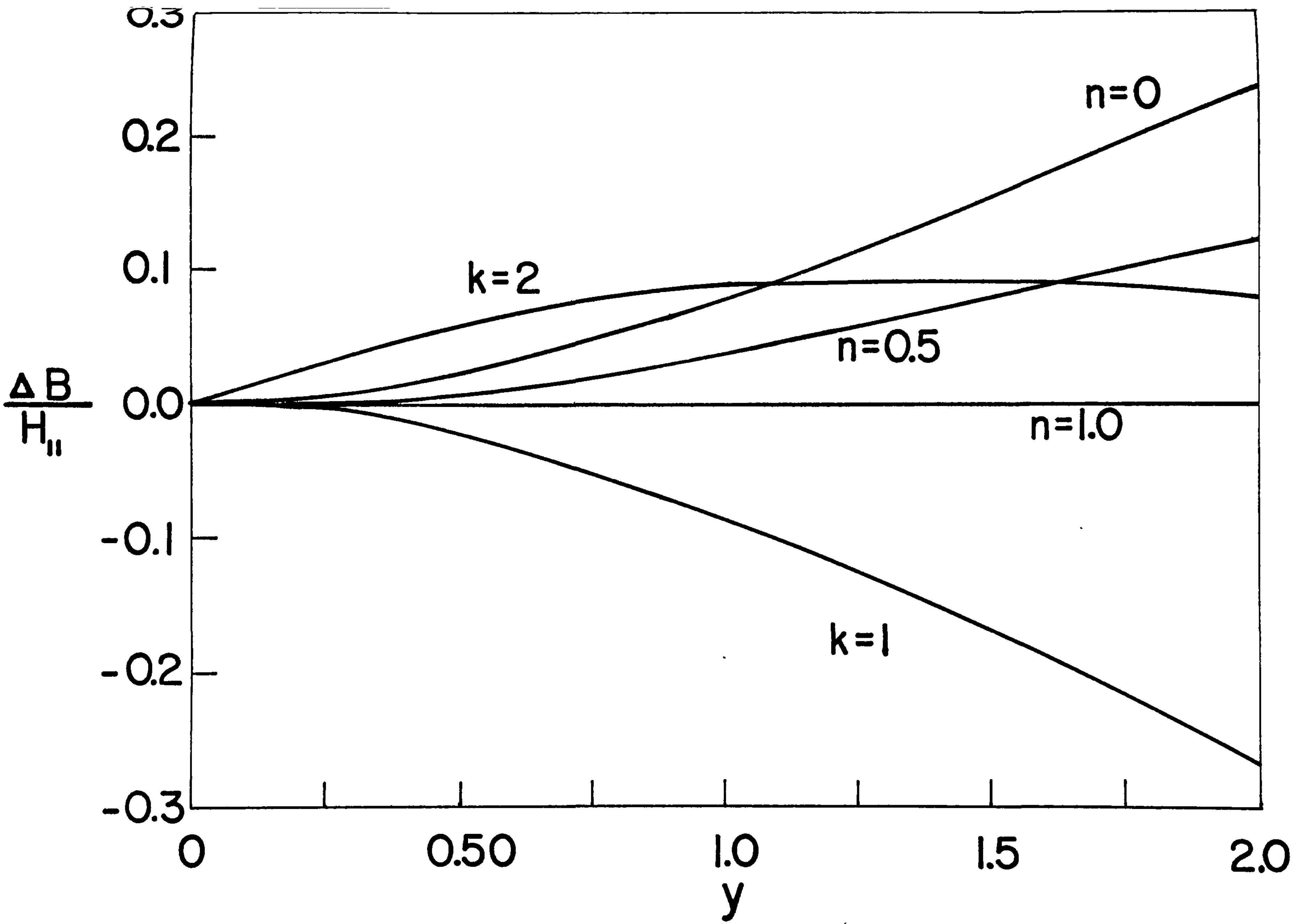

Figure 109: $\Delta B/H_{\parallel}$ versus $y = \Delta/H_{\parallel}$, where $\Delta B = B - B(x_1'')_{k=1}$ and $B = B(x_{oo}'')$ or $B(x_1'')$. Curve k = 2 lies above curve n = 1/2 hence $x_{oo}'' < x_1''$ until Δ becomes large in analysis of VTi.

REFERENCES

Abrikosov (57): Abrikosov A.A., Soviet Phys. JETP 5, 1174 (1957)

Bean (64): Bean C.P., Rev. Mod. Phys. 36, 31 (1964)

Bergeron (63): Bergeron C.J., Appl. Phys. Lett. 3, 63 (1963)

Campbell (72): Campbell A.M. and Evetts J.E., Adv. in Phys. 21, 90 (1972)

Hancox (66): Hancox R., Proc. IEEE 113, 1221 (1966)

LeBlanc (65): LeBlanc M.A.R., Belanger B.C. and Fielding R.M., Phys. Rev. Lett. 14, 704 (1965)

Mattes (70): Mattes H.G. and LeBlanc M.A.R., Jour. Appl. Phys. 41, 1567 (1970)

Ohmer (73): Ohmer M. and Heinrich J.P., J. Appl. Phys. 44, 1804 (1973)

Sekula (63): Sekula S.T., Boom R.W. and Bergeron C.J., Appl. Phys. Lett. 2, 102 (1963)

Sugahara (71): Sugahara M., Jap. J. Appl. Phys. 9, 625 (1971)

Timms (74): Timms W.E. and LeBlanc M.A.R., J. Phys. F. Metal Phys., 4, 136 (1974)

Walmsley (72): Walmsley D.G., J. Phys. F, 2, 510 (1972)

Yamafuji (75): Yamafuji K., Kawashima T. and Ichikawa H., J. Phys. Soc. Japan 39, 581 (1975)

Zahradnitsky (73): Zahradnitsky A., Master's thesis, University of Ottawa, Canada (1973).